HYDRODYNAMICS OF LARGE-SCALE ROUGHNESS IN OPEN CHANNELS

A thesis submitted to Cardiff University

In candidature for the degree of

Doctor of Philosophy

by

Saad Mulahasan

Division of Civil Engineering, Cardiff School of Engineering

Cardiff University, 2016

HYDRODYNAMICS OF LARGE-SCALE ROUGHNESS IN OPEN CHANNELS

Approved by:

PROFESSOR THORSTEN STOESSER, Advisor

Hydro-Environmental Research Centre

Cardiff School of Engineering

Cardiff University

Dr. PETER J CLEALL

Cardiff School of Engineering

Cardiff University

Date Approved: 2016

DECLARATION

This work has not been submitted in substance for any other degree or award at this or any other university or place of learning, nor is being submitted concurrently in candidature for any degree or other award.

Signed……Date ……

STATEMENT 1

This thesis is being submitted in partial fulfilment of the requirements for the degree of PhD

Signed……Date ……

STATEMENT 2

This thesis is the result of my own independent work/investigation, except where otherwise stated. Other sources are acknowledged by explicit references. The views expressed are my own.

Signed……Date ……

STATEMENT 3

I hereby give consent for my thesis, if accepted, to be available for photocopying and for inter-library loan, and for the title and summary to be made available to outside organizations.

Signed……Date ……

STATEMENT 4

I hereby give consent for my thesis, if accepted, to be available for photocopying and for inter-library loans **after expiry of a bar on access previously approved by the Academic Standards & Quality Committee.**

Signed……Date ……

ACKNOWLEDGEMENTS

The undertaking of this thesis has been above all a great human adventure, which would not have been possible without the support of many.

First, I would like to thank my supervisor, Professor Thorsten Stoesser who shared his wealth of knowledge and guided me. I have been extremely lucky to have a supervisor who cared so much about my work, and who responded to my questions and queries so promptly.

I am very grateful to my second supervisor, Dr. Peter J Cleall for providing valuable comments and discussions due to last three annual reviews that helped me to improve my dissertation.

I want to thank Iraqi government for the financial support.

I would also like to thank all the members of staff and students of the Hydro environmental Research Centre at Cardiff University for their support and guidance.

I would like to thank all staff members in research office and finance office in school of engineering for their help due to my research period.

Thanks to all IT staff members who support my research with continuously supplying network and helps.

Finally, I must express my gratitude to Suhailah my wife, for her continued encouragement.

SUMMARY

This thesis investigates the hydrodynamics of flow around/and or above an obstacle(s) placed in a fully turbulent developed flow such as flow around lateral bridge constriction, flow over bridge deck and flow over square ribs that are characterized with free surface flow. Also this thesis examines the flow around one-line circular cylinders placed at centre in a single open channel and floodplain edge in a compound, open channel.

*Hydrodynamics studies of compound channels with vegetated floodplain have been carried out by a number studies of authors in the last three decades. To enrich our understanding of the flow resistance, comprehensive experiments are carried out with two vegetation configurations-wholly vegetated floodplain and one-line vegetation and then compared to smooth unvegetated compound channel. The main result of the flow characteristics in vegetated compound channels is that spanwise velocity profiles exhibit markedly different characters in the one-line and wholly-vegetated configurations. Moreover, flow resistance estimation results are in agreement with other experimental studies.

*A complementary experimental study was carried out to investigate the water surface response in an open-channel flow through a lateral channel constriction and a bridge opening with overtopping. The flow through the bridge openings is characterized by very strong variation of the water surface including undular hydraulic jumps. The results of simulation that was carried by (Kara et al. 2014, 2015) showed a reasonable agreement between measured and computed water surface profiles for the constriction case and a fairly good was achieved for the overtopping case.

*Evaluation of the shear layer dynamics in compound channel flows is carried out using infrared thermography technique with two vegetation configurations - wholly vegetated floodplain and one-line vegetation in comparison to non-vegetated floodplains. This technique also manifests some potential as a flow visualization technique, and leaves space for future studies and research. Results highlight that the mixing shear layer at the interface between the main channel and the floodplain is well captured and quantified by this novel approach.

*Flume experiments of turbulent open channel flows over bed-mounted square bars at low and intermediate submergence are carried out for six cases. Two bar spacings, corresponding to transitional and *k*-type roughness, and three flow rates, are investigated. This experimental study focused on two of the most aspects of channel rough shallow flows: water surface profile and mean streamwise vertical velocity. Results show that the water surface was observed to be very complex and turbulent for the large spacing cases, and comprised a single hydraulic jump between the bars. The streamwise position of the jump varied between the cases, with the distance of the jump from the previous upstream bar increasing with flow rate. The free surface was observed to be less complex in the small spacing cases, particularly for the two higher flow rates, in which case the flow resembled a classic skimming flow. The Darcy-Weisbach friction factor was calculated for all six cases from a simple momentum balance, and it was shown that for a given flow rate the larger bar spacing produces higher resistance. The result of the simulation that was carried out by Chua et al. (2016) shows good agreement with the experiments in terms of mean free surface position and mean streamwise velocity.

*Drag coefficient empirical equations are predicted by a number of authors for an array of vegetation. The research aims to assess the suitability of various empirical formulations to predict the drag coefficient of in-line vegetation. Drag coefficient results show that varying the diameter of the rigid emergent vegetation affects significantly flow resistance. Good agreement is generally observed with those empirical equations.

Key Words: Flow Visualization; Infrared Thermography; Shallow Flows; Shear layer; Image processing; Experiment; Free surface; Bridge hydrodynamics; Bridge overtopping; Vegetation roughness, Emergent vegetation, Drag coefficient, blockage; Compound channel, Lateral velocity profiles; Hydraulic resistance; Hydraulic jump, Square bars.

Table of Contents

CHAPTER ONE

INTODUCTION

1 INTRODUCTION

1.1 BACKGROUND OF THE STUDY

River flows, flows over weirs, water waves and man-made channels convey free surface water whose surface is exposed to the atmosphere. The study of the flow around an obstacle(s) placed in a fully developed channel flow such as cylinders, bridge constrictions, flows over bridge decks/ ribs, is characterized by free surface variations which is fundamental to the understanding of the flow mechanisms for complex two- and three dimensional geometries.

In open channel flow, the presence of a hydraulic structure such as a weir or bridge controls the flow rate over it as well as the position of the free surface. In flood conditions, increasing discharge may cause bridge failure due to scouring at the sediment bed. The water level is significantly raised, existing bridges may become fully submerged with submerged orifice flow occurring through the bridge opening and overtopping of the bridge deck, and bridges may be damaged during flood events. Martín V. (2002) studied the cause of failure for 143 bridges worldwide; it was found that 49% out of 143 bridges failed due to flood events (after Kingston (2006)). The flood of 1993 in the Midwestern US paralysed a nine state area with flood recurrence intervals varying from 100 to 500 years. Two months after the flood, a scour hole with a depth of 17 m was mapped near the abutment of an interstate bridge (Parola et al. 1998). In 2009, at the Atlanta metropolitan area, Georgia, there was extensive damage to bridge abutments and embankments due to overtopping (Gotvald and McCallum 2010). These examples of bridge failures highlight the importance of understanding the interaction of water flow with bridge abutment and embankments rather than considering the bridge structure in isolation. Knowing the maximum increase of the water level in front of the obstruction is essential during the flood seasons in order to best design future water resources systems and hydraulic structures. There is still limited works which investigate the response of the water surface profile in an open channel flow through different forms of bridge openings; there are only a few physical modelling studies reported in the literature of flow over inundated bridges and the accompanying water surface profiles (Merville 1995, Oliveto and Hager 2002, Sturm 2006).

A bridge, including deck and abutments, is considered in this study to investigate the response of the water surface in an open-channel flow through different forms of bridge openings.

In rough open channel flows of steep slopes with low and intermediate submergence such as steep slope mountain streams, the free surface profile carries the signature of the bed roughness and flow regime while it affects the turbulent flow structures and bed forms; and individual hydraulic jumps may be observed. There is no standard analytical expression of the flow resistance equation for the determination of the mean flow velocity for turbulent rough open channel flows making the application of the flow resistance equation challenging for specialists. Numerous friction factor equations were derived relative to parameters such as roughness spacing, relative submergence, and bed material concentration, (Bathurst 1978, Bray 1979, Hey 1979, Thompson and Campbell 1979, Bathurst et al. 1981, Bathurst 1985, Bathurst 2002, Pagliara and Chiavaccini 2006, Rickenmann and Recking 2011). Knowing the parameters of influence helps researchers and practitioners in solving hydraulic engineering problems relative to bed slopes, water depths, submergence ratios, and roughness concentrations. There are limited works investigating flow resistance due to large-scale roughness at steep bed slopes of low relative submergence. In this research, the hydrodynamics of shallow flows that are strongly influenced by water surface deformation, and to quantify the effect of roughness spacing and relative submergence on hydraulic resistance in such flows is displayed.

When the water surface of the river flow just reaches its banks, the discharge flowing through the river is called bank full discharge. If the flow exceeds the main channel capacity, the water will overflow the banks and will immerse the floodplains. In this case the river capacity decreases due to the generation of shear layers and the free surface of water is controlled by the density, distribution and configuration of the vegetation elements on the floodplain. Large scale horizontal coherent structures generated near the interface between the main channel and the floodplain of compound channels have been observed with different techniques by a number of authors (Tamai et al. 1986, Tominaga and Nezu 1991, Nezu and Onitsuka 2001, van Prooijen et al. 2005, Rummel et al. 2006, White and Nepf 2007, Nezu and Sanjou 2008, Stocchino and Brocchini 2010). These coherent structures (shear layers) are

influenced by the density of the vegetation elements and their configurations on the floodplain. To better understand the above phenomenon a novel approach of visualization technique can be used. In this research, a thermal camera SC640 and heat tracer (hot water) is used to track the coherent structures at the water surface at the interface between the main channel and the floodplain in the compound channel flow.

Open channel flow through a one-line array of vertically-oriented circular rods of varying diameters still comprises limited works (Sun and Shiono 2009, Terrier et al. 2010, Terrier et al. 2011, Shiono et al. 2012, Miyab et al. 2015), particularly with regards to drag coefficient calculations. Drag coefficient is calculated in terms of emergent vegetation from equalling gravity force to drag force (Petryk and Bosmajian 1975). A new idea was used to compare the drag coefficient results from one-line vegetation to drag coefficient from an array of vegetation elements as proposed by a number of researchers. In this research, drag coefficients are compared to a number of expressions that have been proposed for an array of emergent rigid vegetation cylindrical cylinders.

The presence of vegetation on the edge of the floodplain reduces the section capacity of the river and its floodplain, and makes the interaction between the main channel and the floodplain complex. Some common patterns of vegetation that is growing at the edge of UK Rivers are straight lines, such as the River Dove at Dovedale, the River Dove at Milldale, and the River Severn at Ironbridge Gorge. Flooding in these areas usually arises from water overtopping the banks of streams. Flow structure of water through a one-line array and fully vegetation distribution of vertically-oriented circular cylinders placed along the edge of the floodplain adjacent to the main channel, and on the entire width of the floodplain in a compound channel have been considered by a number of authors (Tominaga and Nezu 1991, van Prooijen et al. 2005, Yang et al. 2007, Sun and Shiono 2009, Vermaas et al. 2011, Aberle and Järvelä 2013). In this research vegetation elements are modelled by emergent rigid wooden rods of circular cross-section. For the vegetated cases the effect of vegetation density is investigated, and in all cases three flow rates were tested. The effect of vegetation density and distribution on the floodplain on the rating curve, the drag coefficients and the stream-wise velocity distribution in an asymmetric

compound channel is investigated experimentally. Additional focus is placed upon the importance of interfacial shear stress in drag coefficient calculations.

1.2 VISUALIZATION MEASUREMENT TECHNIQUES

Visualization of water flow through vegetation elements is mainly carried out by different techniques such as adding different materials to the flow and then using optical imaging technique to track the motion of the flow. In such case, the tracer motion is measured instead of the flow itself considering the tracer to be passive. Rhodamine dye tracer can be tracked visually, and can be used for measuring the surface velocity of the flow. However, there are increasing concerns over the use of dyes that can cause environmental impacts such as the colour and the toxic properties of the dyes (Chequer et al. 2013).

Over the years, significant improvements and developments in visualization techniques have been performed not only resulting in higher accuracy and quality of the obtained data, but also with the evolution of powerful new techniques with new abilities and features, benefiting from the great development of technology in other areas of knowledge. Flow visualization techniques such as digital cameras, laser based methods (particle image velocimetry (PIV)/ particle tracking velocimetry (PTV), laser induced fluorescence (LIF), laser Doppler anemometer (LDA), and infrared thermography techniques (IF) have been developed in the last three decades. Thermal cameras have been developed and widely propagated in the world since the mid- 1990s.

Infrared thermography is a technique for detecting and measuring the energy that radiates through the surface, not the temperature of the object itself. Thermal cameras with special lens are used to detect, measure and collect the radiated thermal energy and then convert to signals that can be processed to obtain the image with a colour code.

Infrared thermography techniques (IR) may be used in different parts of water science applications such as water resources, hydraulics, hydrology, fluid dynamics, and soil and water preservation.

One of the choices with thermography techniques is that hot water is applied as heat tracer and is then used for visualization. Using thermography technique makes it

possible to detect more information about the flow crisis such as coherent structures (vortices) at the water surface and details of the flow can be extracted. The use of IR thermography technique for flow measurements has not been extensively explored yet, and its capabilities have yet to be studied.

Recording the spatial state of the free surface profile of water requires various accumulations of sensors. Instead of these sensors, a particle image velocimetry (PIV) is used that is capable of obtaining qualitative and quantitative information such as velocity fields at any plane of shallow flows and not in a point as with ADV. A PIV provides data measuring of flow velocities that vary in both time and space. In addition, this technique can also be used as a non-intrusive visualization device which make it possible to detect more information about the flow such as turbulent coherent structures (eddies), and can be used to track the water surface profile. A PIV system mainly consists of CCD camera, and flash stroboscope for illumination. Seeding particles are added to the flow and illuminated by the halogen lamps.

The understanding of the free surface response of water flowing in steep ribbed flumes remains limited; mainly, the impact of (roughness spacing, λ, to roughness height, k) i.e. λ/k ratio, and (water depth, H, to roughness height, k) submergence ratio, H/k on the water surface profile. Applying these visualization techniques (IR thermography and PIV), various flow phenomena can be visualized and deeply studied and then unclear aspects of their behaviour can be better explained.

The visualization techniques used in this research are thermal camera (SC 640) to report and visualize the free surface flow at the interface between the vegetated or the non-vegetated floodplain and the main channel in a compound channel flow, while a particle image velocimetry (PIV) is used with flow above the ribbed single channel to monitor the free surface profiles flowing over a ribbed flume at steep slopes; a large number of captured video images are recorded in which seeding particles are used as tracer.

1.3 AIMS AND OBJECTIVES

The scientific research objectives of the experiments with steady uniform flow are as follows:

a) For rough beds (Friction factor, and water surface dynamics)

- Identifying flow resistance for transverse roughness elements and compare it with Bathurst (1981 and 1983)'s data.
- Qualification of the effect of roughness spacing, λ/k, and relative submergence, h/k, on hydraulic resistance in shallow flows.
- Describing, for a fixed roughness element's height, the impact of steep bed slope and roughness spacing (pitch to pitch) influence on the free surface deformation of the flow.
- Investigate whether the water surface profile in a steep slope ribbed flume can be simulated numerically.
- Understanding of the mean flow characteristics for flow over square bars at low and intermediate submergence.

b) For bridge constrictions

- Investigation of the effect of lateral channel constriction and a submerged bridge on the water surface profile.
- Understanding of the mean flow characteristics for an inundated bridge.

c) For a compound channel flow

- Investigate use of infrared thermography technique to capture thermal shear layers generated at the interface between main channel and floodplain.

d) For a one-line vegetation in single open channel flows

- Quantification of the drag coefficient of one-line vegetation and assessment of the empirical expressions' reliability for the prediction of the drag coefficient.
- Clarification of the influence of the bed slope on the rating curves of a one-line of vertically-oriented circular rods of varying diameters.

e) For one-line vegetation in compound open channel flows placed at the interface between the main channel and the floodplain and wholly vegetated floodplain cases

- Investigation of the effect of vegetation density and vegetation distribution on the rating curve, drag coefficients and lateral velocity profiles in a compound channel at uniform flow conditions in comparison to non-vegetated floodplain case.
- Identification of the bulk changes in drag coefficient around a one-line of vertically oriented circular rods of varying diameters when moved from the centre of a symmetrical open channel of simple cross-section to the floodplain edge of a symmetric compound channel flow.

1.4 THESIS STRUCTURE

The experimental study of this research is structured as follows:

Chapter **1** presents an introduction to background of the research subject areas, visualization techniques, aim and objectives and the thesis structure.

Chapter **2** describes water surface response to flow through bridge openings. Two bridge forms were considered as lateral constriction and submerged deck. This chapter mainly focuses on flow dynamics through a submerged bridge opening with overtopping. This experimental study provides a useful contribution to overtopping case and then simulated numerically by Kara et al. (2014, 2015) which revealed the complex nature of the flow around the bridge.

Chapter **3** presents the dynamics of shear layers at the interface between the main channel and the floodplain in a compound channel flow. Image processing techniques is used to extract such shear layers to state the dynamics of mixing shear layers. Thermal snapshots are analysed in visualizing these shear layers. In addition, two kinds of vortices are specified as shear layer vortices and von Karman street vortices which enrich specialists to characterise fluid dynamics of flow through cylinders.

Chapter **4** clarifies experimentally hydrodynamics of one-line of vertically-oriented circular rods of varying diameters placed at regular spacing along the mid-width of the single open channel flow. This study focuses on drag coefficient calculations based on Petryk and Bosmajian's equation.

Chapter **5** investigates the effect of vegetation density and vegetation distribution on the rating curve, drag coefficients and lateral velocity profiles in a compound channel flow with a vegetated floodplain at uniform flow conditions.

Chapter **6** presents the friction factor results of the ribbed steep slope open channel flows. The water surface profiles of ribbed steep slope open channel flows are presented and discussed. Vertical velocity profiles at different vertical sections are examined. Finally, the effects of roughness spacing and relative submergence on hydraulic resistance in shallow flows are simulated by Chua et al. (2016) to reveal explicit contributions to the overall momentum balance due to form-induced and turbulent stresses and the pressure drag is also quantified.

Chapter **7** summarises the research findings, conclusions and provides ideas for future research.

CHAPTER TWO

WATER SURFACE RESPONSE TO FLOW THROUGH BRIDGE OPENINGS

2 WATER SURFACE RESPONSE TO FLOW THROUGH BRIDGE OPENINGS

2.1 INTRODUCTION

The presence of a bridge in a river triggers a highly turbulent flow field including 3D complex coherent structures, e.g. (Koken and Constantinescu 2009) around the structure. These turbulence structures are highly energetic and possess high sediment entrainment capacity, which increases scouring around the bridge foundation, and consequently lead to structural stability problems. During extreme hydrological events, existing bridges may become fully submerged with submerged orifice flow occurring through the bridge opening and weir flow over the bridge deck. Most bridges were not designed for such flow conditions. In 1994, tropical storm Alberto dumped as much as 71 cm of rainfall over widespread areas of Georgia (USA), which resulted in damage to more than 500 bridges. The primary cause of damage to bridges was scour around abutments and approach embankments accompanied by bridge overtopping in many cases. The flood of 1993 in the Midwestern US paralysed a nine state area with flood recurrence intervals varying from 100 to 500 years. Two months after the flood, a scour hole with a depth of 17 m was mapped near the abutment of an interstate bridge on the Missouri River (Parola et al. 1998). Epic flooding with the flood recurrence interval in excess of 500 years occurred in Georgia in 2009 in the Atlanta metropolitan area with extensive damage to bridge abutments and embankments due to overtopping (Gotvald and McCallum 2010). These examples of bridge abutment and embankment failures highlight the need for additional research in this area. Currently, no formula for abutment scour is widely applicable because of difficulties in understanding the complicated hydrodynamics that lead to scouring near bridge abutments. A submerged bridge, including deck and abutments, is a significant obstacle to the flow, creating a backwater effect upstream of the bridge and a distinct and strongly varying water surface profile over the bridge deck and immediately downstream. Most studies in the literature examined experimentally the flow characteristics of free surface flow through the bridge opening, including complex 3D coherent structures and scouring mechanisms around abutments (Merville 1995, Oliveto and Hager 2002, Sturm 2006) and numerically

(Biglari and Sturm 1998, Chrisohoides et al. 2003, Paik et al. 2004, Nagata et al. 2005, Paik and Sotiropoulos 2005, Koken and Constantinescu 2008, Koken and Constantinescu 2009, Teruzzi et al. 2009, Koken and Constantinescu 2011). However, there are only few studies reported in the literature on flow over inundated bridges and the accompanying water surface profiles. Picek et al. (2007) conducted experiments to derive equations for backwater and discharge for flows through partially or fully submerged rectangular bridge decks. Malavasi and Guadagnini (2003) carried out experiments to examine the hydrodynamic loading on a bridge deck having a rectangular cross-section for different submergence levels and deck Froude numbers. The experimental data were used to analyse the relationship between force coefficients, the deck Froude number and geometrical parameters. They extended their experimental studies to analyse mean force coefficients and vortex shedding frequencies for various flow conditions due to different elevations of the deck above the channel bottom (Malavasi and Guadagnini 2007). Guo et al. (2009) investigated hydrodynamic loading on an inundated bridge and the flow field around it. An experiment was conducted for a six-girder bridge deck model and the experimental data were used to validate complementary numerical simulations. In the experiments, the PIV technique was used to obtain velocity distributions. The numerical data were analysed for different scaling factors to determine the effects of scaling on hydrodynamic loading. Lee et al. (2010) focused on water surface profiles resulting from flow around different bridge structures. They investigated three cases: a cylindrical pier, a deck, and a bridge (i.e. cylindrical pier and deck). Overtopping flow was considered only for the deck and bridge cases. In the experiment, the PIV method was used to measure the velocity. A 3D Reynolds-Averaged Navier Stokes (RANS) model with k-ε turbulence closure was used to simulate all the cases. The volume of fluid method was utilized for free surface modelling. Finally, comparisons of velocity distributions and water surface levels obtained from experiments and simulations showed that the model estimates velocity distributions very well. However, the model underestimates the water level rise around the structure due to the inability of the k-ε turbulence model to represent such a complex flow having significant streamline curvature and body force effects. The key objectives of this study are (1) to contribute to existing literature in understanding the water surface

response to the complex flow around a lateral channel constriction and a submerged bridge, (2) to quantify the mean and instantaneous flow through a bridge opening with overtopping, and (3) to elucidate the complex three-dimensional hydrodynamics and discuss their potential effects on the local scour mechanism. A complementary experimental study is reported which demonstrates the details of the water surface deformation and then its turbulence characteristics was simulated numerically by (Kara et al. 2015) to validate the LES.

2.2 EXPERIMENTAL SETUP

The physical model experiments were carried out in Cardiff University's hydraulics laboratory in a 10 m long, 0.30 m wide tilting flume with a bed slope of 1/2000 (see Fig. 2.1). Two bridge constrictions were chosen as sidewall abutments and submerged rectangular bridge. The lateral constriction cases were L = 29 cm long and B = 15 cm wide which gave a contraction ratio (B/W) of 0.5, L = 20 cm long and B = 15.5 cm wide which gave a contraction ratio (B/W) of 0.516 and L = 9.0 cm long and B = 9.0 cm wide which gave a contraction ratio (B/W) of 0.30. The laboratory setup of the sidewall abutment of L = 29 cm long and B = 15 cm wide (the LES domains and experimental) are presented in Figures 2.2 and 2.3, respectively. In the LES drawing, all dimensions are normalized with the length/width of the abutment, *L (Kara et al. 2014)*.

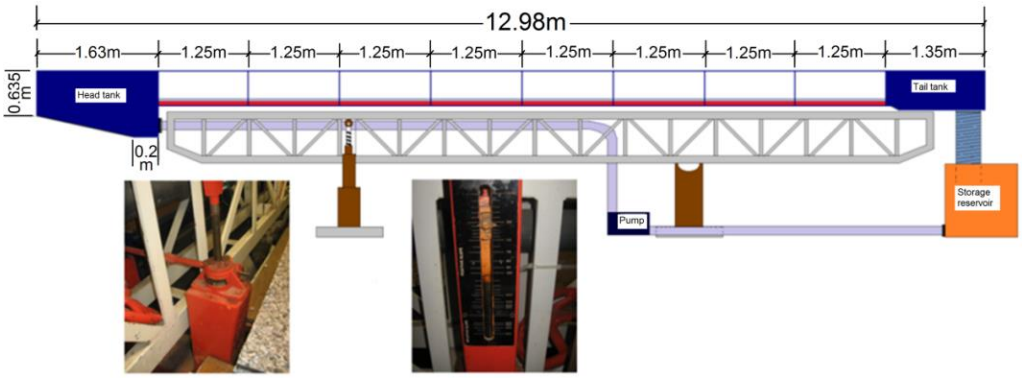

Figure 2.1: Schematic diagram of the flume of 30 cm width.

Before inserting bridge structures into the flume, uniform flow conditions were established for different flow cases (Fig. 2.4).

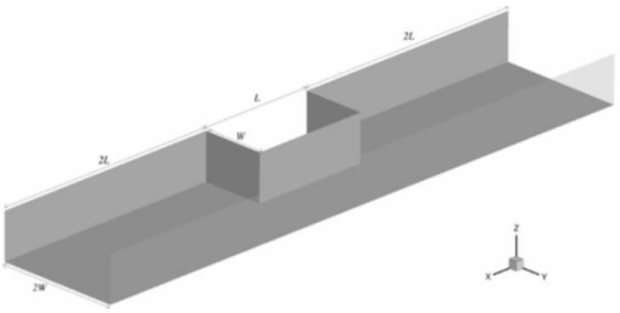

Figure 2.2: Computational setup for the LES of the lateral constriction (*Kara* et al. *2014*).

For the lateral constriction case of L = 29 cm long and B = 15 cm wide the discharge was chosen as $Q = 4.6$ l s^{-1} for which the uniform flow depth was $H = 6.4$ cm. This resulted in a bulk velocity of $U_b = 0.24$ m s^{-1} and a mean shear velocity of $u_* = 0.015$ m s^{-1}. The Reynolds number based on U_b and four times the hydraulic radius, R was Re = 42,730 and the Froude number was Fr = 0.30. Point locations of water level measurements for the lateral constriction model along the lines A, B, C, D and a, b, c, d, and e are as shown in Fig. 2.3. For the other lateral constriction models point locations of water level measurements were carried out at mid width between the lateral constriction and the flume sidewall in the same manner as with the first model. Three flow rates of 2.0 l s^{-1}, 3.0 l s^{-1} and 4.0 l s^{-1} were tested with these two lateral constriction models.

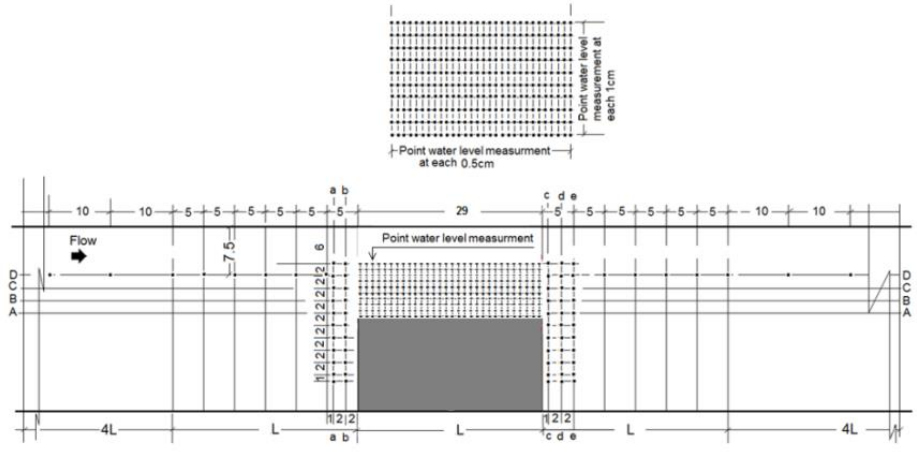

Figure 2.3: Schematic diagram showing locations of water level measurements for the lateral constriction model along the lines A, B, C, D, a, b, c, d and e. (All the dimensions are in centimetres).

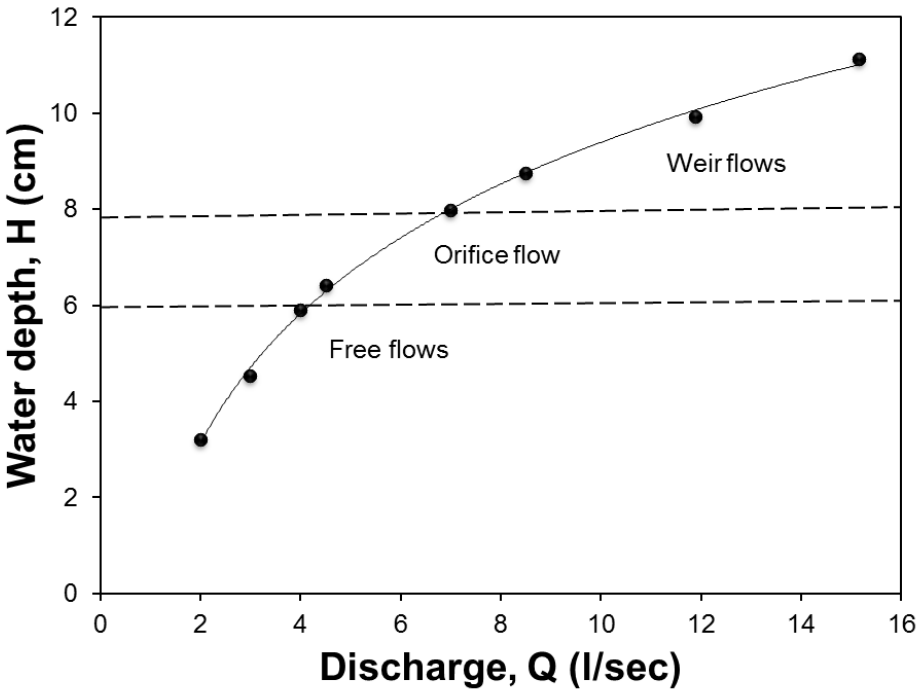

Figure 2.4: Water depth- discharge relationship.

For the overtopping case, the model bridge consisting of a square abutment with length of $L = 10$ cm, width of 9 cm, and height of $h_a = 5.0$ cm and a rectangular bridge deck of thickness of $h_d = 2.4$ cm, which extended across the channel (see Fig. 2.5).

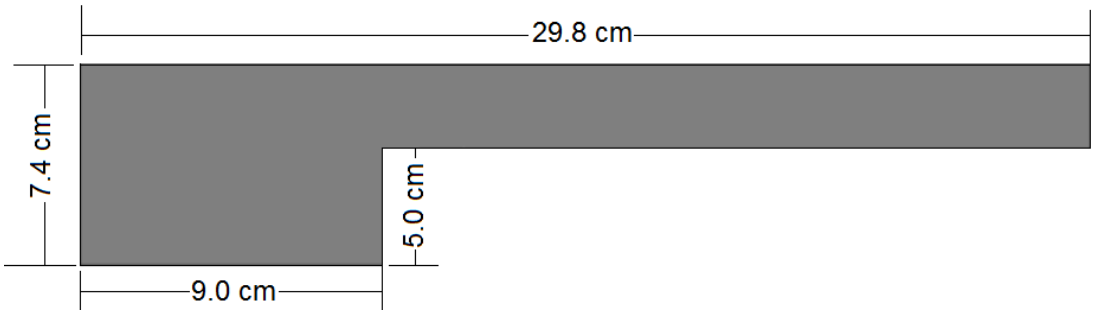

Figure 2.5: A physical bridge model for water surface measurements.

The geometric contraction ratio of bridge opening width to channel width was 0.70. The model bridge is an idealized version of the Towaliga River Bridge near Macon, Georgia. Before inserting the bridge model into the flume, the stage-discharge relationship for uniform flow was established (Fig. 2.4), for which the flow depth

was controlled via a weir at the downstream end. With the bridge in place, the water backed up and caused an increase of water depth upstream of the bridge. The discharges, chosen are as $Q = 7.0$ l s^{-1}, 8.5 l s^{-1}, 12.0 l s^{-1} and 15.0 l s^{-1} correspond to an extreme flood events and the corresponding uniform flow depths were H = 7.98 cm, H = 9.2 cm, H = 9.93 cm and 11.53 cm. For comparison purposes with the numerical approach the flow rate 8.5 l s^{-1} was chosen this resulted in a bulk velocity of $U_b = 0.31$ m s^{-1} and a mean shear velocity of $u_* = 0.017$ m s^{-1}. The Reynolds number based on U_b and four times the hydraulic radius was Re = 69, 800, and the Froude number of the uniform flow was Fr = 0.32. In the experiment, detailed water surface profiles were measured using a point gauge. Point locations of water level measurements for the submerged rectangular bridge model for the 8.5 l s^{-1} were carried out along the lines A, B and a, b, c, d and e are shown in Fig. 2.6 while for the other flow rates (7.0 l s^{-1}, 12.0 l s^{-1} and 15.0 l s^{-1}) water surface profiles were measured just along the mid width of the flume over the bridge model. Fig. 2.7 shows the laboratory and numerical setups for the 8.5 l s^{-1}, In the LES drawing all dimensions are normalized with the length/width of the abutment, *L (Kara et al. 2015).*

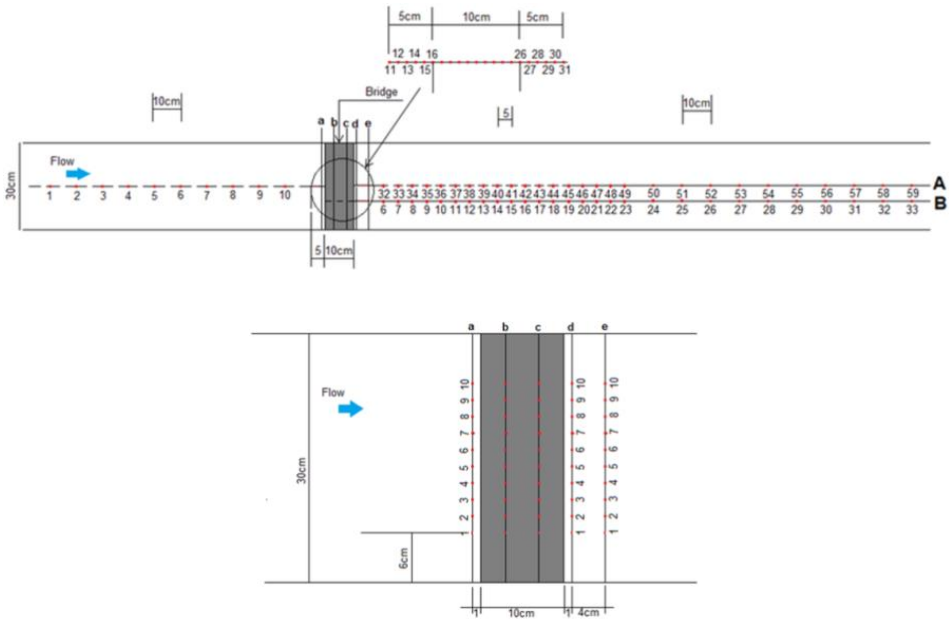

Figure 2.6: Schematic diagram showing locations of water level measurements for the submerged rectangular bridge model along the lines A, B (top) and a, b, c, d and e (bottom).

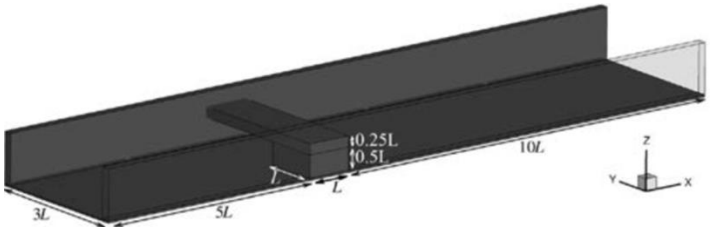

Figure 2.7: Computational setup for the LES of the model bridge (*Kara* et al. *2015*).

Flow rates for the overtopping bridge model were measured by separating the flow into weir flow and an orifice flow. Point velocity measurements were carried out using Nixon probe velocimetry. For the broad crested weir, velocity measurements were carried out at six sections at two positions along each section at 0.2h and 0.8h with an averaged velocity is $U_{avg.}$ = (0.2Hs+0.8Hs)/2, where Hs is the flow depth over the bridge deck. For the orifice flow, velocity measurements were carried out at two positions, 0.2Ho and 0.8Ho for the four selected sections as shown in Fig. 2.8, where Ho is the flow depth of the orifice flow opening. The rotary of the probe was positioned at the downstream edge of the bridge model at these two positions.

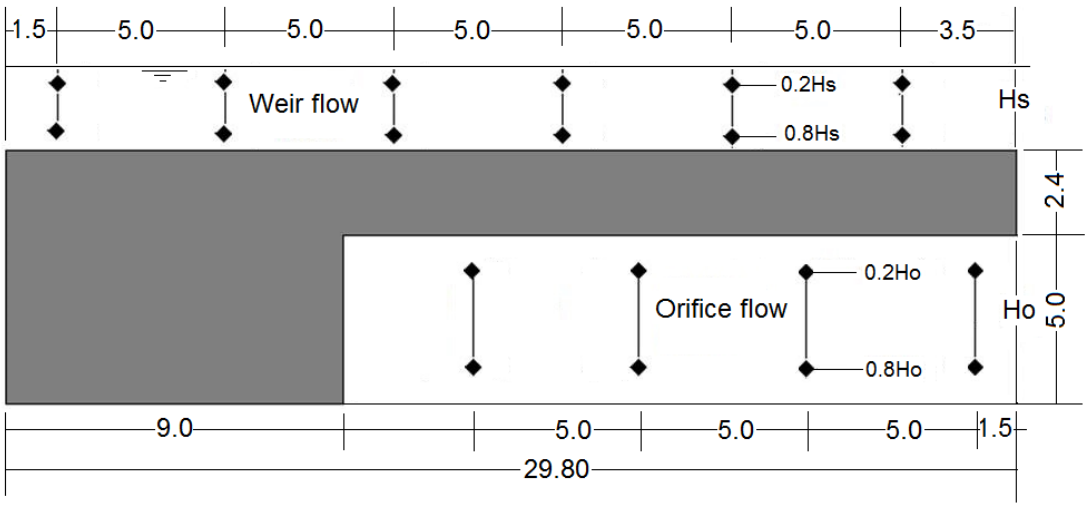

Figure 2.8: Point velocity measurements of separating the flow to an orifice flow and broad crested weir flow.

If the flow occurs along the entire bridge with the water level upstream the bridge below the upper edge of the bridge deck, the flow is called the full-flowing-orifice type of flow. Only one case was considered as full flowing orifice flow with a flow rate of 4.5 l s^{-1}. Water level measurements were carried out along the mid width

upstream and downstream the bridge opening at distances as with the overtopping case studies.

2.3 RESULTS AND DISCUSSIONS

Figure 2.9 presents the water surface elevation measurement locations for the two cases along which LES carried out by Kara et al. (2015) and experimental data which will be compared . Profiles denoted with a capital letter represent longitudinal profiles, and profiles denoted with a small letter are cross-sectional profiles.

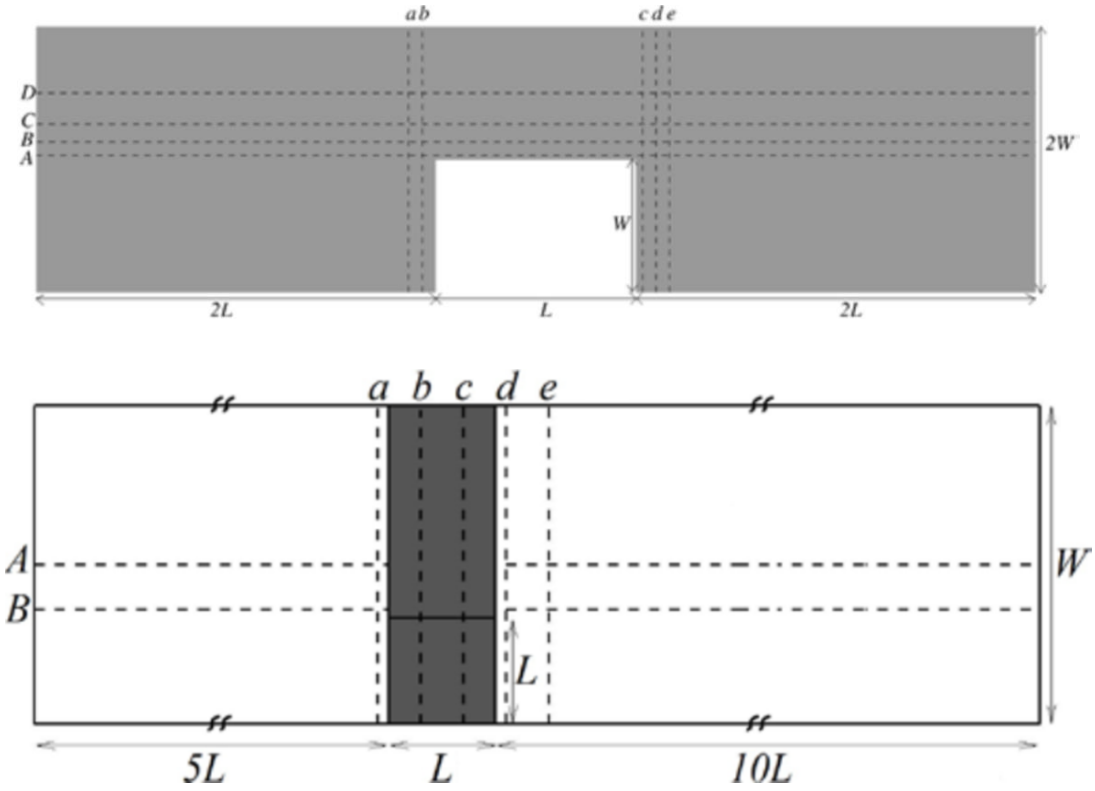

Figure 2.9: Water surface elevation measurement locations of the lateral constriction (top) and model bridge cases (*Kara* et al. *2014*).

2.3.1 Lateral Constriction

The water surface profiles in longitudinal profiles A-D are presented in Figure 2.10. The water surface elevations are normalized with *H*. Overall, the profiles obtained from the LES show reasonable agreement with the experimental data. The water is backed up quite significantly upstream of the structure and the LES predicts this quite well. A bit upstream of the structure (indicated by the dashed lines) the flow

starts to accelerate and the water surface drops rapidly and significantly. The flow creates a very distinct local dip in the area of local recirculation as a result of flow separation at the leading edge of the constriction. The water surface recovers markedly approximately half way through the constriction in form of a standing wave. The simulation is reproducing this fairly well away from the structure (Profiles C and D), however very close (e.g. Profile A) the agreement is not so good. This can be attributed to the lack of mesh resolution of the simulation and apparently the LES cannot resolve the steep gradients well enough. Near the end of the constriction, the water surface drops further quite significantly. The flow downstream of the constriction is subjected to a large very shallow recirculation zone just behind the abutment, which contracts and accelerates the flow. The LES reproduces this part of the water surface response quite well.

Figure 2.11 presents cross-sectional water surface profiles immediately before (profile a-b) and after (profile c-e) the constriction as obtained from experiment and LES. The match between simulation and experiment upstream of the constriction is quite satisfying and the lateral gradient is reproduced very well. This gradient reflects the acceleration of the fluid in the non-constricted area due to the presence of a recirculation zone just up-stream of the constriction. The gradient of water surface increases closer to the constriction. The cross-sectional profiles downstream of the constriction exhibit a very significant jump in the water surface. The recirculation zone downstream of the constriction is significantly lower elevation than the rest of the channel. The water that rushes out of the constricted area has a significant amount of stream wise momentum prohibiting the filling of the recirculation zone with fluid. The features described in conjunction with Figures 2.10 and 2.11 can be observed in Figure 2.12, depicting a photograph looking from downstream of the constriction. Aforementioned water surface features are highlighted in the photograph and accordingly in the visualized large-eddy simulation. The local depression at the leading edge of the constriction is marked with a black arrow; the recovery of the depressed water in the constriction is highlighted by yellow arrows and the recirculation zone is denoted RZ. All these features are predicted well qualitatively by the LES. Moreover, there is a small ridge in the water surface between the depressed recirculation zone and the elevated flow out of the

constriction, which is not picked up in the measurements (see profiles c, d, e) but is clearly visible in the photograph and in the simulation (highlighted by a thin orange line).

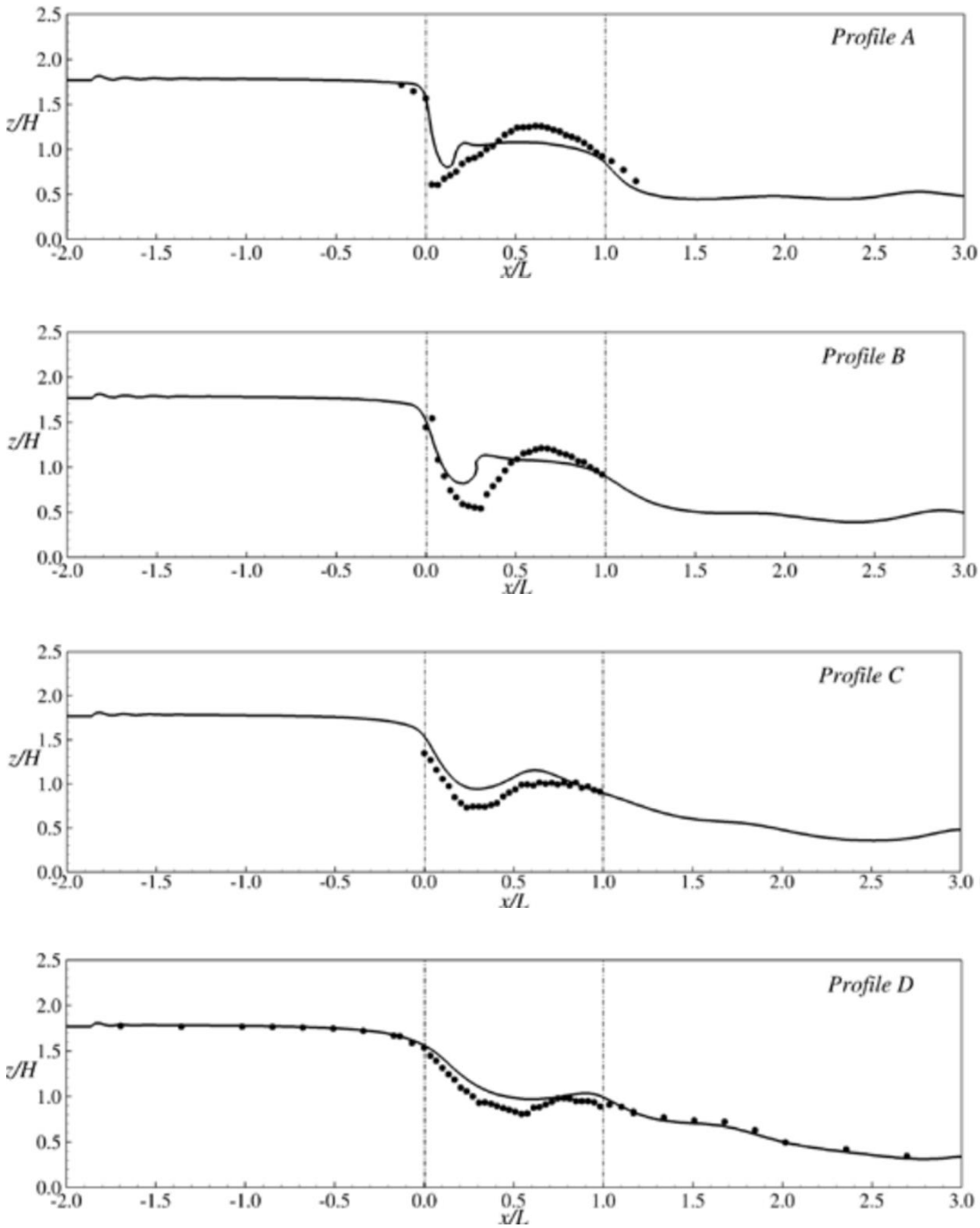

Figure 2.10: Longitudinal water surface profiles (dots represent the experimental data. Solid black line represents fine grid LES result) (*Kara* et al. *2014*).

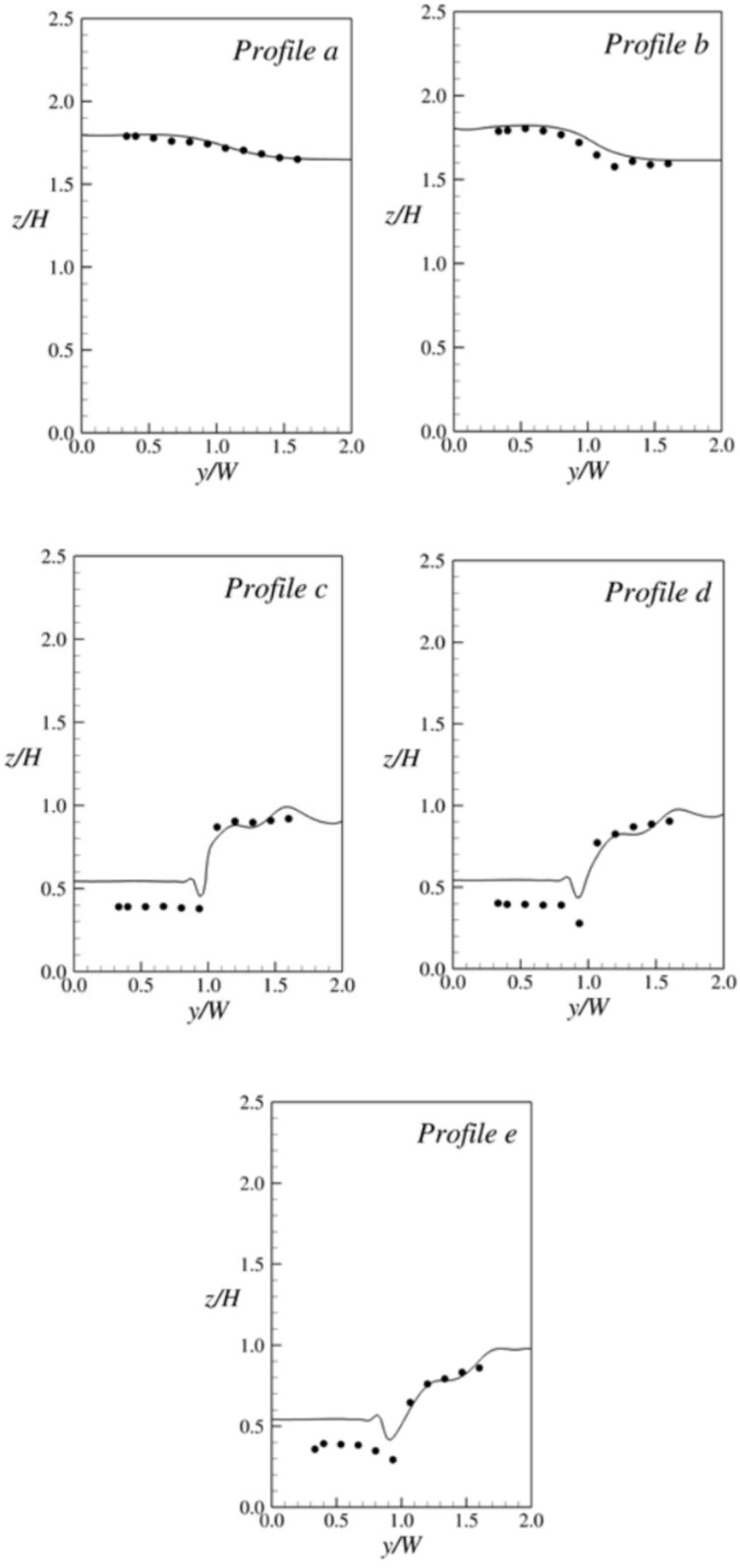

Figure 2.11: Water surface profile comparisons for cross sections (dots represent the experimental data. Solid black lines represent LES results) (*Kara* et al. *2014*).

The flow in the constriction changes criticality and it is supercritical for approximately 6-8*L* downstream of the constriction before the flow returns to subcritical in a weak hydraulic jump. In the LES this happened very close to the domain exit and posed a challenging task in terms of numerical stability.

Free surface profiles along the mid width of the lateral constriction and the flume sidewall for the other lateral constrictions (L = 20 cm long and B = 15.5 cm wide and L = 9.0 cm long and B = 9.0 cm wide) for the three flow rates 2.0 l s^{-1}, 3.0 l s^{-1} and 4.0 l s^{-1} were shown in Figs. 2.13 an d 2.14 respectively. Combining these two lateral constrictions in a one drawing was shown in Fig. 2.15. The most important features of these water surface profiles are a marked drop of the water surface, increasing the blockage ratio influences the water surface meandering exhibiting wavy motion to the uniform flow condition and results in complex water surface profiles and for large blockage the height of local up swell locates a bit upstream of the structure decreased with the increasing depth of water.

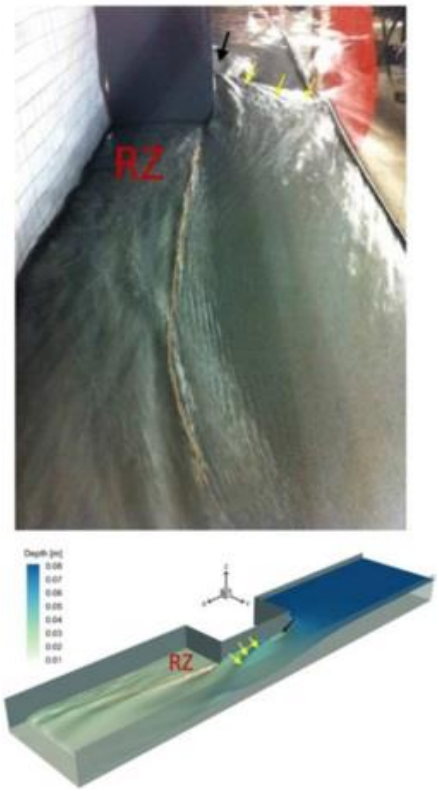

Figure 2.12: Snapshots of the instantaneous water surface from experiment and as predicted by the LES (*Kara* et al. *2014*).

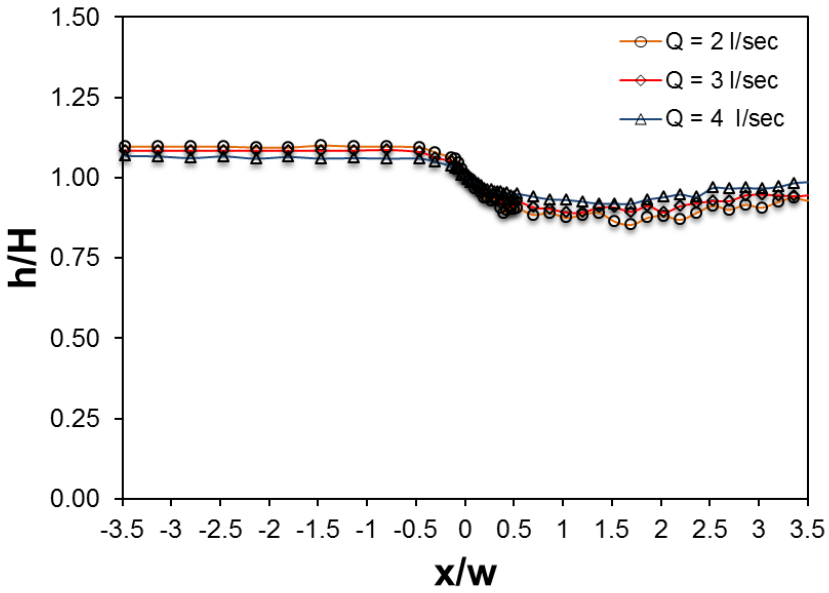

Figure 2.13: Free water surface profiles in presence of a lateral constriction of dimensions 9 cm X 9 cm.

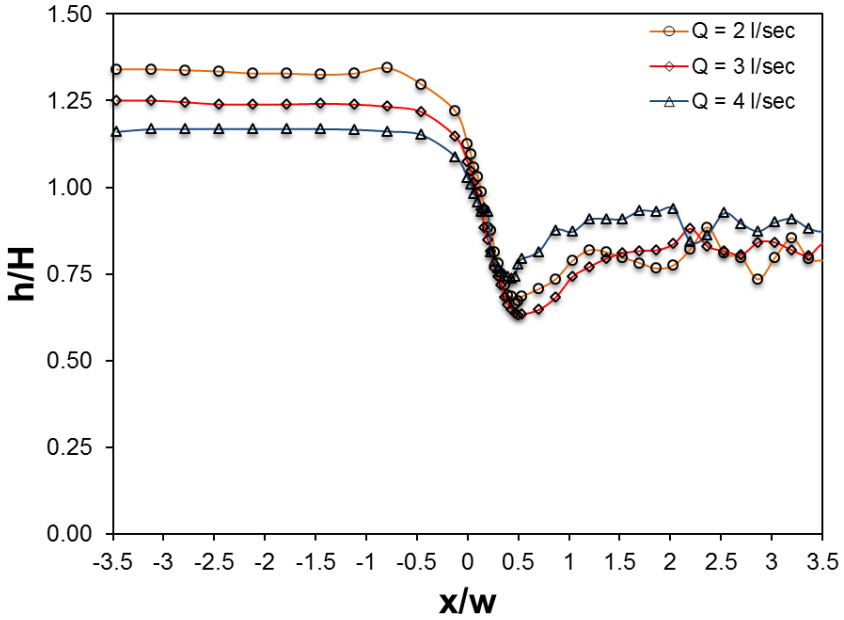

Figure 2.14: Free water surface profiles in presence of a lateral constriction of dimensions 20 cm X 15.5 cm.

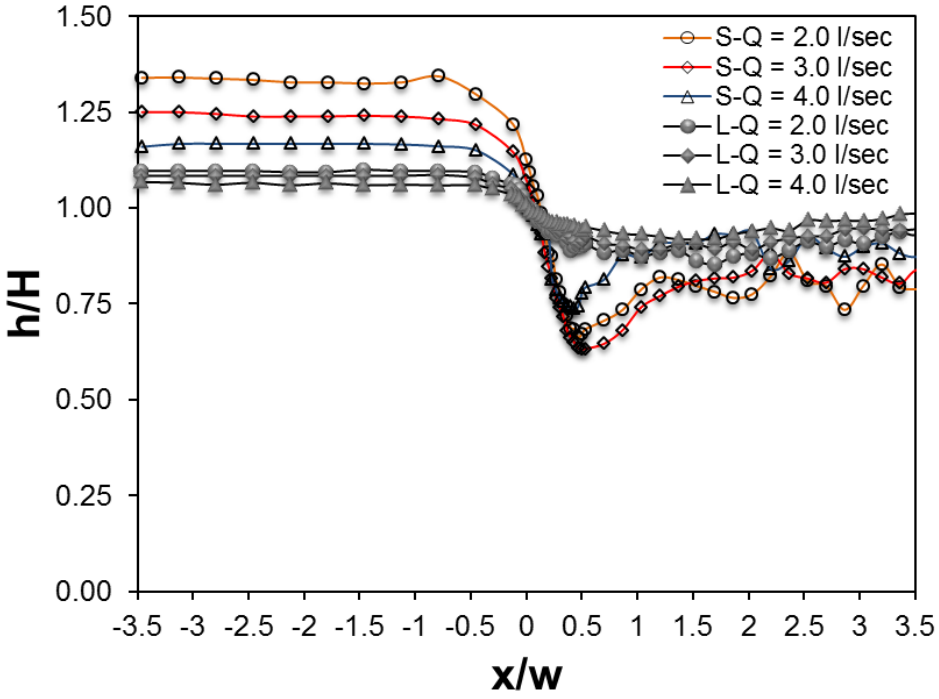

Figure 2.15: Free water surface profiles in presence of the lateral constrictions of dimensions 9 cm X 9 cm and 20 cm X 15.5 cm.

2.3.2 Submerged Rectangular Bridge

Figure 2.16 (top) presents an overall three-dimensional view of the time-averaged water surface of this flow as predicted by a numerical simulation (Kara et al. 2015). Also plotted (bottom right) is a close up photograph of the corresponding flow over the bridge in the experiment. The flow accelerates over the bridge causing a marked drop of the water surface. The flow plunges downstream of the bridge, which results in a standing wave or an Undular hydraulic jump. Downstream of the standing wave the flow recovers gradually, exhibiting wavy motion, to the uniform flow condition. In general, Fig. 2.16 shows very good qualitative agreement between the numerical results and the conditions observed in the laboratory experiment.

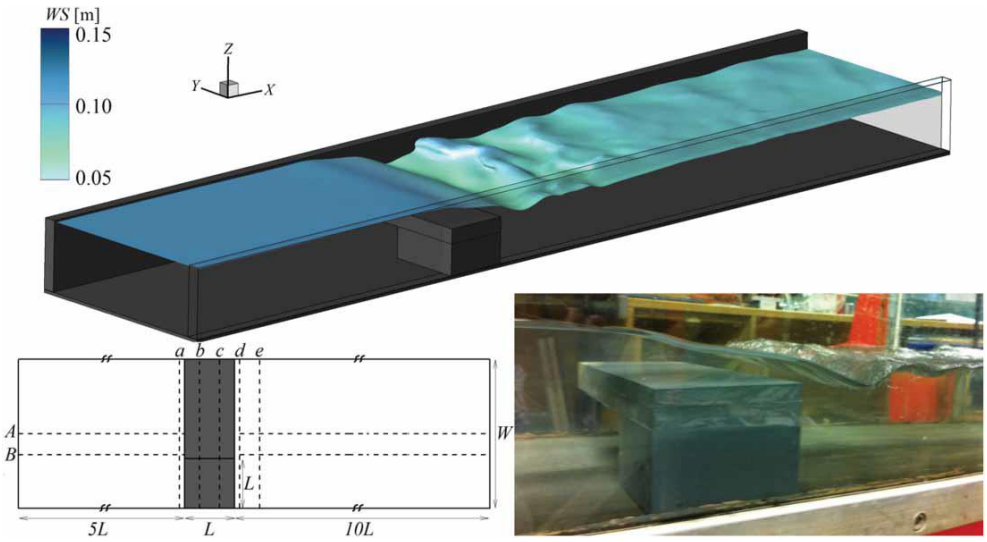

Figure 2.16: Simulated water surface (top), measurement locations (bottom left) and close-up photograph of the laboratory experiment (bottom right).

A more quantitative assessment of the predictive capabilities of the simulation results is provided in Figs 2.17 and 2.18, which depict measured (dots) and simulated (lines) longitudinal (Fig. 2.17) and cross-sectional profiles (Fig. 2.18) of the water surface. The simulated longitudinal profiles (Fig. 2.17) along A and B (see the sketch in the lower left of Fig. 2.16) are in very good agreement with the observed data. There is a small, but consistent overestimation of the water surface elevation upstream of the bridge. The reason for this discrepancy is that the height of the bridge deck in the simulation was chosen to be exactly 50% of the depth of water underneath the deck. The height of the bridge deck in the experiment was 48% of the depth of water underneath it. There is some discrepancy between numerical prediction and measurement in the vicinity of the standing wave, an area that is highly turbulent and where accurate water surface measurements using a point-gauge are difficult to achieve. Figure 2.18 presents measured and simulated cross-sectional water surface profiles at selected locations (a–e, see Fig. 2.16). Upstream and on the bridge (profiles a and b) the numerically predicted profiles are slightly higher than the measured ones, whereas numerically predicted profiles c, d and e are in very good agreement with the measurements.

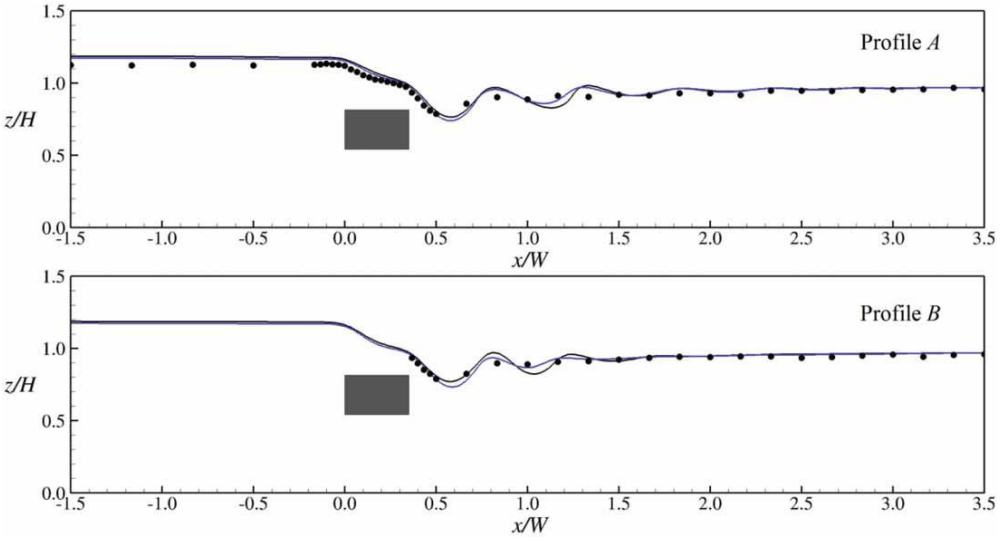

Figure 2.17: Longitudinal water surface profiles along two locations, which are channel centre line (profile A) and one-third of the channel width (profile B) at the abutment face (*Kara* et *al*. *2015*).

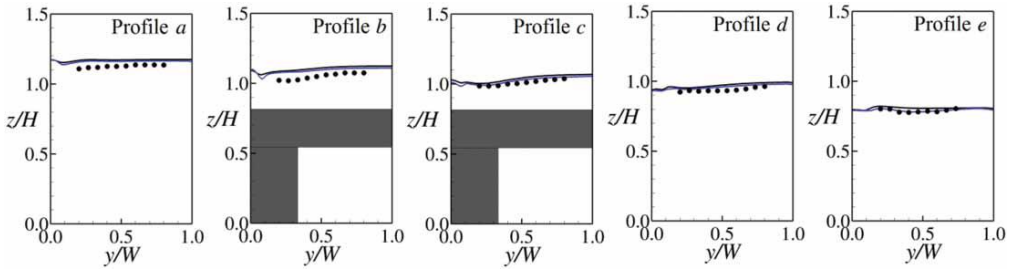

Figure 2.18: Cross-stream water surface profiles along six locations (profiles a–e) looking upstream (*Kara* et al. *2015*).

A quantitative view of the flow is provided with the help of Fig. 2.19, in which the time-averaged stream-wise velocity together with streamlines in three longitudinal planes are plotted. The time-averaged flow over the bridge is subdivided into two portions: 74.4% of the discharge is forced underneath the bridge deck as submerged orifice flow, whilst the remaining 25.6% discharges over the deck as a weir flow. The deck acts similarly to a broad-crested weir and the critical depth of the portion over the deck is $y_c = (q^2/g)^{1/3} = 1.73$ cm, which is attained at 0.93L, i.e. very close to the trailing edge of the deck. The flow plunges into the downstream area as supercritical flow, and undergoes an 'Undular' hydraulic jump. A vertical recirculation zone forms downstream of the abutment as depicted in Fig. 2.19a. On the side of the abutment the standing wave is not as steep as in the middle of the

channel, a feature that was also observed in the experiment. At y/W = 0.33 the separation vortex over the deck interacts with the lateral flow separation and recirculation from the abutment generating a vortex core at x/W= 0.7 and a saddle point underneath (Fig. 2.19b). At y/W = 0.67 (Fig. 2.19c) the submerged orifice flow features stream-wise velocities up to almost three times the bulk velocity, which is due to the lateral and vertical contraction of the flow not only by the abutment and deck but also by the vertical and horizontal recirculation zones of the separated flow.

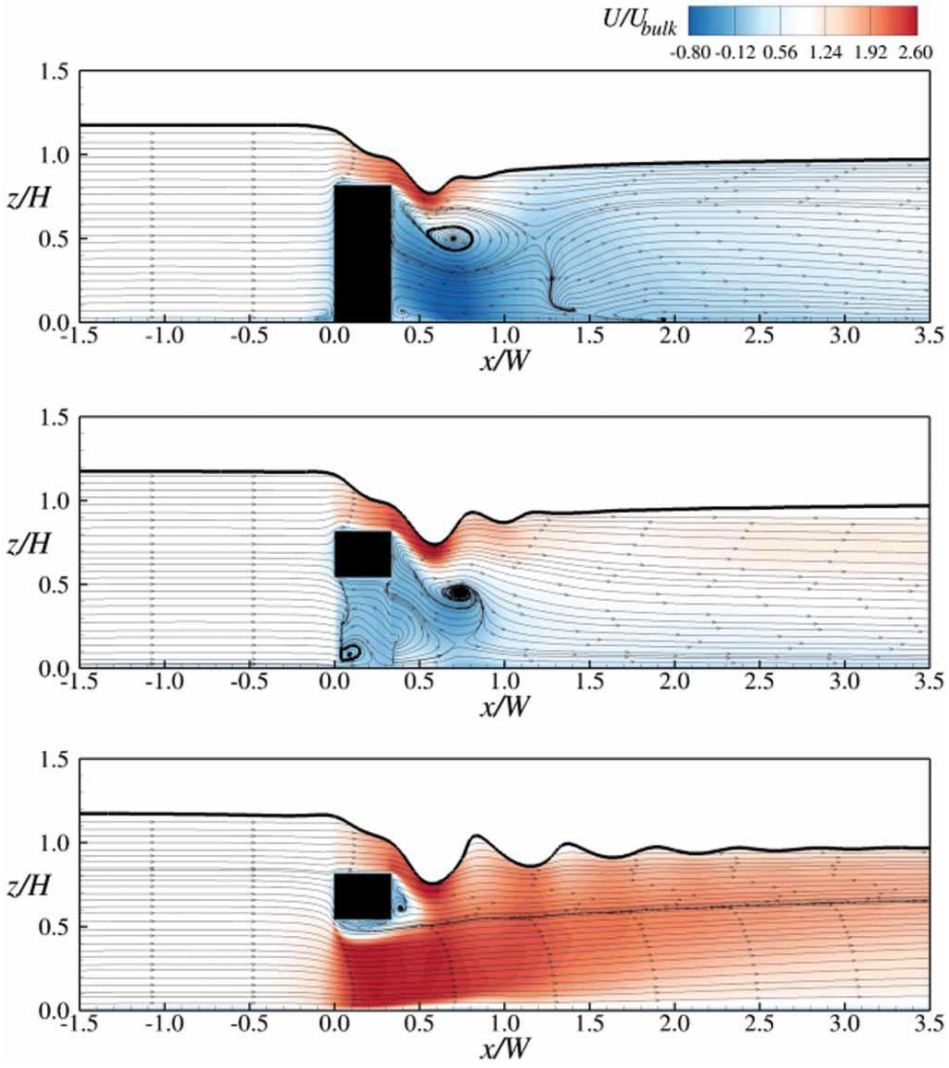

Figure 2.19: Time-averaged velocity contours together with streamlines of the flow in three selected longitudinal-sections: (a) *y/W* = 0.17; (b) *y/W* = 0.33; (c) *y/W* = 0.67 (*Kara* et al. *2015*).

Figure 2.20 quantifies the complex flow over the submerged bridge in terms of bed shear stress τ, normalized with the mean boundary shear stress ($\langle\tau\rangle = \rho gRS$) for uniform flow, and tke, normalized with the squared mean shear velocity for uniform flow, ${u^2}_*$. The highest values of bed shear stress are observed in the bridge cross-sections and are close to the leading edge of the abutment, which is where the flow is contracted. There is also a region of high bed shear slightly downstream of the abutment. The area of highest near-bed tke does not coincide with the area of highest bed shear is found where the plunging flow from over the deck coincides with the edge of the lateral recirculation zone of the separated flow. This is significant for local scour. Hong et al. (2014), who report on experimental investigations of local scour around a submerged bridge, show that the location of the deepest scour hole occurs downstream of the bridge, and in fact at an analogue location to the high- tke -area identified herein.

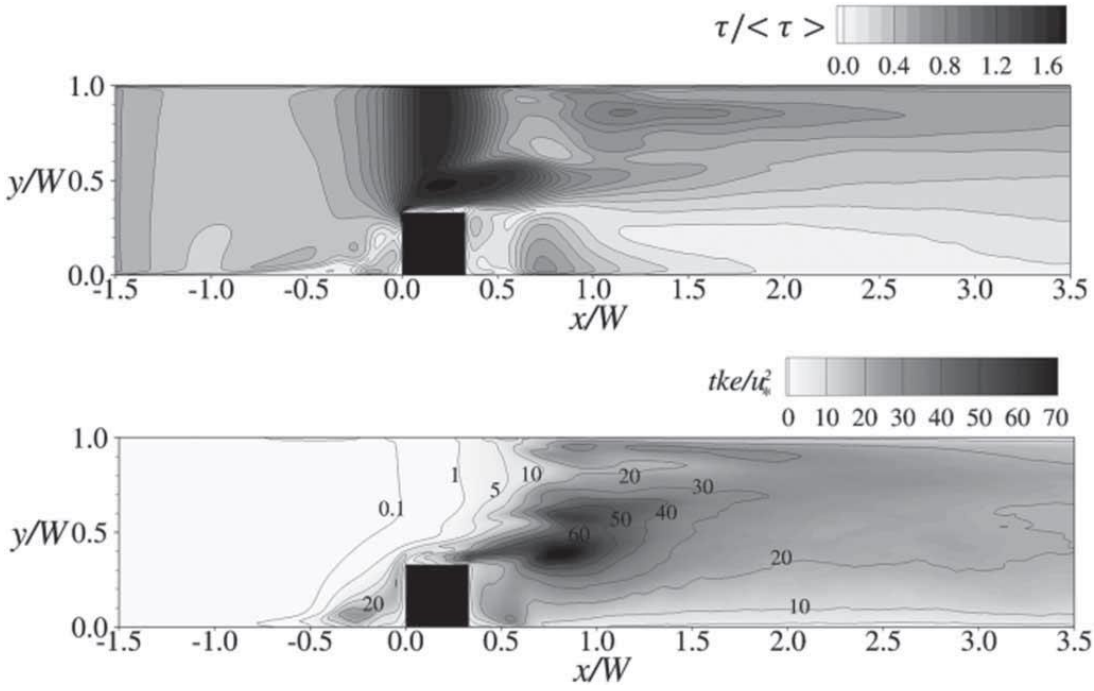

Figure 2.20: (a) Contours of the normalized bed-shear stress and (b) contours of the normalized turbulent kinetic energy in a horizontal plane at $z+ = 50$ (*Kara* et al. *2015*).

The measurements of water surface profiles through entirely submerged bridge deck of a rectangular shape was carried out for all the flow rates of 7.0 l s^{-1}, 8.5 l s^{-1}, 12.0 l s^{-1} and 15.0 l s^{-1} showed that the shape of profiles are complex.

The most features of the water surface profiles are the height of local upswell locates a bit upstream of the structure decreased with the increasing depth of water above the bridge deck and Undular hydraulic jumps were observed in all the flow rates. Strong hydraulic jumps were shown in high flow rates downstream of the abutment as depicted in Fig. 2.21.

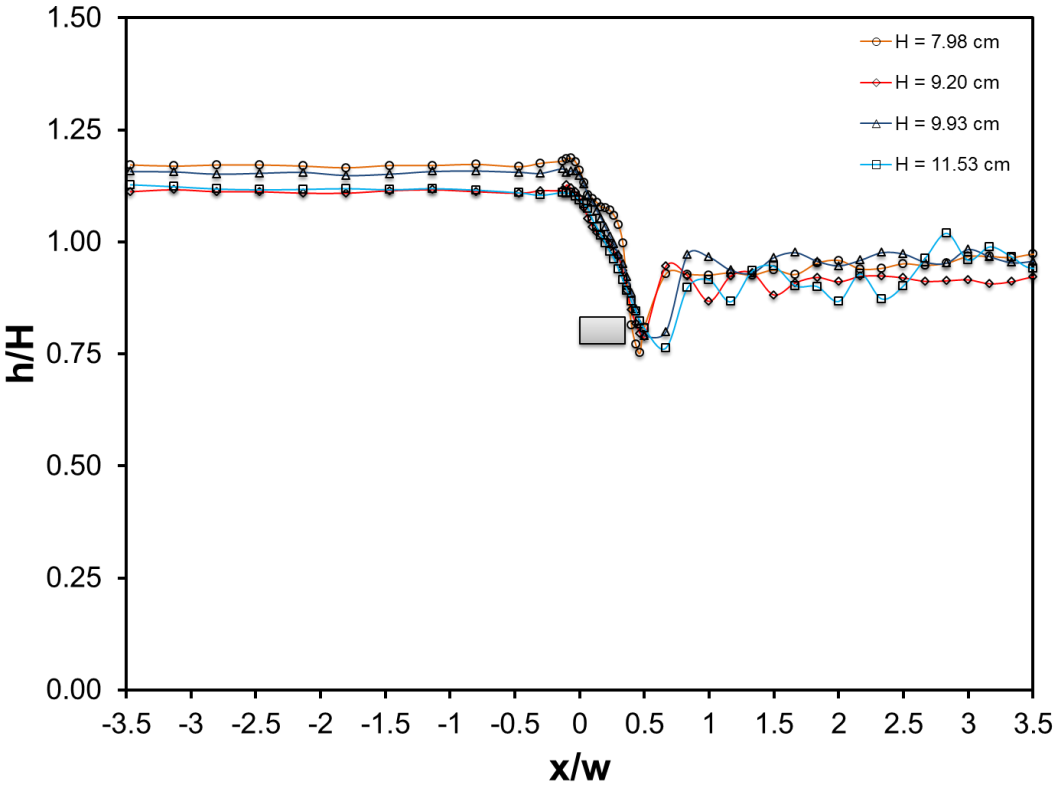

Figure 2.21: Water surface profiles of the flow over the submerged bridge deck.

The time-averaged flow over the bridge as mentioned earlier is subdivided into two portions: a submerged orifice flow and a broad crested weir flow was explained in Fig. 2.22 shows 49.9%, 38.9%, 25.6% and 21.9% for the flow rates 15.0 l s^{-1}, 12.0 l s^{-1}, 8.5 l s^{-1} and 7.0 l s^{-1} is running as a weir flow respectively.

Water surface profile for the full-flowing-orifice type of flow was represented by the full line with circles as shown in Fig. 2.23.

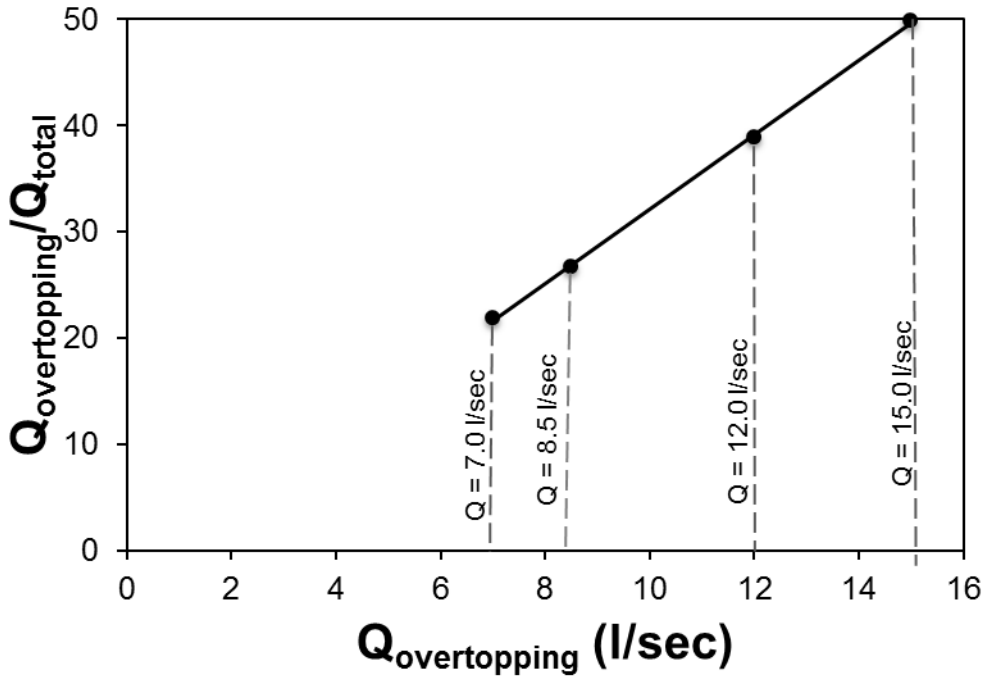

Figure 2.22: Percent submergence ratio versus discharge relationship.

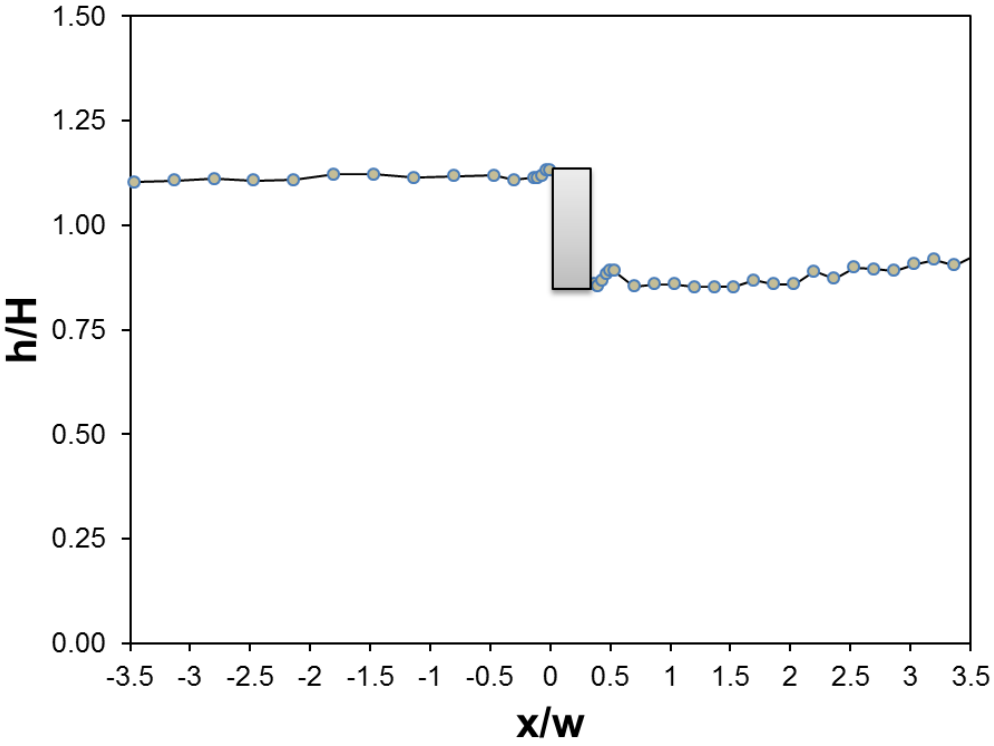

Figure 2.23: Schematic picture of observed water-surface profile of flow through the full-flowing-orifice type of flow.

2.4 CHAPTER SUMMARY

This chapter explains experimentally and then compares numerically the calculations of the longitudinal free surface profiles and the cross sectional profiles for two case studies of bridge constrictions such as lateral constriction and bridge overtopping. For the purpose of comparison the numerical approach with the experimental data, two flow rates were considered from the rating curve for the case studies. For the lateral constriction case the discharge was $Q = 4.6$ l s^{-1} for which the uniform flow depth was $H = 6.4$ cm. For the overtopping case, the discharge, chosen as $Q = 8.5$ l s^{-1} corresponds to a uniform flow depth of $H = 9.2$ cm. For the lateral constriction, the profiles obtained from the LES show reasonable agreement with the experimental data. A detailed description of the flow along the water surface profiles was presented. In a similar way the flow was described for the cross sectional profiles and fitted qualitatively well with the numerical simulation by the LES. In the second case study of bridge constriction as bridge overtopping showed very good agreement between the observed and simulated data for the longitudinal and the cross sectional water profiles. The overtopping creates a horizontal recirculation zone downstream of the abutment and flow contraction occurs underneath the deck. The overtopping flow reaches critical conditions on the deck and creates areas of very high turbulence as it plunges in the form of an undular hydraulic jump downstream of the bridge. The area where horizontal and vertical recirculation zones meet is characterized by high magnitudes of turbulent kinetic energy, *tke*, and the formation of substantial shear layers. The location of highest bed-shear stress, i.e. underneath the deck where the flow is contracted and accelerated, does not correspond to the location of maximum *tke*. These features of the complex turbulent flow structure induced by the bridge obstruction and flow contraction with overtopping have broader implications, relative to the scour of a moveable sediment bed near a bridge abutment, that are being explored further. These two case studies are representing a conference and a published journal paper as shown in (Kara et al. 2014, Kara et al. 2015) references. In addition, a number of flow rates were considered in this study representing three types of flows as weir flows, full-flowing orifice flow and free flows. The most important of the weir flows are the height of local upswell locates a bit upstream of the structure decreased with the increasing

depth of water above the bridge deck and strong hydraulic jumps were shown in high flow rates downstream of the abutment. Free flows in presence of lateral constrictions resulted in complex water surface profiles and the water surface meandering is increased as the blockage increases. Full-flowing-orifice type of flow showed that with the bridge in place, the water backed up and caused an increase of water depth upstream of the bridge.

For a calculation of the discharge through entirely submerged bridge decks using the scheme dividing the total flow into the orifice flow and the weir flow, the study shows a very well relationship between percent submergence ratios and the discharge.

CHAPTER THREE

MIXING LAYER DYNAMICS IN COMPOUND CHANNEL FLOWS

3 MIXING LAYER DYNAMICS IN COMPOUND CHANNEL FLOWS

3.1 INTRODUCTION

Shallow flows are defined as open channel flows with transverse velocity gradient. These flows are shallow because their mixing layer width is larger than the water depth (Jirka and Uijttewaal 2004). The examples of shallow flow in nature include flows such as in lakes, bays, estuaries, lowland flows, and river confluences. Lowland rivers generally present a compound channel section configuration, which consists of a main channel, and one or two floodplains. Floodplains are usually rougher than main channels due to growth of different types of vegetation in different alignment and configurations such as one-line vegetation and wholly vegetated floodplain. When the flow exceeds the main channel, the faster flow in the main channel interacts with the slower flow velocity on the floodplain. Such interaction generates mixing shear layers (turbulent structures) near to the interface between the main channel and the floodplain that producing extra resistance. Mass and momentum transfer occurs due to the velocity difference between the main channel and the floodplains (Shiono and Knight 1991, Tominaga and Nezu 1991, Soldini et al. 2004, van Prooijen et al. 2005, Nugroho and Ikeda 2007, White and Nepf 2007, Leal et al. 2010, Vermaas et al. 2011, Azevedo et al. 2012).

Shear layers have been visualized by a number of authors using different techniques such as a dye tracer, Particle Image Velocimetry (PIV), Laser Doppler Anemometer (LDA), Acoustic Doppler Velocimetry (ADV), and numerically (e.g. large eddy simulation, LES, technique). Sellin (1964) injected aluminium powder on the water surface between the main channel and the floodplain in a straight compound channel flow; and then visualized strong vortex structures at the interface between the main channel and the floodplain. These vortices were recorded by photography means. Pasche and Rouvé (1985) experimentally investigated the flow structures in compound channel flows with and without vegetated floodplain using Laser-Doppler Velocimetry (LDV) and Priston-tube techniques; and then visualized the formation of eddies at the interface between the main channel and the floodplain. Tamai et al. (1986) observed periodic large eddies (vortices) at the water surface at the interface

between the main channel and the floodplain of a uniform compound channel flow using flow visualization of hydrogen bubble method. These vortices are generated by the local shear at the interface. Shiono and Knight (1991) used an analytical model for steady, uniform, turbulent flow experiments in a compound channel. They showed that in such channels the vertical distributions of Reynolds shear stress τ_{yx} and τ_{zx} in the regions of strongest lateral shear near to the interface between the main channel and the floodplain, an upwelling which causes variation in $U, V,$ and τ_{yx} leads to transfer of momentum from the main channel to the floodplain relative to the eddies movement along the interface between the main channel and the floodplain. Tominaga and Nezu (1991) presented the interaction between the main-channel and floodplain flow in fully developed compound open channel flows using a fibre-optic laser Doppler anemometer. The contribution of secondary currents on momentum transport is very large near the junction, at which strong inclined secondary currents associated with a pair of longitudinal vortices on both sides of the inclined up-flows are generated from the junction edge toward the free surface; and then the effects of channel geometry and bed roughness on turbulent structure are examined. Tominaga and Nezu (1991) showed that as the relative depth (water depth on a floodplain, h_f divided by water depth in the main channel, H_{mc}) decreases, strong vortices appear near the free surface of the floodplain, and the main channel vortices expand in the span-wide direction. Nezu and Onitsuka (2001) observed turbulent structures (vortices) generated at the edge of the vegetated channel flow located for half of the channel width using Laser Doppler Anemometer (LDA) and Particle Image Velocimetry (PIV). Carling et al. (2002) investigated vertical two-layer turbulent structures around the main channel-floodplain interface and substantial anisotropy of turbulence. Bennett (2004) experimentally showed that various turbulent flow structures are created in association with different vegetated zones. These included surface waves, dead zones, flow separation, and small-scale and large-scale vortices. These turbulent flow structures significantly increased fluid mixing processes within the channel. Soldini et al. (2004) investigated, within the framework of the non-linear shallow water equations (NSWE), the generation and evolution of large-scale eddies with vertical axis (macro vortices) which are responsible for the horizontal mixing happening at the interface between the main

channel and the floodplain of a compound channel flow. They revealed that the interaction occurs in the form of vortex pairing with a consequent increase in lateral mixing, and hence providing a means to quantify the momentum transfer across the channel. van Prooijen et al. (2005) investigated eddy viscosity model for the transverse shear stress in a mixing region that is responsible for momentum exchange between the main channel and the floodplain in a straight uniform compound channel flow, and then assumed horizontal coherent structures movement dominate the mechanism for momentum exchange between the compound channel sections (the main channel and the floodplain) that resulted in lowering the total discharge capacity of the compound channel flow. Rummel et al. (2006) focused on the shear layer formed at the water surface of a straight compound channel flow basing on Particle Tracking Velocimetry (PTV) and PIV analysis of free surface velocities forms, especially on macro vortices and the horizontal flow mixing. Mazurczyk (2007) recognized experimentally the scales of turbulent eddies in compound channels with emergent rigid vegetated floodplain using ADV. Nugroho and Ikeda (2007) applied a large eddy simulation SDS-2DH model to study the lateral momentum transfer in compound channels that the instantaneous structure of horizontal vortices and temporally-averaged velocity distribution have a significant effect. The results showed that, the horizontal vortices occur at the boundary between the main channel and the floodplain channel where significant momentum exchange happens. White and Nepf (2007) carried out experiments to study the characteristics of the shear layer generated at the interface between an array of circular cylinders in emergent case in a shallow open channel flow. They found that across the interface, mass and momentum transfer are occurred due to the generation of the coherent structures. The induced vortex structures showed strong cross flows with sweep from the main channel and ejection from the array. Nezu and Sanjou (2008) investigated turbulence structures and coherent large-scale eddies in the vegetated canopy open channel flows based on LDA and PIV measurements. These coherent eddies such as sweeps and ejections in the mixing zone were highlighted based on instantaneous contours of Reynolds stress and vortices. In addition, they investigated turbulence structures and coherent motion in vegetated canopy open-channel flows using LES technique. They showed instantaneous vortices in the non-

wake plane in every 0.5 seconds. White and Nepf (2008) defined the flow structures in a partially emergent vegetated single shallow open channel flow; and then described the formation of shear layer with regular periodic oscillations of vortex structures at the edge of the vegetation-main channel. They showed that the shear layer is asymmetric about the vegetation interface and has a two-layer structure; (i) an inner region of maximum shear near the interface contains a velocity inflection point and establishes the penetration of momentum into the vegetation and (ii) an outer region, resembling a boundary layer, forms in the main channel, and establishes the scale of the vortices. Such vortex structures show strong cross flows with sweeps from the main channel and ejections from the emergent vegetation, that create significant momentum and mass fluxes across the interface. The sweeps maintain the coherent structures by enhancing shear and energy production at the interface. Fraselle et al. (2010) observed strong turbulent structures in compound channels in the shear layer region by injecting a tracer, Sodium Chloride solution (NaCl solution) at successive positions in the main channel. Results mainly show an expansion of solute more developed towards the floodplains than towards the main channel. Leal et al. (2010) found that in shallow flows, mixing shear layers that are developed between the main channel flow and the floodplain flow generate complex flow structures such as horizontal shear layer, streamwise and vertical vortices and momentum transfer. Stocchino and Brocchini (2010) investigated experimentally the generation and evolution of large-scale vortices in a straight compound channel under quasi-uniform flow conditions, shallow streams of different velocities using particle image velocimetry (PIV). Instantaneous measurements of the surface flow velocity were analysed by means of vortex identification and vorticity fields. Terrier (2010) observed large vortices at the interfaces between the main channel and the presence of a one-line rigid emergent vegetation along the floodplain edge based on flow visualization. Jahra et al. (2011) visualized “experimentally and simulated numerically” large-scale horizontal vortices along the interface between the main channel and the vegetated floodplain with three different cases of vegetation placement patterns on the floodplain under emergent condition. Uijttewaal (2011) investigated experimentally the impact of bed level and bed roughness on the eddy formations between the main channel and the floodplain in compound shallow flows.

The impact of transverse depth variation can be explained as the vertical compression which accelerate the flow towards the floodplain and decelerate the reverse flow leading to a deformation of the eddy structures. Vermaas et al. (2011) investigated experimentally the mechanisms control the momentum transfer in compound channel flows with different bed roughness. They noticed that with two parallel flow lanes of different bed roughness, three mechanisms for exchange of streamwise momentum are distinguished namely: cross-channel secondary circulations, turbulent mixing resulting from vortices acting in the horizontal plane, and mass transfer from the decelerating flow over the rough-bottomed lane to the accelerating flow in the parallel smooth-bottomed lane. Azevedo et al. (2012) investigated experimentally the flow structure in a compound channel flow in the presence of one-line vegetation along the edge of the floodplain using LDV. They found that the interaction of the faster flow in the main channel and the slower flow velocity on the vegetated floodplain has a complex turbulent 3D field composed of large-scale horizontal structures and secondary cells. These turbulent structures are responsible for significant lateral momentum transfer. Biemiiller et al. (2012) investigated the structure of turbulent flows that have been performed at the interface between the main channel and the floodplain in a compound channel flow using LES techniques. The results showed large scale streamwise vortices move along the whole length of the channel at the interface between the main channel and the floodplain. Koftis et al. (2014) numerically presented the evolution of vortices with the strongest one found at the interface region between the main channel and the vegetated floodplain of flow in compound channels. Kozioł and Kubrak (2015) used Acoustic Doppler Velocimeter (ADV) recording the instantaneous velocities to investigate the changes in spatial turbulence intensity, water turbulent kinetic energy, the time and spatial scales of turbulent eddies (macro and micro eddies) in a compound channel with and without floodplain roughness.

This study aims to evaluate a new technique that applies infrared thermography as a novel approach to predict the mixing shear layer at the interface between the main channel (MC) and the floodplain (FP). This technique has been proposed for analysis of the surface water temperature distribution and the thermal images are considered as a tracer of the coherent structures generated at the MC/FP interface. Two setups of

vegetated floodplain are adopted in this research as shown in Fig. 3.1. These setups are one-line vegetation along the edge of the floodplain adjacent to the main channel and wholly vegetated floodplain, which are then compared with the non-vegetated floodplain.

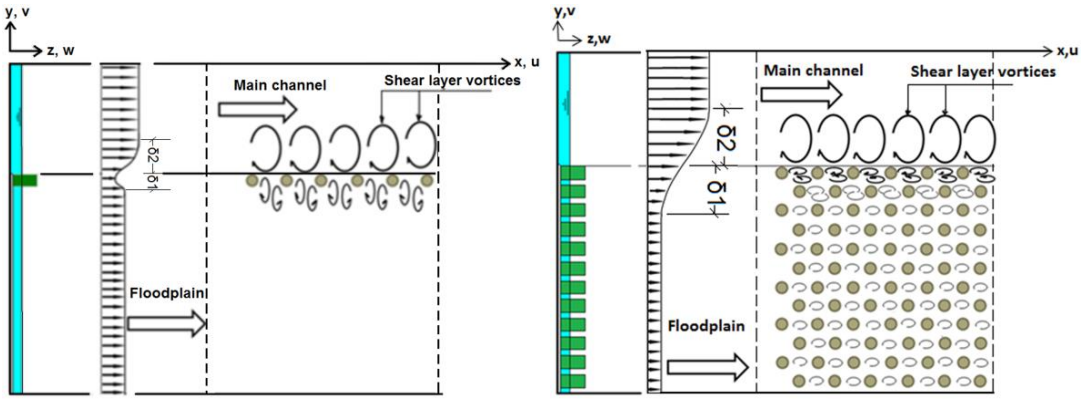

(a) (b)

Fig. 3.1: Mixing process models in compound channel flows of the vegetated floodplain (a) one-line vegetation along the edge of the floodplain, and (b) wholly vegetated floodplain with a staggered arrangement.

3.2 METHODOLOGY AND EXPERIMENTS SET UP

The experiments were carried out in the Hyder Hydraulics Laboratory at Cardiff University, UK, using a 10 m long laboratory glass-walled flume of a recirculating system, 1.2 m wide and 0.3 m deep. The flume slope was set up with 0.001 for all of the experiments. A compound channel was designed with shallow flow conditions by attaching plastic sheets along one side of the flume, with a width of 76 cm, a thickness of 2.4 cm and channel side slope as 1(H):1(V). Holes were made along the entire floodplain width with staggered arrangements with $a_x = a_y = 12.5$ cm. Circular wooden rods were selected of diameters D = 1.25 cm, 2.5 cm and 5.0 cm, attached to the bed of the floodplain in two configurations; first, wholly vegetated floodplain with vegetation density defined by a solid volume fraction (SFV) as sparse (D = 1.25 cm and SVF = 1.5%), medium (D = 2.5 cm and SVF = 6.2%) and dense (D = 5.0 cm and SVF = 24.8%) as shown in Fig. 3.2; second, a one-line array of vertically-oriented rod diameters placed along the edge of the floodplain adjacent the main channel at 12.5 cm apart as shown in Fig. 3.3;. Transverse strips of 1.3 mm

thickness and 4.8 mm width were fixed on the entire width of the floodplain at distances of 6.25 cm apart along the floodplain length. A tail gate that fixed at the end of the flume was used to control the water levels. A point gauge and Nixon Probe Velocimetry were used for measuring water levels and point velocities

(a) (b)

(c)

Fig. 3.2: Wholly vegetated floodplain's physical model (a) D = 1.25 cm, SVF=1.5%, (b) D = 2.5 cm and SVF = 6.2%, and (c) D = 5.0 cm and SVF = 24.8%.

(a) (b)

Fig. 3.3: Examples of a one-line vegetated floodplain model fixed along the edge of the floodplain adjacent to the main channel for (a) D = 2.5 cm, (b) D = 5.0 cm.

Discharges were measured using the flow meter and calibrated by velocity measurements and volume flow rate.

A thermal system was used that consists of a thermal camera of 30 Hz image frequency and (640 X 480) pixel images resolution. This camera collects the infrared radiation from objects in the scene and creates an electronic image based on information about the temperature differences. The other parts of the thermal system are water tank with heater and thermostat, injected tube and computer with FLIR research IR software connects which is directly to FLIR thermal imaging cameras to acquire thermal snapshots or movie files that can be stored on the SD-card. Two moving rails across the compound channel section were used; at the first rail, a thermal camera SC640 was mounted vertically above the water surface at a distance of about 65 cm from the water surface of the flow for high resolution purposes and in a section where the fully developed flow condition was achieved and a video capture rate of five frames per second was applied. An arrangement was also achieved across the rail to move the thermal camera laterally across the flume section by a slide mean. On the second rail, the other parts of the thermal system were fixed, in which the water tank connected to an injected tube, and the free end of the injection tube was fixed at the water surface under a fully developed flow condition at 7.6 m from the up-stream end of the flume working section. Figures (3.4 & 3.5) show a schematic diagram of the thermal system arrangement that was used with the compound channel flow section and a photograph of the system layout.

At the start, the flow runs under a uniform flow condition, hot water releases from the water tank into the flume working section continuously via the injection tube with a velocity equal to the velocity of the compound channel at the interface between the main channel and the floodplain. As the thermal camera was fixed near to the water surface, the area to be captured is in a part of the entire shear layer area, which consists of 15 squares, five in the longitudinal direction and three squares in the transverse direction, which were checked before the actual runs. Experiments were achieved in such a way that the images have to be overlapped. To increase the number of image sequences that are used in the analysis, two video files each of 187 sequences were recorded for each square.

The experiments were divided into three groups. Group one represents the case without vegetation on the floodplain, with discharges of 4.66 l s^{-1} and 11.03 l s^{-1}. The second group is considering a one-line of vegetation along the edge of the floodplain, and three rod diameters were selected of D = 1.25 cm, 2.5 cm and 5.0 cm. With each rod size two discharges (4.66 l s^{-1} and 11.03 l s^{-1}) were applied, as in the first group.

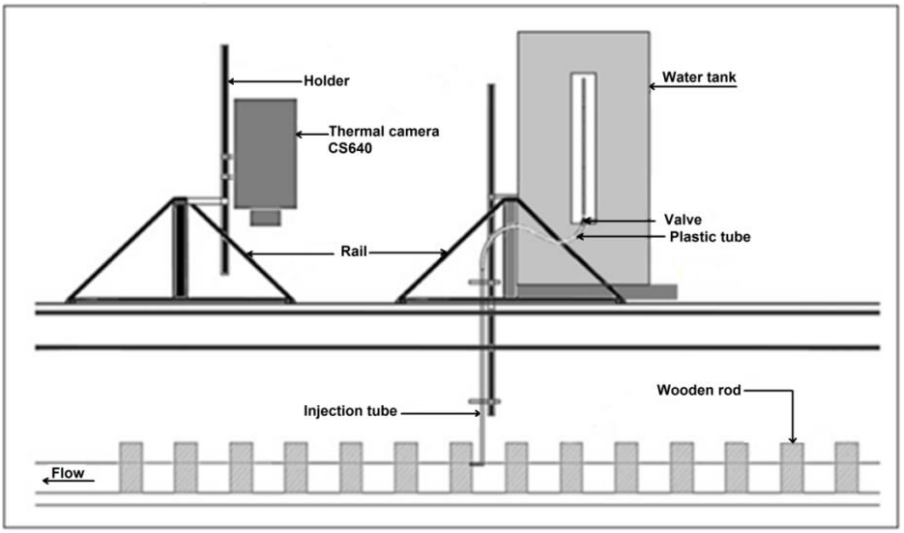

(a)

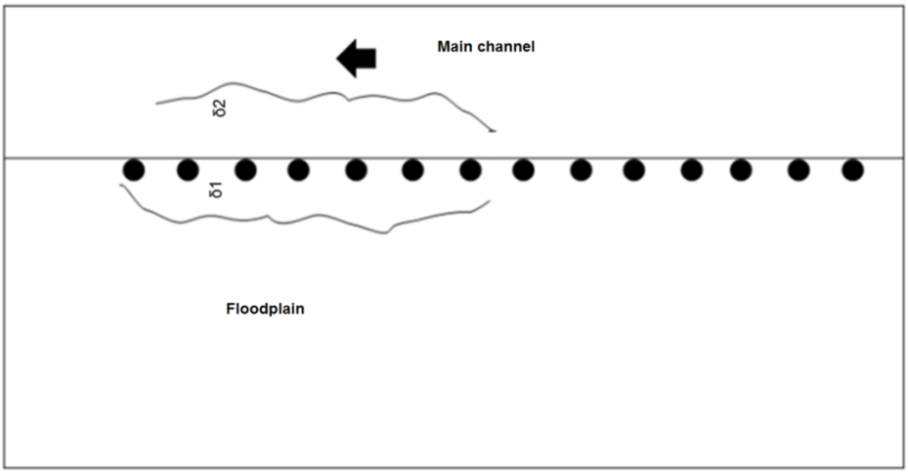

(b)

Fig. 3.4: A schematic diagram of system layout of the thermal camera across the compound channel flow section.

Fig. 3.5: A photograph of the system layout showing the thermal camera, the injection tube, the water tank, and a computer that were fixed at two rails across the compound channel section flow of 1.2 m width in the presence of one-line vegetation along the edge of the floodplain.

The third group is dealing with the wholly vegetated floodplain with the same rod diameters as described in group two (D = 1.25 cm, 2.5 cm and 5.0 cm), and with vegetation densities as a solid volume fraction, of sparse (SVF = 1.5%), medium (SVF = 6.2%) and dense (SVF = 24.80%) respectively. Similarly, two discharges were used as with the case studies of one-line vegetation and without vegetation on the floodplain tests (Q = 4.66 l s^{-1} and 11.03 l s^{-1}).

The hydraulic characteristics of the experiments are explained in the Table 2.1. In this table calculation of the Reynolds numbers is based on the bulk velocity, U_b and the cylinder diameter, $Re_D = U_bD/\nu$ for the compound channel flows with vegetated floodplain, and based on the bulk velocity , U_b and the water depth, H for the non-vegetated floodplain cases. The Reynolds number range in the compound channel flows is, Re_D = 1700 - 12200. The Froude number calculations for uniform flow was in the range of Fr = 0.16 - 0.26 which states subcritical flow, is based on the bulk velocity, U_b as $Fr = U_b/(gH)^{0.5}$, where H is the flow depth in the main channel, and g is the gravitational acceleration.

Table 2.1: Hydraulic characteristics of flow conditions in compound channel section with and without vegetated floodplain.

Case study	Discharge Q (l/s)	Water depth H_{mc} (cm)	Water depth h_f (cm)	Bulk velocity U_b (cm/s)	Reynolds number Re_D	Reynolds number Re_H	Froude number Fr
Without vegetation	4.66	3.96	1.56	16.07	-	6327	0.26
	5.82	4.61	2.21	15.82	-	7249	0.24
	7.51	5.26	2.86	16.84	-	8806	0.23
	8.87	5.59	3.19	18.27	-	10152	0.25
	11.03	6.12	3.72	20.08	-	12214	0.26
Wholly vegetated (Dense) D=5.0cm	4.66	4.46	2.06	13.32	6619	-	0.20
	5.82	5.14	2.74	13.48	6699	-	0.19
	7.51	6.18	3.78	13.50	6709	-	0.17
	8.87	6.99	4.59	13.57	6746	-	0.16
	11.03	7.95	5.55	14.34	7128	-	0.16
Wholly vegetated (Medium) D=2.5cm	4.66	4.37	1.97	13.74	3415	-	0.21
	5.82	5.01	2.61	13.98	3475	-	0.20
	7.51	6.20	3.80	13.44	3340	-	0.17
	8.87	7.00	4.60	13.55	3367	-	0.16
	11.03	7.95	5.55	14.34	3564	-	0.16
Wholly vegetated (Sparse) D=1.25cm	4.66	4.35	1.94	13.87	1724	-	0.21
	5.82	4.89	2.49	14.48	1800	-	0.21
	7.51	6.05	3.65	13.89	1726	-	0.18
	8.87	6.69	4.29	14.36	1785	-	0.18
	11.03	7.78	5.38	14.73	1831	-	0.17
One-line vegetation D=5.0cm	4.66	4.39	1.99	13.64	6782	-	0.21
	5.82	5.12	2.72	13.55	6736	-	0.19
	7.51	5.83	3.43	14.60	7257	-	0.19
	8.87	6.49	4.09	14.94	7428	-	0.19
	11.03	6.98	4.58	16.90	8400	-	0.20
One-line vegetation D=2.5cm	4.66	4.22	1.82	14.51	3606	-	0.23
	5.82	4.71	2.31	15.31	3804	-	0.23
	7.51	5.39	2.99	16.27	4044	-	0.22
	8.87	5.95	3.55	16.78	4169	-	0.22
	11.03	6.54	4.14	18.39	4570	-	0.23
One-line vegetation D=1.25cm	4.66	4.22	1.82	14.51	1803	-	0.23
	5.82	4.69	2.29	15.41	1914	-	0.23
	7.51	5.34	2.94	16.49	2049	-	0.23
	8.87	5.78	3.38	17.45	2168	-	0.23
	11.03	6.14	3.74	19.99	2484	-	0.26

3.3 RESULTS AND DISCUSSIONS

3.3.1 Image Processing Technique

At the end of recording video files, the next step is to export these sequences from the thermal camera into the FLIR software first, and then transferred them from the FLIR software to Matlab files. The information that transmitted in Matlab files is not directly temperatures. The information was in another sort of scale which is called a colour code that should be converted into temperature values. When getting the images with FLIR, the user has to set up the maximum and minimum range for the temperature. In the Matlab files, it is specified the maximum and minimum values for the colour code for getting out the relationship between the colour code values and temperature values. Knowing this fact, enables transformation the Matlab values into Celsius values. The average temperature calculation from a series of sequences of 187 images (640 X 480 pixels) was carried out for each part of the shear layer area. Since the recorded sequences were carried out for each part of the entire shear layer twice, an average temperature of each two recording videos was achieved for the entire shear layer parts. Then, a longitudinal overlapping for the entire shear layer parts at the centre, left and right is required.

Overlapping between the successive squares was done first for the centre part as follows; between the first and the second images to get a new image. Then the new image overlaps with the third image and so on till the fifth image. Any overlap between any two successive images had to go through a trial and error process with high accuracy in order to select the most suitable overlap. In a similar way the longitudinal overlapping was achieved to the left and right parts. At the end, three parts (centre, left and right) were being prepared for the second step. A horizontal overlapping may be needed between the centre and the left and the centre and the right parts. An example of introducing a shear layer form in a compound channel flow at the interface between the main channel and the floodplain was presented with wholly vegetated floodplain of sparse density. The results showed the mean (187x2) raw shear layer images of wholly vegetated floodplain as explained in Fig. 3.6.

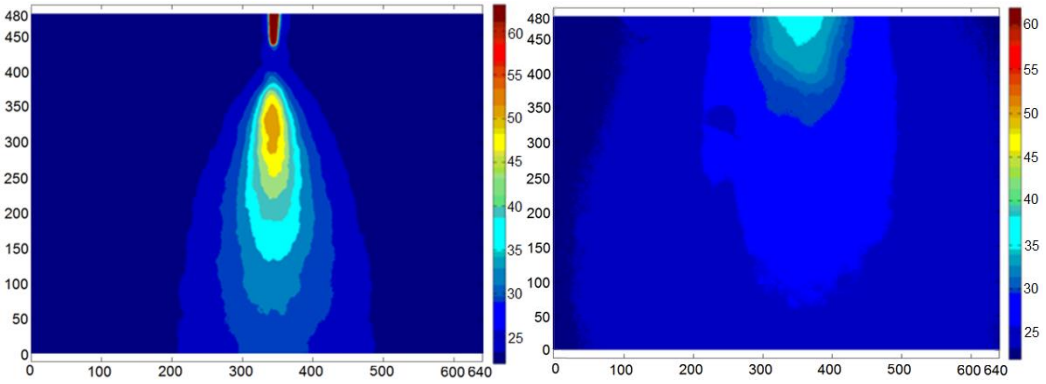

(a) (b)

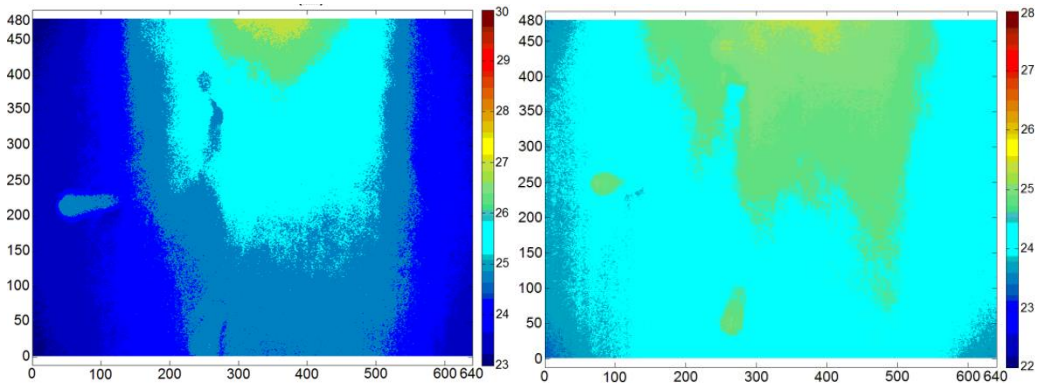

(c) (d)

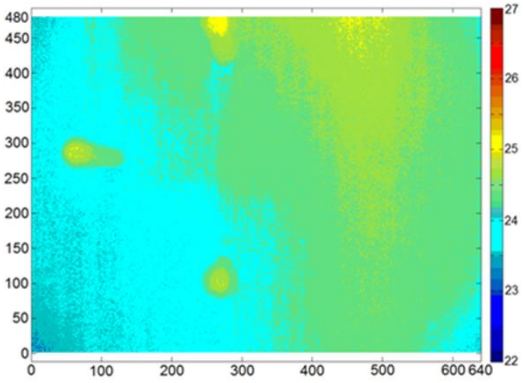

(e)

Fig. 3.6: Raw images at five longitudinal locations for a wholly vegetated floodplain with rod diameter, D = 1.25 cm, SVF = 1.5% and flow rate, Q = 4.66 l s^{-1}. (a) Raw image of the first square (b) Raw image of the second square (c) Raw image of the third square (d) Raw image of the forth square (e) Raw image of the fifth square. (All the dimensions in pixels).

Figure 3.7 shows the steps of the longitudinal overlapping at the centre location between the first and the second squares represents overlap 1, and then between the results of the first overlap with the third square and so on up to the end of the squares. The other five locations on either side of the centre part were similarly carried out with longitudinal overlaps to create the second and the third parts for the entire shear layer as left and right parts (see Fig. 3.8).

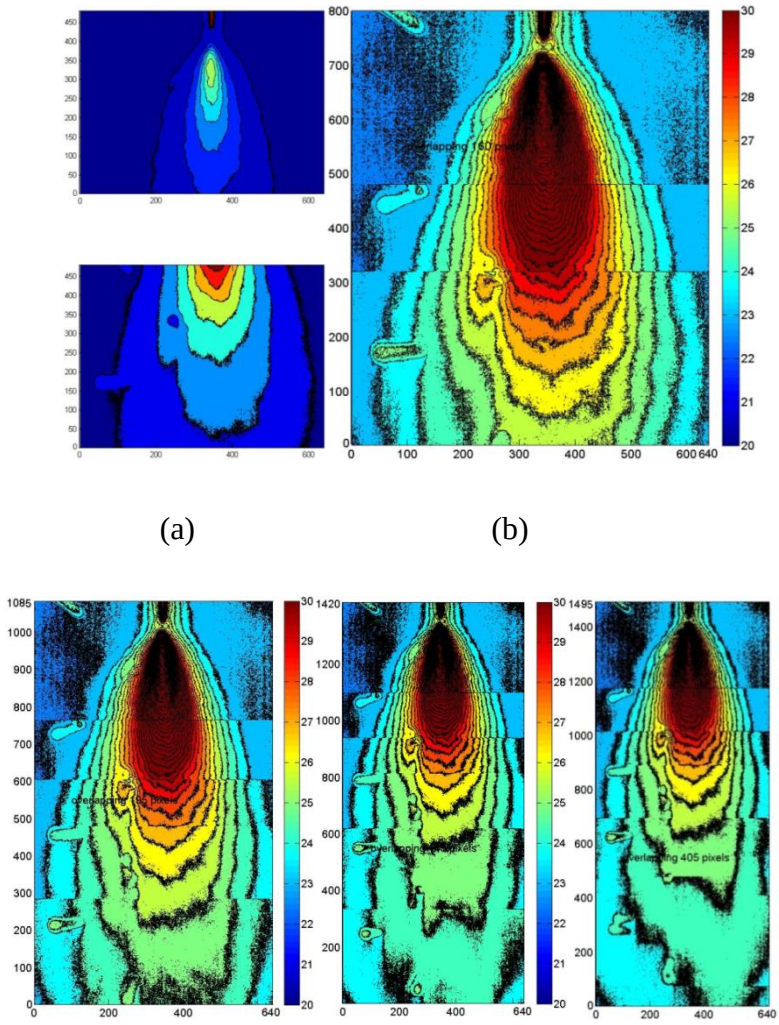

Fig. 3.7: Image processing in the longitudinal direction of the centre part at five squares for the case study of wholly vegetated floodplain with rod diameter, D = 1.25 cm, SVF = 1.5% and flow rate Q = 4.66 l s^{-1}. (a) Raw images of the first and the second squares (b) Overlap 1 between the first and the second raw images (c) Overlap 2 between the result of overlap 1 and the third raw image (d) Overlap 3 between the result of overlap 2 and the fourth image (e) Overlap 4 between the result of overlap 3 and the fourth image. (All the dimensions in pixels).

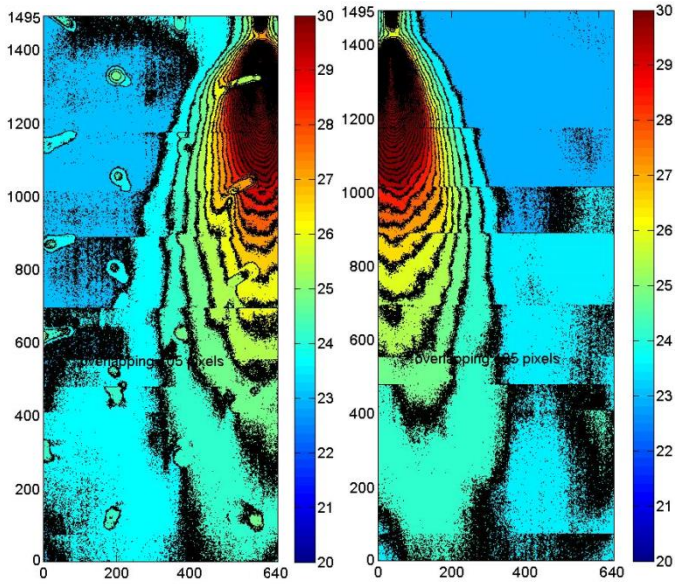

(a) (b)

Fig. 3.8: Left and right parts of the shear layer resulted from the image processing technique in the longitudinal direction for the five squares for the case study of wholly vegetated floodplain with rod diameter, D = 1.25 cm, SVF = 1.5% and flow rate, Q = 4.66 l s^{-1}. (a) Left side part of the shear layer on the floodplain shows the rod diameters within the flow (b) Right side part of the shear layer on the main channel. (All the dimensions in pixels).

To extract the final shear layer from the obtained three shear layer parts, a horizontal overlapping was done for the left and the centre part of the shear layer first, and then between the right part and the result of the overlap between the centre and the left parts. The final results from Matlab of shear layer images were then exported into Tec plot software as shown in Fig. 3.9.

In a similar way the longitudinal and the lateral overlaps were done for the other case studies. The aforementioned description of image processing techniques using Matlab and FLIR softwares was submitted as a conference paper (Mulahasan et al. 2015).

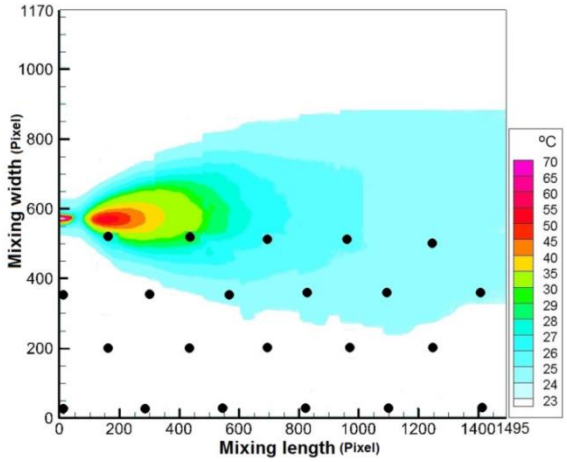

Fig. 3.9: Shear layer form at the interface between the main channel and the floodplain for a wholly vegetated floodplain case of sparse vegetation density with rod diameter of 1.25 cm and flow rate of 4.66 l s^{-1}. (All the dimensions in pixels).

3.3.2 Images of the Shear Layers

Two selected examples of time-averaged thermal images of 187 sequences are shown in Fig. 3.10 as a part of the whole shear layer in the longitudinal direction of the mixing shear layer that is generated at the interface between the main channel and the floodplain in a compound channel flow. These are a wholly vegetated floodplain with D = 5.0 cm and Q = 4.66 l s^{-1}, and with a one-line vegetation along the edge of the floodplain with D = 2.5 cm and Q = 4.66 l s^{-1}. The x and y axis of the drawings in Fig. 3.10 are normalized to water depth on the floodplain.

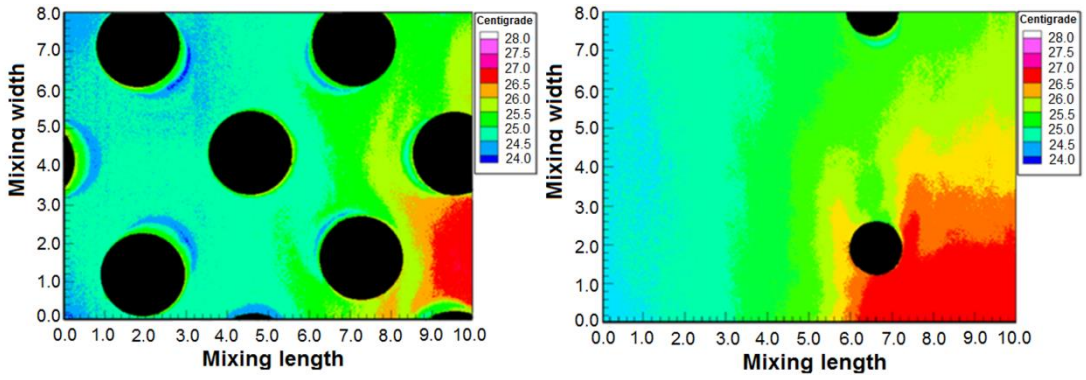

(a) (b)

Fig. 3.10: Examples of time-averaged thermal images normalized with flow depth on the floodplain for the case of (a) Wholly vegetated floodplain with D = 5.0 cm and Q = 4.66 l s^{-1} and (b) One-line vegetation with D = 2.5 cm and Q = 4.66 l s^{-1}.

To explain the evolution of the thermal distributions at different time intervals, snapshots with intervals of 1/5 second were selected for the wholly vegetated floodplain with rod diameter, D = 5.0 cm and flow rate, Q = 11.03 l s^{-1} as shown in Fig. 3.11 which describes the penetration of the temperature inside the vegetated floodplain.

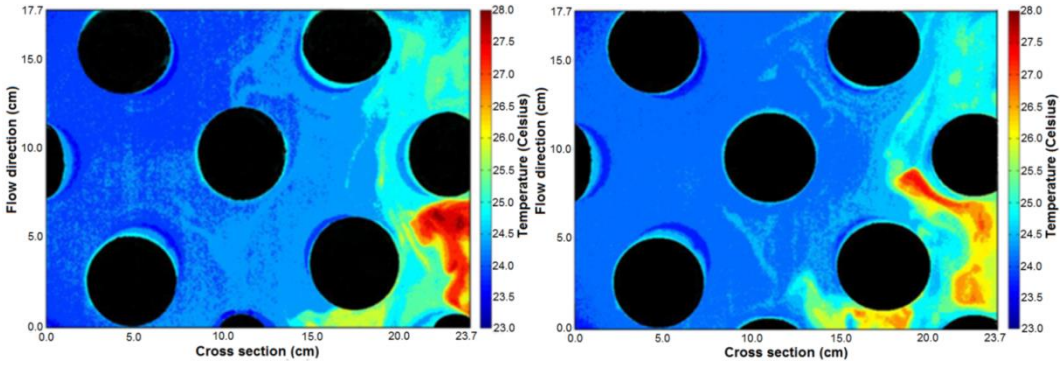

(a) Snapshot after 1/5 second (b) Snapshot after 2/5 seconds

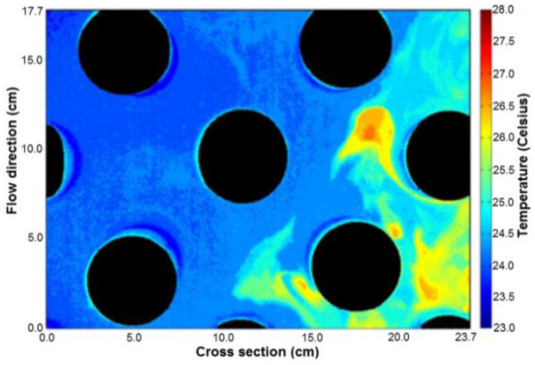

(c) Snapshot after 3/5 seconds

Fig. 3.11: Snapshots of the thermal images at time intervals of 1/5 second in the case of the wholly vegetated floodplain with rod diameter D = 5.0 cm and Q = 11.03 l s^{-1} which is showing the impact (relative to shading factor due to drag by vegetation causing lateral distribution) of the shear layer inside the vegetation elements and how the temperature dissipates within the rods arrangements due to stream-wise velocity and shear layer generated.

3.3.3 Effects of Vegetation

To visualize and evaluate the shear layer evolution at the interface between the main channel and the floodplain, fourteen examples are considered to review the results of

two setups one-line vegetation and wholly vegetated floodplain compared to without vegetation case. The final images of the shear layers are shown in Figs. (3.12-3.17); these figures represent time-averaged temperature distribution. The mixing length and the mixing width of the shear layers were normalized with water depth on the floodplain. The analysis showed that the structure of turbulent mixing shear layers (vortices) for a shallow water depth is very well captured and quantified by this novel approach as described by the physical model in Fig. 3.1.

The impact of transverse flow depth variation and bed roughnessess are considered. The impact of the roughness results in asymmetric shear layer about the vegetation interface and the eddy structures are deformed due to mass and momentum transfer between the main channel and the floodplain in the compound channel flows. The shear layer evolution at the interface between the main channel and the floodplain can be discussed as follows:

In the case of non-vegetated floodplain a symmetric leaf-shaped shear layer was observed in the case of Q = 11.03 l s^{-1}. That is to say the penetration thickness inside the vegetation $\delta 1$ equal to the penetration thickness inside the main channel $\delta 2$ as shown in Fig. 3.15. However, the shear layer distribution at the interface between the main channel and the floodplain is asymmetric for the case of Q=4.66 l s^{-1} due to the impact of the flow depth variation between the main channel and the floodplain that influencing the velocity gradient as shown in Fig. 3.12.

Figures of the shear layers manifest the evolution of the temperature distribution in the x-y plane. The longest shear layer was monitored and observed in the non-vegetated floodplain case studies in comparison with the cases of vegetated floodplain. This can be imputed to absence of vegetation elements on the floodplain that results in a less drag force. This is also can be seen in the time averaged temperature distribution diagrams in Figs. 3.18 & 3.21.

In the one-line vegetation case, a similar trend to the non-vegetated floodplain was observed with much more deformation to the shear layer shape, and the shear layer length is shorter than that in the non-vegetated floodplain case due to the drag by the one-line vegetation along the edge of the floodplain-main channel interface as shown

in Figs. 3.13 and 3.16 for the rod diameters (D =1.25, 2.5, and 5.0 cm) and flow rates Q = 4.66 l s^{-1} and Q = 11.03 l s^{-1} respectively. The shear layer shape is significantly influenced by the vegetation elements due to the increasing the velocity gradients between the main channel and the floodplain in the compound channel flow, the presence of dip velocity at the junction and due to the wake by the successive rods. The velocity gradient reflects the momentum transfer between the vegetated and non-vegetated sections. The length of the shear layer is decreased as the rod diameter is increased or in increasing floodplain's blockage factor (D/W), where D = cylinder diameter and W = flume width. The rod diameter, D = 5.0 cm shows a significant decrease in the shear layer length in comparison to the other two diameters (D = 1.25, and 2.5 cm), and the temperature distribution has a different propagation .The (thermal) shear layer distribution for the smallest two diameters (D =1.25, and 2.5 cm) at the interface between the main channel and the floodplain shows the same trend as with non-vegetated floodplain cases.

It was observed that the temperature distributions inside the main channel much more than inside the floodplain and can be expressed by ($\delta 1/\delta 2$) < 1. This scenario can also be seen in Figs. (3.19 & 3.22) in time averaged water temperature distributions for Q = 4.66 l s^{-1} and Q = 11.03 l s^{-1} respectively.

The results of the shear layer distribution with the wholly vegetated floodplain case studies are shown in Figs. (3.14 & 3.17) for sparse, medium and dense vegetation densities, with Q = 4.66 l s^{-1} and Q = 11.03 l s^{-1} respectively. The mixing shear layers have shown more penetration insde the main channel than that on the floodplain as with one-line vegetation case studies and ($\delta 1/\delta 2$) < 1. This is because the drag increases on the floodplain with increasing the vegetation density or with high blockage and due to the wake of neighbouring cylinders. Figs. 3.14 (a, b and c) show a significant impact of vegetation density on the shear layer length with Q = 4.66 l s^{-1}. Increasing the vegetation density on the floodplain results in a higher the velocity gradient between the main channel and the floodplain; decreases the shear layer length and increases the temperature distribution inside the vegetation elements than that with one-line vegetation. Mass and momentum transfer between the vegetated and non-vegetated sections due to the velocity differences. At high flow

rate (Q = 11.03 l s^{-1}), the impact of vegetation density on the shear layer length shows almost the same explanations as with low discharge (Q = 4.66 l s^{-1}) as shown in Fig. 3.17.

The shear layer shape for the wholly vegetated floodplain case studies has a less deformed than that in one-line vegetation case studies. This scenario can be also seen in Figs. (3.20 & 3.23) in time-averaged water temperature distributions with Q = 4.66 l s^{-1} and Q = 11.03 l s^{-1} respectively.

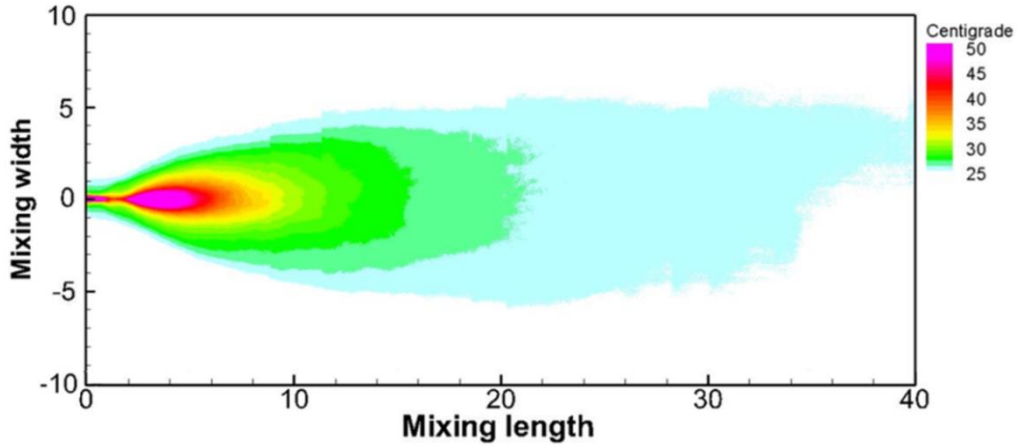

Fig. 3.12: Shear layer evolution at the interface between the main channel and the floodplain in a compound channel flow for the case of non-vegetated floodplain with Q = 4.66 l s^{-1}.

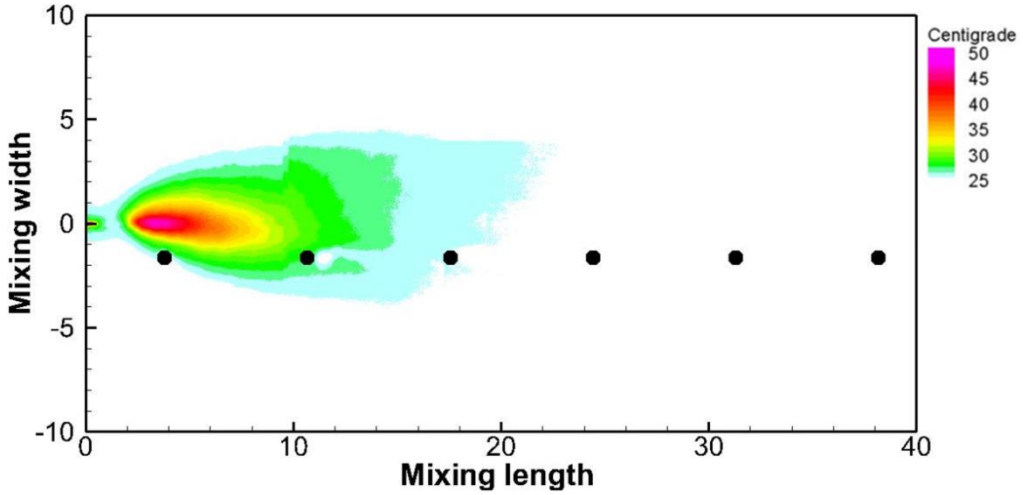

(a)

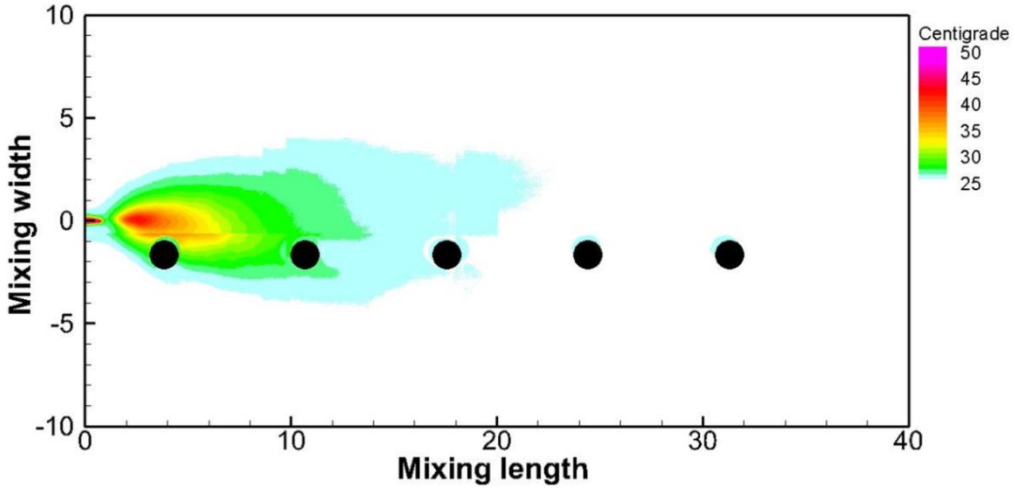

(b)

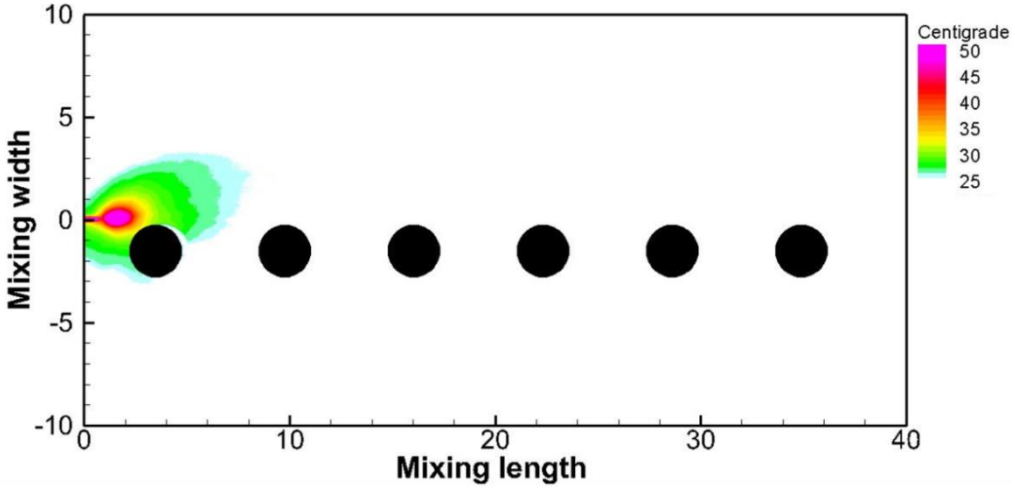

(c)

Fig. 3.13: Shear layer evolution at the interface between the main channel and the floodplain in a compound channel flow in presence of one-line vegetation along the edge of the floodplain adjacent to the main channel with Q = 4.66 l s^{-1} and rod diameter of (a) D = 1.25 cm (b) D = 2.5 cm, and (c) D = 5.0 cm.

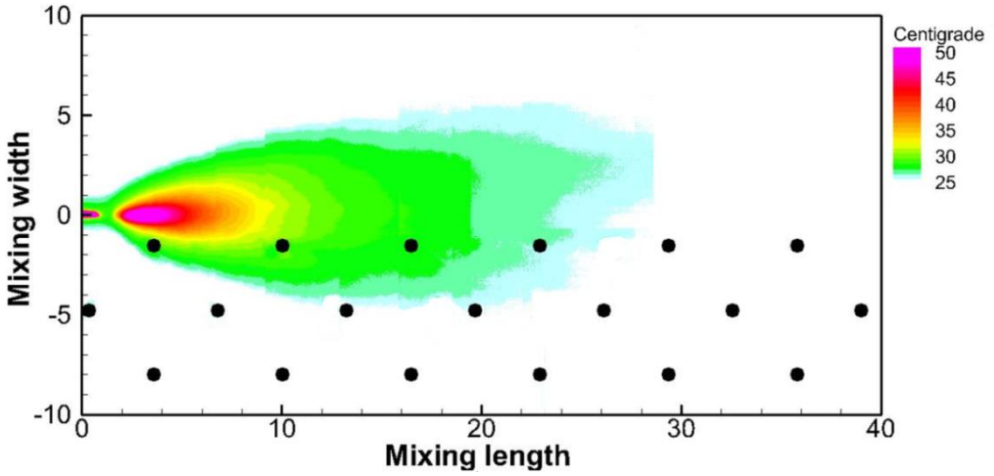
Centigrade
50
45
40
35
30
25
Mixing width
10
5
0
-5
-10
0
10
20
30
40
Mixing length

(a)

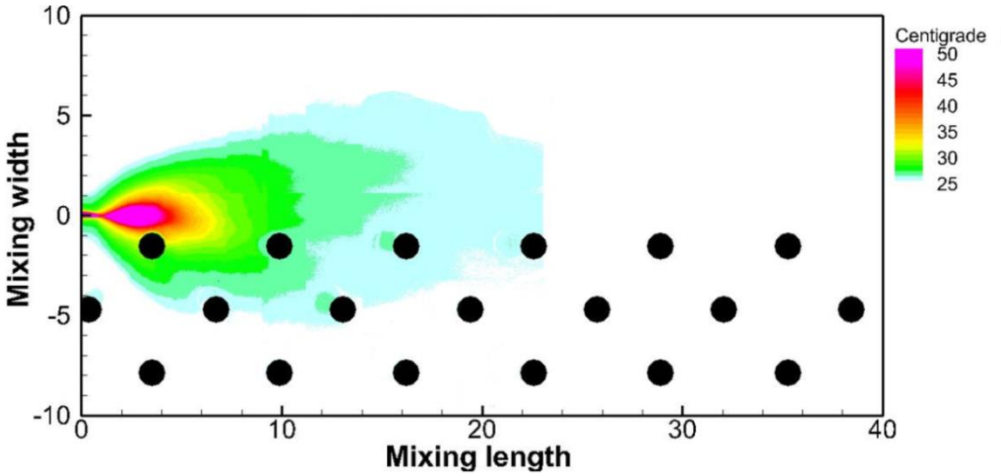
Centigrade
50
45
40
35
30
25
Mixing width
10
5
0
-5
-10
0
10
20
30
40
Mixing length

(b)

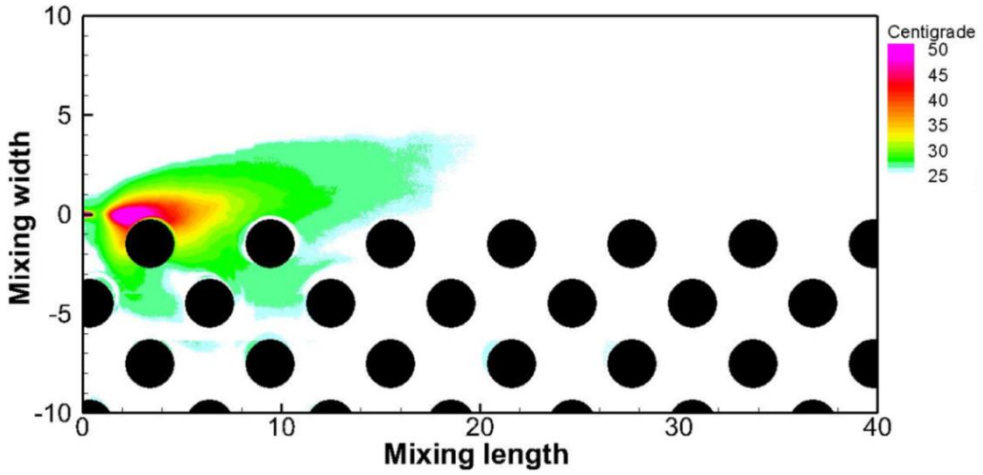
Centigrade
50
45
40
35
30
25
Mixing width
10
5
0
-5
-10
0
10
20
30
40
Mixing length

(c)

Fig. 3.14: Shear layer evolution at the interface between the main channel and the floodplain in a compound channel flow for the case of the wholly vegetated floodplain with Q = 4.66 l s^{-1} for vegetation density as (a) sparse (b) medium (c) dense.

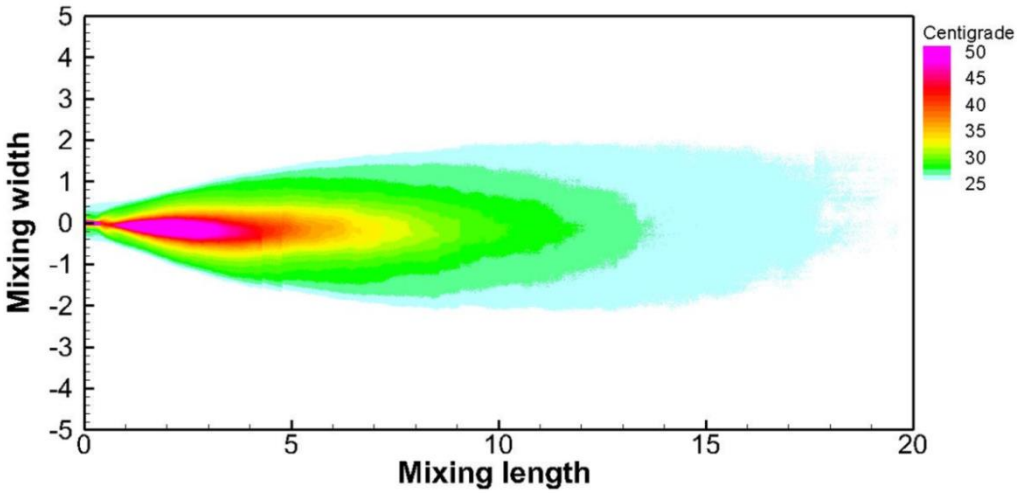

Fig. 3.15: Shear layer evolution at the interface between the main channel and the floodplain in a compound channel flow for the case of non-vegetated floodplain for Q = 11.03 l s^{-1}.

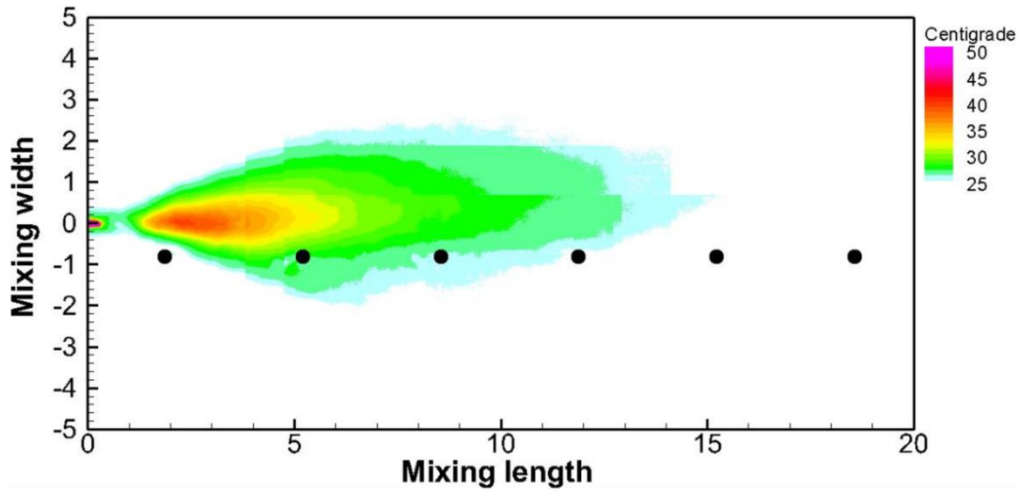

(a)

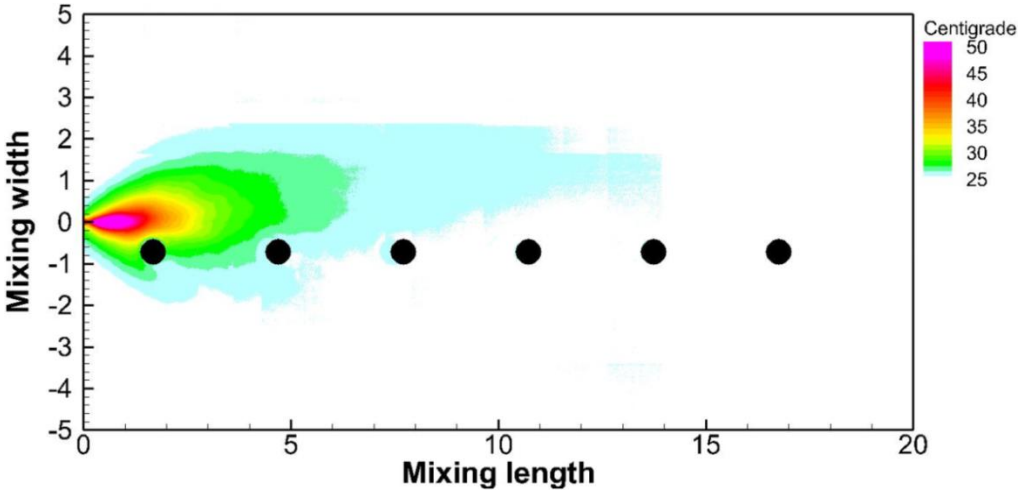

(b)

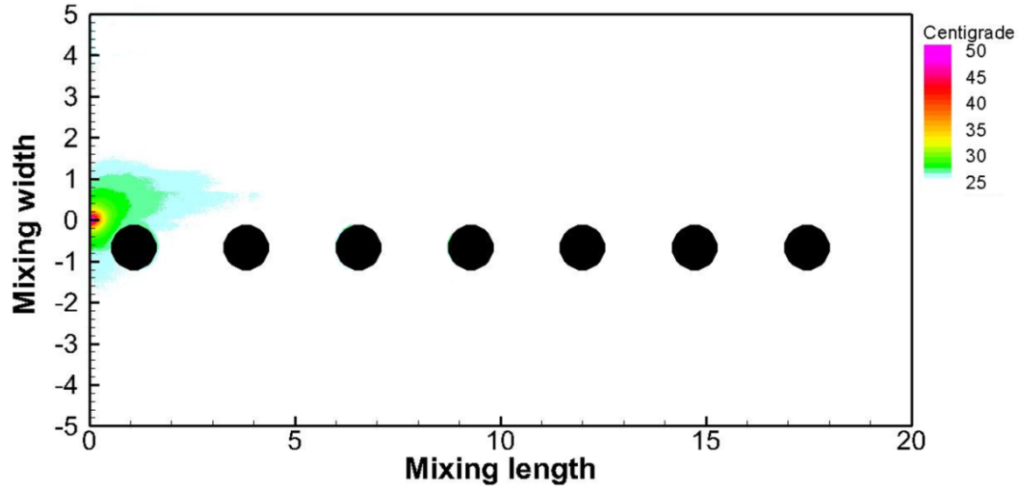

(c)

Fig. 3.16: Shear layer evolution at the interface between the main channel and the floodplain in a compound channel flow in presence of one-line vegetation along the edge of the floodplain adjacent to the main channel with Q = 11.03 l s^{-1} for rod diameter of (a) D = 1.25 cm (b) D = 2.5 cm, and (c) D = 5.0 cm.

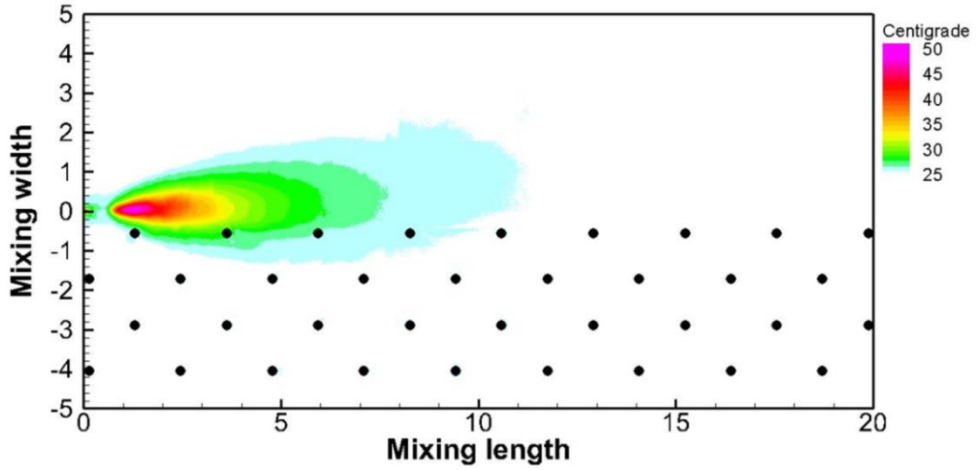
Centigrade
50
45
40
35
30
25
Mixing width
Mixing length
5
4
3
2
1
0
-1
-2
-3
-4
-5
0
5
10
15
20

(a)

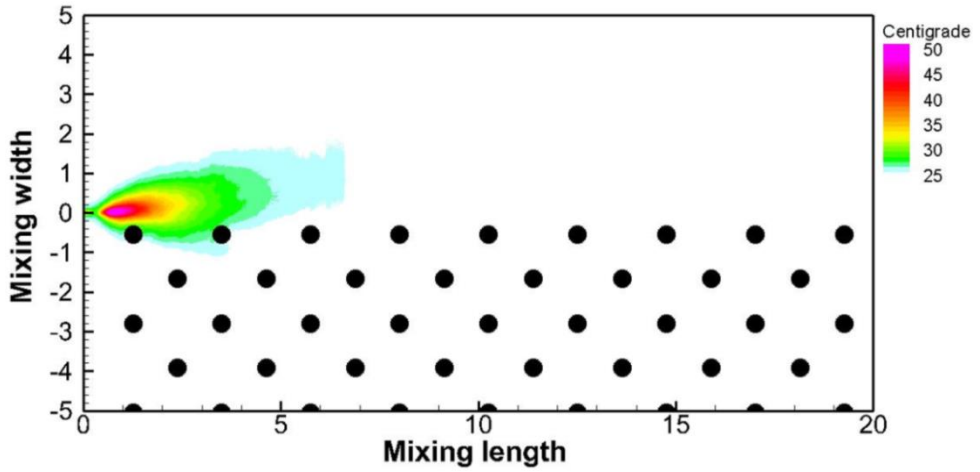
Centigrade
50
45
40
35
30
25
Mixing width
Mixing length
5
4
3
2
1
0
-1
-2
-3
-4
-5
0
5
10
15
20

(b)

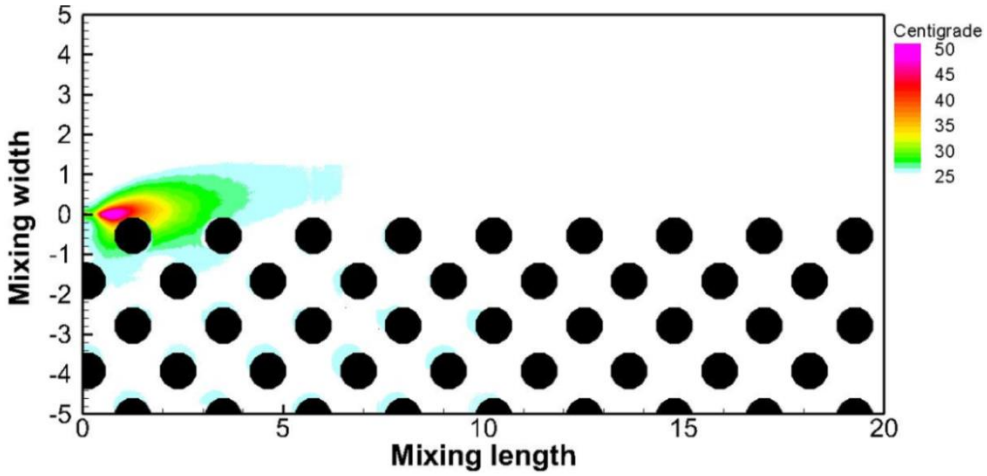
Centigrade
50
45
40
35
30
25
Mixing width
Mixing length
5
4
3
2
1
0
-1
-2
-3
-4
-5
0
5
10
15
20

(c)

Fig. 3.17: Shear layer evolution at the interface between the main channel and the floodplain in a compound channel flow for the case of the wholly vegetated floodplain with Q = 11.03 l s^{-1} and vegetation density as (a) sparse (b) medium and (c) dense.

3.3.4 Time-averaged temperature distribution

Time-averaged temperature distributions were extracted at four sections across the shear layer evolution. These sections were normalized to water depth on the floodplain, h_f and represented by (0h, 2h, 4h and 10h). Results of time-averaged temperature distributions reflect an index of penetration the shear layer within the vegetation zone and inside the main channel, and shear layer evolution as shown in Figs. (3.18-3.23).

Fig. 3.18 shows the time averaged-temperature distribution in the case of the non-vegetated floodplain for flow rate of Q = 4.66 l s^{-1}. It has been shown that time averaged-temperature distributions were conducted at sections downstream the ambient of the injected hot water. After a small distance from the source of injecting the hot water, steep variation in the temperature distribution was observed, for example, the peak temperature (about 80 centigrade) sharp decreases in the direction of the flow and its peak after a small distance was reduced to less than 40-60% of its peak value at the point where the hot water was released. In addition, the lateral distribution displays the peak value which is considered at the interface where the point of injection hot water, while it continuously decreases laterally, in which after a small distance the temperature reaches the temperature degree of the running water in the flume. A significant decrease in the water temperature degree from a peak to a value of 23 ^{o}C is due to the turbulent mixing between compound channel sections. In a similar way, at high discharge case (Q = 11.03 l s^{-1}), the shear layer is showing the same trend as for (Q = 4.66 l s^{-1}), but with less shear layer thickness as shown in Figure (3.21). Mass and momentum transfer from the main channel (high velocity) to the floodplain (low velocity).

The vegetated floodplain case studies (Figures 3.19, 3.20, 3.22 and 3.23) were analysed. It has been shown that with the one-line vegetated floodplain (Figs. 3.19 & 3.22), the time averaged water temperature distributions depend on rod diameter,

blockage and flow rate considerations for Q = 4.66 l s^{-1} and Q = 11.03 l s^{-1} respectively. The temperature distribution in the longitudinal and transvers directions was also explained in the shear layer evolution plots (see section 3.3.3).

Time averaged water temperature distributions with wholly vegetated floodplain shows the evolution of the shear layers inside the vegetation and is affected by the vegetation density as shown in Figs. 3.20 and 3.23 for Q = 4.66 l s^{-1} and Q = 11.03 l s^{-1} respectively. The distribution of the (thermal) shear layer inside the vegetation elements is increased with increasing vegetation density due to the velocity reduction on the floodplain in comparison with one-line vegetation.

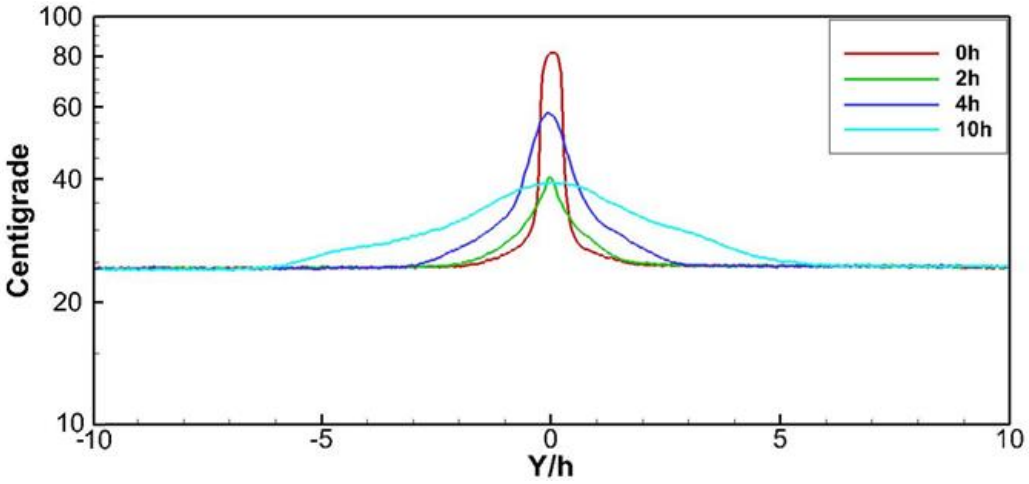

Fig. 3.18: Time-averaged water temperature distribution at the interface between the main channel and the floodplain for a compound channel flow of non-vegetated floodplain for Q = 4.66 l s^{-1}.

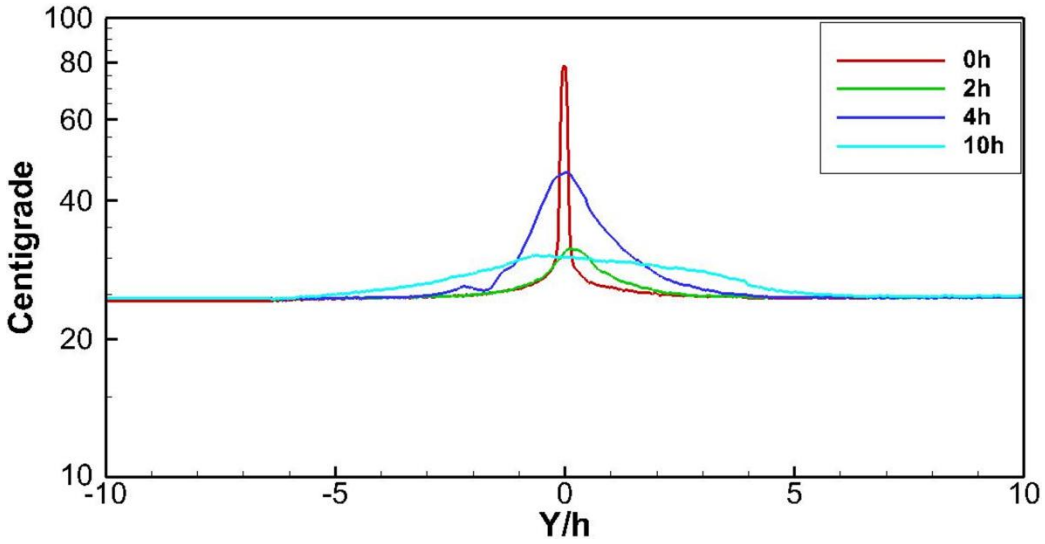
100
80
60
40
20
10
Centigrade
-10
-5
0
5
10
Y/h
0h
2h
4h
10h

(a)

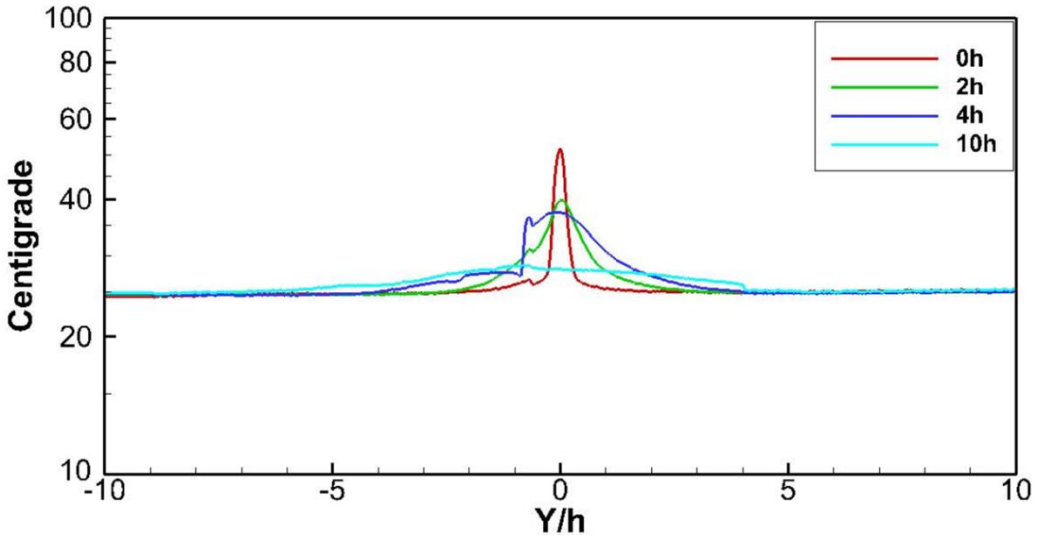
100
80
60
40
20
10
Centigrade
-10
-5
0
5
10
Y/h
0h
2h
4h
10h

(b)

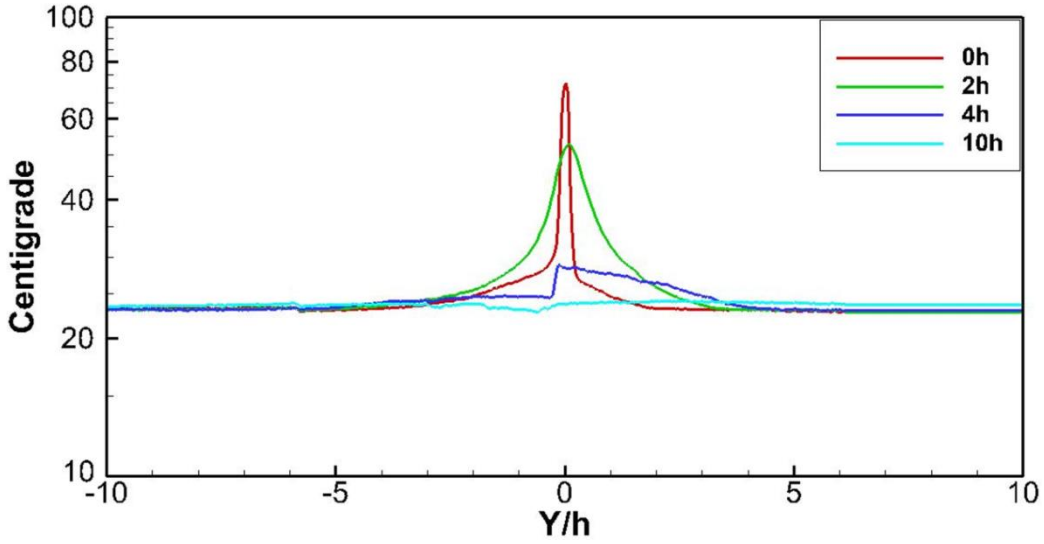

(c)

Fig. 3.19: Time-averaged water temperature distribution at the interface between the main channel and the floodplain for a compound channel flow of one-line vegetation along the edge of the floodplain with Q = 4.66 l s^{-1} and rod diameter of (a) D = 1.25 cm (b) D = 2.5 cm and (c) D = 5.0 cm.

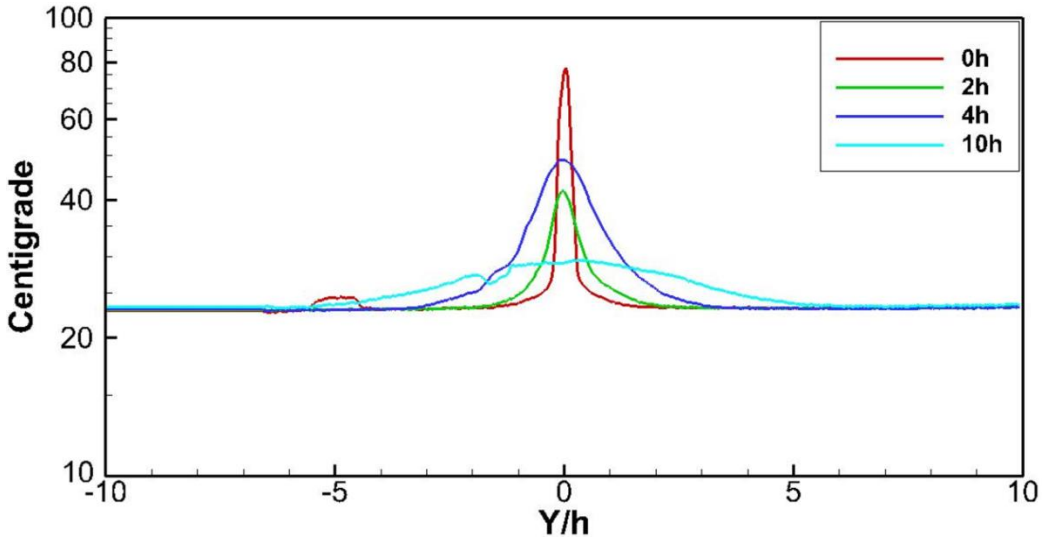

(a)

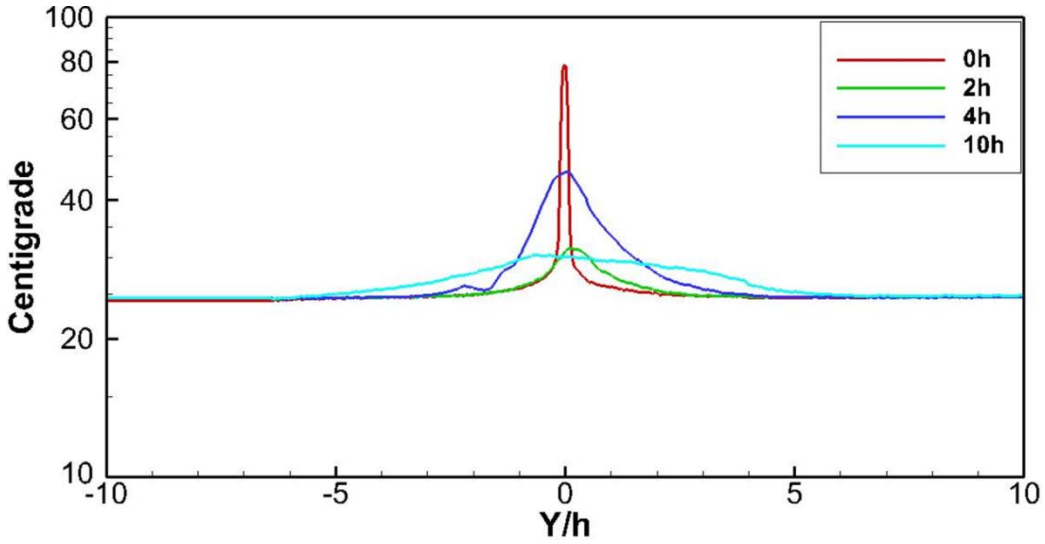

(b)

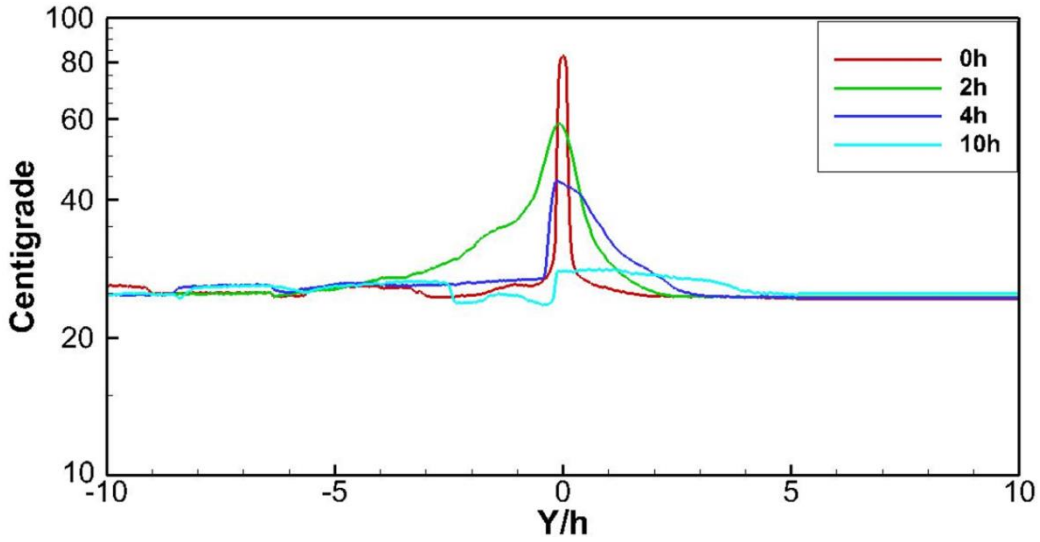

(c)

Fig. 3.20: Time-averaged water temperature distribution at the interface between the main channel and the floodplain for a compound channel flow of the wholly vegetated floodplain with Q = 4.66 l s^{-1} for vegetation density as (a) sparse (b) medium and (c) dense.

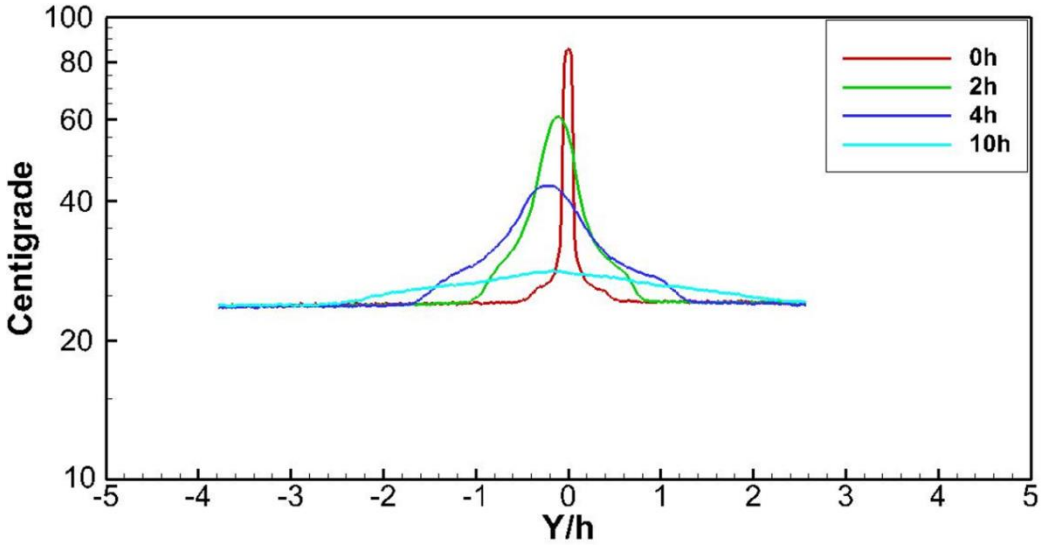

Fig. 3.21: Time-averaged water temperature distribution at the interface between the main channel and the floodplain for a compound channel flow of non-vegetated floodplain for Q = 11.03 l s^{-1}.

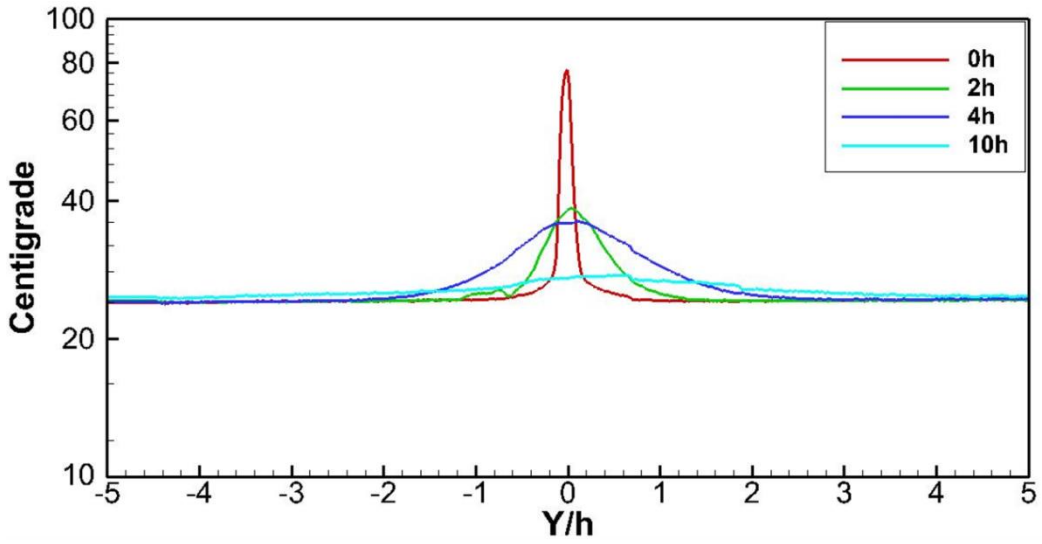

(a)

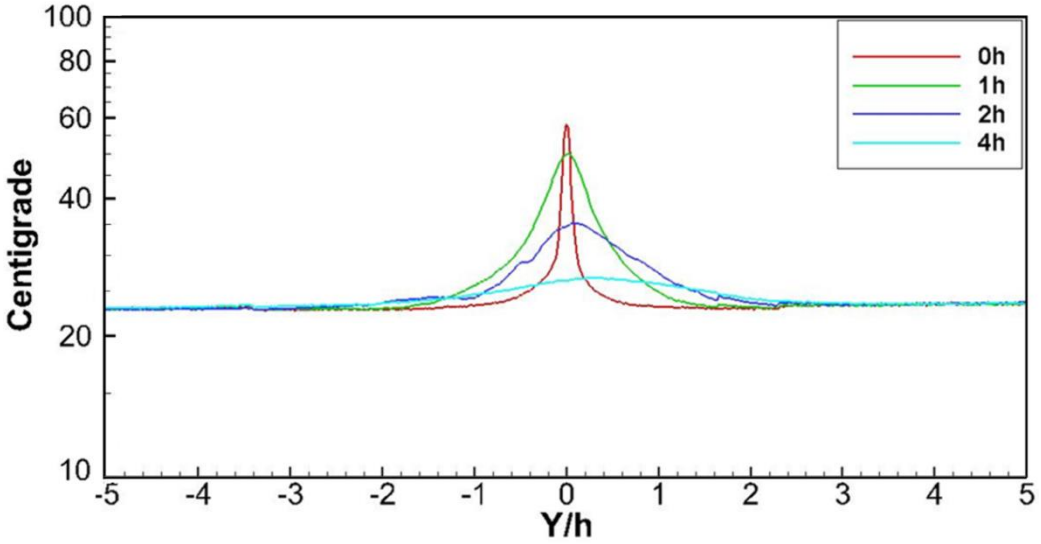

(b)

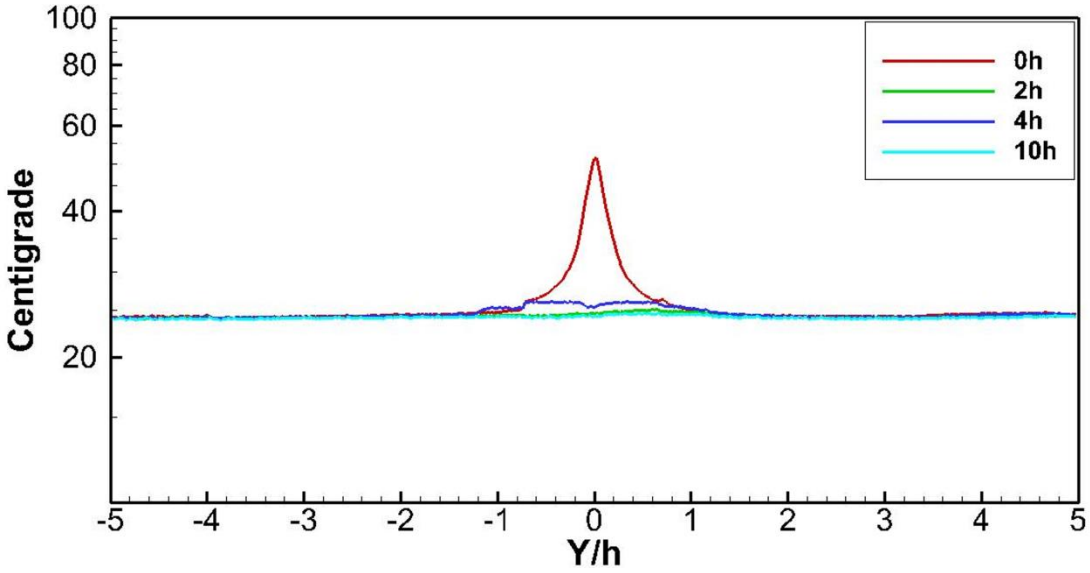

(c)

Fig. 3.22: Time-averaged water temperature distribution at the interface between the main channel and the floodplain for a compound channel flow of one-line vegetation along the edge of the floodplain with Q = 11.03 l s^{-1} and rod diameter of (a) D = 1.25 cm (b) D = 2.5 cm and (c) D = 5.0 cm.

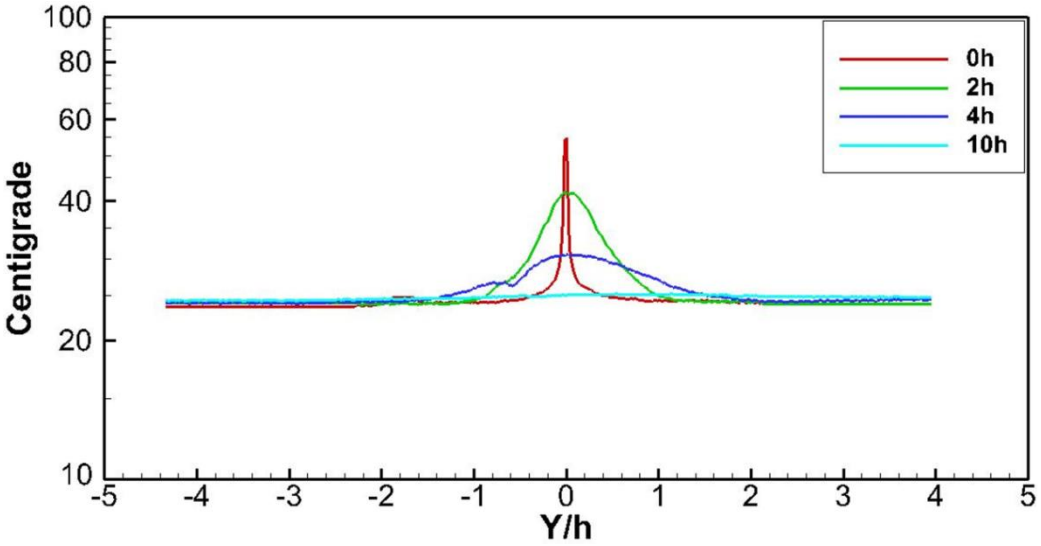

(a)

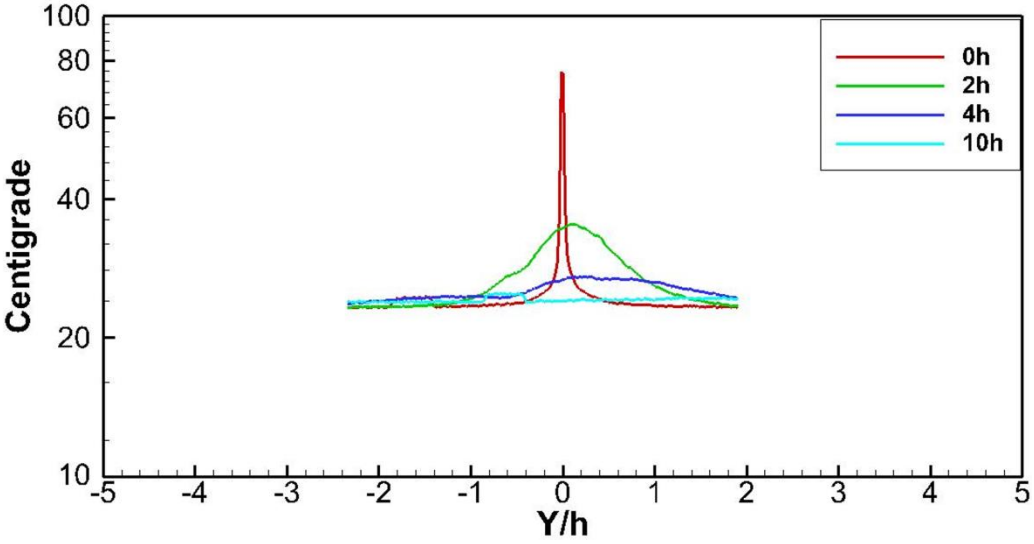

(b)

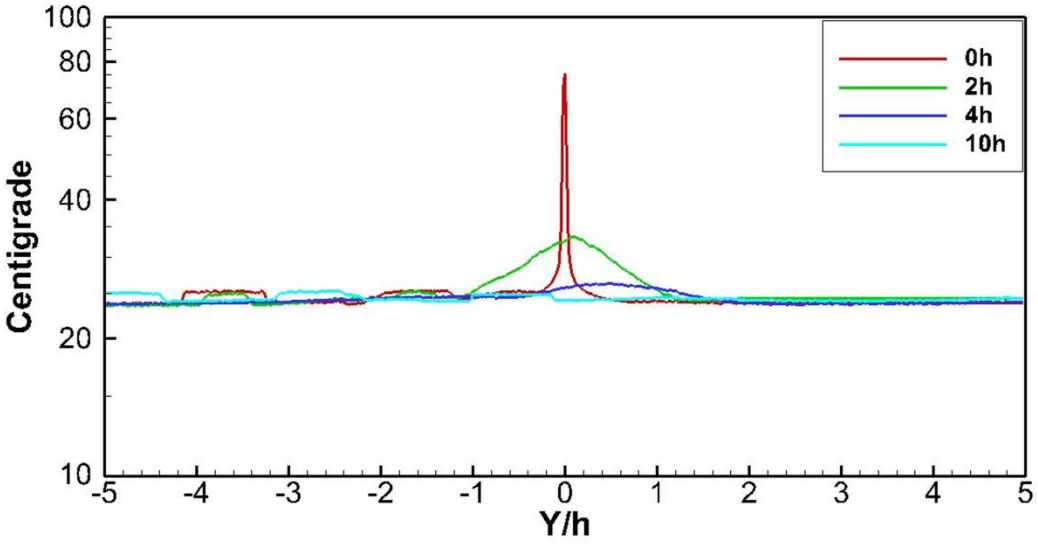

(c)

Fig. 3.23: Time-averaged water temperature distribution at the interface between the main channel and the floodplain for a compound channel flow of the wholly vegetated floodplain with Q = 11.03 l s^{-1} for the vegetated density of (a) sparse (b) medium and (c) dense.

3.3.5 Confirmation of the Models

For high image resolution, temperature values were extracted for each sequence at five selection points in the wake region using Matlab software. The results showed that the two kinds of vortices (shear layer vortices and von Karman vortices) that were suggested in the model in Fig. (3.1) may be produced and good results can be expected as shown in Figure (3.24).

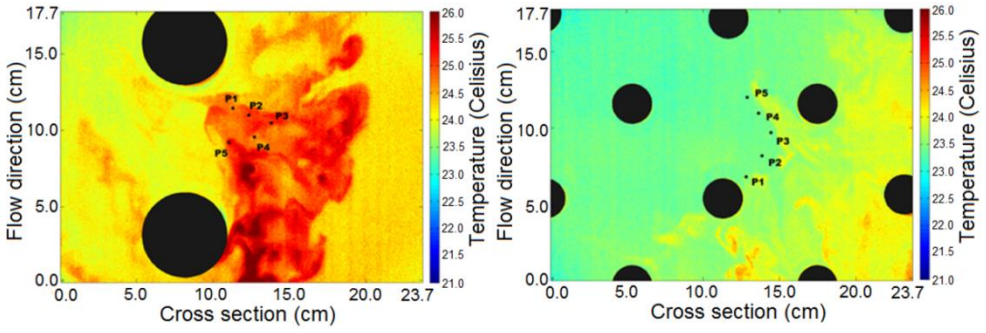

(a) (b)

Fig. 3.24: Two kinds of coherent structures (shear layer vortices and von Karman vortices) generated at the interface between the main channel and the floodplain with (a) One-line vegetation, with D = 5.0 cm and Q = 11.03 l s^{-1} and (b) Wholly vegetated floodplain, D = 2.5 cm and Q = 11.03 l s^{-1}.

3.3.6 Properties of the Vortices

To evaluate the development of eddies in the wake of the rods for the numbers of runs that were carried out with thermal camera SC640, it was shown that vortical structures are very clear in the densely vegetated floodplain (see Figure 3.25) as shown in the most suitable areas for eddies and turbulences in the selected run (wholly vegetated floodplain, D = 5.0 cm and Q = 4.66 l s^{-1}) after watching many videos of the entire shear layer squares, where the rate of vortex rotating is very high. This was done for five selection points in the wake area as shown in Figures (3.24) for other vegetation cases. A clear wake behind the cylinder in the case of medium vegetation case (D = 2.5 cm) is shown in Figure (3.24 b) and an area of high velocities between the cylinders is observed, while in the case of dense vegetated floodplain, flow field exhibits large velocity gradients in both stream-wise and span-wise directions as shown in Figure (3.25), these were described in details in (Stoesser et al. 2010) reference.

Shear layer vortices are usually occurring at the interface between vegetated and non-vegetated zones as shown in Figure (3.24 a) for a one-line vegetation, while von Karman vortices are formed behind the cylinder at short distance as a counter rotating vortex pair for the case of D = 2.5 cm as shown in Figure (3.24 b), while for dense vegetated floodplain D = 5.0 cm, the interaction of the stream-wise velocity and span-wise velocity between rods inhibit these types of vortices. The time series of temperature for the 187 sequences of the five selected points in the area of eddy formation that locates between successive rods which were located in staggered arrangements is shown in Figure (3.26). Successive peaks are shown in Figure (3.26) along the time series frame (37 seconds) for all the five selected points in the wake region relative to the stream-wise velocity and the rotation of the vortices. To extract the energy of these eddies for the selected five points in the wake of the rods; Fourier transforms are used and explained in Figure (3.27). This graph shows that the energy

of the eddies is small at high frequency, while for low frequencies there are large eddies.

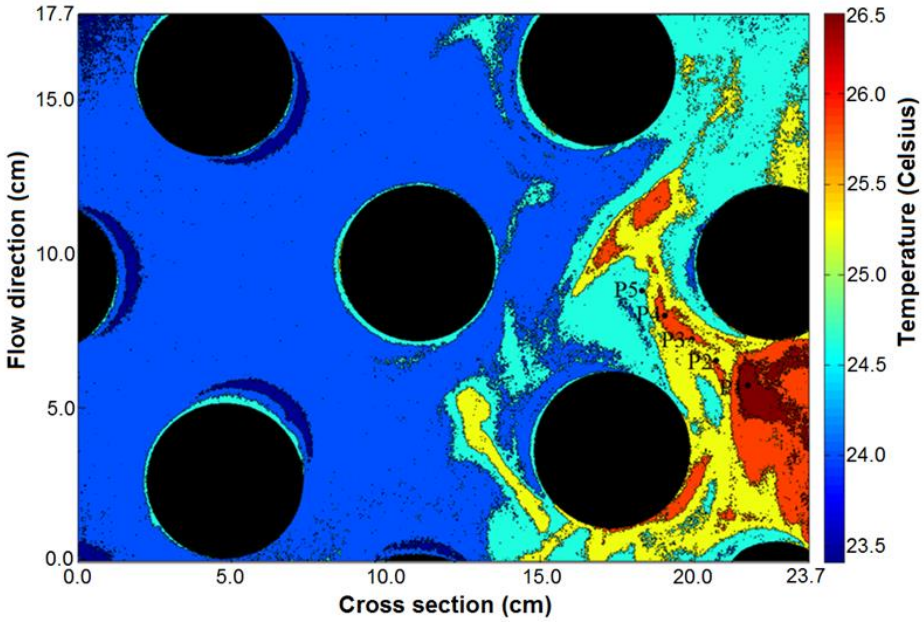

Fig. 3.25: Example of eddies formation in the wake of the rods for wholly vegetated floodplain with D = 5.0 cm and flow rate of Q = 4.66 l s^{-1} which shows location of five selection points.

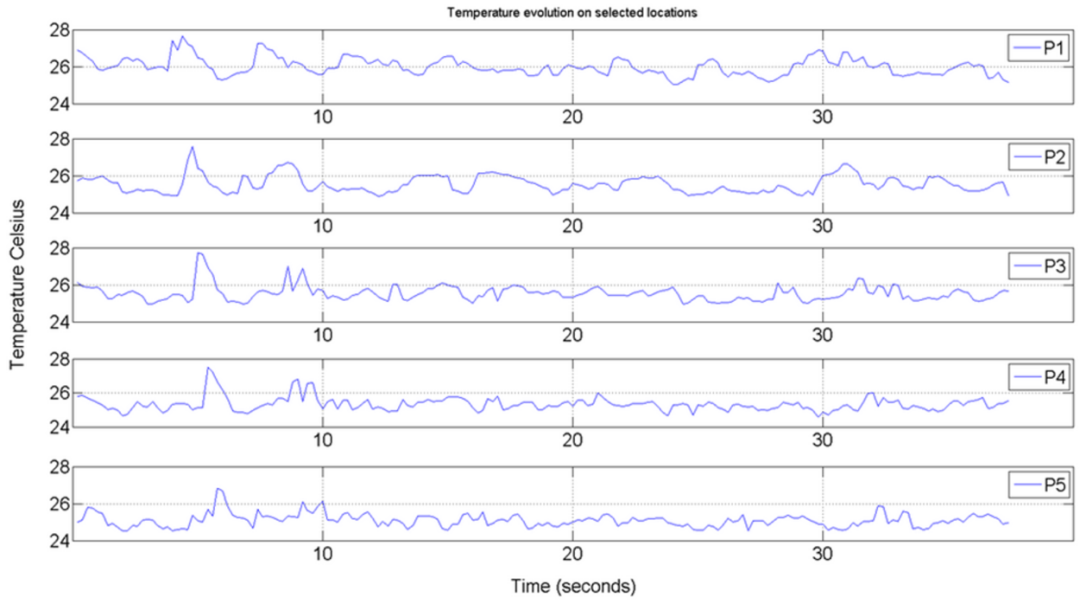

Fig. 3.26: Time series for the five point selection in the wake of the rods for a period of 37 seconds and the 187 sequences for wholly vegetated floodplain of D = 5.0 cm and flow rate of Q = 4.66 l s^{-1}.

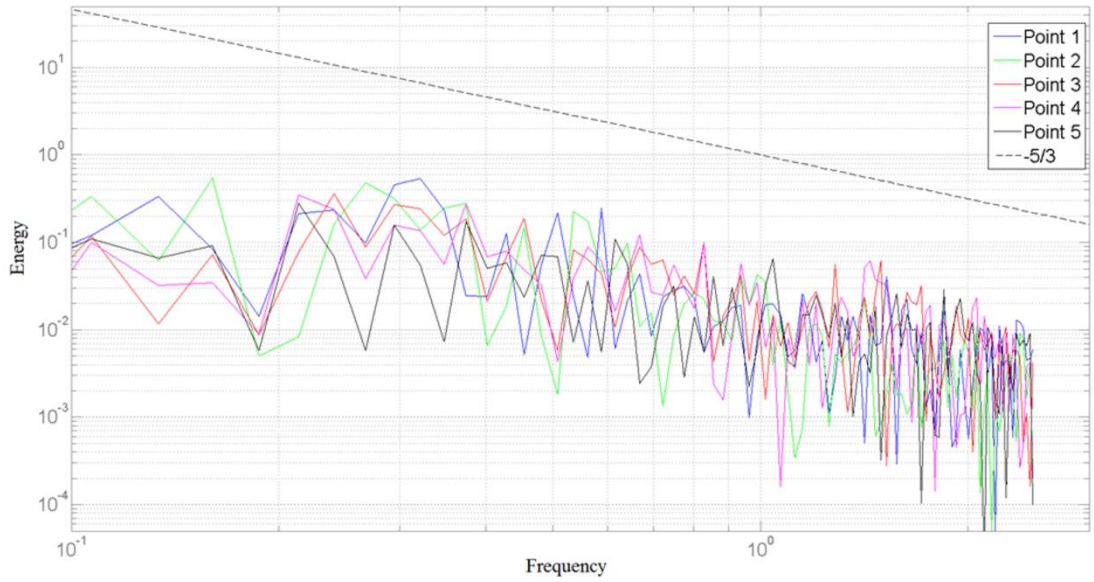

Fig. 3.27: Fourier transforms for the five selected points in the wake of the rods for the case of the wholly vegetated floodplain of D = 5.0 cm and flow rate of Q = 4.66 l s^{-1}.

3.4 CHAPTER SUMMARY

This chapter explains a novel approach to predicting and visualizing the evolution of shear layer formation using thermal video sequences at the interface between the main channel and the floodplain in a compound channel of shallow uniform flow. Experiments were carried out in a laboratory flume of 10 m length and 1.2 m width and for which uniform flow conditions were established for different flow rates. Hot water was added at the water surface using a small tube at ambient condition and at the interface between the main-channel and the floodplain where a fully developed flow had been achieved. A thermal camera (SC640) operates at 5Hz frequency and 640X480 pixels resolution was mounted vertically at 0.65 m above a shallow flow compound channel at the interface between the main channel and the floodplain at a section where a fully developed flow had been achieved. This set-up enabled the capturing of the flow temperature differences at 5 locations longitudinally and at 3 locations transversely.

Flir's image processing software and Matlab were used to extract and analyse the captured water surface temperature data. Image processing was done for the first to fifth location at the junction edge of the floodplain adjacent to the main channel with longitudinal overlaps to the images; between the first and the second image thus creating the first overlap and then between the first image overlap and the third image to create the second overlap and so on to the fifth image, thus creating the first part of the shear layer at the centre. The other five locations on either side of the first part that are located at the centre were similarly carried out with longitudinal overlaps to create the second and the third parts of the shear layer as left and right parts. At the end, three parts were acquired representing the entire shear layer. In order to visualize the final shear layer (from these three parts), a horizontal overlap was done for the left and the centre parts first, and then overlap between the right and the results of the overlapping between the centre and left parts was achieved secondly. The created shear layer image was then exported into Tecplot software. The analysis showed that the shear layer at the interface between the main channel and the floodplain is well captured and quantified by this technique.

Dynamics of shear layer evolution at the interface between the main channel and the floodplain in compound channel flows with and without vegetation on its floodplain was well quantified and evaluated by the thermal camera technique. The two setups are shown in Figs. (3.24 a and b) which verified the aim of acquiring the shear layer and von Karman street vortices. The shear layer elongation and propagation at the interface between the main channel and the floodplain showed that the penetration of the temperature inside the main channel is more than that on the floodplain for all the vegetated floodplain cases and the distribution of the shear layer in the x-y plane is influenced by the vegetation density, vegetation configuration and the flow rate. The impact of the flow depth variation and roughness are explained in asymmetric shear layer about the MC/FP interface. Time-averaged temperature distribution was well described in all the case studies to appear as the shear layer evolution along the streamwise direction and its propagation inside the floodplain and on the main channel in the compound channel.

Eddies characteristics at the wake of the neighbouring rods are well described by Fourier transforms graph as shown in Fig. (3.27). The results showed that the energy of the eddies is small at high frequency, while for low frequencies they are large eddies.

CHAPTER FOUR

FLOW RESISTANCE OF IN-LINE VEGETATION IN OPEN CHANNEL FLOW

4 FLOW RESISTANCE OF IN-LINE VEGETATION IN OPEN CHANNEL FLOW

4.1 INTRODUCTION

Naturally-occurring vegetation in waterways is usually arranged in an irregular, spatially heterogeneous fashion as a result of local variations in hydro-geomorphology. In recent years several researchers have studied experimentally and numerically the drag characteristics of arrays of submerged and emergent flexible and non-flexible idealized vegetation arrays (Nepf 1999, Wu et al. 1999, Tsihrintzis et al. 2001, Järvelä 2008, Stone and Shen 2002, Jarvela 2004, Jordanova et al. 2006, James et al. 2008, Tanino and Nepf 2008, Kothyari et al. 2009, Stoesser et al. 2010, Cheng and Nguyen 2011, Aberle and Järvelä 2013, Cheng 2013, Marjoribanks et al. 2014) or individual plants, e.g. (Yagci and Kabdasli 2008, Wunder et al. 2011). However, under flood conditions when overbank flow produces a compound channel, riparian vegetation such as trees and bushes may form one-line arrays of emergent vegetation at the main channel-floodplain interface. This scenario is known to make significant contributions to the overall hydraulic resistance of the channel (Sun and Shiono 2009, Terrier et al. 2010). For instance, Terrier et al. carried out compound channel experiments in a flume of length 8 m and width 1.2 m, with one line of 9 mm diameter rods placed along the edge of the floodplain. They found that the presence of the vegetation on the edge of the floodplain has a clear impact on the stage-discharge curve compared to the case without vegetation. Detailed measurements of the hydrodynamic behaviour of in-line vegetation are scarce. Shiono et al. (2012) carried out flow measurements using an Acoustic Doppler Velocimeter (ADV) in a single rectangular channel that was 9.0 m long and 91.5 cm wide. Wooden rods of 9.0 mm diameter were fixed at the centre line of the channel with a rod spacing L_s/D= 17.8 and a bed slope of 0.001. As would be expected, slower velocities were observed near the rods.

Some common patterns of vegetation is growing at the edge of UK Rivers are straight lines, such as the River Dove at Lovedale, the River Dove at Milldale, and the River Severn at Ironbridge Gorge as shown in Figure 4.1.

Figure 4.1: Some common patterns of vegetation at the edge of UK Rivers are straight lines, such as the River Dove at Lovedale, the River Dove at Milldale, and the River Severn at Ironbridge Gorge.

In order to carry out accurate predictions of flood stages in natural waterways lined with vegetation on its banks or floodplains accurate knowledge of the prevailing drag coefficient (C_D) is needed. Kim and Stoesser (2011) have demonstrated that numerical models that are employed to predict flow resistance of emergent vegetation rely heavily on accurate knowledge of the drag coefficient C_D. Based on laboratory and numerical data Tanino and Nepf (2008), Kothyari et al. (2009), Cheng and Nguyen (2011) and Cheng (2013) propose simple empirical equations to predict C_D; these equations can be very useful for practitioners and numerical modellers. However, they are based on experiments of arrays of vegetation and it is unclear whether they are accurate in a one-line (or in-line) vegetation scenario.

The main aim of this research is to assess the suitability of various empirical formulations to predict the drag coefficient of in-line vegetation. Equations evaluated are the ones proposed by comparing predicted drag coefficients against experimental data obtained as part of this study.

4.2 FLOW RESISTANCE IN VEGETATED STREAMS

For steady uniform flow, flow resistance through rigid emergent cylinders can be estimated by equating the driving (gravitational) force of the flow to the bed resistance and form drag (Figure 4.2), as given by Petryk and Bosmajian (1975):

$$F_G = F_f + F_D \tag{4.1}$$

where F_G is the gravitational force, F_f is the wall friction drag force, and F_D is the drag force exerted by the cylinders.

For identical rigid cylindrical rods of diameter D, substituting each term of equation (4.1) by its definition results in Eq.4.2 (James et al. 2004, Huthoff and Augustijn 2006, Jordanova et al. 2006, Aberle and Järvelä 2013):

$$\rho g S H \left(1 - m\frac{\pi D^2}{4}\right) = \tau_b \left(1 - m\frac{\pi D^2}{4}\right) + \frac{1}{2} m \rho C_D H D {U_v}^2 \qquad (4.2)$$

where $\rho =$ density of the fluid, $g =$ gravitational acceleration, $S =$ bed slope, $H =$ flow depth, $D =$ rod diameter, $m\frac{\pi D^2}{4} =$ bed area occupied by cylinders, $\tau_b = \rho g R S =$ bed shear stress, C_D = drag coefficient, $U_v =$ flow velocity through the vegetation elements, $R =$ hydraulic radius and $m =$ number of cylinders per unit area.

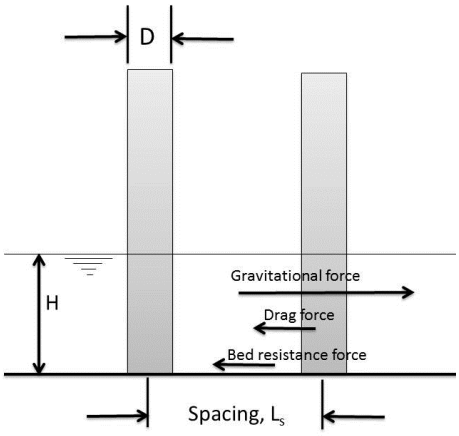

Figure 4.2: Hydrodynamic forces present in the water balance equation for emergent vegetated streams.

As mentioned above empirical expressions for the calculation of the drag coefficient were proposed by a number of authors.

Tanino and Nepf (2008) formulated an expression for the drag coefficient of rigid circular cylinders as follows:

$$C_D = 2\left\{\frac{\alpha_0}{Re_D} + \alpha_1\right\} \qquad (4.3)$$

where Re_D is the cylinder or stem Reynolds number and α_0 and α_1 are functions of the vegetation volume fraction (ϕ), which is the fraction of the overall volume that is occupied by vegetation. α_0 and α_1 are empirical parameters which can be found in Tanino and Nepf (2008).

Kothyari et al. (2009) proposed the following equation for the drag coefficient of emergent cylindrical stems based on a set of fluid force measurements in subcritical and supercritical flows:

$$C_D = 1.8\xi {Re_D}^{-0.06}[1 + 0.45\ln(1 + 100\phi)] * (0.8 + 0.2Fr - 0.15Fr^2) \qquad (4.4)$$

where, ξ = parameter representing the cylinder staggered pattern, with $\xi = 0.8$ for a regular square staggered pattern and $\xi = 1.0$ for the triangular-staggering stem pattern, $\phi = m\pi D^2/4$ (area concentration of stems), and $Fr = \frac{U}{\sqrt{gH}}$ (Froude number), where U is the bulk velocity, D is the stem diameter, g the acceleration due to gravity and H is the flow depth.

Cheng and Nguyen (2011) related the drag coefficient to the stem Reynolds number using a new parameter, r_v, which represents the vegetation-related hydraulic radius in a rectangular channel, which is defined as the ratio of the volume occupied by water to wetted surface area of all cylinders as:

$$r_v = \frac{\pi D}{4}\left(\frac{1-\phi}{\phi}\right) \qquad (4.5)$$

The drag coefficient is derived by considering the stream-wise force balance equation for uniform flow and by neglecting frictional losses the drag coefficient is calculated as:

$$C_D = 2\frac{g r_v S}{{U_v}^2} \qquad (4.6)$$

Cheng and Nguyen (2011) found that the dependence of C_D on Re_D varies with vegetation density and configuration (random or staggered). They showed that drag coefficient decreases as Reynolds numbers increases.

Cheng (2013) proposed an alternative expression for the drag coefficient C_D acting on a sparse cylinder array and which he called the pseudofluid model:

$$C_D = \frac{\pi}{2}\frac{1}{\phi}\frac{gDS}{{U_v}^2} \tag{4.7}$$

where U_v is the average flow velocity through emergent vegetation elements.

The suitability of equations (4.3) to (4.7) for the calculation of C_D of in-line vegetation is assessed and for which experiments were carried out.

4.3 EXPERIMENTAL PROCEDURE

Experiments were performed in the hydraulics laboratory of the School of Engineering at Cardiff University, UK, using a recirculating glass-walled flume of 10 m length and 0.3 m width. Two uniform flow cases were investigated using bed slopes of 0.001 and 0.0005. One line of wooden rods was attached to the bottom of the flume, along its entire centreline, and the longitudinal centre-to-centre spacing of the rods was 12.5 cm. Three different rod diameters were tested: D = 5.0 cm, 2.5 cm and 1.25 cm, producing three corresponding spacing ratios of L_s/D = 2.5, 5 and 10 respectively. The experimental setup is illustrated in Figure 4.3.

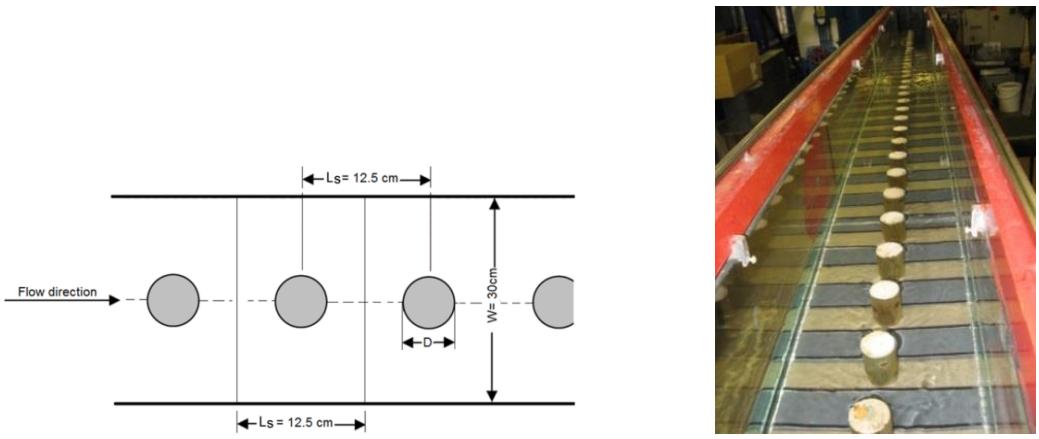

(a) (b)

Figure 4.3: Schematic diagram and photograph illustrating the experimental set-up with one-line rod array in place.

Table 4.1 Hydraulic characteristics of open channel flow in the presence of one-line vegetation at the centre line of the flume width.

Case	Vegetation diameter D (cm)	L_s/D	Bed slope %	Water depth H (cm)	Bulk velocity U_b (cm/s)	Shear stress ρgRS τ (N/m^2)x10^{-2}	Froude number $Fr=U_b/(gH)^{0.5}$	Reynolds number $Re_D=U_bD/v$	Reynolds number $Re_H=U_bH/v$
1	Lateral strips		0.05	3.8	17.63	14.8	0.29	-	6624
			0.05	5.2	19.16	19.0	0.27	-	9936
			0.05	6.1	22.03	21.1	0.29	-	13249
			0.05	7.1	23.40	23.7	0.28	-	16561
			0.05	8.3	24.06	26.2	0.27	-	19875
			0.05	8.9	26.24	27.4	0.28	-	23188
			0.05	9.6	27.69	28.8	0.28	-	26506
			0.05	10.3	29.04	30.0	0.29	-	29819
			0.05	10.7	31.18	30.6	0.30	-	33133
2	D=1.25	10	0.05	4.9	13.68	18.0	0.20	1700	-
			0.05	6.1	13.77	21.1	0.18	1711	-
			0.05	6.9	14.40	23.3	0.17	1789	-
			0.05	7.6	15.37	24.7	0.18	1910	-
			0.05	8.5	15.68	26.6	0.17	1948	-
			0.05	10.1	16.56	29.5	0.17	2058	-
3	D=2.5	5	0.05	5.6	10.47	19.9	0.14	2602	-
			0.05	6.2	10.72	21.6	0.14	2662	-
			0.05	7.5	11.05	24.6	0.13	2746	-
			0.05	9.0	11.17	27.5	0.12	2776	-
4	D=5.0	2.5	0.05	6.9	7.27	23.1	0.09	3613	-
			0.05	7.6	7.67	24.7	0.09	3812	-
			0.05	8.3	8.01	26.2	0.09	3981	-
			0.05	9.0	8.31	27.6	0.09	4130	-
			0.05	9.7	8.58	28.9	0.09	4264	-
			0.05	10.3	8.94	29.9	0.09	4443	-
5	Lateral strips		0.1	3.0	22.01	24.7	0.40	-	6607
			0.1	3.6	27.70	28.5	0.47	-	9940
			0.1	4.4	30.59	33.1	0.47	-	13227
			0.1	5.0	33.23	36.8	0.47	-	16549
			0.1	5.5	36.54	39.3	0.50	-	19868
			0.1	6.2	37.91	42.8	0.49	-	23176
			0.1	6.6	40.62	44.8	0.51	-	26488
			0.1	7.2	41.62	47.7	0.50	-	29788
			0.1	7.6	43.85	49.5	0.51	-	33127
6	D=1.25	10	0.1	3.8	17.37	29.9	0.28	2158	-
			0.1	5.3	19.01	38.2	0.26	2362	-
			0.1	6.7	19.90	45.4	0.25	2473	-
			0.1	8.0	20.84	51.1	0.24	2589	-
			0.1	9.0	22.28	55.1	0.24	2768	-
			0.1	10.0	23.40	58.8	0.24	2908	-
			0.1	11.4	23.47	63.4	0.22	2916	-
7	D=2.5	5	0.1	4.0	13.62	31.0	0.22	3385	-
			0.1	4.5	14.84	33.9	0.22	3688	-
			0.1	5.4	15.46	38.9	0.21	3842	-
			0.1	6.2	16.14	43.0	0.21	4011	-
			0.1	7.0	16.70	46.7	0.20	4150	-
			0.1	7.7	17.28	50.0	0.20	4294	-
8	D=5.0	2.5	0.1	5.3	10.34	38.3	0.14	5139	-
			0.1	6.4	10.43	44.0	0.13	5184	-
			0.1	7.7	10.77	50.0	0.12	5353	-
			0.1	9.0	11.11	55.2	0.12	5522	-

To ensure uniform flow conditions, the flow depths were controlled by a tailgate that was located at the downstream end of the flume's working section. Water depths were measured using point gauges located at 1 m intervals along the approach flow section, upstream of the rods, to ensure no effects of incoming turbulence and backwater impact. Depending on vegetation diameter, four to six flow rates were tested for each rod diameter to investigate the rating curves, while nine flow rates were used for the non-vegetated flume section with lateral strips. In all tests the stem Reynolds numbers ($Re_D = \frac{U_b D}{\nu}$), were in the range 1700 < Re_D < 5500, and Froude numbers, $Fr = U_b/\sqrt{gH}$ ranged from 0.09 to 0.51 (details of all experiments are provided in Table 4.1). Uniform flow conditions were achieved for each experiment.

4.4 RESULTS

4.4.1 Water Level-Discharge Relationship

Figures 4.4 (a) and (b) present the water depth-discharge relationship with and without one-line vegetation, for bed slopes of 0.0005 (a) and 0.001 (b) respectively. The figures reveal that the introduction of one-line vegetation has a significant impact on the water depth for a given discharge, i.e. for a given discharge, the water depth increases as vegetation density, ϕ, is increased. For very low discharges, the curves are close to each other, but the curves diverge as discharge increases. For the large-diameter rods the water depth rose very quickly above the length of the rods, which only allowed maximum discharges of approximately 3 l/s.

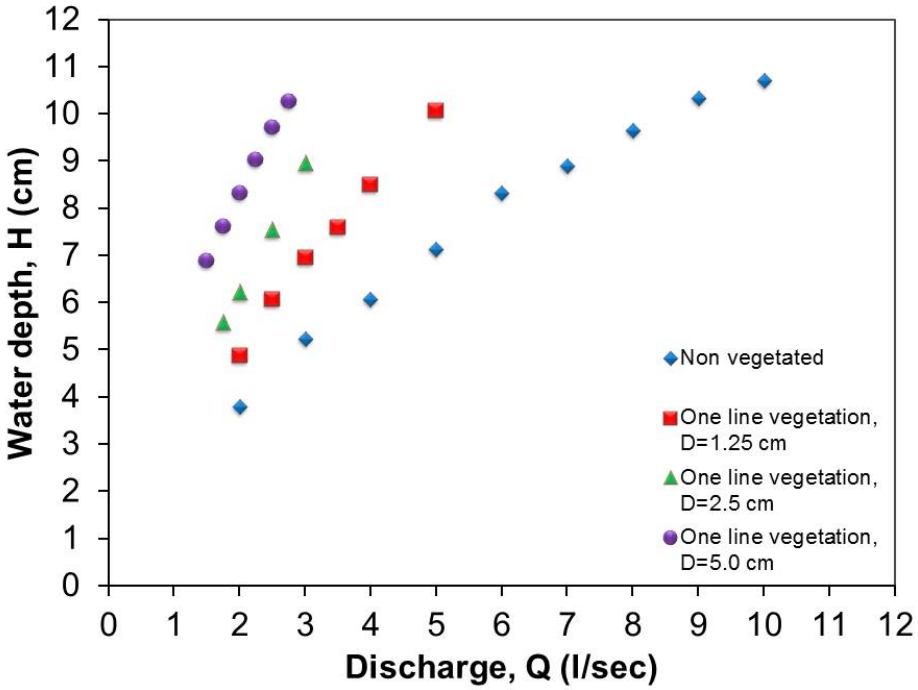

(a)

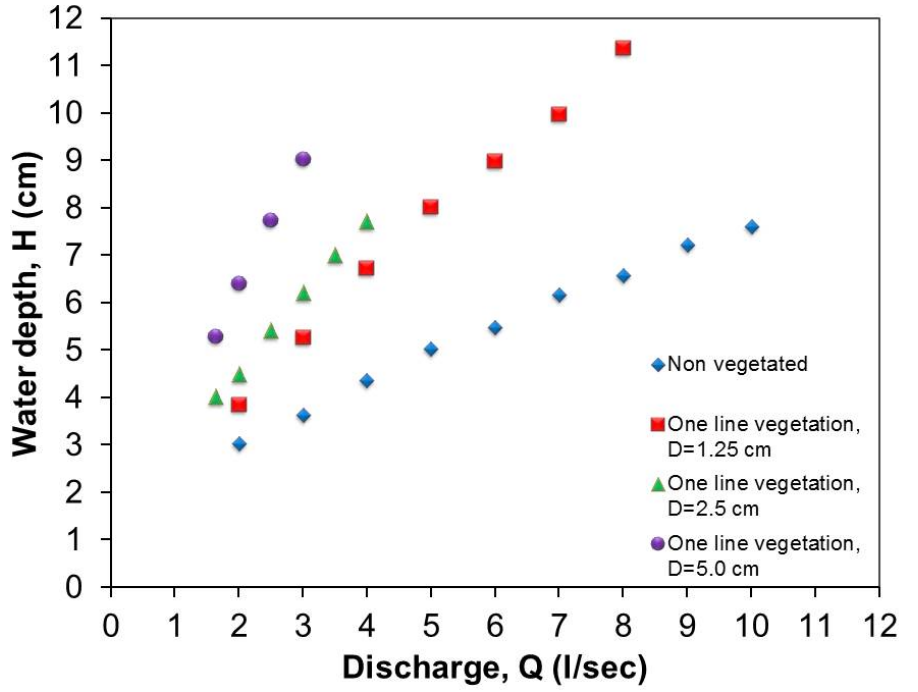

(b)

Figure 4.4: Water depth-discharge relationships: a) bed slope 0.0005; b) bed slope 0.001.

4.4.2 Drag-Coefficient-Stem Reynolds Number Relationship

For steady uniform flow conditions, the flow resistance in a vegetated channel with one–line rigid emergent cylinders can be estimated from equation (4.2). The drag coefficient for a range of stem Reynolds numbers (Re_D = 1700-5500) was calculated with a mean value of $C_D \cong 0.65$. The flume was relatively narrow so that the calculated C_D values were corrected for flow blockage as proposed by Shields Jr and Gippel (1995):

$$C'_D = \frac{C_D}{(1-F_B)^2} \tag{4.8}$$

where F_B is the blockage factor, which is defined as the ratio between the cylinder diameter, D, to the flume width, W.

Figure 4.5 plots the drag coefficient as a function of stem Reynolds number using the empirical equations proposed by Tanino and Nepf (2008), Kothyari et al. (2009), Cheng and Nguyen (2011) and Cheng (2013) and the ones obtained from the measurements of the present study for the 0.1% slope. The drag coefficient varies between $C_D \approx 0.6$ and $C_D \approx 1.0$ and does appear to be somewhat sensitive to the stem Reynolds number. Employment of Tanino and Nepf's and Kothyari et al.'s equation slightly overpredict the measured drag coefficients irrespective of Re_D, however the general trend that C_D increases with increasing Re_D is predicted rather well by these two equations. Cheng's pseudo-fluid model and Cheng and Nguyen's equations obviously overpredict the viscous effect: their equations yields too large values at lower stem Reynolds number, on the other hand the match between measured and predicted C_D is remarkably good at higher stem Reynolds number flows.

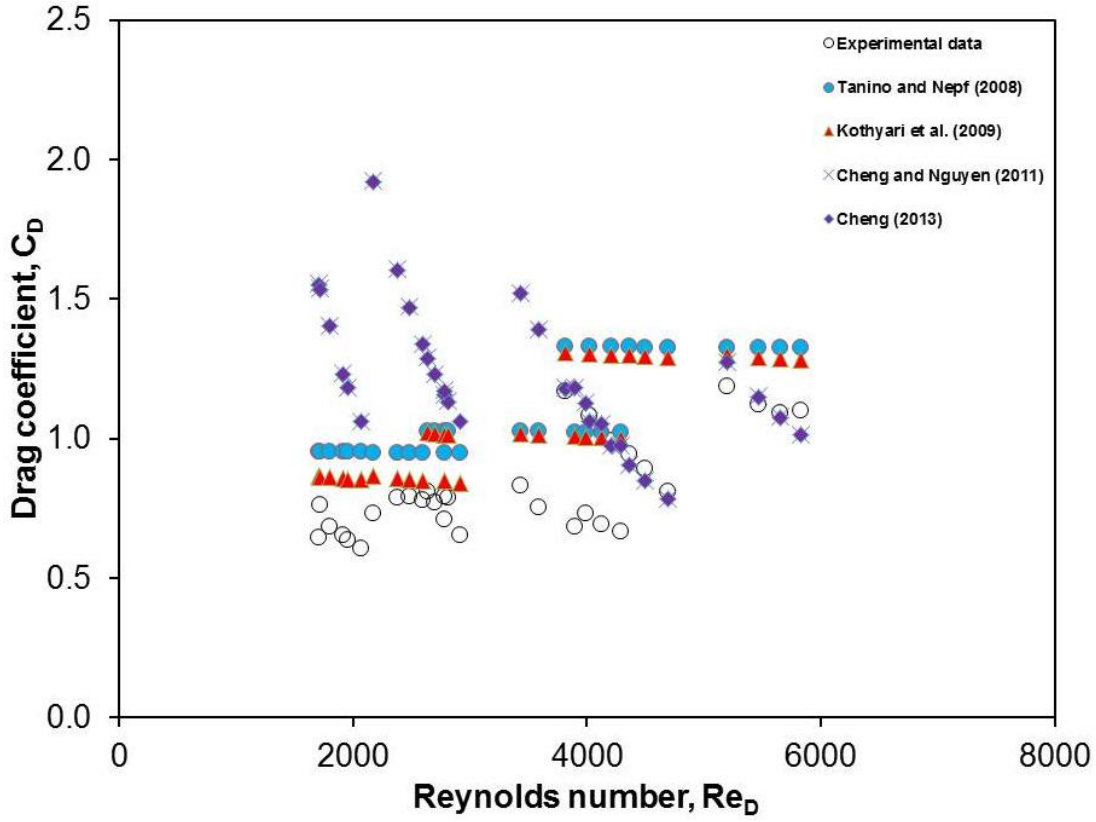

Figure 4.5: Drag coefficients as a function of stem Reynolds number as obtained from measurements of this study and as computed using expressions from various researchers.

A more quantitative comparison of predicted and measured drag coefficients for in-line vegetation is possible with Figure 4.6, which plots measured drag coefficients vs. those obtained using the four equations introduced above for both channel slopes. Tanino and Nepf's and Kothyari's equations (Figure 4.6a and b) predict fairly similar values throughout the range of Reynolds numbers covered. Tanino and Nepf's expression results in a consistent overestimation, probably because the expression is based on their own experiments in which the vegetation was randomly arranged and covered the entire width of the flume, whereas the drag coefficients of the present study might benefit from a "shading effect", i.e. the downstream cylinder is positioned in the wake of the upstream cylinder and hence does not experience the full hydrodynamic load. Kothyari's expression also results in a consistent overestimation of the drag coefficient, however slightly closer to the measured C_D values at lower Re_D than the ones predicted by Tanino and Nepf's expression. Similarly, Kothyari's expression may only be suitable for in-line vegetation if

"shading" is taken into account. Cheng's and Cheng and Nguyen's expressions overestimate vegetation drag for small to medium stem diameters irrespective of channel slope. On the other hand a fairly good match is obtained for large stem diameters. What is apparent from the experimental data is that in-line vegetation is not very sensitive to the stem Reynolds number, if at all, then C_D increases with increasing Re_D, whereas Cheng's and Cheng and Nguyen's expressions suggest an opposite trend.

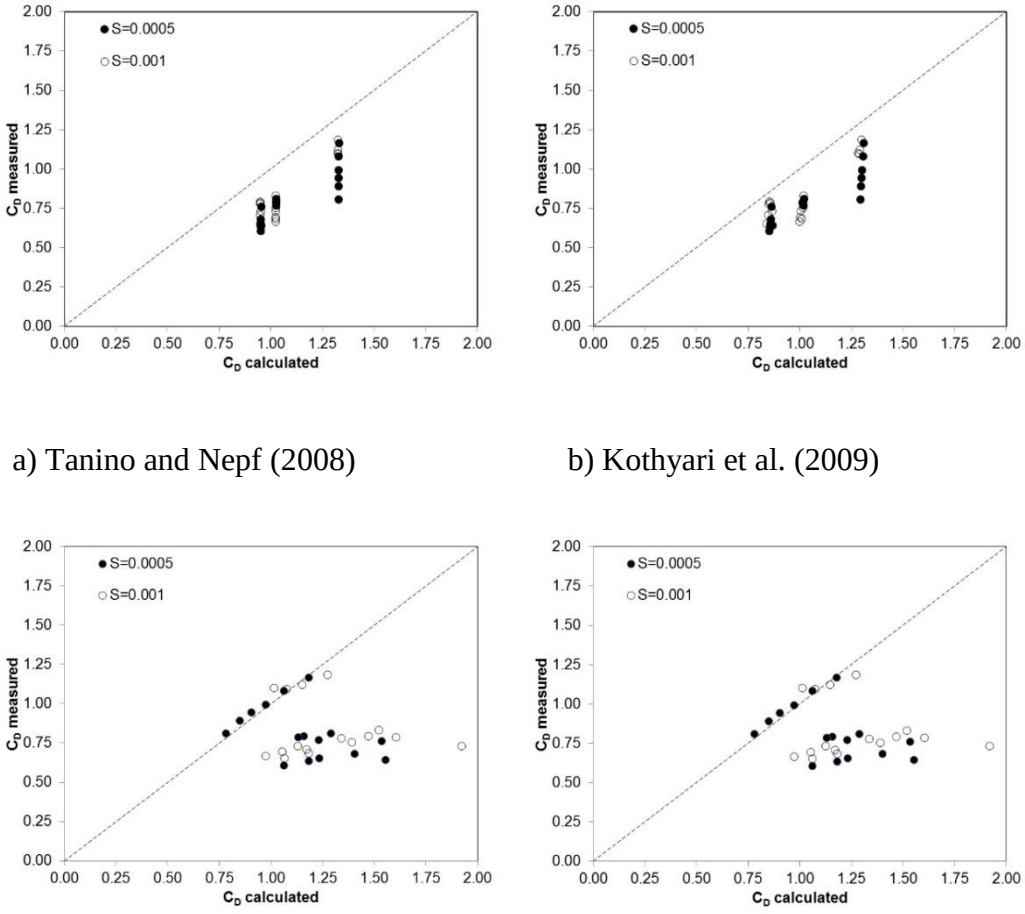

a) Tanino and Nepf (2008) b) Kothyari et al. (2009)

c) Cheng and Nguyen (2011) d) Cheng (2013)

Figure 4.6: Comparison of drag coefficient (measured versus calculated) for different models.

4.5 CHAPTER SUMMARY

Experiments have been performed to measure the stage–discharge behaviour of open channel flow through one line of vertically-oriented circular rods which mimics in-line vegetation. Two bed slopes have been used, along with a range of rod diameters which yielded different spacings between cylinders. For a series of uniform flows the drag coefficient was calculated based on the measured uniform flow depth and under consideration of the bed friction. Then the most prominent equations for calculating the drag coefficient, C_D, of vegetation have been employed to predict C_D for the experiments of in-line vegetation. Tanino and Nepf's and Kothyari's equations consistently overestimate the measured drag coefficients but match the overall trend of an increase of C_D with increasing stem Reynolds number. Cheng's and Cheng and Nguyen's expressions overestimate vegetation drag for low to medium values of Re_D whilst a good match has been achieved for the higher stem Reynolds numbers. On the other hand the latter two expressions do not reflect the trend that of an increase of C_D with increasing stem Reynolds number.

CHAPTER FIVE

HYDRODYNAMICS OF COMPOUND CHANNELS WITH VEGETATED FLOODPLAIN

5 HYDRODYNAMICS OF COMPOUND CHANNELS WITH VEGETATED FLOODPLAIN

5.1 INTRODUCTION

The middle and lowland stretches of most rivers are characterised by compound cross sections that comprise one or two floodplains and a deeper main channel. Vegetation may be distributed across the floodplains in a variety of ways, including patches of bushes, grassy meadows and regular arrays of trees that line the edges of the main channel and follow its meanders. Such arrays may occur naturally or by design as part of flood protection or habitat creation programs, and may exert significant influence on the hydraulic properties of the compound channel during flood events. One of the most prevalent arrangements is commonly known as "one-line" vegetation which comprises a single line of trees along the side of the main channel, but arrays of trees that extend much further across the floodplain may also occur.

Although a number of studies have focused on turbulence, secondary currents and momentum transfer in non-vegetated compound channels (Tominaga and Nezu 1991, van Prooijen et al. 2005, Yang et al. 2007, Vermaas et al. 2011), the influence of floodplain vegetation on the flow conditions in compound channels is less well understood. The impact of vegetation density, ϕ on the water depth-discharge curve has been studied experimentally by a number of authors for different vegetation configurations; Ismail and Shiono (2006), Sun and Shiono (2009) and Terrier (2010) considered one-line vegetation, while Nehal et al. (2012) and Hamidifar and Omid (2013) investigated a wholly-vegetated floodplain. Masterman and Thorne (1992) established a theoretical method to estimate the effects of bank vegetation on the channel flow capacity, and showed that it is possible to relate these effects to the channel width-to-depth ratio; the authors showed that the effect of bank vegetation on channel discharge capacity declines rapidly as the width-to-depth ratio increases. Ben-sheng et al. (2002) carried out experiments on a compound channel with a narrow floodplain and showed that the influence of vegetation on the floodplain flow capacity in such cases is not significant. Ismail and Shiono (2006) performed

experiments in compound meandering channels with floodplains that were covered with small rectangular blocks to simulate vegetation. The authors carried out tests with fixed and mobile bed sediments to assess the influence of floodplain vegetation on sediment transport. The results showed that the influence of vegetation density on stage discharge curve was minimal for the fixed bed case, but some variation was observed for the mobile bed case. Yang et al. (2007) performed experiments in a compound channel that was either unvegetated or fully covered with model structures that were intended to represent grass, shrubs and trees. The authors found that for a non-vegetated channel the streamwise velocities always followed a logarithmic distribution, whereas S-shape velocity profiles were observed when vegetation was introduced on the floodplain. Hirschowitz and James (2009) estimated the total channel discharge in the presence of emergent vegetation along the banks of a river as the sum of the discharges of the vegetated and clear channel zones calculated seperately.

A number of researchers have studied the impact of vegetation density on the drag coefficient for flow past arrays of emergent rigid cylinders (Petryk and Bosmajian 1975, Nepf 1999, Tanino and Nepf 2008, Kothyari et al. 2009, Stoesser et al. 2010, Cheng and Nguyen 2011, Tinoco and Cowen 2013). Nepf (1999) proposed a model for drag, turbulence and diffusion within emergent vegetation and showed that the bulk drag coefficient decreases as vegetation density increases for both random and staggered arrays. Tanino and Nepf (2008) conducted experiments involving flow through a random array of emergent, rigid cylinders, investigating the effect of Reynolds number and vegetation density on the resistance properties. It was found that the bulk resistance decreased with increasing Reynolds number and increased with increasing solid volume fraction.

Nehal et al. (2012) performed experiments to investigate the resistance properties of one specific type of aquatic plant, *Acorus Calmus L*, showing that increases in vegetation density are accompanied by significant increases in the water depth; a staggered arrangement of the plants was found to produce the largest decrease in flow rate. Hamimed et al. (2013) also found that the relationship between flow depth and discharge depends strongly on the vegetation density; higher density leads to

larger water depth except for very shallow flows, which are largely insensitive to changes in vegetation density. Hin et al. 2008 performed in situ flow measurements in vegetated equatorial streams in Malaysia, arriving at an expression for the apparent friction factor for a natural compound channel in terms of easily measurable hydraulic parameters. The floodplains of the streams were very densely vegetated, and as a result the floodplain flow was very small except when the overbank flow was very large. The researchers observed that the apparent shear was very high at the interface between the main channel and floodplain. Järvelä (2002) studied the hydraulic characteristics of natural willows and sedges to understand how type, density and combination of vegetation affects the bulk resistance in a channel. It was shown that the resistance is highly dependent on the flow depth, velocity, Reynolds number and vegetal characteristics.

In the case of one-line vegetation, a number of researchers have chosen to focus on the influnece of the spacing ratio L_s/D, where L_s is the centre-to-centre distance between the trees and D is the trunk diameter. Terrier (2010), for example, carried out experiments for two spacing ratios, $L_s/D = 8$ and 16. Circular cylinders and brushes were employed to represent vegetation without and with foliage, respectively. The results showed that flow rate increased as L_s/D increased (i.e. vegetation density decreased), except when foliage was added. Sun and Shiono (2009) investigated the flow characteristics in a straight compound channel, with and without one-line vegetation. Two vegetation densities were applied, $L_s/D = 3.8$ and 13.3, and it was observed that spanwise distribution of streamwise velocity changed markedly with the introduction of vegetation. The boundary shear stress was also significantly lower with one-line vegetation than without, which lead the authors to conclude that sediment transport and bed scour during flood events will be reduced by the introduction of rigid vegetation along floodplain edges, although there will be an associated increase in water levels. Sun and Shiono (2009) also reported that the discharge was reduced by 20-26% for L_s/D = 13.3 and 21-36% for L_s/D = 3.8 compared to the unvegetated floodplain case. Sanjou et al. (2010) tested a spacing ratio of L_s/D = 5 in a compound channel of width ratio B_{comp}/B_{mc} = 2.50, where B_{comp} is the overall width and B_{mc} is the main channel width. They reported reduced

main channel velocities and altered spanwise distribution of velocities with the inclusion of the one-line vegetation compared to the unvegetated base case; with one-line vegetation two inflection points were observed in the spanwise profiles near the main channel-floodplain interface, while there was just one inflection point for the unvegetated compound channel section. These results suggest that significantly less momentum transfer occurs between the main channel and floodplain when one-line vegetation is introduced. Shiono et al. (2012) carried-out experiments in a flume of length 9 m and width 0.915 m, with one-line vegetation with L_s/D = 17.8 and bed width ratio B_{comp}/B_{mc} = 2.0. The velocity distribution was characteristics by bulges in at the shear layer region near the water surface. Azevedo et al. (2012) modelled one-line vegetation using steel rods of diameter D = 1.0 cm placed at a distance 1.0 m apart, i.e. L_s/D = 100. Laser Doppler Velocimetry (LDV) was used to measure velocities in a flume of length 11.6 m and width 0.79 m with B_{comp}/B_{mc} = 3.85. Secondary currents were observed and two types of vortical structures, "bottom vortex" and "free surface vortex", that were absent from the unvegetated case, were identified. Inclined up-flows were also observed to have higher magnitudes than in the unvegetated case. Time-averaged velocities at different vertical cross sections were shown to be similar except in the area near to the free surface due to the presence of secondary currents. In the centre of the main channel the velocity profiles were similar with and without one-line vegetation.

The effects of flow interaction between vegetated and non-vegetated regions in compound open channels result in a spanwise distribution of the depth-averaged mean velocity that is of tangential hyperbolic shape (van Prooijen and Uijttewaal 2002, White and Nepf 2007). Physical, mathematical, and analytical models have been studied by a number of authors with a view of achieving accurate representations of the spanwise distribution of streamwise velocities (Shiono and Knight 1991, Pasche and Rouvé 1985, Pope 2000, van Prooijen and Uijttewaal 2002, van Prooijen et al. 2005, Rameshwaran and Shiono 2007, White and Nepf 2007, Liu and Shen 2008 , White and Nepf 2008, Tang and Knight 2008, Chen et al. 2010, Tang et al. 2010, Teymourei et al. 2013, Yang et al. 2013, Li et al. 2014). Experimentally, Pasche and Rouvé (1985) confirmed that depth-averaged velocities

are affected by vegetation in compound channel flows and showed that the inclusion of vegetation reduced longitudinal flow velocities. van Prooijen et al. (2005) proposed mechanisms for the momentum exchange in a straight uniform compound channel flow by considering the spanwise profile of streamwise velocity. White and Nepf (2007) showed that the velocity profiles separate the channel into two sections of uniform velocity; vegetated and open channel, and a transitional region between them. The spanwise variation of streamwise velocity in this transitional region is characterised by a hyperbolic tangent curve. Yang et al. (2007) showed that spanwise distribution of velocity in vegetated compound channels followed an S-shaped curve with three distinct flow regions. Hamidifar and Omid (2013) found that inclusion of vegetation on floodplains led to a decrease in the depth-averaged velocity over the floodplain and an increase in the main channel. In their study the depth-averaged velocity in both the main channel and floodplain decreased as vegetation density increased. Valyrakis et al. (2015) showed experimentally how increasing riverbank vegetation density on decreases the streamwise velocity on the riverbank while increasing it at the main channel.

In this study, the effects of vegetation density and distribution on the rating curve, the drag coefficients and the stream-wise velocity distribution in an asymmetric compound channel are investigated experimentally. This study is organised as follows: The next sections outline the theoretical framework on which the analysis is based; after which the experimental methodology and set-up are introduced; the experimental results are then, presented and discussed; and then finally some conclusions are drawn.

5.2 THEORETICAL CONSIDERATIONS

Flow resistance in vegetated streams is due to a combination of form drag and skin friction. The vegetation-induced drag force is given as follows:

$$F_D = \frac{1}{2}\rho C_D A_f {U_a}^2 \tag{5.1}$$

where F_D is the drag force acting on an individual stem, C_D is the drag coefficient, A_f is the frontal area of the stem, ρ is the density of water and U_a is the average velocity

approaching the stem, which Cheng and Nguyen (2011) propose can be well approximated by the average pore velocity through the vegetated region, $U_{veg} = (Q/W\mathrm{H})/(1-\phi)$, where Q is the bulk flow rate, W is the channel width, H is the flow depth and ϕ is the vegetation volume fraction or vegetation density, defined as the ratio of the volume occupied by vegetation, V_{veg}, to the total volume, V_{tot}. Note also that Cheng and Nguyen (2011) suggest $U_{veg} = U_a = U_b$ for low vegetation density, where U_{veg} is the flow through the vegetation and U_b is the bulk flow velocity.

Estimation of the drag coefficient induced by vegetation elements in streams under steady, uniform flow conditions can be established by equating the gravity force, F_G, to the drag force exerted by the vegetation elements, F_D, as follows:

$$F_G = F_D \tag{5.2}$$

where,

$$F_G = \rho g(Al)S \tag{5.3}$$

where ρ is the fluid density, g is the gravitational acceleration, A is the channel cross-sectional area, l is the channel reach, and S is the bed slope. Equations (5.1-5.3) can be rearranged to give the following expression for the drag coefficient:

$$C_D = \frac{2gS}{{U_a}^2 a} \tag{5.4}$$

where a is the vegetation density per unit length of the reach (m^{-1}), and can be expressed as $a = mD$, where m is number of stems per unit area occupied by the stems. a and ϕ are related as $\phi = \frac{\pi}{4}aD$. Equation 5.4 shows that the drag will decrease as a increases.

Tanino and Nepf (2008) formulated the drag coefficient for floodplain flow through an array of rigid circular cylinders as:

$$C_D = \left\{\frac{\alpha_0}{Re_D} + \alpha_1\right\} \tag{5.5}$$

where α_0 and α_1 are functions of the vegetation volume fraction, $\alpha_1 = 0.46 + 3.8\,\phi$, $\alpha_0 = 5.0 + 313.17\phi$, and $Re_D = U_{veg}D/\nu$ is the cylinder Reynolds number, where ν is the fluid kinematic viscosity and U_{veg} is defined by Petryk and Bosmajian (1975) as:

$$U_{veg} = \sqrt{\frac{2gS}{C_D m D}} \tag{5.6}$$

Kothyari et al. (2009) proposed the following equation for the drag coefficient of emergent cylindrical stems based on a set of fluid force measurements in subcritical and supercritical flows:

$$C_D = 1.8\xi {Re_D}^{-0.06}[1 + 0.45\ln(1 + 100\phi)] * (0.8 + 0.2Fr - 0.15Fr^2) \tag{5.7}$$

where, ξ is a parameter representing the effect of the vegetation staggering pattern, with ξ = 0.8 for a regular square staggering pattern and $Fr = \frac{U_{veg}}{\sqrt{gH}}$ is the Froude number. The authors found that the drag coefficient varied only slightly with Reynolds number but was very sensitive to changes in vegetation density. It should be noted that, owing to the shortness of the vegetated area, the flow was not fully developed and the authors speculated that drag coefficients were therefore higher than they would have been for fully developed flow.

Cheng and Nguyen (2011) related the drag coefficient to Reynolds number by a new parameter, the vegetation-related hydraulic radius, r_v, which is defined as the ratio of the volume occupied by water to the wetted surface area of all cylinders:

$$r_v = \frac{\pi D}{4}\left(\frac{1-\phi}{\phi}\right) \tag{5.8}$$

The drag coefficient and vegetation Reynolds number can then be expressed as follows:

$$C_D = 2gr_vS/{U_{veg}}^2 \tag{5.9}$$

$$Re_v = U_{veg}r_v/\nu \tag{5.10}$$

The authors found that dependence of C_D on Re_v varies with vegetation density and

configuration (random or staggered) as also observed by (Tanino and Nepf 2008, Kothyari et al. 2009).

In compound channel flows an apparent shear stress, τ_{int}, arises due to the high velocity gradients that are experienced at the interfaces between neighbouring regions of the cross-section. The shear stress force F_τ is considered as:

$$F_\tau = \tau_{int} A_{shear} \tag{5.11}$$

where, A_{shear} is the shear area, and τ_{int} is the apparent shear stress.
This apparent shear stress, τ_{int} was defined by Huthoff (2007) as follows:

$$\tau_{int} = \frac{1}{2}\Psi\rho\left(U^2{}_{mc} - U^2{}_{fp}\right) \tag{5.12}$$

where, $\psi =$ a dimensionless interface coefficient, $\Psi \approx 0.020$, $U_{mc} =$ velocity of the flow in the main channel, $U_{fp} =$ velocity of flow above the floodplain.

For one-line vegetation, because there are two dips at the interface between the main channel and the floodplain, the interfacial shear stress is expressed as follows:

$$\tau_{int} = \frac{1}{2}\psi\rho[\left(U^2{}_{mc} - U^2{}_{dip}\right) + \left(U^2{}_{fp} - U^2{}_{dip}\right)] \tag{5.13}$$

where, $U_{dip} =$ velocity of the flow near to the interface.

In addition to the Huthoff (2007)'s expression, a number of methods for quantifying the apparent shear stress at the interface between the main channel and the floodplain were reviewed in (Thornton et al. 2000). Two of these methods have been used in the present study. The first of these was derived by Rajaratnam and Ahmadi (1981) and is defined as follows:

$$\tau_{int} = 0.15\left(\frac{H_{mc}}{h_f} - 1\right)^2 \left(\gamma h_f S\right) \tag{5.14}$$

where, $H_{mc} =$ depth of flow in the main channel, $h_f =$ depth of flow on the floodplain, $\gamma =$ specific weight of water and $S =$ friction slope.

The second approach relates the shear stress, percentage blockage due to vegetation, F_B , flow depth, and flow velocities as follows:

$$\tau_{int} = 0.1025\tau_b \left(\frac{U_{fp}}{U_{mc}}\right)^{-3.4148} \left(\frac{h_f}{H_{mc}}\right)^2 (1 - F_B) \quad (5.15)$$

With one-line vegetation, drag coefficient is calculated from the following expression:

$$F_D = F_G - F_S + F_\tau \quad (5.16)$$

where F_S is the bed shear stress force and can be written as:

$$F_S = \rho g R S \quad (5.17)$$

where R is the hydraulic radius.

5.3 EXPERIMENTAL METHODOLOGY AND SETUPS

Experiments were carried out in a 10 m × 1.2 m × 0.3 m glass-walled recirculating flume in the Hyder Hydraulics Laboratory at Cardiff University, UK. The bed slope was set to 0.001 for all test cases. A compound channel with one floodplain was installed in the flume by attaching slabs of plastic, 76 cm wide and 2.4 cm thick, alongside one of the side walls. The floodplain was therefore 76 cm wide, and the bankfull depth of the main channel was 2.4 cm (Fig. 5.1). The floodplain bed slope was equal to that of the main channel, i.e. $S_{mc} = S_{fp} = S = 0.001$. Flow depths were controlled by a tailgate that was located at the downstream end of the flume's working section. Discharges were measured using a flow meter and calibrated by velocity measurements and volumetrically. A point gauge and Nixon Probe Velocimeter were used to measure water levels and point velocities respectively.

Wooden rods of three different diameters (D = 5.0 cm, 2.5 cm and 1.25 cm) were used as laboratory models for rigid emergent vegetation elements. Three canonical configurations were tested: unvegetated channel, wholly-vegetated floodplain and one-line vegetation. For the case of the wholly-vegetated floodplain the rods were inserted into holes that were drilled into the plastic floodplain in a staggered fashion; the centre-to-centre separation of the holes in streamwise and spanwise directions was 12.5 cm (Fig. 5.1a). This arrangement produced solid volume fractions of 24.8% (dense vegetation), 6.2% (medium) and 1.5% (sparse) for the three different rod

diameters. For the case of one-line vegetation the rods were inserted into holes that were drilled along a line parrallel to the sides of the flume: the streamwise centre-to-centre separation of the holes was 12.5 cm and the hole centres were 2.5 cm from the edge of the main channel (Fig. 5.1b). This arrangement produced normalised vegetation spacings of L_s/D= 2.5, 5 and 10 for the three different rod diameters.

Five discharges were tested for all vegetation configurations and rod diameters: 4.66 l s^{-1}, 5.87 l s^{-1}, 7.51 l s^{-1}, 8.87 l s^{-1} and 11.03 l s^{-1}. Table 5.1 provides a summary of flow conditions for all test cases.

For each discharge the water depth at the centre of the main channel was measured at streamwise intervals of 1 m in the section 3 m $\leq x \leq$ 9 m. Measurements of mean streamwise velocity, *U*, were carried out in sections in which the flow was considered to be fully developed: for the wholly-vegetated floodplain, velocities in two sections were measured (x = 4.76 m, and 8.52 m), while for the one-line case four sections were considered (x = 4.76 m, 7.76 m, 8.15 m and 8.52 m). In the main channel velocities were measured at two depths, $0.2H_{mc}$ and at $0.8H_{mc}$, and the average was taken ($U = \frac{U_{0.2Hmc}+U_{0.8Hmc}}{2}$). The first spanwise measurement location was 6.5 cm from the main channel side-wall, and further measurements were taken at 5 cm spanwise intervals until a distance 7 cm from the edge of the floodplain; over this last 7 cm measurements were taken at 1 cm spanwise intervals to improve the resolution in this complex region. On the floodplain the velocity was measured at the mid-depth, i.e. $U = U_{0.5h_f}$, with two measurements between neighbouring rods in the same row taken. For the one-line vegetation case the same procedure was followed in the main channel as for the wholly-vegetated case but on the floodplain the velocities were measured at 5 cm spanwise intervals from the rod centre to the side wall. For the unvegetated channel case the same procedure was adopted for the main channel as for the other two cases, while on the floodplain measurements were taken 5 cm spanwise intervals between the edge of the main channel and the side wall.

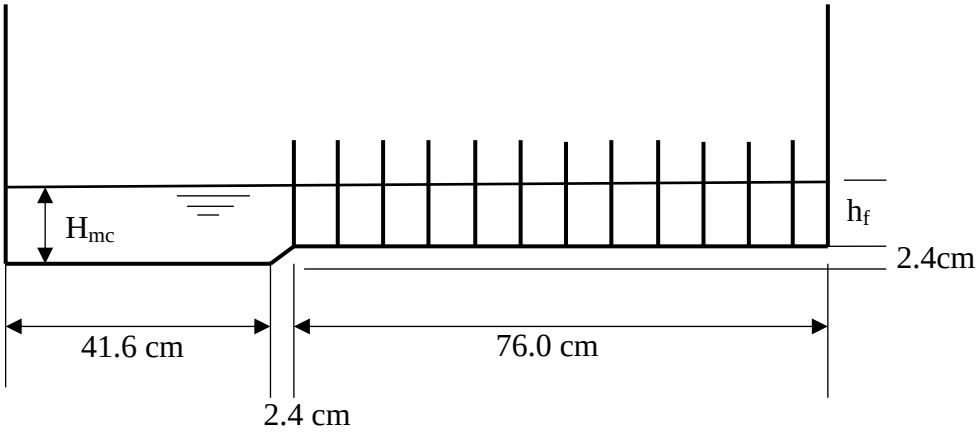

(a)

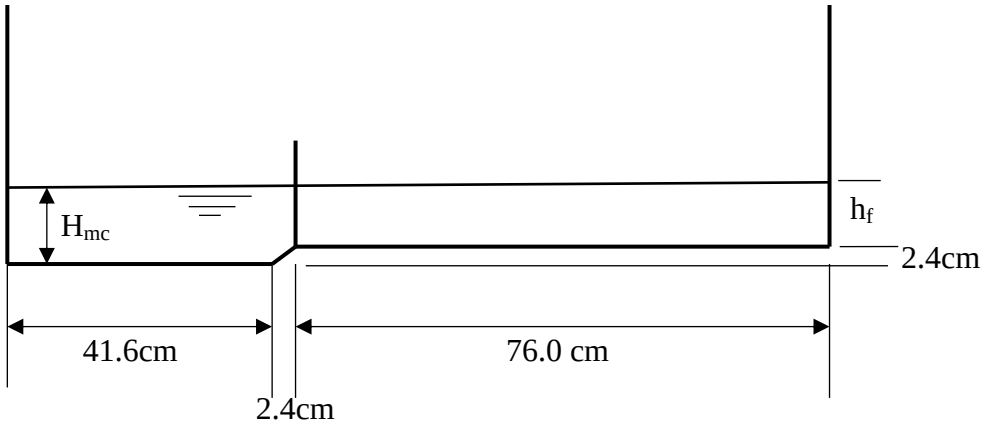

(b)

Fig. 5.1: Experimental set-ups: a) wholly-vegetated floodplain b) one-line vegetation along the edge of the floodplain.

Table 5.1 Summary of flow conditions

Config.	D (cm)	Q (l/s)	H_{mc} (cm)	h_f (cm)	u_{bulk} (cm/s)	Re_D	Re_R	Fr	SVF (%)	L_s/D
Non-vegetated floodplain	-	4.66	3.96	1.56	16.07	-	3661	0.26	-	-
	-	5.82	4.61	2.21	15.81	-	4523	0.24	-	-
	-	7.51	5.26	2.86	16.84	-	5782	0.23	-	-
	-	8.87	5.59	3.19	18.27	-	6794	0.25	-	-
	-	11.03	6.12	3.72	20.08	-	8376	0.26	-	-
One-line	5.00	4.66	4.39	1.99	13.64	6781	3635	0.21	-	2.5
	5.00	5.82	5.12	2.72	13.55	6736	4486	0.19	-	2.5
	5.00	7.51	5.83	3.43	14.60	7257	5730	0.19	-	2.5
	5.00	8.87	6.49	4.09	14.94	7427	6699	0.19	-	2.5
	5.00	11.03	6.98	4.58	16.90	8400	8267	0.20	-	2.5
	2.50	4.66	4.22	1.82	14.51	3606	3646	0.23	-	5.0
	2.50	5.82	4.71	2.31	15.31	3804	4516	0.23	-	5.0
	2.50	7.51	5.39	2.99	16.27	4044	5770	0.22	-	5.0
	2.50	8.87	5.95	3.55	16.78	4169	6756	0.22	-	5.0
	2.50	11.03	6.54	4.14	18.39	4570	8323	0.23	-	5.0
	1.25	4.66	4.22	1.82	14.51	1803	3646	0.23	-	10
	1.25	5.82	4.69	2.29	15.41	1914	4517	0.23	-	10
	1.25	7.51	5.34	2.94	16.49	2049	5774	0.23	-	10
	1.25	8.87	5.78	3.38	17.45	2168	6774	0.23	-	10
	1.25	11.03	6.14	3.74	19.99	2484	8374	0.26	-	10
Wholly-vegetated	5.00	4.66	4.46	2.06	13.32	6619	3633	0.20	24.8	-
	5.00	5.82	5.14	2.74	13.48	6699	4486	0.19	24.8	-
	5.00	7.51	6.18	3.78	13.50	6709	5700	0.17	24.8	-
	5.00	8.87	6.99	4.59	13.57	6746	6650	0.16	24.8	-
	5.00	11.03	7.95	5.55	14.34	7128	8148	0.16	24.8	-
	2.50	4.66	4.37	1.97	13.74	3415	3638	0.21	6.2	-
	2.50	5.82	5.01	2.61	13.98	3475	4495	0.20	6.2	-
	2.50	7.51	6.20	3.8	13.44	3340	5699	0.17	6.2	-
	2.50	8.87	7.00	4.6	13.55	3367	6649	0.16	6.2	-
	2.50	11.03	7.95	5.55	14.34	3564	8148	0.16	6.2	-
	1.25	4.66	4.35	1.94	13.87	1724	3639	0.21	1.5	-
	1.25	5.82	4.89	2.49	14.48	1800	4503	0.21	1.5	-
	1.25	7.51	6.05	3.65	13.89	1726	5712	0.18	1.5	-
	1.25	8.87	6.69	4.29	14.36	1785	6681	0.18	1.5	-
	1.25	11.03	7.78	5.38	14.73	1831	8169	0.17	1.5	-

5.4 RESULTS AND DISCUSSIONS

5.4.1 Impact of Vegetation on the Water Depth-Discharge Curve

The influence of vegetation density on the water depth-discharge relationship for the wholly-vegetated floodplain case is shown in Fig. 5.2. The plot clearly illustrates that in general the inclusion of a wholly-vegetated floodplain produces a marked increase in water depth compared to the unvegetated case for a given flow rate. The increase is smallest at the lowest flow rate and becomes more noticeable as flow rate increases. As would be expected, increasing the rod diameter, and therefore the vegetation density, results in further increases in water level. The water level increases with flow rate in all cases: interestingly, water depth appears to increase linearly with flow rate when the floodplain is vegetated but this is not the case for the unvegetated channel. The mean increase in the water depth is 15.88%, 15.13% and 13.1% for dense, medium and sparse vegetation densities respectively.

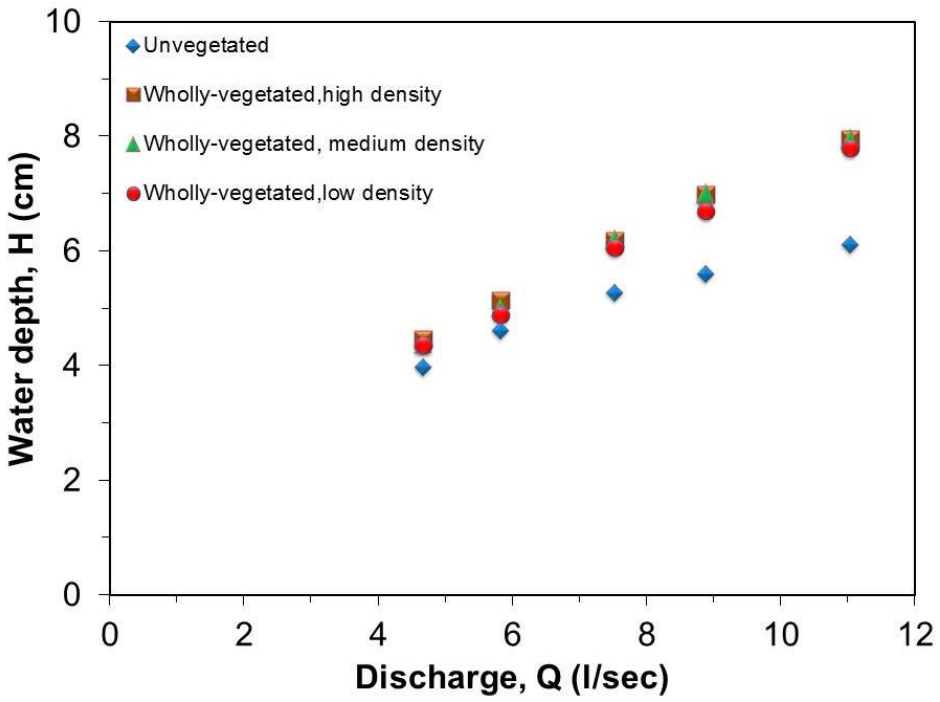

Fig. 5.2: Stage-discharge curves for compound channel flow with wholly-vegetated and unvegetated floodplains.

Figure 5.3 presents the variation of water depth with flow rate for the one-line vegetation case. The inclusion of one-line vegetation produces a much smaller

increase in water depth compared to the wholly-vegetated floodplain (Fig. 5.2). This is due to the fact that the overall vegetation density, and therefore flow blockage, for the one-line case is naturally much smaller than in the full-vegetated case. The plot does indicate, however, that water depth is noticeably more sensitive to changes in L_s/D for one-line vegetation than to changes in density for a wholly-vegetated floodplain. It can clearly be seen that there has been a significant increase in the water depth as the vegetation density is increased in comparison with non-vegetated floodplain (Fig. 5.2).

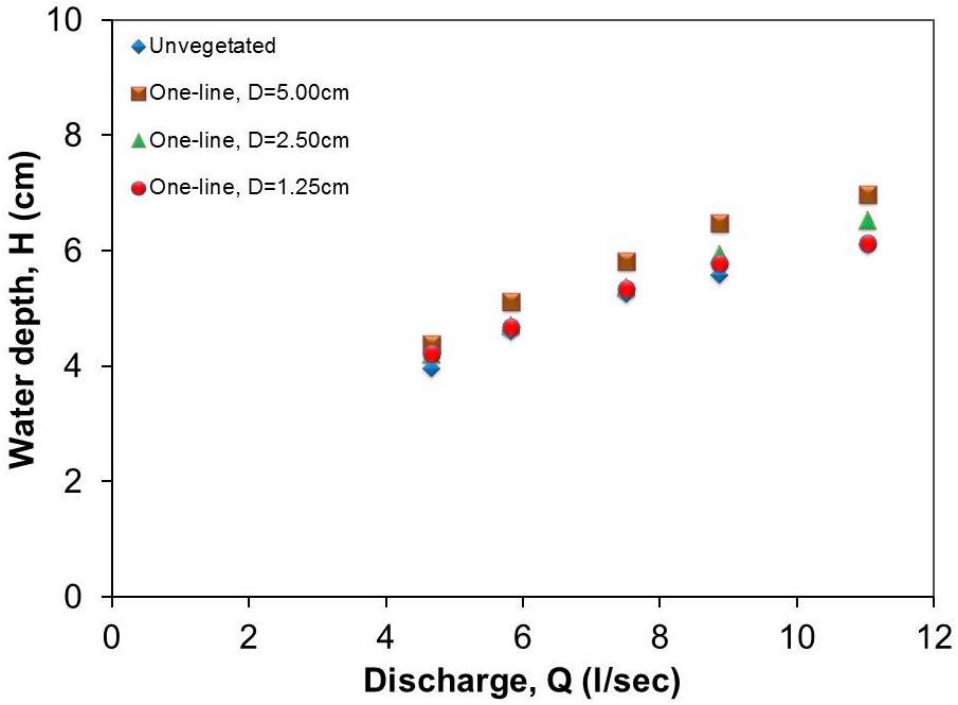

Fig. 5.3: Stage-discharge curves for compound channel flow with one-line vegetation and unvegetated floodplain.

5.4.2 Estimation of mean drag coefficients

Fig. 5.4 presents the variation of drag coefficient with Reynolds number, based on the bulk flow velocity and stem diameter, for the wholly-vegetated floodplain case. The experimental drag coefficient values for the present study have been estimated using the simple streamwise momentum balance, and are plotted alongside experimental data from a number of previous experimental studies. In addition, empirical relationships proposed by Tanino and Nepf (2008), Kothyari et al (2009) and Cheng and Nguyen (2011) have been applied to the hydraulic conditions

investigated in the present study, and the resulting drag coefficient estimates have also been included in the plot. Clearly the collated data shows that the drag coefficient displays a high degree of sensitivity to changes in both Reynolds number and vegetation density. The experimental data from the present study appears to follow the general trend displayed by the other data sets, although there is considerable scatter. It is interesting that the lowest density ratio data sets of Tinco and Cowen (2013) (ϕ = 1.0%) is the notable outlier from the general trend; in this case the drag coefficient appears to be largely independent of Reynolds number. Application of the empirical relationships to the hydraulic conditions tested in the present study generally produces very close agreement with the measured drag coefficients.

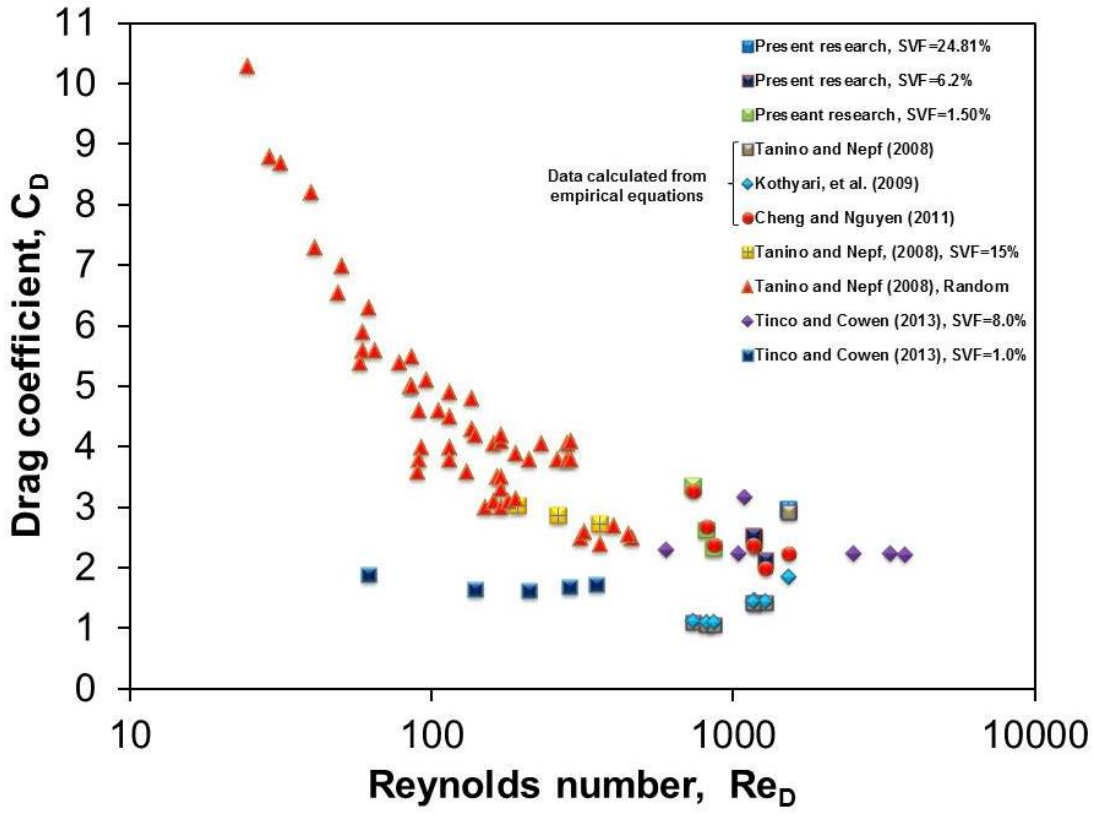

Fig. 5.4: Drag coefficient-Reynolds number relationship for wholly-vegetated floodplain.

Fig. 5.5 shows the influence of rod diameter on the drag coefficient-Reynolds number relationship for the case of one-line vegetation. The figure clearly shows that drag coefficient decreases with increasing Reynolds number, and the range of

measured drag coefficient increases with decreasing rod diameter. As discussed in the "Theoretical Considerations" section of this article, various researchers have proposed different empirical relationships to allow the determination of the interfacial shear stress in compound channels. Equations 5.12 to 5.15 have been used to estimate the interfacial shear stress for the flow cases investigated in the present study, and Fig. 5.6 reveals the effect of the choice of equation on the estimated drag coefficient. Also included in the plot are data from the experimental study of Tanino and Nepf (2008) and Tanino and Nepf (2008)'s proposed drag coefficient equation for the wholly vegetated case. The plot reveals that the data from the present investigation, which populate the Reynolds number range $1800 < Re < 8400$, largely follow the same trend as the experimental data of Tanino and Nepf. The plot also suggests that the choice of empirical equation does not significantly affect the estimation of drag coefficient: there is relatively little scatter between the four data sets, with the exception of the lowest Reynolds number point when Equation 5.11 is used.

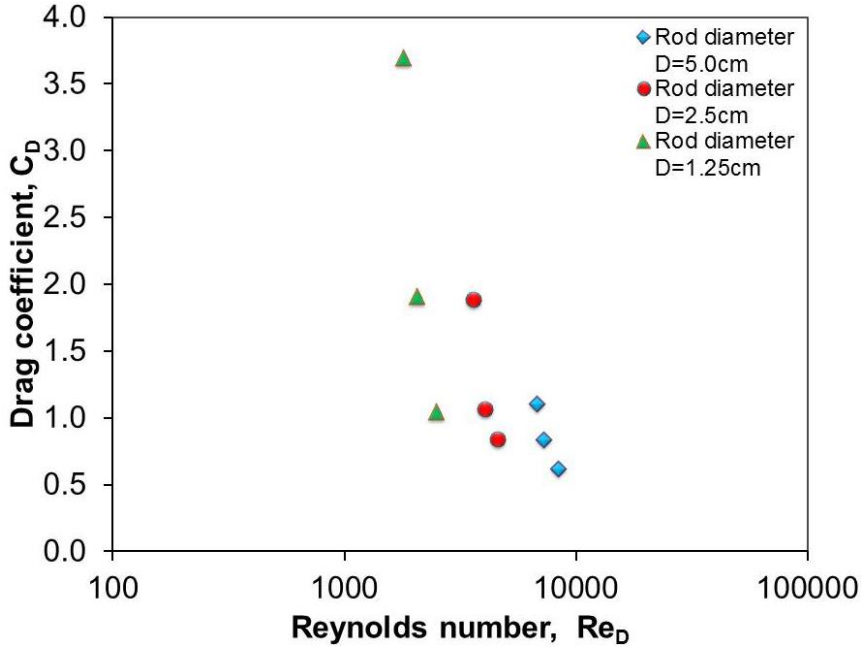

Fig. 5.5: Impact of rod diameter on the drag coefficient-Reynolds number relationship from water balance equation ($F_D = F_G - F_T - F_S$) for one-line vegetation.

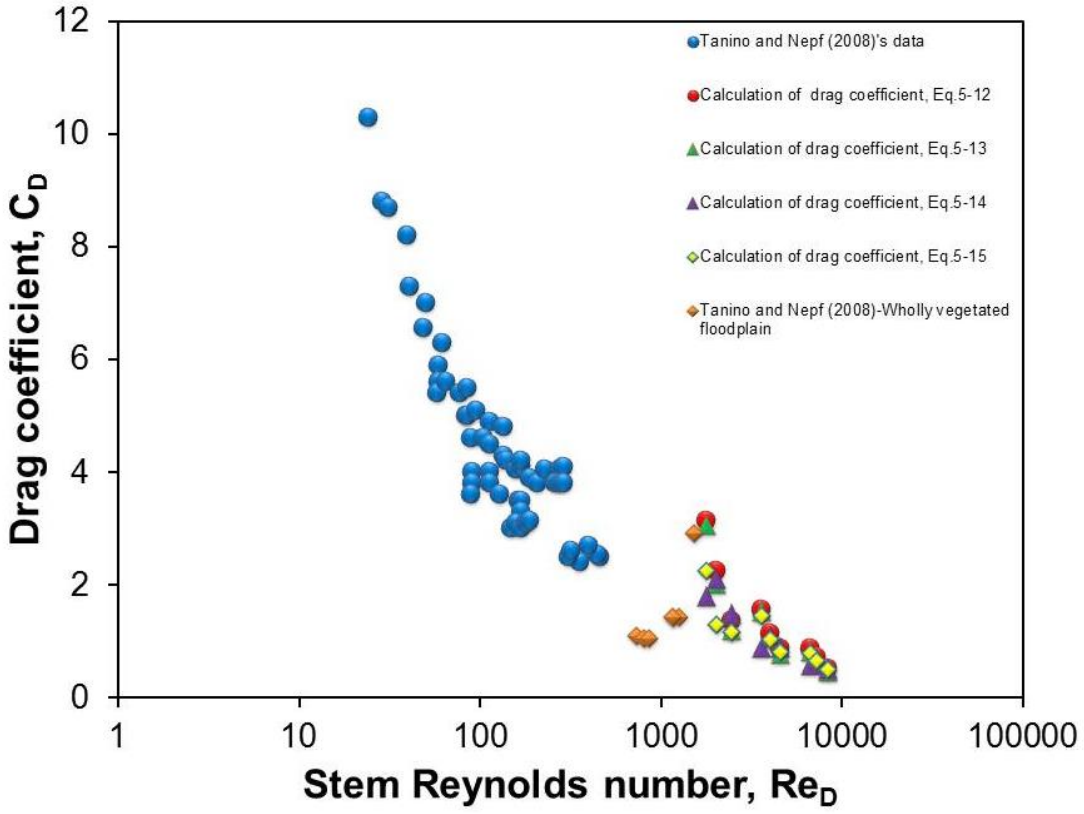

Fig. 5.6: Drag coefficient-Reynolds number relationship: effect of choice of theoretical approach to calculate interfacial shear stress.

5.4.3 Spanwise distribution of streamwise velocity

Figs 5.7 and 5.8 present spanwise profiles of mean depth-averaged streamwise velocity for the wholly-vegetated floodplain and one-line vegetation cases respectively. In each case the three sub-figures present data for the three different flow rates that have been tested. Note that the velocity has been normalised on the bulk streamwise velocity, u_{bulk}. Profiles measured at two (Fig. 5.7) or four (Fig. 5.8) streamwise locations are presented: the close agreement between profiles measured at different streamwise locations indicates that the flow in the measurement section of the flume was fully developed.

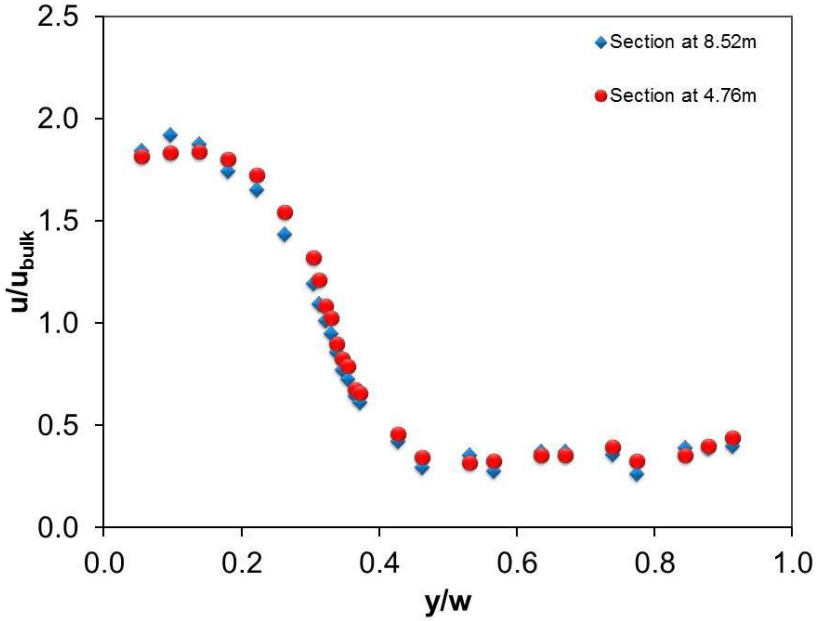
Section at 8.52m
Section at 4.76m
u/u_bulk
y/w
0.0
0.5
1.0
1.5
2.0
2.5
0.0
0.2
0.4
0.6
0.8
1.0

(a)

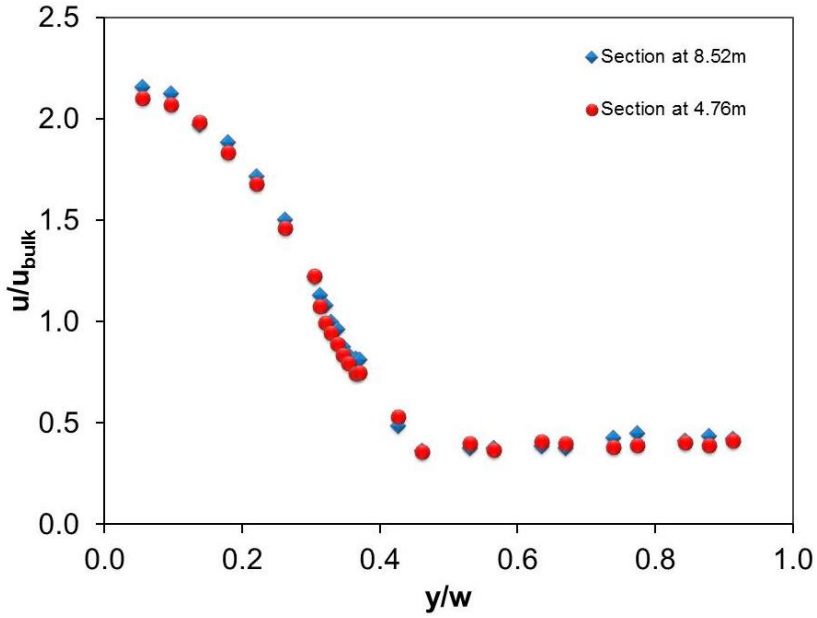
Section at 8.52m
Section at 4.76m
u/u_bulk
y/w
0.0
0.5
1.0
1.5
2.0
2.5
0.0
0.2
0.4
0.6
0.8
1.0

(b)

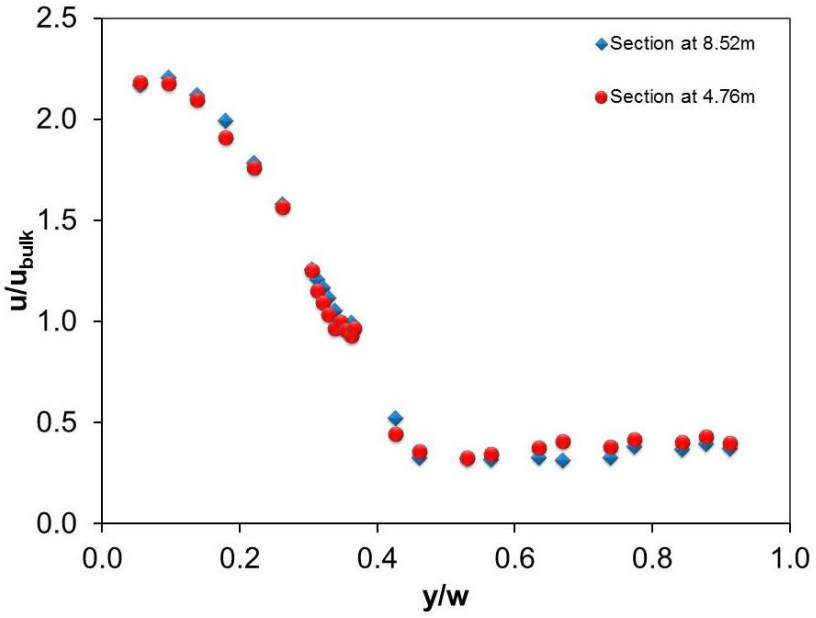

(c)

Fig. 5.7: Spanwise profiles of mean depth-averaged streamwise velocity for wholly-vegetated floodplain with medium vegetation density (D = 2.5cm): a) Q = 4.66 l s^{-1}; b) Q = 7.51 l s^{-1}; and c) Q = 11.03 l s^{-1}.

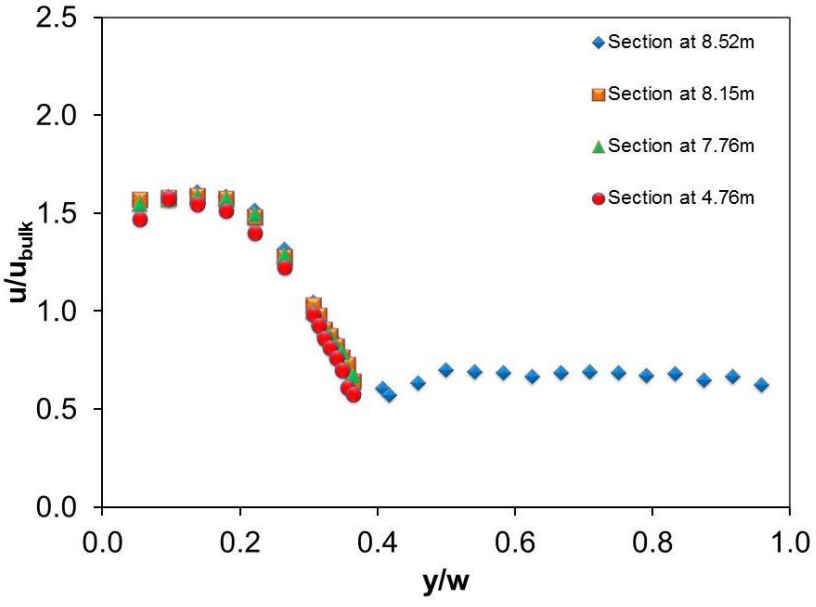

(a)

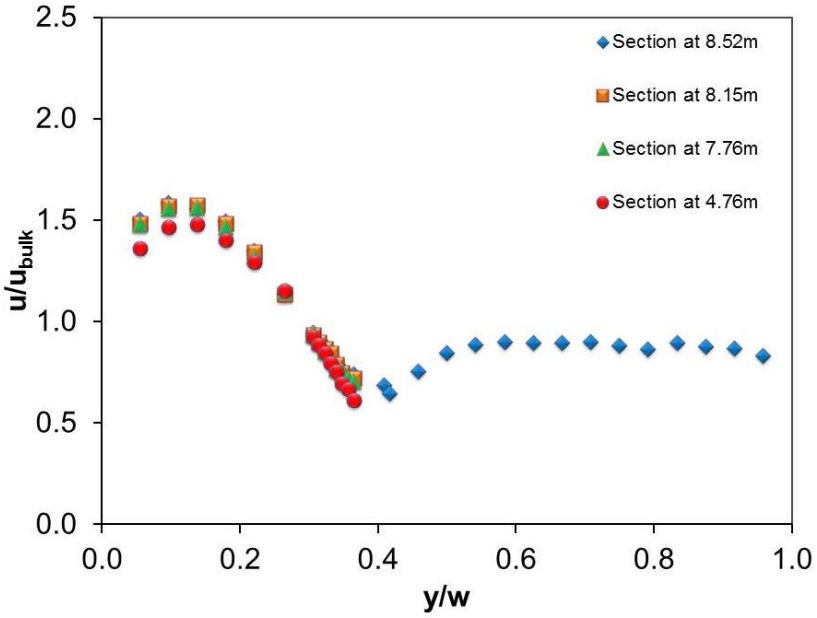

(b)

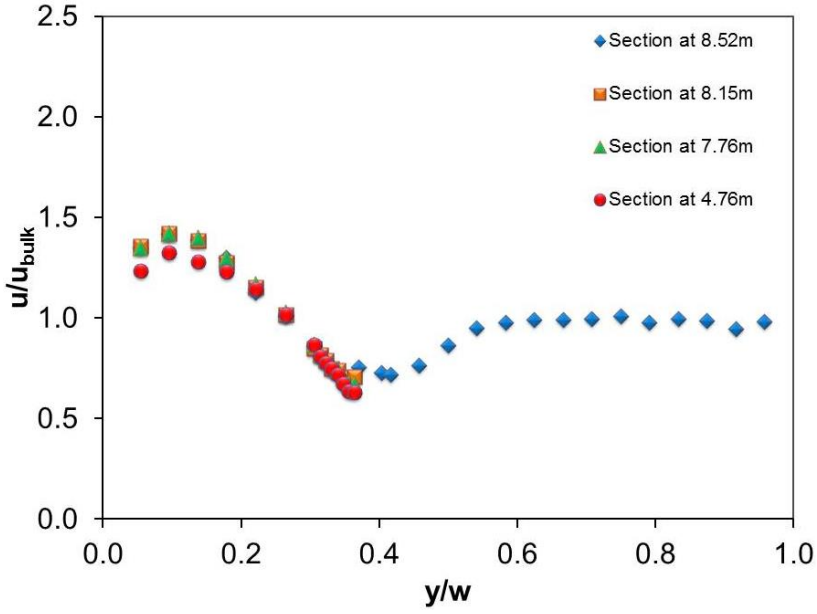

(c)

Fig. 5.8: Spanwise profiles of mean depth-averaged streamwise velocity for one-line vegetation with rod diameter (D = 2.5cm): a) Q=4.66 l s^{-1}; b) Q = 7.51 l s^{-1}; and c) Q = 11.03 l s^{-1}.

Fig. 5.9 presents comparisons of spanwise profiles of mean depth-averaged streamwise velocity for the different configurations (unvegetated, wholly-vegetated and one-line) for the three flow rates that were tested. Note that for the wholly-vegetated floodplain and one-line cases only data pertaining to the D = 2.5cm cases have been presented. Once again the velocity is normalised on u_{bulk}. The plots provide clear confirmation that, as would be expected, flow velocity above a wholly-vegetated floodplain is noticeably lower than that above an unvegetated floodplain. However the plots also reveal that the inclusion of one-line vegetation produces higher velocities above the floodplain compared to the unvegetated case. Correspondingly, the streamwise velocities in the main channel are highest for the wholly-vegetated floodplain case, lowest for the unvegetated case and intermediate for the one-line case. Also noteworthy are the characters of the velocity distributions: for the wholly-vegetated and unvegetated floodplains the spanwise profiles follow an S-shaped curve but for one-line vegetation the profiles exhibit a distinct dip at the interface between the main channel and the floodplain.

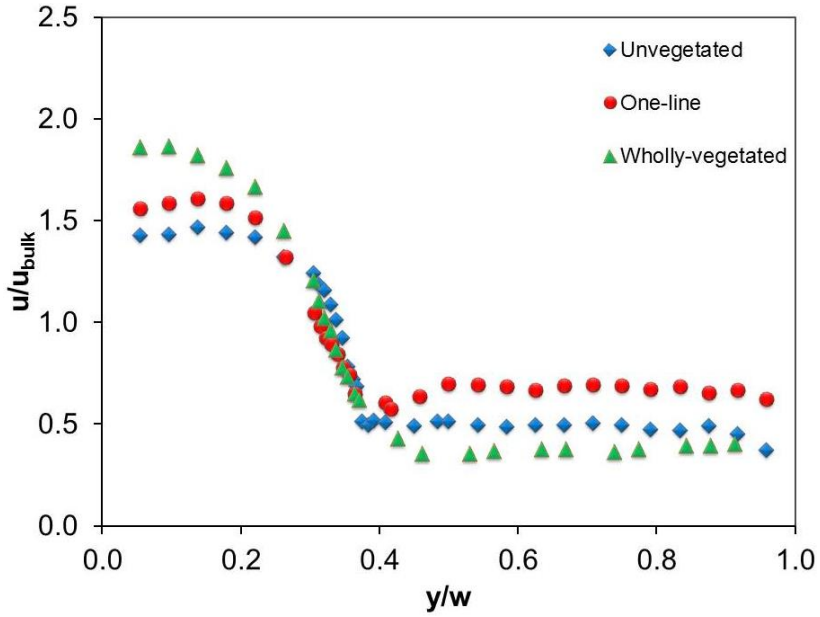

(a)

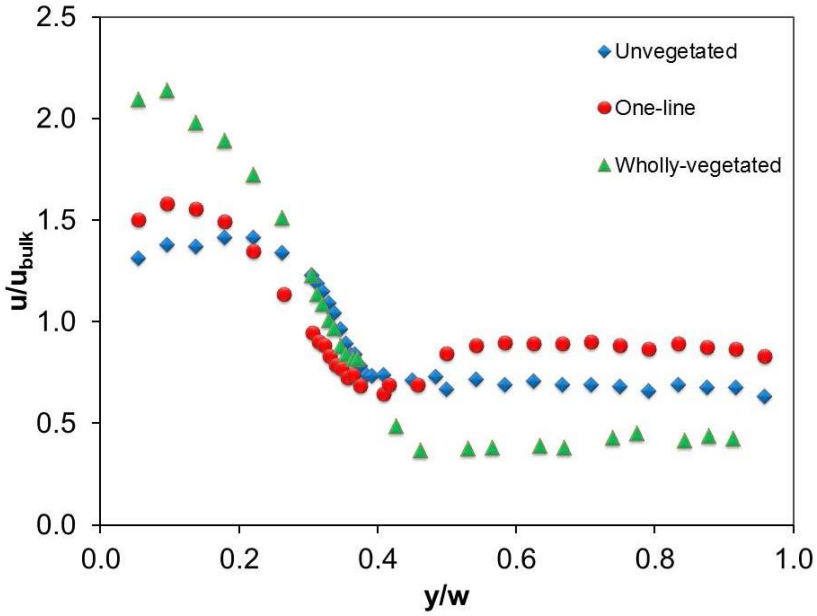

(b)

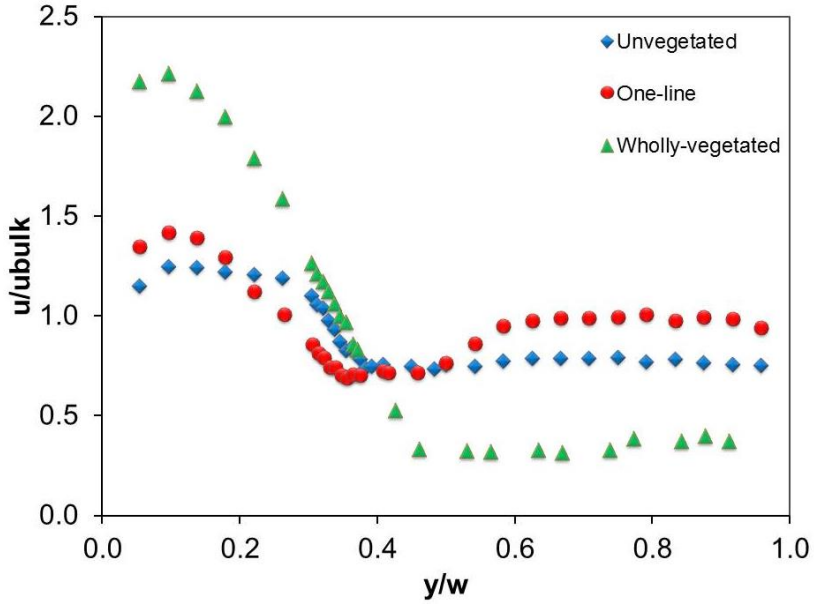

(c)

Fig. 5.9: Spanwise profiles of mean depth-averaged streamwise velocity for wholly-vegetated floodplain and one-line vegetation in comparison to non-vegetated floodplain: a) Q = 4.66 l s^{-1}; b) Q = 7.51 l s^{-1}; and c) Q = 11.03 l s^{-1}.

Spanwise profiles of depth-averaged mean streamwise velocity for the case of an unvegetated floodplain are shown in Fig. 5.10, illustrating the effect of flow rate on the velocity distribution. The plot reveals that the normalised velocity in the main channel decreases with increasing flow rate, while increasing above the floodplain.

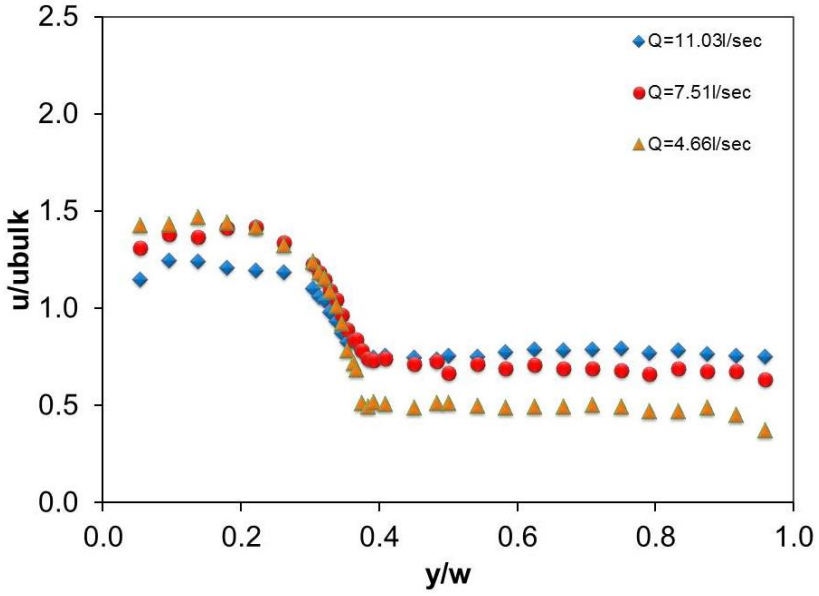

Fig. 5.10: Spanwise profiles of mean depth-averaged streamwise velocity for unvegetated compound channel.

Fig. 5.11 presents spanwise profiles of depth-averaged mean streamwise velocity for the case of a wholly-vegetated floodplain. Each of the three sub-figures corresponds to a different flow rate, and in each sub-figure data pertaining to the three vegetation densities are plotted. In all cases the data exhibit S-shaped spanwise profiles, and the velocity in the main channel increases with increasing vegetation density. The floodplain velocities are shown to be largely independent of vegetation density, with the exception of the highest flow rate case (Fig. 5.11c), where the floodplain velocity is slightly larger for the lowest vegetation density.

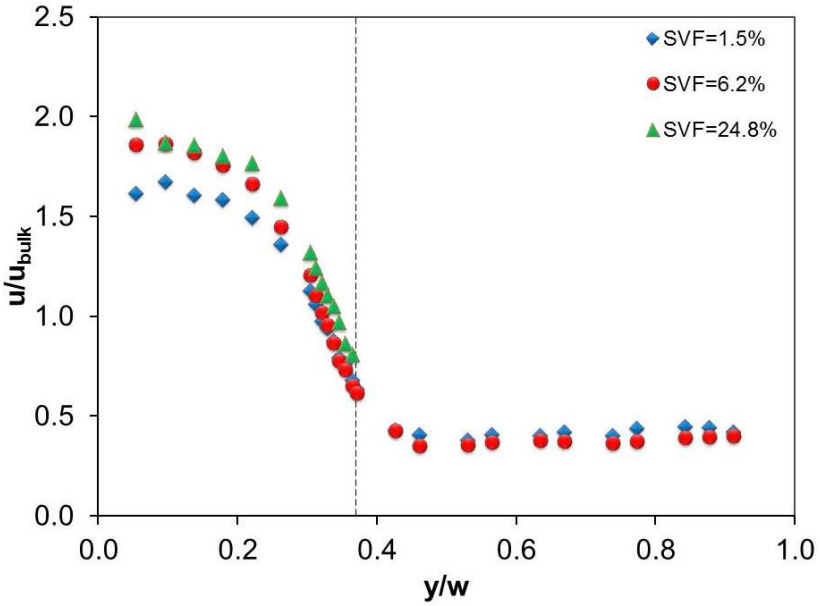
SVF=1.5%
SVF=6.2%
SVF=24.8%
u/u_bulk
y/w
0.0
0.5
1.0
1.5
2.0
2.5
0.0
0.2
0.4
0.6
0.8
1.0

(a)

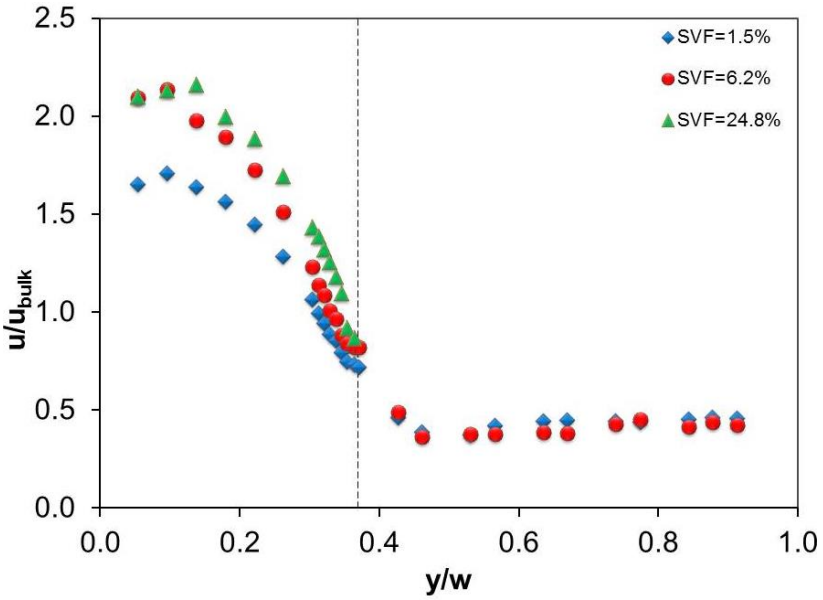
SVF=1.5%
SVF=6.2%
SVF=24.8%
u/u_bulk
y/w
0.0
0.5
1.0
1.5
2.0
2.5
0.0
0.2
0.4
0.6
0.8
1.0

(b)

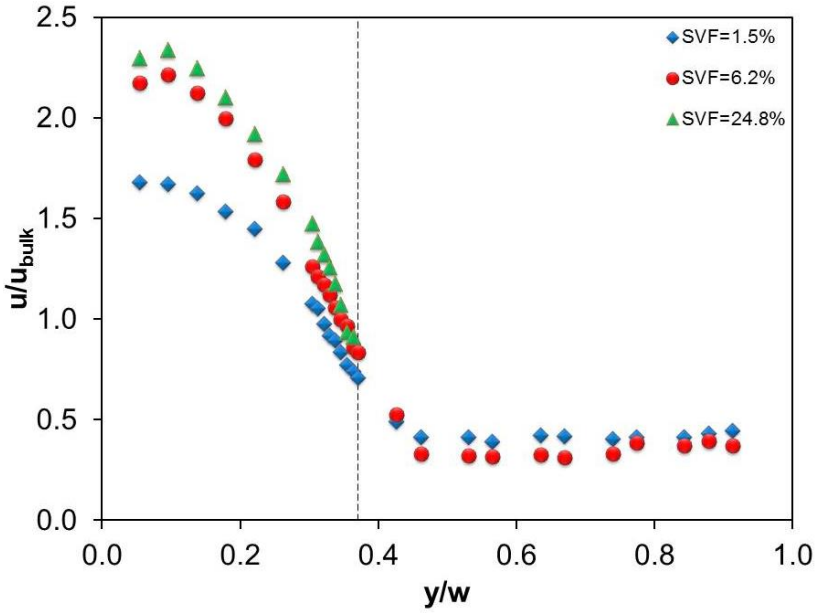

(c)

Fig. 5.11: Impact of the vegetation density on the spanwise velocity profiles: a) Q = 4.66 l s^{-1}; b) Q = 7.51 l s^{-1}; and c) Q = 11.03 l s^{-1}.

Fig. 5.12 presents spanwise profiles of depth-averaged mean streamwise velocity for the case of one-line vegetation, for the three different flow rates that have been considered. The velocity gradients either side of the interface between the main channel and the floodplain are very strong, leading to very high shear stresses and strong large scale vortices. The profiles also reveal very pronounced local minima close to the line of vegetation, indicating suppression of momentum transfer between the main channel and the floodplain, which is in agreement with the findings of Sun and Shiono (2009) and Shiono et al. (2012).

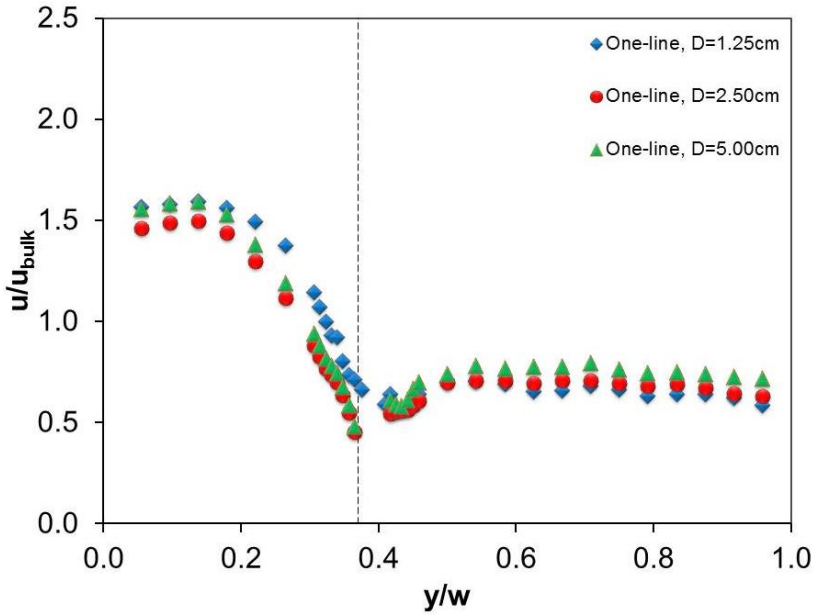
One-line, D=1.25cm
One-line, D=2.50cm
One-line, D=5.00cm
u/u_bulk
y/w
0.0
0.5
1.0
1.5
2.0
2.5
0.0
0.2
0.4
0.6
0.8
1.0

(a)

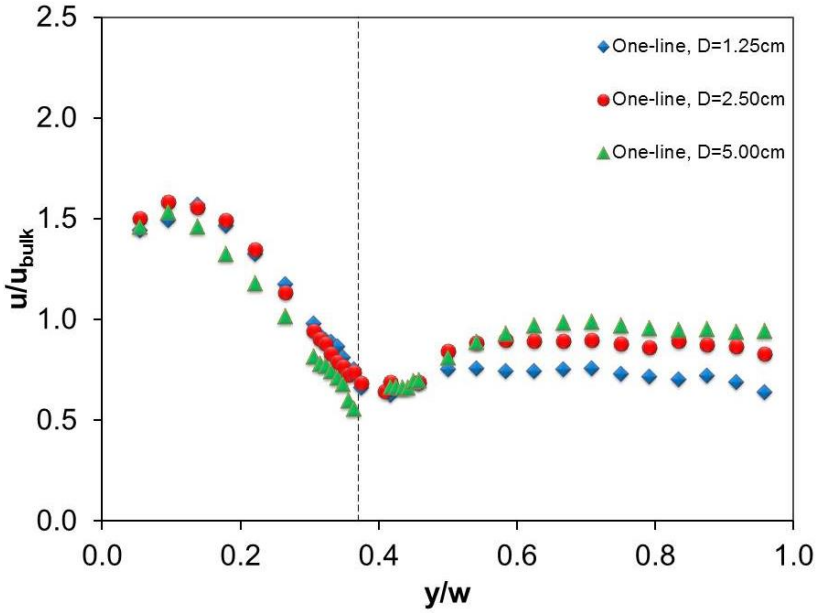
One-line, D=1.25cm
One-line, D=2.50cm
One-line, D=5.00cm
u/u_bulk
y/w
0.0
0.5
1.0
1.5
2.0
2.5
0.0
0.2
0.4
0.6
0.8
1.0

(b)

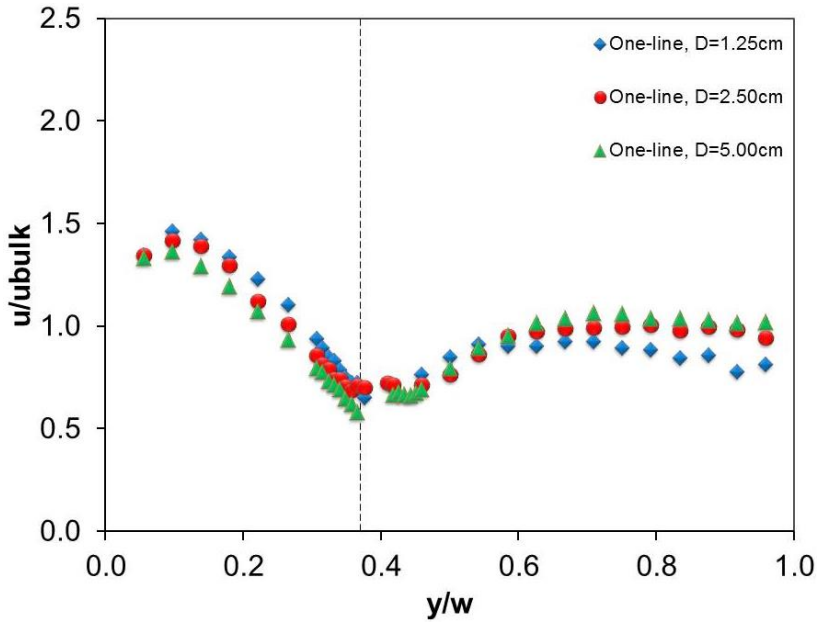

(c)

Fig. 5.12: Impact of one-line vegetation on the spanwise velocity profiles: a) Q = 4.66 l s^{-1}; b) Q = 7.51 l s^{-1}; and c) Q = 11.03 l s^{-1}.

5.5 CHAPTER SUMMARY

Laboratory experiments were carried out to quantify the influence of floodplain vegetation on the rating curve, mean drag coefficient and spanwise distribution of streamwise velocity in compound open channels. Two vegetation configurations - wholly-vegetated floodplain and one-line vegetation - were tested along with a smooth unvegetated compound channel. Vegetation elements were modelled by emergent rigid wooden rods of circular cross-section. For the vegetated cases the effect of vegetation density was investigated, and in all cases three flow rates were tested.

The results showed that for a wholly-vegetated floodplain the water depth increased by 15.88%, 15.13% and 13.1% for dense, medium and sparse vegetation densities, respectively, compared to the unvegetated case. One-line vegetation produced a smaller increase in flow depth than the wholly-vegetated floodplain. The results for one-line vegetation showed that the water depth increased by 11.26%, 4.62% and

2.59% for vegetation diameters of 5.0cm, 2.5cm and 1.25cm, respectively, compared to the unvegetated case.

It was observed that for a wholly-vegetated floodplain the drag coefficient increases with increasing vegetation density. For all vegetation densities the drag coefficient was observed to decrease as Reynolds number increased. Applying the empirical equations of Tanino and Nepf (2008), Kothyari, et al. (2009) and Cheng and Nguyen (2011) to estimate the drag coefficients for the hydraulic conditions presently tested produced values in the range of experimental data from the literature, with relatively little scatter. The experimentally-recorded drag coefficients agreed well with Tinco and Cowen's (2013) results for medium vegetation density, but the agreement for low vegetation density is less convincing.

For one-line vegetation, it was observed that drag coefficient increases with decreasing rod diameter. Empirical equations from the literature were used to estimate the interfacial shear stress at the interface between the main channel and the floodplain: accounting for the interfacial shear stress in this way produced more accurate estimations of the overall drag coefficient compared to simply equating drag force to the overall bed shear stress. Using Tanino and Nepf's (2008) empirical equation for the range of hydraulic parameters presently tested produced estimations for drag coefficient in the region of 1.0.

Spanwise profiles of depth-averaged mean streamwise velocity confirmed that introduction of a wholly-vegetated floodplain results in a considerable reduction in floodplain velocities compared to the unvegetated case, while one-line vegetation produces an increase in floodplain velocity. Velocity in the main channel is lower for wholly-vegetated floodplains and higher for one-line vegetation. The spanwise distributions of streamwise velocity for wholly-vegetated and unvegetated floodplains follow S-shaped curves whereas for one-line vegetation a very pronounced dip is observed at the interface between the main channel and the floodplain.

CHAPTER SIX

FREE SURFACE FLOW OVER SQUARE BARS AT LOW AND INTERMEDIATE RELATIVE SUBMERGENCE

6 FREE SURFACE FLOW OVER SQUARE BARS AT LOW AND INTERMEDIATE RELATIVE SUBMERGENCE

6.1 INTRODUCTION

Although important advances have been made in recent decades, a comprehensive understanding of turbulence structure and flow resistance in rough-bed flows remains elusive. In civil and environmental engineering applications the situation is further complicated by the fact that most flows of interest are relatively shallow and/or have steep slopes. Bathurst (1985) summarised that most standard resistance equations are applicable only to rivers with gentle slopes, and those that have been developed for steep stretches are either empirical or valid only at high flows. In many flows of practical interest the mean flow depth, H, is comparable to the roughness height, *k*, and the concept of the Logarithmic Boundary Layer (LBL) is no longer applicable (Jiménez 2004, Raupach et al. 1991). The LBL is, nonetheless, widely used to study such flows, often leading to erroneous and misleading interpretations of the flow physics.

Several early attempts at modifying the LBL for application to gravel bed rivers with steep slopes and low submergences resulted in a number of empirical or semi-empirical formulations for the well-known Darcy-Weisbach friction factor, f, which is defined for flow in an open channel as follow:

$$\sqrt{\frac{8}{f}} = \frac{U_b}{(gHS)^{1/2}} \tag{6.1}$$

where U_b is the bulk flow velocity, g is acceleration due to gravity, H is the flow depth and S is the bed slope. A brief review of these approaches was given by Bathurst (1985), who considered a semi-empirical equation proposed by Hey (1979) to be the most complete. However, based on a thorough analysis of field and flume data from his own measurement campaigns and those performed by others, Bathurst concluded that the Hey equation was subject to large errors in f for shallow flows. Bathurst therefore proposed an alternative equation that was more applicable to low submergence flows but was nonetheless characterised by a possible error of between

± 25% and • ±35%. Bathurst was left to conclude that "the complicated nature of the flow resistance processes, coupled with the lack of available data, currently prevent the development of a satisfactory practical method for predicting flow resistance in steep mountain rivers". More recently, (Pagliara and Chiavaccini 2006, Pagliara et al. 2008) investigated flow resistance in steep chutes with large-scale roughness that comprised protruding boulders in some cases. Bed slope, relative submergence and boulder arrangement were systematically altered and a logarithmic expression for *f* was obtained and was shown to fit the available experimental data well. Furthermore, it was observed that *f* increased with increasing slope for a given relative submergence and roughness arrangement and the influence of larger boulders on the overall resistance was shown to decrease with increasing submergence.

To achieve a rigorous understanding of low submergence flows over rough beds, (Nikora et al. 2001, Nikora et al. 2007a, Nikora et al. 2007b) applied the double-averaging methodology to the governing Navier Stokes equations and identified four distinct flow regimes based on relative submergence. Flow type I (high submergence) comprises the outer, logarithmic, form-induced and interfacial sub-layers; flow type II (intermediate submergence) is characterised by the absence of a genuine universal logarithmic layer because H/*k* is too small to sustain it; in flow type III (low submergence) the roughness layer (= interfacial + form-induced) extends to the free surface; and in flow type IV (partially-inundated roughness) only the interfacial sub-layer is present. Alongside the question of relative submergence, the geometrical characteristics of the roughness itself clearly play an important role. Perry et al. (1969) were the first to identify two types of roughness, *d*-type and *k*-type, which give rise to fundamentally different roughness functions. Their pipe flow experiments showed that for *k*-type roughness the roughness function depended on the size of the roughness elements, whereas in *d*-type roughness it depended on the pipe diameter. For a flow of given bulk Reynolds number, Re, over two-dimensional roughness elements, the transition between *d*- and *k*-type roughness depends solely on the streamwise spacing of the elements. Many researchers have chosen to focus on square bar roughness to investigate the effect of spacing on turbulence structure and mean flow characteristics, both experimentally (Okamoto et al. 1993, Djenidi et

al. 1999, Krogstad et al. 2005, Coleman et al. 2007, Djenidi et al. 2008, Roussinova and Balachandar 2011) and numerically (Cui et al. 2003, Stoesser and Rodi 2004, Ikeda and Durbin 2007, Stoesser and Nikora 2008). Simpson (1973), Tani (1987), Jiminez (2004) and Coleman et al. (2007) all proposed that the transition from *d*- to *k*-type roughness occurs at around $\lambda/k = 5$, where λ is the crest-to-crest bar spacing and k is the roughness height. Leonardi et al. (2003) carried out a series of Direct Numerical Simulations (DNS) of flow over 2D bars aligned transverse to the main flow direction, varying λ/k between 1.33 and 20, and found that bars are considered isolated (flow completely reattaches to bed before next roughness structure) when λ/k is greater than 8. Stoesser & Nikora (2008) also confirmed this finding in a large-eddy simulation (LES) study, revealing how wall shear stress increases from *d*- to *k*-type roughness. Roussinova & Balanchandra (2011) investigated the effect of altering the submergence for two different *k*-type spacings, $\lambda/k = 9$ and 18, and found that for the larger spacing case the effects of roughness are felt only in the region $0 \leq z/k \leq 3$ while for the closer spacing case they are felt throughout most of the flow in the outer layer.

It is generally accepted that *d*-type roughness is characterised by stable separated vortices occupying the entire cavity between roughness elements while *k*-type roughness entails a mean recirculation bubble in the wake of the roughness elements, with reattachment to the bed occurring at successive elements (Stoesser and Rodi 2004).

Nikora (2009) applied the double-averaging methodology to develop a theoretical expression that explicitly showed that the friction factor can be accounted for by six additive components, and in two-dimensional uniform spatially-averaged flow without secondary currents only three are present: (1) viscous stress; (2) turbulent stress; and (3) form-induced stress. The friction factor for such flows can therefore be expressed as follows:

$$f = \underbrace{\frac{48}{Re}\frac{1}{G}}_{1} + \underbrace{\frac{48}{Q^2 G}\int_{z_t}^{z_{ws}} (H_m - z)\varphi \,\langle \overline{-u'w'} \rangle \, dz}_{2} + \underbrace{\frac{48}{Q^2 G}\int_{z_t}^{z_{ws}} (H_m - z)\varphi \,\langle -\tilde{u}\tilde{w} \rangle dz}_{3} \qquad (6.2)$$

where Re is the bulk Reynolds number, Q is the flow rate, H_m is the maximum depth (i.e. distance between the highest point on the free surface and the lowest point on the bed), z is the vertical elevation, and u' and w' are the velocity components in the streamwise and vertical directions, respectively. The roughness geometry function, φ, is the ratio of the volume occupied by fluid, V_f , within the total volume, V_0, over which the spatial averaging operation is performed. The parameter $G = [3(L_\tau/H_m)^2 - 1](H_m/H)^2$ characterises flow-roughness interaction, where L_τ is a characteristic 'drag' length scale that depends on the roughness geometry and distribution of drag force within the roughness layer. In Eq. 6.2 the overline and angular bars denote temporally- and spatially-averaged variables, respectively. The approach makes use of the Reynolds decomposition $\theta = \bar{\theta} + \theta'$ for instantaneous variables, and the decomposition $\bar{\theta}=\langle\bar{\theta}\rangle + \tilde{\theta}$ is used for temporally averaged variables where the tilde denotes the spatial fluctuation of that variable. The contribution of the form-induced stress, $\langle\tilde{u}\tilde{w}\rangle$, has recently attracted substantial attention as it has been shown to play an important role in the overall streamwise momentum balance in the near-bed region (Aberle et al. 2008, Dey and Das 2012, Ferreira et al. 2010, Giménez-Curto and Corniero Lera 1996, Giménez-Curto and Corniero Lera 2003, Manes et al. 2007, Manes et al. 2008, Mignot et al. 2009a, Mignot et al. 2009b, Nikora et al. 2007b, Sarkar and Dey 2010). Indeed, (Giménez-Curto and Corniero Lera 1996, Giménez-Curto and Corniero Lera 2003) suggested that at very low submergences the form-induced stress could become the dominant component in the streamwise momentum balance, while Manes et al. (2007) found that the relative contribution of form-induced stress increased as submergence decreased in their experiments in open channel flow over closely-packed spheres.

For isolated (*k*-type) roughness at small submergences the local Froude number may become large enough to produce a hydraulic jump or standing wave at the free surface. These features are characterised by extremely vigorous turbulence production, formation of large-scale turbulent structures, air spray, air entrainment and energy dissipation (Chanson and Brattberg 2000, Chanson 2009). Although such features are ubiquitous in civil and environmental engineering scenarios, their

contribution to the overall streamwise momentum balance in open channel flows has not been studied with reference to hydraulic resistance.

The aim of present study is to investigate the effect of roughness spacing and relative submergence on hydraulic resistance in turbulent open channel flows using complimentary laboratory flume experiments and comparing the results with large-eddy simulations (Chua et al. 2016). Six flow cases have been investigated, spanning the flow types II and III Nikora et al. (2007a) and transitional (between *d*- and *k*-type) and *k*-type roughness. The double-averaging methodology is applied to the simulated flow to reveal explicit contributions to the overall momentum balance due to form-induced and turbulent stresses and the pressure drag is also quantified. The remainder of the chapter is organised as follows: Section 6.2 outlines the experimental set-up; Section 6.3 presents and discusses the results. Finally some conclusions are drawn in Section 6.4.

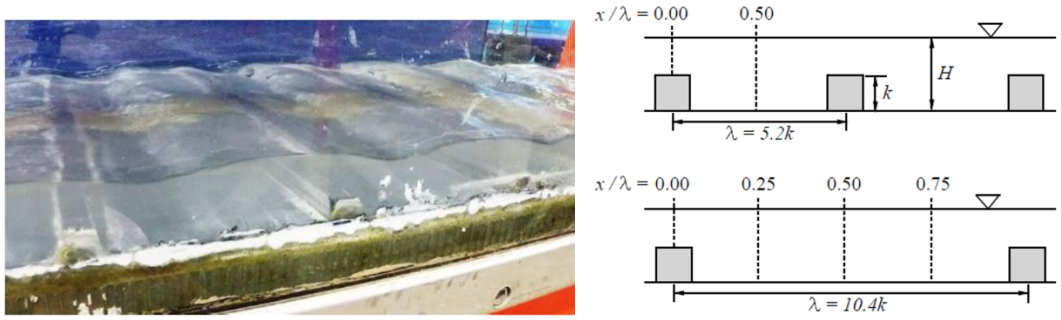

(a) (b)

Figure 6.1: Experimental set-up. (a) the flume equipped with square bars and (b) the two geometries, with velocity measurement locations denoted by dashed lines.

6.2 EXPERIMENTAL SET-UP

Experiments were carried out in a 10 m long, 30 cm wide glass-walled recirculating flume in the Hyder Hydraulics Laboratory at Cardiff University. A series of plastic square bars of width 30 cm and cross-section 12 mm × 12 mm were installed along the length of the flume, perpendicular to the direction of mean flow (Fig. 6.1). The roughness height, *k*, was therefore 12 mm. Two different bar spacings were investigated, λ = 62.5 mm and λ = 125 mm, corresponding to normalised spacings

λ/k = 5.2 and λ/k = 10.4, respectively. According to Coleman et al. (2007), the λ/k = 5.2 case should be classified as transitional roughness as it is very close to the boundary between *d*- and *k*-type roughnesses, while the λ/k = 10.4 case constitutes *k*-type roughness. Bed slope was fixed at 1:50 for all experiments and three flow rates were tested for each bar spacing (Q = 1.7, 2.5, 4.0 l s^{-1}), giving a total of six experimental cases. Each case had a different relative submergence, H/k, where H is the double-averaged height of the free surface above the channel bed and the double-averaged bulk velocity, $U_{b,}$ ranged from 0.20 m s^{-1} to 0.36 m s^{-1}. Note that the angular brackets and overbar have not been used for H and U_b in the interest of simplicity. Table 6.1 provides a summary of the flow conditions for each case.

Measurements of instantaneous velocity and free surface position were taken in a section of the flume where the flow was considered to be uniform and fully-developed. The flow was also considered to be spatially periodic with wavelength λ in the streamwise direction, that is to say the temporal mean values of all flow variables in successive cavities between bars were considered to be the same. The bulk Reynolds number was in the range $5700 \leq Re \leq 13000$ and the friction Reynolds number $Re_\tau \left(= \frac{u_* H}{\nu}\right)$ where u_* is the global friction velocity based on the bed shear stress, was in the range $1.8 \times 10^3 \leq Re_\tau \leq 3.7 \times 10^3$. The global Froude number of the flows, $Fr = (\frac{U_b}{\sqrt{gH}})$, was in the range $0.38 \leq Fr \leq 0.59$; local values based on local depths and velocities can be much higher.

A Nixon propeller meter was used to measure streamwise velocities at the channel centreline, at two streamwise positions for the λ/k = 5.2 case and four streamwise positions for the λ/k = 10.4 case. At each streamwise location the velocity was measured at between four and eleven discrete depths, to reveal vertical velocity profiles. At each depth measurements were taken during 120 seconds at a sampling frequency of 1 Hz; 120 samples of instantaneous velocity were therefore available, from which the temporal mean was calculated.

Water surface position was measured using Particle Image Velocimetry (PIV). A Baumer TXG14F CCD camera was used in conjunction with a Polytec BUS-11

Wotan Flash stroboscope and a halogen lamp to capture the dynamic free surface. Seeding particles that had the same approximate density of water, making them neutrally buoyant, were used. The camera recorded images during 50 seconds for each flow case, at a rate of 30 frames per second.

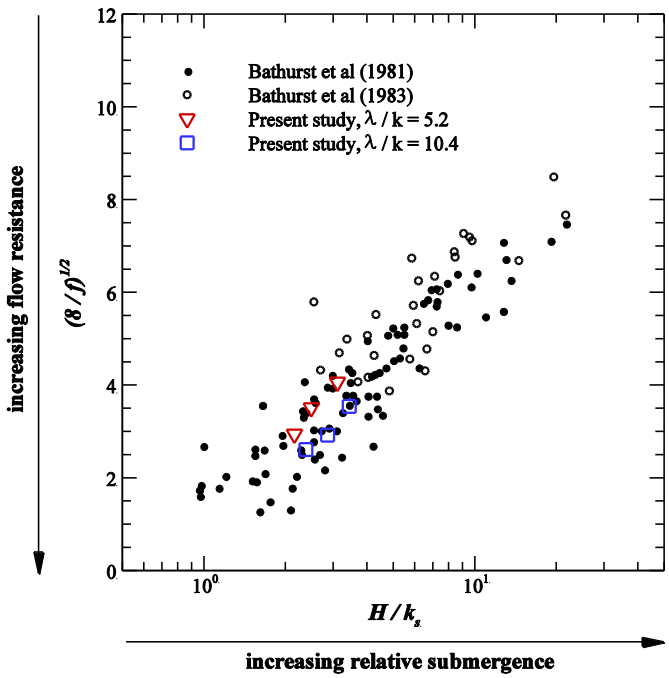

Figure 6.2: Variation of friction factor with relative submergence for the flume experiments.

Table 6.1: Hydraulic characteristics of the flow conditions.

Case	λ/k	H/k	U_b (m s^{-1})	Re	Re_τ	Fr	Lx/H	Ly/H	Δx^+	Δy^+	Δz^+
C1	5.2	2.4	0.22	5.7×10^3	1.8×10^3	0.43	4.8	2.3	69.9	66.8	35.6
C2	5.2	2.7	0.28	8.3×10^3	2.3×10^3	0.51	4.2	2.0	75.1	71.8	38.8
C3	5.2	3.3	0.36	13.3×10^3	3.2×10^3	0.59	3.4	1.6	83.8	80.2	42.8
C4	10.4	2.5	0.20	5.7×10^3	2.1×10^3	0.38	4.4	2.1	73.2	70.0	37.4
C5	10.4	3.0	0.24	8.3×10^3	2.8×10^3	0.42	3.7	1.8	80.3	76.9	41.0
C6	10.4	3.5	0.32	13.3×10^3	3.7×10^3	0.51	3.0	1.5	88.2	84.3	45.0
F1	5.2	2.7	0.28	8.3×10^3	2.3×10^3	0.51	4.2	2.0	37.5	35.9	19.1
F2	10.4	2.5	0.20	5.7×10^3	2.1×10^3	0.38	3.7	1.8	36.6	35.0	18.7
F3	10.4	3.0	0.24	8.3×10^3	2.8×10^3	0.42	3.7	1.8	40.2	38.4	20.5
D1	10.4	3.0	0.24	8.3×10^3	2.8×10^3	0.42	7.4	3.6	80.3	76.9	41.0

Each recording therefore comprised 1500 individual frames, which were then transformed into binary images to smear the water surface profile using Matlab software. These data were then averaged to give a temporal mean of the free surface position. Figure 6.4(a) presents an individual frame from one of the cases, showing the instantaneous free surface deformation. It should be noted that the free surface elevation recorded by this technique was noticeably different from the elevation observed in the centre of the channel due to Meniscus effects that were observed at the channel sidewalls. This has the effect of thickening the appearance of the free surface and "smearing" the profiles of the standing waves that occurred in the λ/k = 10.4 cases.

In addition to the PIV measurements a point gauge was used to measure free surface elevation at the channel centreline. Measurements were taken over a length spanning two or more cavities, at streamwise intervals of between 2.5 mm and 10 mm. Point gauge measurements were taken for all flow cases except C6, which was characterised by an extremely dynamic free surface with a significant spanwise wandering motion of the hydraulic jump, and was therefore impossible to measure with a point gauge (Figs.0-13 in appendix I).

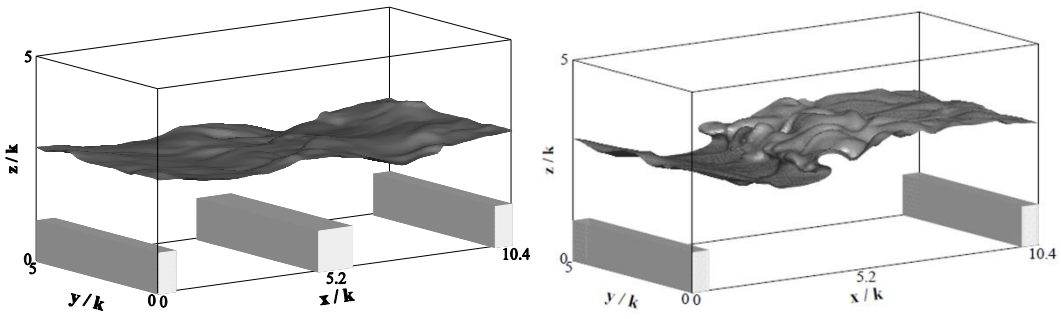

(a) λ /k = 5.2 (b) λ/k = 10.4

Figure 6.3: Computational domains with instantaneous free surface response (*Chua et al. 2016*).

Figure 6.2 presents the variation of the friction factor, presented as $(8/f)^{\frac{1}{2}}$ and calculated from Eq. 6.1, with relative submergence for the six cases that have been studied. Flume data from Bathurst (1985) are included for comparison. Note that the

Bathurst data correspond to gravel bed roughness and were originally presented in terms of H/D_{84}, where D_{84} is the size of median axis of the bed material which is larger than 84% of the material. The data has been replotted in terms of the equivalent grain roughness, k_s, and the relationship $k_s = 3.5D_{84}$ (Dietrich and Whiting 1989) has been used to equate the two measures of roughness height. With regards to the data from the present experimental tests, the equivalent grain roughness is assumed to be equal to the bar height ($k_s = k$); this relationship is likely to be subject to significant error but has been used to permit a crude comparison with the Bathurst flume data. Interestingly the data lie within the spread of Bathurst data and agree very well with the general trend of decreasing resistance with increasing relative submergence. It is noteworthy that, for a given submergence, that the small bar spacing produces less resistance than the large bar spacing.

In addition, more experiments were done to monitor the water surface profiles and to measure the vertical velocity profiles for rough open channel flows with a bed slope (S = 1:200) for two bar spacing (H/k= 5.2 and H/k=10.4) and three flow rates were tested for each bar spacing (Q = 1.7 l s^{-1}, 2.5 l s^{-1}, 4.0 l s^{-1}) which results in different submergence ratios, are presented in appendix I.

6.3 RESULTS AND DISCUSSION

With the help of Fig. 6.4, an instantaneous free surface profile recorded by the PIV can be qualitatively compared to an instantaneous plot of the water surface from the corresponding LES. Although an exact match cannot be expected due to the Meniscus effect that affected the experiments (refer to Section 6.2), the agreement is nonetheless very encouraging. The standing wave is very clear in both experiment and simulation, and its height and streamwise position is very accurately predicted by the LES.

The free surface fluctuations properties are presented including the mean and fluctuating profiles. The longitudinal free surface profiles were recorded for twelve experiments and compared with the numerical approach for six experiments for the steep bed slope S = 1/50.

Statistical analysis of the experimental data for the longitudinal profiles was examined. The standard deviation of the longitudinal free surface profiles were calculated for the six relative submergences. Small free-surface fluctuations were observed and recorded in the case of the small roughness spacing.

A significant increase in free surface fluctuation was observed in the small scale roughness at low submergence, and the free-surface fluctuations reached a maximum value for the large-scale roughness spacing. This maximum value increased with increasing relative submergence, for which large standard deviations in free-surface elevations were linked. The drawings of the standard deviation hrms/H were explained as a non-dimensionalized relative to the uniform flow depth versus x/k. Standard deviation results of the free surface elevations were explained in Figures (6.5 to 6.10). For small spacing the mean free surface in all three small spacing cases is relatively flat and standard deviation values are increased with decreasing the submergence ratio and some undulation was observed. Upstream the bars large magnitudes of the standard deviation were shown (see Figs. 6.5 to 6.7). For large spacing the standard deviation values are increased and coincide with the observed strong hydraulic jumps for all the submergence ratios (see Figs. 6.8 to 6.10).

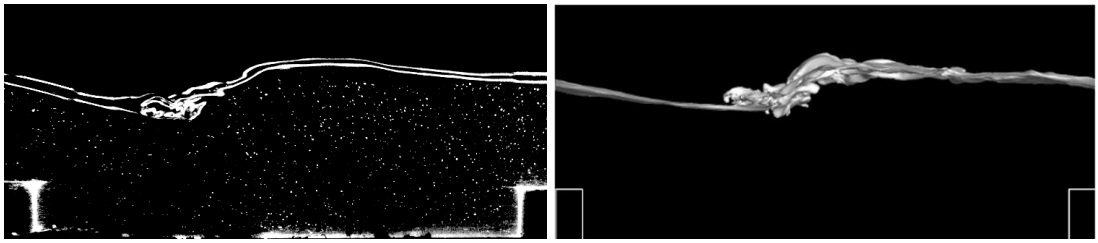

(a) Experiment (b) LES

Figure 6.4: Visualisation of instantaneous free surface profiles, $\lambda/k = 10.4$, $H/k = 2.4$.

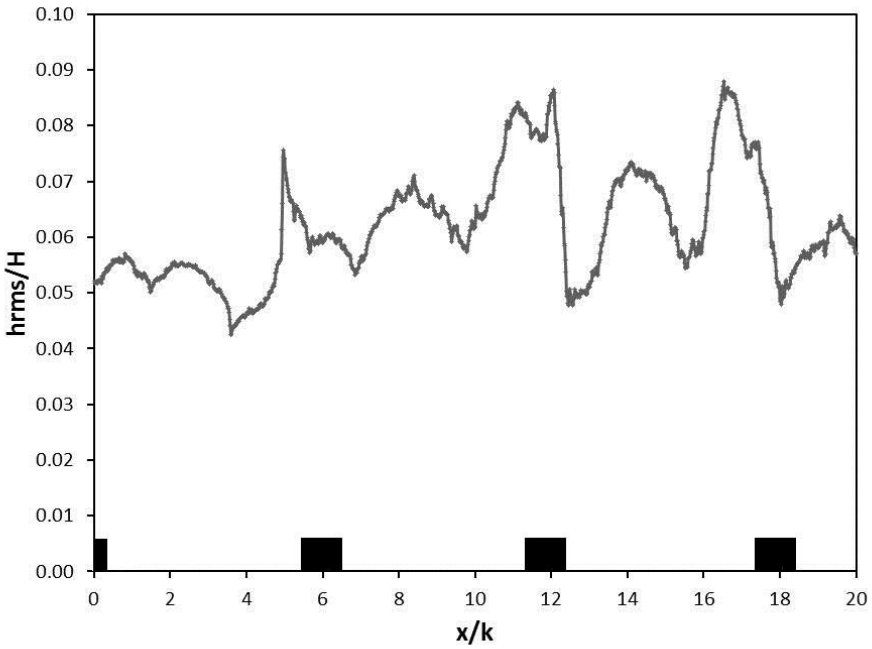

Figure 6.5: Dimensionless longitudinal profiles of free surface fluctuations hrms/H for Q = 1.7 l/s, S = 1:50, H = 2.53 cm and p/k = 5.2.

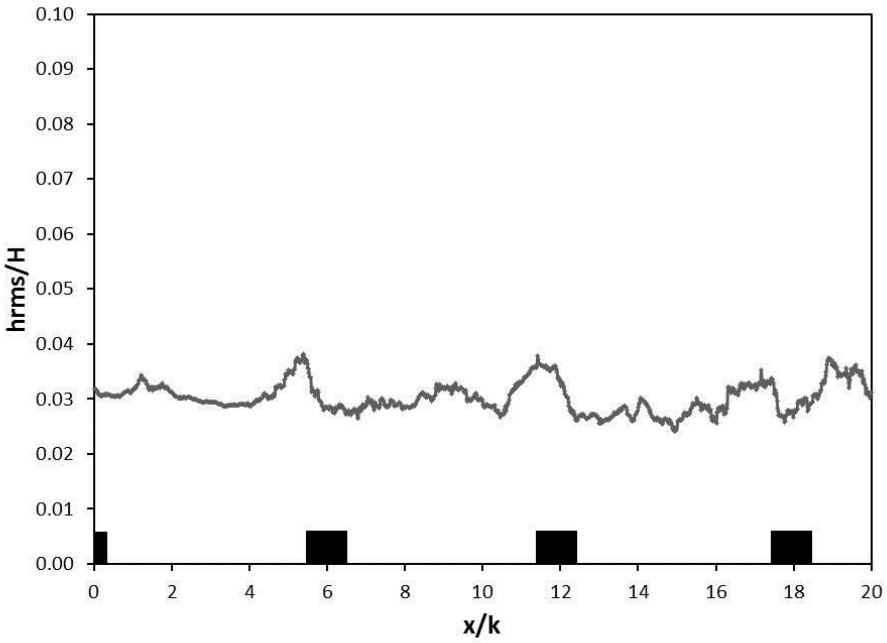

Figure 6.6: Dimensionless longitudinal profiles of free surface fluctuations hrms/H for Q = 2.5 l/s, S = 1:50, H = 2.93 cm and p/k = 5.2.

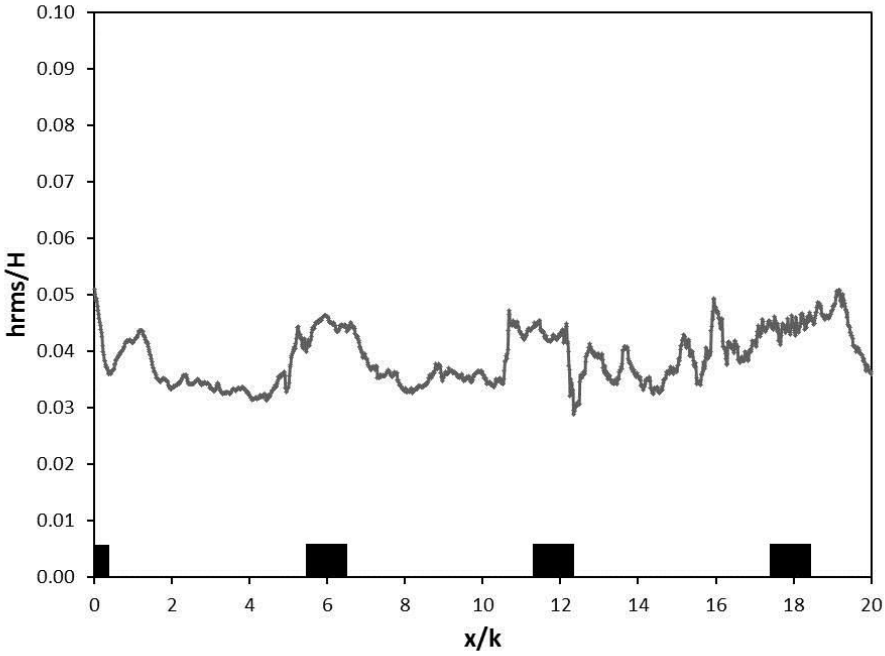

Figure 6.7: Dimensionless longitudinal profiles of free surface fluctuations hrms/H for Q = 4.0 l/s, S = 1:50, H = 3.52 cm and p/k = 5.2.

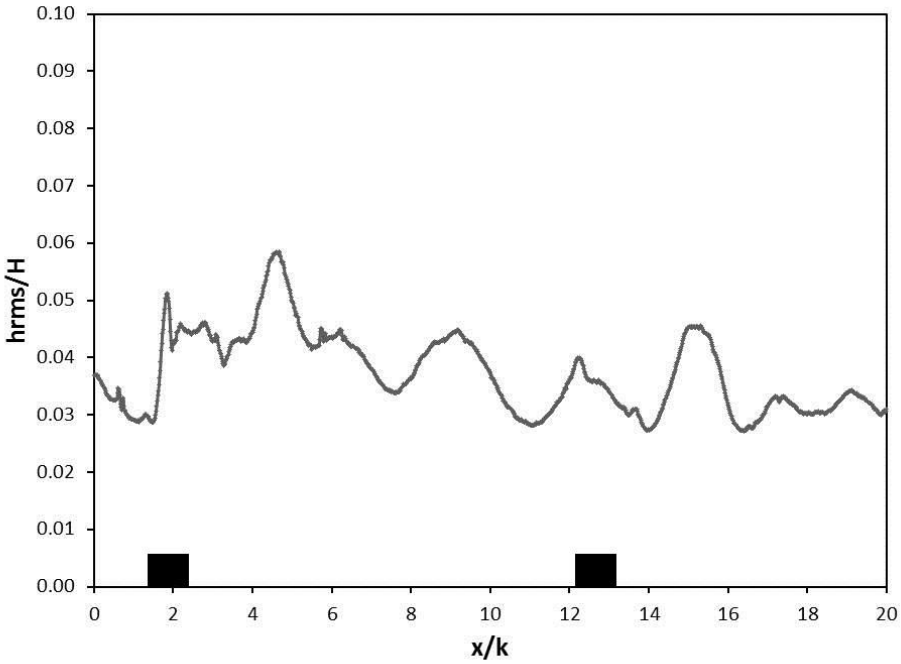

Figure 6.8: Dimensionless longitudinal profiles of free surface fluctuations hrms/H for Q = 1.7 l/s, S = 1:50, H = 2.96 cm and p/k = 10.4.

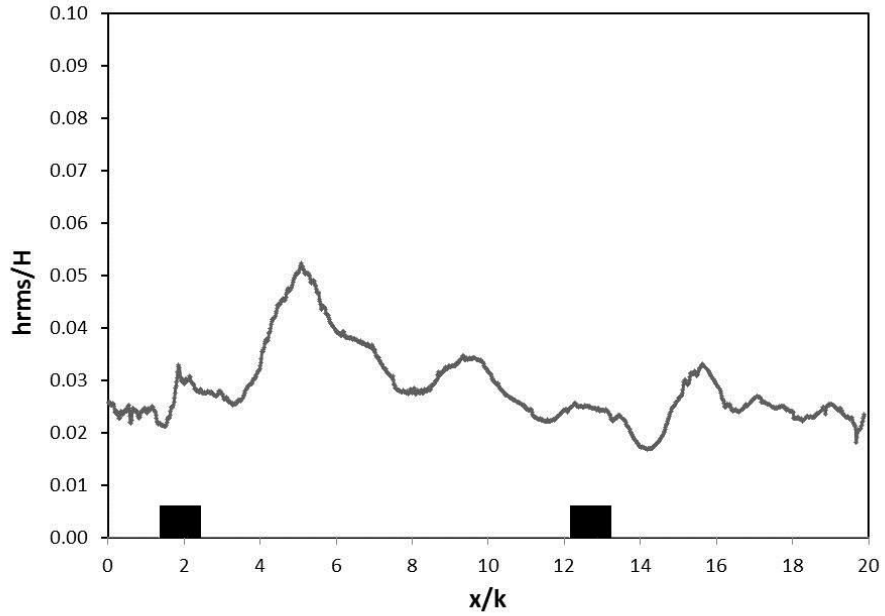

Figure 6.9: Dimensionless longitudinal profiles of free surface fluctuations hrms/H for Q = 2.5 l/s, S = 1:50, H = 3.54 cm and p/k = 10.4.

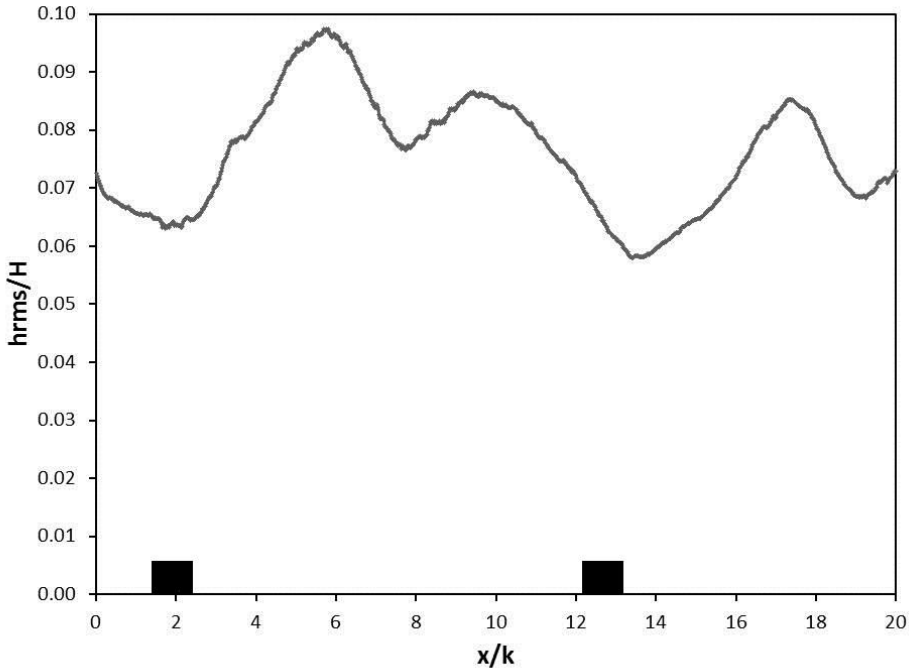

Figure 6.10: Dimensionless longitudinal profiles of free surface fluctuations hrms/H for Q = 4.0 l/s, S = 1:50, H = 4.24 cm and p/k = 10.4.

A more quantitative evaluation of the match between LES and experiment can be achieved with the help of Fig. 6.11, which presents water surface profiles for the six flow cases.

Plotted are the spanwise mean of the temporal mean water surface predicted by the LES and the means that were measured using PIV and the point gauge. The agreement between experiments and LES is particularly good for the small spacing ($\lambda/k = 5.2$) cases.

The mean free surface in all three small spacing cases is relatively flat, although some undulation is noticeable in the lowest submergence case (Fig. 6.11(a)). In fact two unsteady undular jumps are present in this flow case, slightly upstream of the bars. These jumps establish and disestablish periodically. In the large spacing cases well defined hydraulic jumps are visible between the bars, where the local Froude number approaches unity and the flow becomes critical.

For the low submergence, large spacing case (Fig. 6.11(d)) the elevation predicted by LES C4, is noticeably higher than the measured elevations. The agreement in the medium submergence, large spacing case (Fig. 6.11(e)) appears to be very convincing.

As stated in Section 6.2, point gauge measurements were not possible in the high submergence, large spacing case (Fig. 6.11(f)) due to the extremely dynamic nature of the surface and very significant spanwise components of motion that were observed in the undular jump. This spanwise behaviour is also the reason for the poor agreement between the LES and the PIV in this case. Further validation of the LES is provided by vertical profiles of the spanwise and temporal mean of the streamwise velocity from the LES in Figs. 6.12 and 6.13, alongside the experimental data, which were recorded at the channel centreline using the Nixon propeller meter.

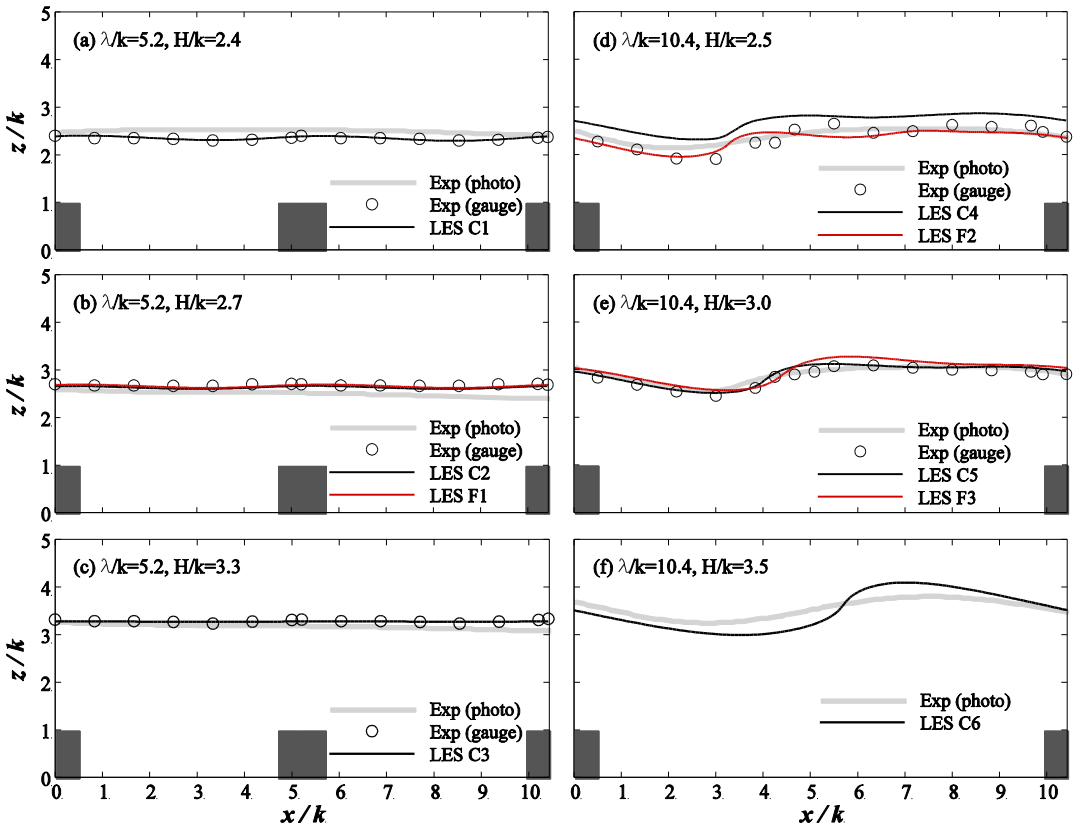

Figure 6.11: Longitudinal profiles of temporal and spanwise mean free surface elevation for three approaches (experimental using PIV, experimental using point gauges and numerical using LES).

The measurement locations are illustrated in Fig. 6.1: two profiles were measured in the λ/k = 5.2 cases and four were measured in the λ/k = 10.4 cases.

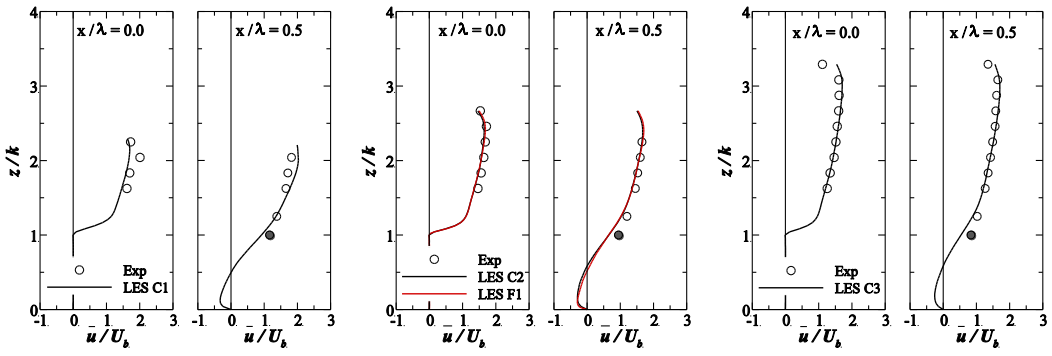

(a) H/k = 2.4 (b) H/k = 2.7 (c) H/k = 3.3

Figure 6.12: Vertical profiles of mean streamwise velocity: λ/k = 5.2 (*Chua et al. 2016*).

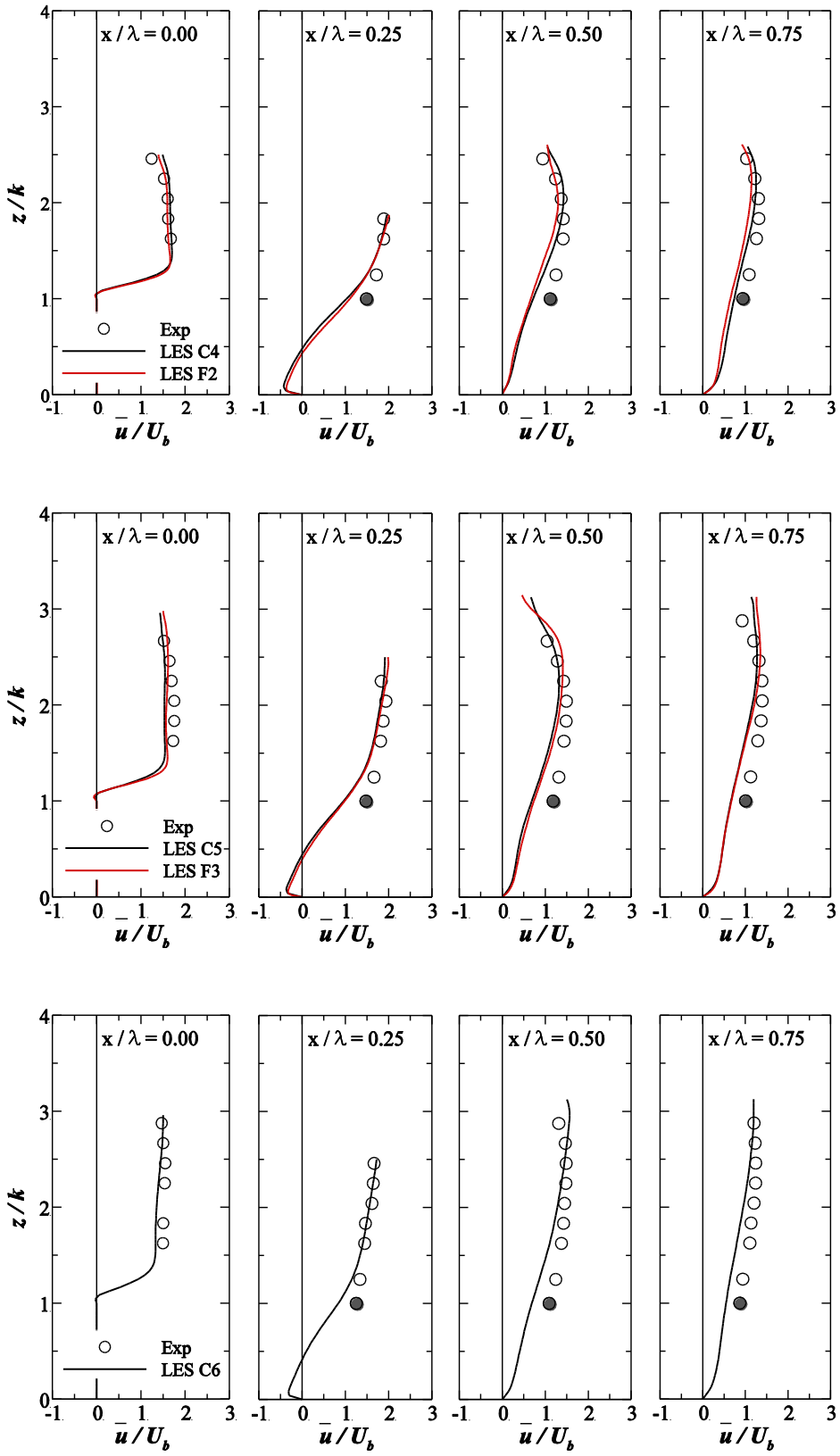

Figure 6.13: Vertical profiles of mean streamwise velocity: λ/k = 10.4 (*Chua et al. 2016*).

In general, the LES data from all six cases show good agreement with the experiments. It should be noted that the experimental data points at $z/k = 1$ have been given a filled symbol to highlight the fact that these measurements are possibly less reliable than the others: these points are located in the shear layer at the top of the roughness elements, and it is known that the Nixon probe is not well suited to regions of high shear and rotation. In the three $\lambda/k = 5.2$ cases significant negative velocity is observed close to the bed in the middle of the cavity, while there is relatively little streamwise variation in the profiles above the roughness top, indicating a skimming type flow with stable or quasi-stable recirculations in the cavities. In each of the larger spacing cases a region of negative mean velocity is observed near the bed at $x/k = 0.25$ but not at $x/k = 0.5$, suggesting that reattachment to the bed occurs in the upstream half of the cavity.

A more detailed understanding of the flow field can be reached by considering the contours of spanwise and temporal mean streamwise velocity that are presented in Fig. 6.14. For the small spacing, low submergence case (Fig. 6.14(a)) the contours reveal that, although the mean water surface is relatively flat, significant velocities are experienced above it. This is due to the periodic establishment and disestablishment of undular hydraulic jumps just upstream of the bars. When such jumps are present the local water surface rises and a non-zero velocity is experienced in the near surface region, contributing to the non-zero mean. Importantly, Fig. 6.14(a) also shows significant streamwise variation of velocity throughout the depth, with local acceleration and deceleration occurring between and above the bars, respectively. In contrast, the two deeper small spacing cases (Figs. 6.14(b) and (c)) are characterised by relatively little streamwise variation of velocity above the bars.

The plots for the large spacing cases, Figs. 6.14(d)-(f), reveal regions of locally-accelerated flow that give rise to local Froude numbers close to 1.0, which in turn lead to dramatic deformations of the water surface and the formation of the hydraulic jumps. The hydraulic jumps are characterised by a small region of negative streamwise velocity produced by the plunging and breaking motion of the standing waves. The plots also confirm the presence of a mean recirculation bubble in the

wake of the upstream bar, as well as a small corner vortex at the leading face of the downstream bar.

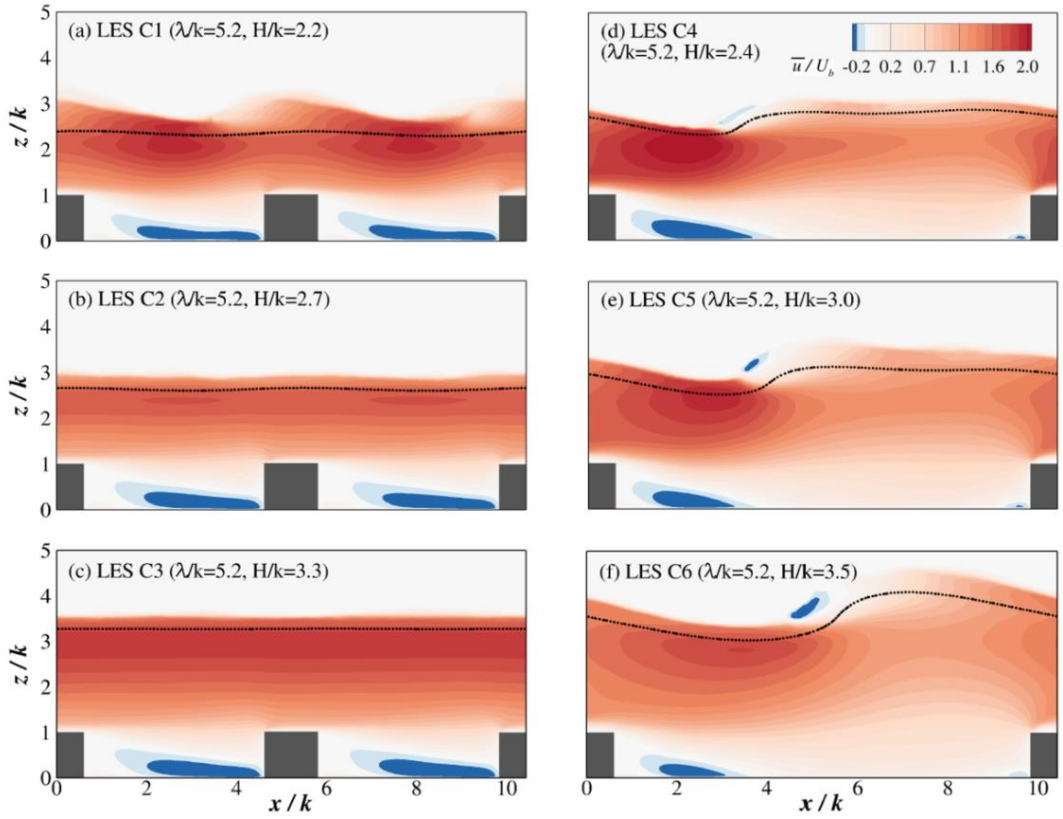

Figure 6.14: Contours of the temporal and spanwise mean normalised streamwise velocity (*Chua et al. 2016*).

Figure 6.15 presents contours of the spanwise and temporal mean of the streamfunction, ψ, for the six cases. Note that positive streamfunction is denoted by solid contour lines while dashed lines denote negative streamfunction. The plots confirm the observations noted above regarding the velocity profiles and contours, and also offer some important additional insights. Firstly, the plots clearly show that the close spacing cases are characterised by large recirculations in the cavities, while the mean flow does reattach to the bed in the large spacing cases. The contours also confirm that the λ/k = 5.2 cases should indeed be classified as transitionally rough, rather than *d*-type, as the streamlines in the shear layer do not quite connect the top of the elements to create a pseudo-smooth wall, as in Stoesser and Rodi (2004) for example.

In fact the $\psi = 0$ contour impinges on the leading faces of the roughness elements, indicating that some form drag will be experienced at the top of the bars and flow in this region will undergo some degree of unsteadiness. Therefore, although the velocity profiles in Fig. 6.12 suggested relatively little streamwise variation in the streamwise velocity, the mean flow field above the roughness crests is not quite homogeneous, as would be the case in a true skimming or psuedo-smooth wall flow. Instead, it can be considered that the bars present a psuedo-rough wall at the crest height, resulting in the streamwise undulations in the streamfunction contours that are visible in the plots.

The lowest submergence case (Fig 6.15(a)) in particular reveals a somewhat wavy streamfunction field and suggests the presence of a fairly strong undular jump at the free surface as discussed above with reference to the contours of mean streamwise velocity. In the λ/k = 10.4 cases the mean flow reattaches to the bed between the bars and can be unequivocally categories *k*-type roughness. The length of the mean recirculation bubble decreases as submergence increases.

Figure 6.16 presents contours of the spanwise and temporal mean of the turbulent kinetic energy, *tke*, normalized on the square of the global friction velocity u_*, for the six flow cases. The mean free surface position is overlaid for reference. A highly turbulent shear layer is present above the roughness crests in the small spacing cases, and in the two higher submergence flows for that spacing (Figs. 6.16(b) and (c)) there appears to be relatively little turbulent activity near the surface.

The low submergence, small spacing case (Fig. 6.16(a)) displays a different character, however, showing high levels of turbulent energy near the surface and a noticeably less turbulent shear layer near the roughness crests compared to the higher submergence cases.

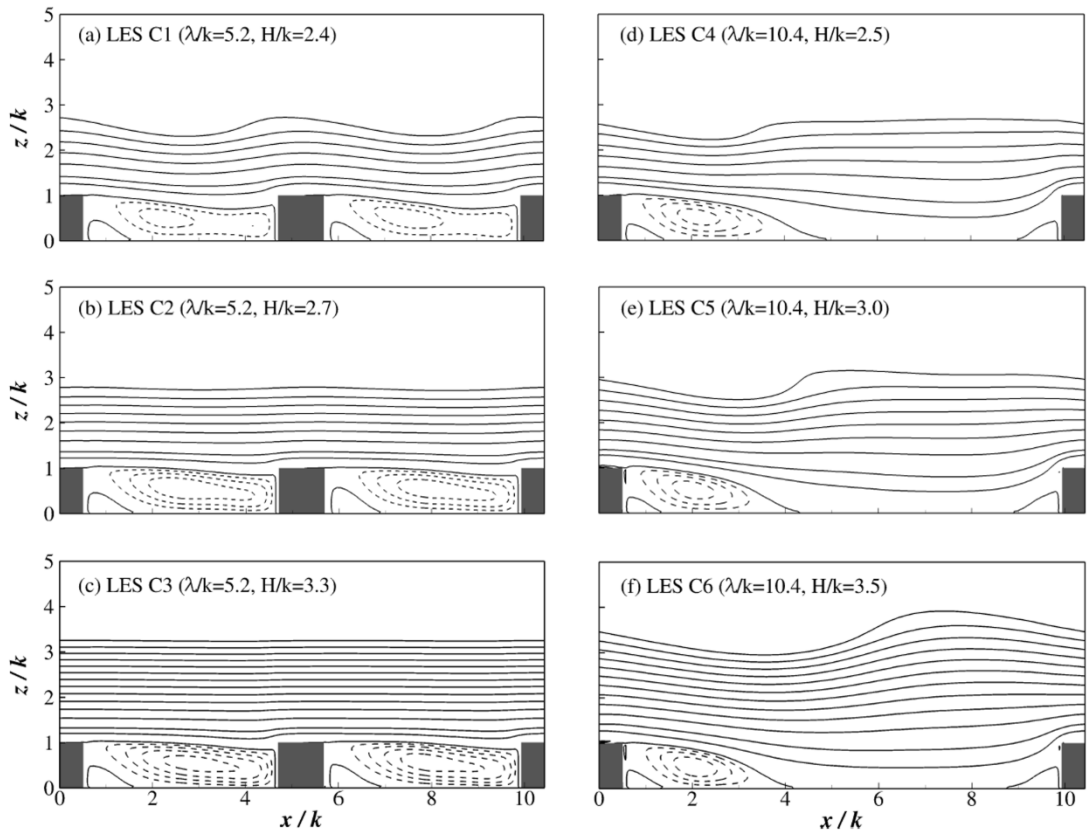

Figure 6.15: Contours of the temporal and spanwise mean of the streamfunction *(Chua et al. 2016).*

The turbulent energy experienced at the free surface is produced by the unsteady undular jumps that were indicated in the corresponding streamfunction plot (Fig. 6.15(a)) and involve the generation of large scale turbulent structures that are convected downstream with the mean flow. The complexity of the flow in the large spacing cases is evident from the *tke* plots. Each case displays a very localised peak in turbulent kinetic energy at the location of the hydraulic jumps that occur between the bars.

All cases under investigation are expected to belong to the class of intermediate submergence (type II) flows as defined by Nikora et al. (2007a). The boundary layer is therefore not expected to comprise the logarithmic layer that occurs in smooth bed and high submergence rough bed flows.

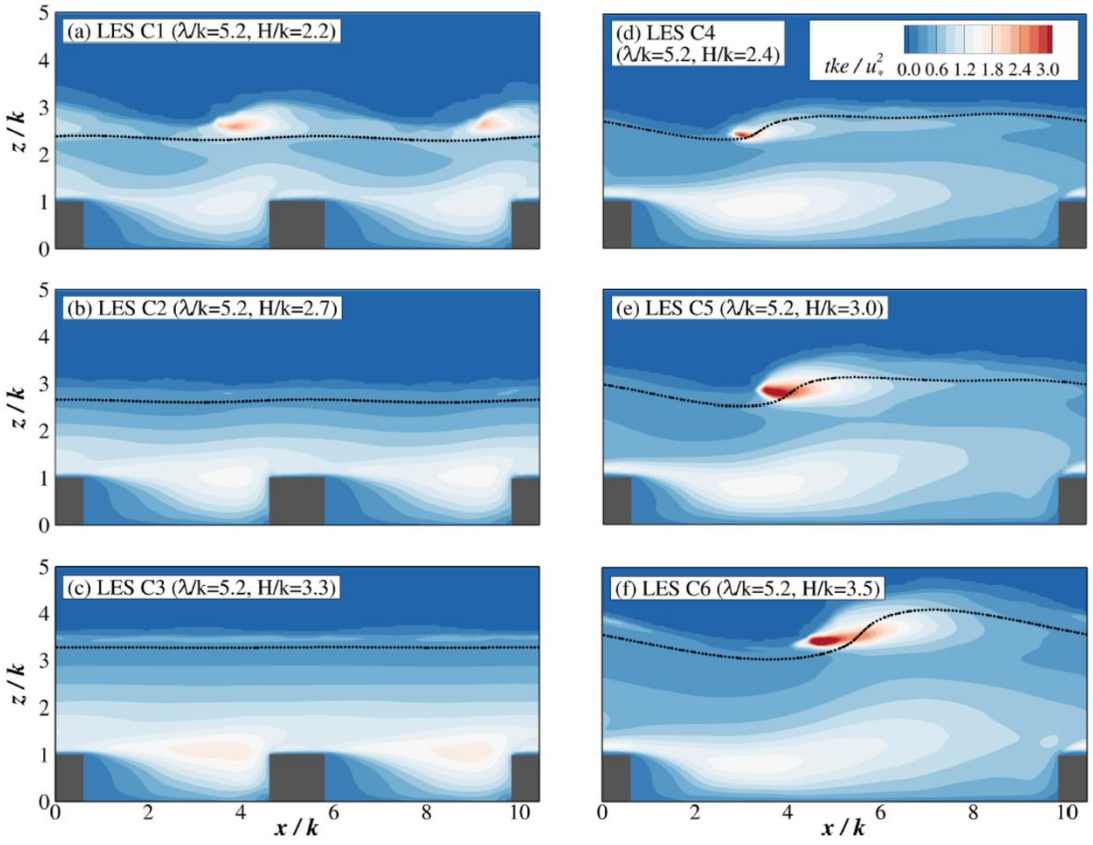

Figure 6.16: Contours of the spanwise mean normalised turbulent kinetic energy *(Chua et al. 2016).*

Figure 6.17 presents profiles of the double-averaged streamwise velocity, $\langle\overline{u^+}\rangle = (\langle\bar{u}\rangle/u_*)$, where u_* is the global shear velocity, the overbar denotes temporal averaging and the triangular brackets denote spatial averaging. In all cases the spatial averaging operation has been performed over the entire computational area. The wall-normal distance in the vertical direction, z^+, is chosen for the x-axis, following the format of the well-known Clauser plot. Cases with the same flow rate (Table 6.1) and therefore similar relative submergence have been plotted together to enable meaningful comparisons. The plots do indeed confirm that no genuine logarithmic layer can be defined for any of the cases, with the possible exception of the high submergence, small spacing case (Fig. 6.17(c)), which does comprise a straight section that extends over a significant section of the water depth and could be considered to be a transitional type I-II flow.

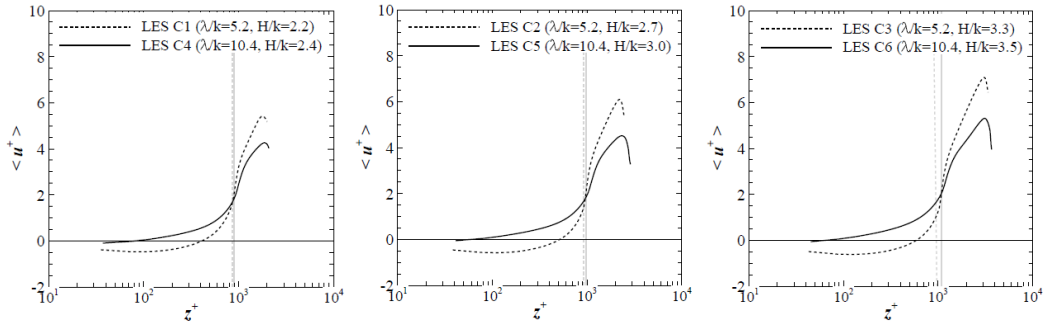

(a) (b) (c)

Figure 6.17: Variation of double averaged streamwise velocity with wall-normal distance *(Chua et al. 2016).*

Figure 6.17 shows that peak double-averaged velocity is significantly higher, and the velocity gradient significantly steeper, in the small spacing cases compared to the large spacing cases. This is due to the constriction on the bulk flow that is imposed by the bars. The pseudo-rough wall, discussed above, that forms at the roughness crests acts to reduce the overall cross-sectional area available to the bulk flow, thereby increasing the velocity in this region relative to the equivalent large spacing case. Note also that the recirculating cavity flow in the small spacing cases produces a significant region of negative double-averaged velocity below $350 \leq z^+ \leq 500$, whereas in the large spacing case only a very small amount of negative flow is observed.

Vertical profiles of normalized spatially-averaged Reynolds shear stress, $\langle\overline{u'w'}\rangle$, are shown in Fig. 6.18. The plots reveal markedly different trends for the small and large spacing cases. For the two small spacing, high submergence cases (Figs. 6.18(b) and (c)), $\langle\overline{u'w'}\rangle$, increases approximately linearly with distance from the free surface, reaching a peak at the height of the roughness crests. This is consistent with other studies of turbulence in rough-bed flows (Bomminayuni and Stoesser 2011, Manes et al. 2007, Singh et al. 2007, Stoesser and Nikora 2008). Below the roughness crests $\langle\overline{u'w'}\rangle$ decreases approximately linearly from the peak until it reaches zero at the channel bed, an observation also made by Stoesser and Nikora (2008). In the corresponding large spacing cases the variation of the Reynolds stress with height is

clearly not linear, either above the crests or below, and displays significant curvature throughout the depth.

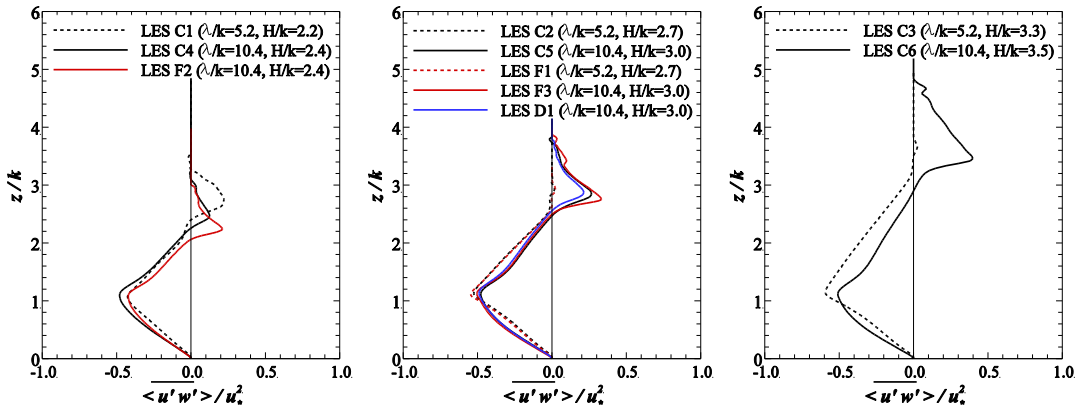

Figure 6.18: Vertical profiles of spatially-averaged Reynolds stress *(Chua et al. 2016)*.

An interesting feature of the Reynolds stress variation in all three large spacing cases, and also in the small spacing, low submergence case, is the portion of significantly positive $\langle\overline{u'w'}\rangle$ that occurs close to the water surface. These positive stresses are the result of turbulence production at the unsteady surface, which has already been discussed with reference to the *tke* contours (Fig. 6.16). The implications of the positive stresses for the streamwise momentum balance and overall hydraulic resistance in the channel can be appreciated by considering Eq. 6.2, which splits the friction factor into additive constituents. The equation indicates that negative spatially-averaged Reynolds stress acts to adds to the friction, while positive stress should acts to reduce it. These results therefore suggest that in open channel flows with unsteady, turbulent free surfaces, turbulent stresses near the surface may produce negative streamwise drag.

Figure 6.19 presents vertical profiles of the spatially-averaged form-induced shear stress,$\langle\tilde{u}\tilde{w}\rangle$, which arises from spatial fluctuations in the mean flow field due to the spatially heterogeneous nature of the rough bed. Examination of Eq. 6.2 reveals that, as with the Reynolds shear stress, a negative spatially-averaged form-induced stress will contribute positively to the overall hydraulic resistance in the channel. The plots show that in all cases $\langle\tilde{u}\tilde{w}\rangle$ increases non-linearly with distance from the bed until it reaches a peak at the height of the roughness crests.

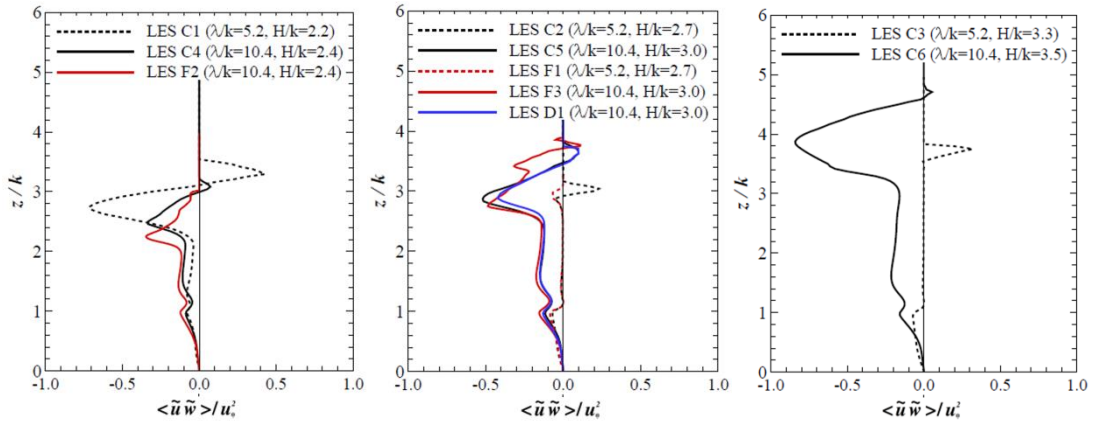

(a) (b) (c)

Figure 6.19: Vertical profiles of spatially-averaged form-induced stress *(Chua et al. 2016).*

This is consistent with previous studies by Manes et al. (2007) and Stoesser and Nikora (2008), for example, who also showed that $\langle \tilde{u}\tilde{w} \rangle$ then decreased fairly rapidly above the roughness crests and remained at zero for the upper part of the water column. Figs 6.19 (b) and (c) confirm that this general trend is also observed in the present study for the two small spacing, high submergence cases. These two cases can therefore be classified as type II (intermediate submergence) flows, since there clearly exists a portion of the depth in which form-induced stresses are not significant. In the other four cases, however, significant non-zero form-induced stresses are observed throughout the whole water depth, indicating that the form-induced sub-layer extends all the way to the free surface. These cases therefore belong to the class of type III (low submergence) flows. Furthermore, the most striking features of Fig. 6.19 are the very large negative stresses in the near-surface region for the four cases in which the surface was observed to be turbulent and unsteady. This result indicates that the standing wave-type responses that were observed at the free surface will make a significant contribution to the overall resistance in the flow.

It is noteworthy that the magnitudes of these negative near-surface peaks in form-induced stress are always larger than the corresponding positive Reynolds stress peaks that are observed in the same region (Fig 6.18): the net contribution of the free surface response to the overall drag is therefore always positive, as confirmed by Fig. 6.20, which presents profiles of the combined (form-induced + Reynolds) stress.

The stress variation above the roughness crests is shown to be approximately linear, even in the large spacing cases in the near-surface region. The plots suggest that extrapolation of the slope from the height of the roughness crests to the x-axis would result in a stress of approximately -1, which is consistent with other studies of flows over rough beds, for example in Manes et al. (2007). The reason that the stress does not reach this value at the bed is the dominance of the form drag in the interfacial sub-layer ($0 \leq z \leq k$), which produces an approximately linear reduction in the contribution of Reynolds and form-induced stresses until they disappear completely at the bed.

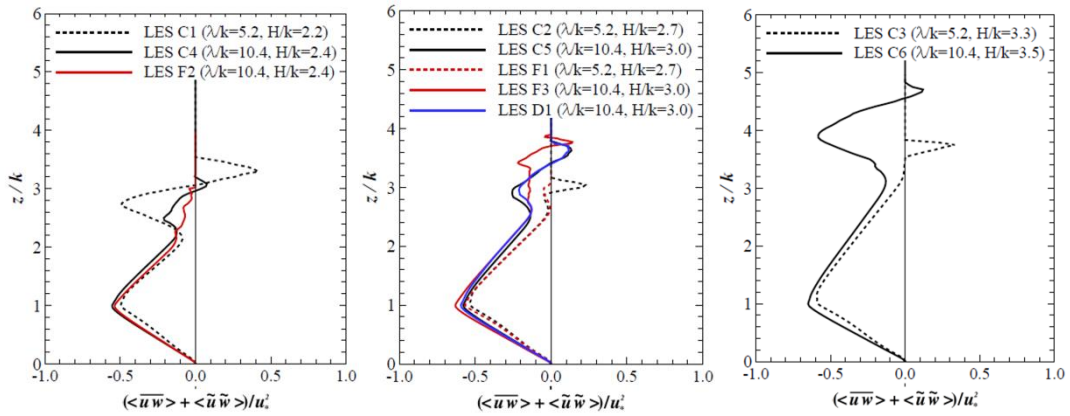

(a) (b) (c)

Figure 6.20: Vertical profiles of combined spatially-averaged Reynolds and form-induced stress *(Chua et al. 2016)*.

Figure 6.21 presents vertical profiles of the span and temporal mean of the pressure differential across a single bar, $(p_u - p_d)$ where p_u and p_d are the pressures on the upstream and downstream faces using two different normalisations. Only the interfacial sub-layer ($0 \leq z \leq k$) is considered. The pressure differential is a measure of the pressure or form drag acting on the individual bars, which is simply the difference between the integrated pressures on each face.

In Fig. 6.21(a) the differential is normalised on $\frac{1}{2}\rho {U_b}^2$, giving a pressure coefficient. The plot shows that the pressure differential, and therefore the form drag, acting on a single bar is consistently higher in the large spacing cases compared to the small spacing cases. The form drag also increases with decreasing relative submergence.

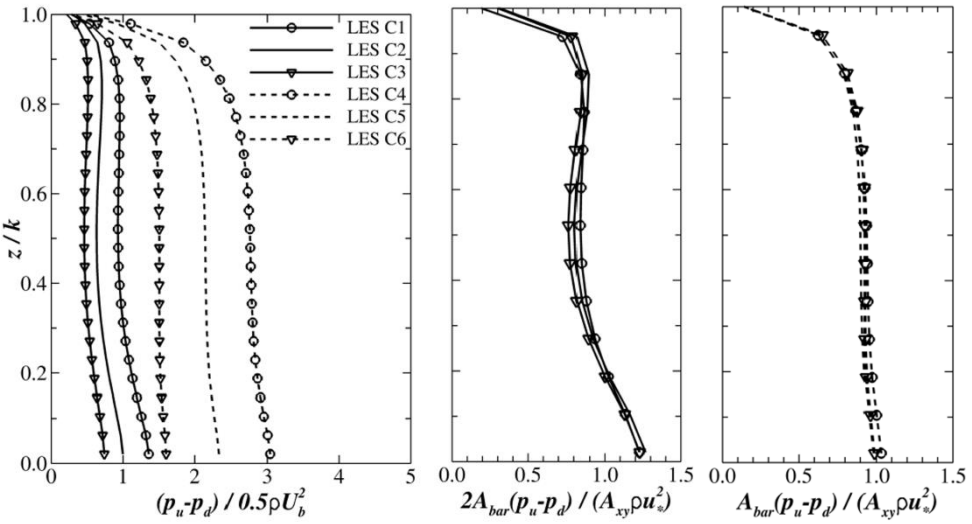

Figure 6.21: Pressure differentials between upstream and downstream faces of a single bar. Note that in plot (b) the pressure force has been multiplied by 2 to account for the presence of two bars in the streamwise direction *(Chua et al. 2016).*

These two findings are consistent with the trends that are illustrated in the plot of friction factor versus relative submergence (Fig. 6.2), and suggest that the form drag is the dominant contributor to overall drag in all cases. The increase in form drag when submergence is reduced is also consistent with the trend for decreasing recirculation bubble length that was observed in the plots of mean streamfunction (Fig. 6.15). Figures 6.21 (b) and (c) present the pressure differential as a force, $A_{bar}(p_u - p_d)$ where $A_{bar}(= k \times L_y)$ is the cross-sectional area presented to the flow by one bar, normalised on the global shear force, $A_{bar}(p_u - p_d)$, where $A_{xy}(= L_x L_y)$ is the planar area on which the shear stress acts. The plots show that the form drag contributes close to 100% of the overall drag in the interfacial sub-layer, and in the small spacing cases (Fig. 21(b)) even contributes more than 100% very close to the bed. This result is explained by the presence of strong recirculation zones with negative flows in the cavities between bars, leading to negative shear stresses that in turn oppose the overall drag force. In order to balance these negative contributions to the overall shear force, some extra form drag must be present close to the bed. In the large spacing cases the form drag is approximately uniform up to a height of approximately 0.8*k*, after which it decreases fairly rapidly.

6.4 CHAPTER SUMMARY

Complementary flume experiments of turbulent open channel flows over bed-mounted square bars at intermediate submergence have been presented. In total six flow cases were investigated, comprising two roughness spacings that correspond to transitional and k-type roughness and three flow rates. The bed slope was held constant for all cases, and relative submergence therefore increased with flow rate. In the experiments the water surface was observed to be very complex and turbulent for the large spacing cases, and comprised a single hydraulic jump between the bars. The streamwise position of the jump varied between the cases, with the distance of the jump from the previous upstream bar increasing with flow rate. The free surface was observed to be less complex in the small spacing cases, particularly for the two higher flow rates, in which case the flow resembled a classic skimming flow. The Darcy-Weisbach friction factor was calculated for all six cases from a simple momentum balance, and it was shown that for a given flow rate the larger bar spacing produces higher resistance.

The predictions of the LES that was achieved by Chua et al. (2016) for the flow over square ribs are shown in good agreement with the experiments in terms of mean free surface position and mean streamwise velocity. The position of the hydraulic jumps was well represented. Contours of spanwise and temporal mean streamlines revealed that the small spacing cases were characterised by classic cavity flow with a quasi-rough wall presented at the height of the roughness crests. In the large spacing cases the length of the mean recirculation bubble was observed to decrease with relative submergence.

Analysis of spatially-averaged Reynolds shear and form-induced stress profiles in the context of the friction factor equation proposed by Nikora (2009) revealed that, in cases in which significant turbulence production occurs at the free surface, the Reynolds stress may be positive near the surface and can therefore act to reduce the overall drag experienced by the flow. Secondly, vertical profiles of form-induced stress revealed significant negative peaks in these complex near-surface regions, resulting from spatial fluctuations in the mean flow due to the presence of hydraulic jumps. The magnitudes of these negative form-induced stresses are larger than those

of the positive Reynolds stresses, and therefore act to produce a net contribution to the overall drag at the free surface. The form drag acting on individual bars was analysed and it was shown that the contribution of form drag is larger in the large bar spacing and increases with decreasing relative submergence.

CHAPTER SEVEN

SUMMARY, CONCLUSIONS AND FUTURE WORK

7 SUMMARY, CONCLUSIONS AND FUTURE WORK

7.1 INTRODUICTON

This chapter presents a summary of research findings, conclusions and future research that is mainly considered as follows:
Section 7.2 summarises devices and equipment that were used to satisfy the research objectives. Section 7.3 presents the findings of the research in open channels, while section 7.4 summarises the research findings on compound channel flows. Recommendations for future research are provided in section 7.5.

7.2 SUMMARY OF RESEARCH FINDINGS

This study aimed of investigating the hydrodynamics of large-scale roughness in open channel flows in different subject areas. Attention was focused on the free surface dynamics at steady uniform flow conditions. Single and compound open channel cross sections were considered for the laboratory experiments. Various devices and equipment were utilized; Nixon probe velocimetry was used for point velocity measurements; point gauge to measure the water depths; particle image velocimetry to monitor and track video images of water surface profiles over rough, steep open channel flow; and a thermal camera was used to capture temperature distribution at the water surface between the main channel and the floodplain in compound open channel flows.

Water surface profile response in the presence of a hydraulic structure, such as lateral channel constriction and submerged bridge constriction as investigated. Flume experiments involved measuring flow depths at different locations in the longitudinal and the lateral directions from the constriction to enrich our understanding on flow dynamics in the presence of such hydraulic structures. This study was achieved in a glass sided flume with a smooth bed of 30 cm width set at a bed slope of 1/2000. Two physical man-made structure models were selected as the lateral constriction and bridge overtopping obstructions. Longitudinal and lateral water surface profiles were examined experimentally and numerically using LES (Kara et al. 2014, Kara et al. 2015) for both constrictions.

Hydrodynamics of one-line vertically oriented cylinders located at the centre of the 30 cm wide flume was considered focusing on drag coefficient calculations. Drag coefficients were calculated and then compared with different analytical expressions derived for an array of vegetation. Experiments were performed to measure the stage–discharge behaviour of open channel flow through one line of vertically-oriented circular rods which mimics in-line vegetation. Two bed slopes were used, along with a range of rod diameters which yielded different spacings between cylinders.

Hydrodynamics of compound channels with vegetated floodplain were investigated. Rigid emergent cylindrical rods were used to simulate the vegetation. Two vegetation configurations – wholly vegetated floodplain and one-line vegetation were considered and the hydraulic properties are compared to those of a smooth unvegetated compound channel. Particular attention was given to the effect of vegetation density on the rating curve, drag coefficient and spanwise profiles of streamwise velocity. Flow resistance was estimated using the approach introduced by Petryk and Bosmajian and the results were in agreement with other experimental studies. It was shown that the vegetation configuration significantly influences the velocity in the main channel and in the case of one line vegetation the floodplain velocity is higher than for unvegetated channel for a given flow rate. Spanwise velocity profiles exhibit markedly different characters in the one line and wholly vegetated configuration.

Free surface flow over square bars at low and intermediate relative submergence was achieved with a complimentary series of flume experiments of flow over square bars of dimensions 12mm x 12mm x 300mm that were attached along the entire flume length with two spacing (pitch to pitch) of 6.25 cm and 12.5 cm. Experiments were carried out with a range of flow rates of 1.6 l s^{-1} to 10 l s^{-1} with flume bed slopes of 0.001, 0.005, and 0.02 with two roughness spacing of 5.2 and 10.4. Monitoring water surface profiles over rough beds was carried out using a PIV system. Particle image velocimetry was used to capture video images to monitor the free surface profiles of the flow over the square bars for two bed slopes (1:50 and 1:200), two roughness spacing (H/k = 5.2 and H/k = 10.4) and three flow rates (Q= 1.7, 2.5 and 4.0 l s^{-1}).

The results of the longitudinal water surface profiles are expressed as mean-averaged of 1500. Point gauge measurements were also carried out between two bars in the experiments for the bed slope 1:50. Measurement of time-averaged longitudinal stream-wise velocities of a steady, fully developed flow in rough open channels were carried out for the entire water depth in the inner and the outer regions of the turbulent boundary layer over a rough surface. With bed slope (S = 0.02) and roughness spacings (λ/k = 5.2 & 10.4), velocity measurements for large roughness spacing (λ/k = 10.4) were taken at four sections, over the rib and three downstream of the rib, which showed that the vertical point velocity values over the mid width of the rib element are less than that at a section 3.125 cm down-stream of the rib centreline for all the flow rates used. As the roughness elements are closer, i.e. λ/k = 5.2, two profiles were measured. The aim was to explore the effect of flow depth and roughness spacing on free surface flow dynamics at low and intermediate relative submergence. Variation of friction factor with relative submergence for the flume experiments was compared with Bathurst (1981 and 1983)'s equation.

Dynamics of the water surface at the interface between the main channel and the floodplain was assessed for a compound channel section using a thermal camera SC 640 with two vegetation configurations - wholly vegetated floodplain and one-line vegetation for the aims; (i) to visualize and evaluate such technique in capturing thermal shear layers at the interface between the main channel and the floodplain, (ii) to understand the effect of vegetation density and configuration and flow depth on the thermal shear layer thickness and its evolution along the floodplain-main channel edge in the compound channel.

A review of the main results obtained and conclusions derived from this study are presented as follows:

7.3 CONTRIBUTIONS TO OPEN CHANNEL HYDRODYNAMICS RESEARCH

Considering the aims outlined at the beginning of this chapter, the achievements of this study can be classified into three major subject areas which are (a) water surface response to flow through bridge openings, (b) hydrodynamics of one-line vegetation

in open channel flows and (c) free surface flow over square bars with low and intermediate relative submergence.

(a) Water surface response to flow through bridge openings

With the lateral constriction, longitudinal water depth measurements showed that the water backed up quite significantly upstream of the structure. A short distance upstream of the structure, the flow starts to accelerate and the water surface drops rapidly and significantly. The flow creates a very distinct dip in the area of localised recirculation as a result of flow separation at the leading edge of the constriction. The water surface recovers markedly approximately half way through the constriction in the form of a standing wave. Towards the end of the constriction, the water surface drops further quite significantly. The flow downstream of the constriction is subjected to a large, very shallow recirculation zone just behind the abutment, which contracts and accelerates the flow.

The cross-sectional profiles downstream of the constriction exhibit a very significant jump in the water surface. The recirculation zone downstream of the constriction is at a significantly lower elevation than the rest of the channel. The water that rushes out of the constricted area has a significant amount of stream wise momentum prohibiting the filling of the recirculation zone with fluid.

The result of LES shows reasonable agreement with the experimental data for both the longitudinal and lateral water surface profiles. However, with the longitudinal profiles in close proximity to the structure, LES shows a weak agreement between the simulated and the measured values due to the lack in mesh resolution of the simulation.

With the bridge overtopping simulation, three types of flows were monitored; subcritical flow upstream of the bridge, critical flow state on the deck of the bridge due to the deck acting as a broad crested weir, and supercritical flow downstream of the deck. The flow recovers to subcritical in the form of an undular hydraulic jump. The simulated longitudinal water surface profiles are in good agreement with the measured data. However, an inconsistency between the simulation and the observed

data was found just upstream of the bridge because the deck of the numerical simulation is slightly higher than the one used in the experiment. The discrepancy between the numerical and the observed values belongs to the difficulty of point-gauge measurements at high turbulence.

Lateral water surface profiles were simulated in good agreement with the observed data, except for the profiles upstream of the bridge; the numerically predicted profiles are slightly higher than the observed ones.

(b) Hydrodynamics of one-line vegetation in open channel flows

For a series of uniform flows the drag coefficient was calculated based on the measured uniform flow depth and under consideration of the bed friction. Then the most prominent empirical equations for calculating the drag coefficient, C_D, of vegetation have been employed to predict C_D for the experiments of in-line vegetation (Tanino and Nepf 2008, Kothyari et al. 2009, Cheng and Nguyen 2011, Cheng 2013). Tanino and Nepf's and Kothyari's equations consistently overestimate the measured drag coefficients but match the overall trend of an increase of C_D with increasing stem Reynolds number. Cheng's and Cheng and Nguyen's expressions overestimate vegetation drag for low to medium values of Re_D whilst a good match has been achieved for the higher stem Reynolds numbers. On the other hand the latter two expressions do not reflect the trend of an increase of C_D with increasing stem Reynolds number. The results show that varying the diameter of the rigid emergent vegetation affects significantly flow resistance.

(c) Free surface flow over square bars with low and intermediate relative submergence

From the experiments it is demonstrated that for a fixed rib height, increasing the flow depth resulted in a decrease of the friction factor. For a constant bed slope, increasing the spacing between rib elements causes an increase in the friction factor, while for a constant roughness spacing, increasing the bed slope causes an increase in friction factor.

The friction factor was compared with the flume data from Bathurst (1985). The data lie within the spread of Bathurst data and agree very well with the general trend of decreasing resistance with increasing relative submergence.

It has been shown that for a given discharge (Q) and roughness spacing (λ/k), the water depth (H) decreases as the bed slope (S) increases, whilst increasing the roughness spacing causes an increase in the water depth for all the selected bed slopes.

The impact of roughness spacing on the dynamics of the free surface flow is such that for a constant roughness spacing of λ/k = 10.4 and a bed slope of 0.02, strong well defined hydraulic jumps with air bubbles between the bars were observed, while weak hydraulic jumps and no trace of the air bubbles were in existence for the same bed slope with roughness spacing λ/k = 5.2. This ensures that roughness spacing plays a crucial role in the configuration of the water surface profile and then on the friction factor. The free surface was observed to be less complex in the small spacing cases, particularly for the two higher flow rates, in which case the flow resembled a classic skimming flow.
The mean free surface in all three small spacing submergence ratios is relatively flat, while some undulation is observable in the lowest submergence case. For the large spacing submergence cases, increasing the submergence ratio, H/*k*, noticeable effects the free surface topology.

The results of the spanwise mean of the temporal mean water surface was also predicted by the LES (Chua et al. 2016) and the mean water surface that were measured using PIV and the point gauge were compared and showed good agreements. The agreement between experiments and LES is particularly good for the small spacing (λ/k = 5.2) cases.

Velocity measurements showed that velocity profiles are closer to each other, or have the same values at the location over the rib element section and in the section down-stream of the rib centreline at a distance of 3.125 cm. Vertical velocity profiles with roughness spacing of 10.4 and a bed slope (S = 0.005) in the four sections showed that, the curves are of much smaller than that with the bed slope of 0.02.

However, these velocity profiles coincide in the case of bed slope of 0.005 and roughness spacing of 5.2 as shown in Fig. 0-16 in Appendix I.

Large-eddy simulations provided contours of mean velocity, mean streamfunction and turbulent kinetic energy and revealed the effect of the roughness geometry on the water surface response. For the low submergence cases dynamic responses were observed at the surface, including the presence of hydraulic jumps which contribute significantly to the overall streamwise momentum balance. Analysis of spatially-averaged Reynolds shear and form-induced stress profiles in the context of the friction factor equation proposed by Nikora (2009) revealed that, in cases in which significant turbulence production occurs at the free surface, interesting results, the Reynolds stress may be positive near the surface and can therefore act to reduce the overall drag experienced by the flow. Secondly, vertical profiles of form-induced stress revealed significant negative peaks in these complex near-surface regions, resulting from spatial fluctuations in the mean flow due to the presence of hydraulic jumps. The magnitudes of these negative form-induced stresses are larger than those of the positive Reynolds stresses, and therefore act to produce a net contribution to the overall drag at the free surface. The form drag acting on individual bars was analysed and it was shown that the contribution of form drag is larger in the large bar spacing and increases with decreasing relative submergence.

7.4 CONTRIBUTIONS TO COMPOUND OPEN CHANNEL FLOW RESEARCH

At shallow, uniform flow a clear impact of floodplain vegetation on the rating curve is found for all vegetation densities and configurations.

The inclusion of a wholly-vegetated floodplain produces a marked increase in water depth compared to the unvegetated case for a given flow rate. Increasing the vegetation density, results in further increase in water levels. The water level increases with flow rate in all cases appears to increase linearly with flow rate when the floodplain is vegetated contrary to the case for the unvegetated channel case.

The inclusion of one-line vegetation at the interface between main channel and floodplain produces a much smaller increase in water depth compared to the wholly-vegetated floodplain cases. That is because flow blockage, for the one-line case is naturally much smaller than in the full-vegetated case. Water depth is noticeably more sensitive to changes in length-to-diameter for one-line vegetation than to changes in vegetation density for a wholly-vegetated floodplain.

Estimation of the drag coefficient for the wholly vegetated floodplain which is based on equating the gravitational force to the drag force exerted by the vegetation elements was analysed and compared with the most applicable empirical equations. These equations are Tanino and Nepf (2008), Kothyari et al. (2009) and Cheng and Nguyen (2011). The experimental results showed good agreement with these equations. The drag coefficient displays a high degree of sensitivity to changes in both Reynolds number and vegetation density.

Based on point velocity measurements, for the wholly-vegetated and unvegetated floodplains the spanwise profiles follow an S-shaped curve but for one-line vegetation the profiles exhibit a distinct dip at the interface between the main channel and the floodplain. Lateral velocity profiles showed two sections of uniform velocity namely vegetated and open channel sections and transitional region. The highest velocity differences between the main channel and the floodplain are observed in the presence of roughness differences between these two sections. Flow velocity above a wholly-vegetated floodplain is noticeably lower than that above an unvegetated floodplain

With a one-line vegetation configuration, strong velocity gradients were seen in the rod area which means that these rods suppress transferring momentum from the main channel to the floodplain for all rod diameters and flow rates, while these velocity gradients were clearly shown to be of less magnitude with the wholly vegetated floodplain. The inclusion of one-line vegetation produces higher velocities above the floodplain compared to the unvegetated case.

Fully turbulent developed flows were observed for the compound channel sections with vegetated and non-vegetated floodplains.

Using image processing techniques together with Matlab software allows visualisation of the shear layer that forms at the interface between the main channel and the floodplain of a compound channel flow. The thermal shear layer at the interface of the vegetated floodplain was shown to be influenced by the flow depth variation and with vegetation density and distribution in comparison to the non-vegetated case due to the drag by vegetation. In addition, for the vegetated floodplain the penetration thickness inside the main channel is greater than that on the floodplain. However, for the non-vegetated floodplain, the penetration thickness was observed to be of equal magnitude inside the main channel and the floodplain and influenced by the flow depth variation. For a given vegetation density on the floodplain, increasing the discharge leads to an elongated shear layer. With a one-line of vegetation, the biggest diameter results in the shortest shear layer elongation, while for the wholly vegetated floodplain, the highest vegetation density results in a wider shear layer distribution.

Time-averaged temperature distribution results were analysed and examined to clarify how temperature dissipates longitudinally and transversely along the stream-wise direction (x-y plane). A steep variation of the temperature values was monitored in the lateral direction for all the tests and a gradual variation of the temperature was observed in the first quarter of the shear layer length in the stream-wise direction. Steep variation of water temperature was observed in all the experiments. The rapid decrease in water temperature from the peak to a value of 23 (laboratory water temperature) refers to the turbulent mixing between the compound channel sections.

Inferring flow properties from the thermal camera temperature series were achieved for the wholly vegetated floodplain to characterize the development of eddies in the wake of the rods. Results showed that two types of vortices (shear layer vortices and von-Karman street vortices) can be distinguished. Shear layer vortices were monitored at the outer edge of the rods, while von Karman vortices are tracked behind the rod with a counter rotating vortex pair. With a rod diameter of D = 2.5 cm the von Karman vortices were shown, while with rod diameter of D = 5.0 cm the interaction of the stream-wise velocity and span-wise velocity between the rods inhibit these types of vortices. More details about the eddy properties were analysed

from the five selected points in the wake region and showed successive peaks along the time series curve. Fast Fourier transform of the time series of temperature for the selected five points showed the energy of the eddies is small at high frequency, while for small frequencies there are large eddies.

Mass and momentum transfer between the main channel and the floodplain due to the effects of the transverse depth variation and the variation of bed roughness. This results in velocity gradients between the main channel and the floodplain and expressed in the lateral distribution of the depth averaged-velocity diagrams.

7.5 RECOMMENDATIONS FOR FUTURE RESEARCH

This research requires further assessment and additional research of:

Dynamics of shear layers in compound channel flows

- In order to further understand the dynamics of shear layers at the interface between the main channel and the floodplain in compound channel flows, more experiments are needed based on particle image velocimetry. These measurements may focus on the instantaneous velocity at the water surface between the main channel and the floodplain to enrich our understanding of flow dynamic properties of flow in compound channels. Investigating the flow properties at the water surface enable comparison between the shear layers that can be extracted by the thermal camera with the PIV results and to explore more details about the vortices that are generated behind the neighbouring cylinders located on the floodplain.
- Using the PIV in tracking the water surface shear layers (vortices) enables us to visualize and evaluate the impact of vegetation density on the interaction of the vortices that cannot be explained by the thermal camera.
- Flow dynamics in the presence of one-line vegetation are needed. The influence of vegetation elements on each other may be explained by the shading factor, S_F. The impact of the shading factor has been explained by Noat et al. (1996) expression and Nepf (1999) diagram. These are not enough to describe the impact of vegetation elements by the shading factor. This is

partly due to limited literature. More experiments are therefore required to investigate the impact of shading factor in the presence of one-line of vertically-oriented circular rods at different aspect ratios. The rod diameters will be investigated both in a single and compound channel flows at a different locations from the sidewall of the stream.

Free surface flow over square bars with low relative submergence

- Accurate estimation of flow resistance in mountain streams requires adequate evaluation of the resistance imposed by bed morphology on the flow. One of the scenarios that should be studied in the hydraulic laboratory is to use more natural 3D large-scale roughness in different arrangements and with different concentrations. Turbulence characteristics of the flow in the area of the rough elements can be extracted by PIV system to measure the flow velocity field. This enables us to understand the effects of bed roughness arrangement and relative submergence on the flow properties.
- Water surface profile over rough beds can be monitored using a thermal camera and a tracer of hot water. An adequate number of video files are required to capture the water surface profile of the running water from the flume sidewall. The tracer can be applied by heating the running water to a degree more than that of the hydraulic laboratory environment.
- Thermal camera can be used to deduct many physical hydraulic phenomena, for example, kolk boils at the water surface in rough open channels, and kolk boils in the presence of lateral constriction such as groins. In addition, PIV can be used to extract more details about these vortices that are generated due to the exchange of momentum between the roughness layers and the overlying flow.

Water surface response to flow through bridge openings

- The use of a submerged bridge can be expanded for more case studies. The bridge opening was considered, in such a way that 74% of the flow is run under the deck. The flow running under the deck can be examined with

different gate openings, such as 50%, 60% and 90%. In addition, an elliptical pier can be used instead of rectangular one.

PUBLICATIONS RELATED TO THIS WORK

Chapter **2** of this thesis will be also referenced in the text as Kara et al. (2014) and Kara et al. (2015) have been published as:

Kara, S., **Mulahasan**, S., Stoesser, T. and Sturm, T. W. (2014) 'Water surface response to flow through bridge opening' River Flow, the 7th International Conference on Fluvial Hydraulics, 3-5 September, Lausanne, Switzerland, Pages 693–699, Print ISBN: 978-1-138-02674-2, eBook ISBN: 978-1-4987-0442-7, DOI: 10.1201/b17133-95'.

Kara, S., Stoesser, T., Sturm, T. W. and **Mulahasan**, S. (2015) 'Flow dynamics through a submerged bridge opening with overtopping', Journal of Hydraulic Research, 53(2), 186-195.

Chapter **3** of this thesis will be also referenced in the text as Mulahasan et al. (2015) and has been published as:

Mulahasan, S., Stoesser, T. and Alvarez, F. (2015) 'Visualization of shear layers in compound channel flows', 10th Pacific Symposium on Flow Visualization and Image Processing Naples, Italy, 15-18 June, Paper ID: 25.

Mulahasan, S., Stoesser, T., Alvarez, F. and Fraga, B. 'Dynamics of mixing shear layers in compound channel flows' (in press).

Chapter **4** has been submitted to International Journal of River Basin Management:

Mulahasan, S. and Stoesser, T. 'Flow resistance of in-line vegetation in open channel flow'.

Chapter **5** has been submitted to Journal of Irrigation and Drainage Engineering as:

Mulahasan, S., Stoesser, T. and McSherry, R. 'Hydrodynamics of compound channels with vegetated floodplain'.

Chapter **6** has been submitted to Journal of Hydraulic Research and will be also referenced in the text as Chua et al. (2016):

Chua, K., McSherry, R., **Mulahasan**, S. and Stoesser, T. 'Free-surface flow over square bars with low relative submergence' (submitted).

REFERENCES

Aberle, J. and Järvelä, J. (2013) 'Flow resistance of emergent rigid and flexible floodplain vegetation', *Journal of Hydraulic Research,* 51(1), 33-45.

Aberle, J., Koll, K. and Dittrich, A. (2008) 'Form induced stresses over rough gravel-beds', *Acta Geophysica,* 56(3), 584-600.

Azevedo, R., Leal, J. B. and Rojas-Solórzano, L. (2012) 'Influence of vegetation on compound-channel turbulent field' in *River Flow 2012*, CRC Press, 209-216.

Bathurst, J. (1985) 'Flow resistance estimation in mountain rivers', *Journal of Hydraulic Engineering,* 111(4), 625-643.

Bathurst, J. (2002) 'At-a-site variation and minimum flow resistance for mountain rivers', *Journal of Hydrology,* 269(1), 11-26.

Bathurst, J., Li, R. M. and Simons, D. B. (1981) 'Resistance equation for large-scale roughness.', *Journal of the Hydraulics Division-ASCE, ,* 107(12), 1593–1613.

Bathurst, J. C. (1978) 'Flow resistance of large-scale roughness. ', *Journal of the Hydraulics Division-ASCE,,* 104(12), 1587–1603.

Ben-sheng, H., Guan-wen, L., Jing, Q. and Shu-zhong, L. (2002) 'Hydraulics of compound channel with vegetated floodplain', *Journal of Hydrodynamics,* Ser.B(1), 23-28.

Bennett, S. J. (2004) *Effects of emergent riparian vegetation on spatially averaged and turbulent flow within an experimental channel, Riparian vegetation and fluvial geomorphology*.

Biemiiller, M., Meyer, L. and Rehme, K. (2012) 'Large eddy simulation and measurement of the structure of turbulence in two rectangular channels connected by a gap', *Engineering Turbulence Modelling and Experiments-3*, 249-258.

Biglari, B. and Sturm, T. (1998) 'Numerical modeling of flow around bridge bbutments in compound channel', *Journal of Hydraulic Engineering,* 124(2), 156-164.

Bomminayuni, S. and Stoesser, T. (2011) 'Turbulence statistics in an open-channel flow over a rough bed', *Journal of Hydraulic Engineering,* 137(11), 1347-1358.

Bray, D. I. (1979) 'Estimating average velocity in gravel-bed rivers', *Journal of the Hydraulics Division,,* Vol. 105, (No. 9,), pp. 1103-1122.

Carling, P., Cao, Z., Holland, M., Ervine, D. and Babaeyan-Koopaei, K. (2002) 'Turbulent flow across a natural compound channel', *Water Resources Research,* 38(12), 6-1-6-11.

Chanson, H. (2009) 'Current knowledge in hydraulic jumps and related phenomena. A survey of experimental results', *European Journal of Mechanics - B/Fluids,* 28(2), 191-210.

Chanson, H. and Brattberg, T. (2000) 'Experimental study of the air–water shear flow in a hydraulic jump', *International Journal of Multiphase Flow,* 26(4), 583-607.

Chen, G., Huai, W., Han, J. and Zhao, M. (2010) 'Flow structure in partially vegetated rectangular channels', *Journal of Hydrodynamics, Ser. B,* 22(4), 590-597.

Cheng, N. (2013) 'Calculation of drag coefficient for arrays of emergent circular cylinders with pseudofluid model', *Journal of Hydraulic Engineering,* 139(6), 602-611.

Cheng, N. and Nguyen, H. (2011) 'Hydraulic radius for evaluating resistance induced by simulated emergent vegetation in open-channel flows', *Journal of Hydraulic Engineering,* 137(9), 995-1004.

Chequer, F. M. D., de Oliveira, D. P., Ferraz, E. R. A., de Oliveira, G. A. R., Cardoso, J. C. and Zanoni, M. V. B. (2013) *Textile dyes: dyeing process and environmental impact,* INTECH Open Access Publisher.

Chrisohoides, A., Sotiropoulos, F. and Sturm, T. W. (2003) 'Coherent structures in flat-bed abutment flow: computational fluid dynamics simulations and experiments', *Journal of Hydraulic Engineering,* 129(3), 177-186.

Chua, K., McSherry, R., Stoesser, T. and Mulahasan, S. (2016) 'Free surface flow over square bars at low and intermediate relative', *Hydraulic research,* Research paper, Manuscript ID: TJHR-2016-0058, 1-21.

Coleman, S., Nikora, V., McLean, S. and Schlicke, E. (2007) 'Spatially Averaged Turbulent Flow over Square Ribs', *Journal of Engineering Mechanics,* 133(2), 194-204.

Cui, J., Patel, V. C. and Lin, C.-L. (2003) 'Large-eddy simulation of turbulent flow in a channel with rib roughness', *International Journal of Heat and Fluid Flow,* 24(3), 372-388.

Dey, S. and Das, R. (2012) 'Gravel-Bed Hydrodynamics: Double-Averaging Approach', *Journal of Hydraulic Engineering,* 138(8), 707-725.

Dietrich, W. E. and Whiting, P. (1989) 'Boundary shear stress and sediment transport in river meanders of sand and gravel', *In S. Ikeda & G. Parker (Eds.), River meandering,* Water Resour. Monogr., 12 (pp. 1–50). Washington, D.C., AGU.

Djenidi, L., Antonia, R., Amielh, M. and Anselmet, F. (2008) 'A turbulent boundary layer over a two-dimensional rough wall', *Experiments in Fluids,* 44(1), 37-47.

Djenidi, L., Elavarasan, R. and Antonia, R. (1999) 'The turbulent boundary layer over transverse square cavities', *Journal of Fluid Mechanics,* 395, 271-294.

Ferreira, R. M. L., Amatruda, M., Simao, J., Ricardo, A. M., Franca, M. J. and Di Cristo, C. (2010) 'Inuence of bed morphology on double-averaged turbulent quantities in low submergence gravel bed flows', *In A. Dittrich et al. (Eds.), River Flow 2010 (pp. 67–74), Braunschweig, Germany.*

Fraselle, Q., Bousmar, D. and Zech, Y. (2010) 'Diffusion and dispersion in compound channels: The role of large scale turbulent structures', *First IAHR European Congress*, 1-6.

Giménez-Curto, L. A. and Corniero Lera, M. A. (1996) 'Oscillating turbulent flow over very rough surfaces', *Journal of Geophysical Research: Oceans,* 101(C9), 20745-20758.

Giménez-Curto, L. A. and Corniero Lera, M. A. (2003) 'Highest natural bed forms', *Journal of Geophysical Research: Oceans,* 108(C2), 1082, 3046, 28, 1-7.

Gotvald, A. J. and McCallum, B. E. (2010) 'Epic flooding in Georgia. USGS Fact Sheet: 2010-3107'.

Guo, J., Zhang, T. C., Admiraal, D. M. and Bushra, A. (2009) 'Computational design tool for bridge hydrodynamic loading ininundated flows of Midwest Rivers', *Report # MATC-UNL: 227.*

Hamidifar, H. and Omid, M. (2013) 'Floodplain vegetation contribution to velocity distribution in compound channels', *Journal of Civil Engineering and Urbanism,* 3(6), 357-361.

Hamimed, A., Nehal, L., Benslemani, M. and Khalid, A. (2013) 'Contribution to the study of the flow resistance in a flume with artificial emergent vegetation', *Layhyss Journal,* 15, 55-63.

Hey, R. D. (1979) 'Flow resistance in gravel-bed rivers', *Journal of the Hydraulics Division,,* Vol. 105,(No. 4,), pp. 365-379.

Hirschowitz, P. M. and James, C. S. (2009) 'Conveyance estimation in channels with emergent bank vegetation', *Water SA,* 35(5), 8.

Hong, S.-H., Sturm, T. W. and Stoesser, T. (2014) 'Prediction of clear-water abutment scour depth in compound channel for extreme hydrologic events', *Journal of Hydraulic Engineering, ASCE, under review*.

Huthoff, F. (2007) *Modeling hydraulic resistance of floodplain vegetation. PhD thesis,* University of Twente.

Huthoff, F. and Augustijn, D. (2006) 'Hydraulic resistance of vegetation: Predictions of average flow velocities based on a rigid-cylinders analogy', *Final Project Report (Project no. U2/430.9/4268)*.

Ikeda, T. and Durbin, P. A. (2007) 'Direct simulations of a rough-wall channel flow', *Journal of Fluid Mechanics,* 571, 235-263.

Ismail, Z. and Shiono, K. (2006) *"The effect of vegetation along cross-over floodplain edges on stage discharge and sediment transport rates in compound meandering channels"Proceedings of the 5th WSEAS International Conference on Environment Ecosystems and Development, Venice, Italy,* translated by.

Jahra, F., Kawahara, Y., Hasegawa, F. and Yamamoto, H. (2011) 'Flow–vegetation interaction in a compound open channel with emergent vegetation', *International Journal of River Basin Management,* 9(3-4), 247-256.

James, C., Birkhead, A., Jordanova, A. and O'sullivan, J. (2004) 'Flow resistance of emergent vegetation', *Journal of Hydraulic Research,* 42(4), 390-398.

James, C. S., Goldbeck, U. K., Patini, A. and Jordanova, A. A. (2008) 'Influence of foliage on flow resistance of emergent vegetation', *Journal of Hydraulic Research,* 46(4), 536-542.

Jarvela, J. (2004) 'Determination of flow resistance caused by non-submerged woody vegetation', *Intl. J. River Basin Management,* 2(1), 61-70.

Järvelä, J. (2002) 'Determination of flow resistance of vegetated channel banks and floodplains', *River Flow 2002, International Conference on Fluvial Hydraulics. September 4 - 6, 2002, Louvain-la-Neuve, Belgium. Swets & Zeilinger, Lisse. p. 311-318. ISBN 9058095096.,* In: Bousmar, D. & Zech, Y. (eds.) 2002.

Järvelä, J. (2008) 'Flow resistance of flexible and stiff vegetation: a flume study with natural plants', *Journal of Hydrology,* 269(1–2), 44-54.

Jiménez, J. (2004) 'Turbulent flows over rough walls', *Annu. Rev. Fluid Mech.,* 36, 173-196.

Jirka, G. H. and Uijttewaal, W. S. J. (2004) 'Shallow Flows', *Research Presented at the International Symposium on Shallow Flows, Delft, Netherlands, 2003*, 1-684.

Jordanova, A. A., James, C. S. and Birkhead, A. L. (2006) 'Practical estimation of flow resistance through emergent vegetation', *Proceedings of the ICE-Water Management,* 159(3), 173-181.

Kara, S., Mulahasan, S., Stoesser, T. and Sturm, T. W. (2014) 'Water surface response to flow through bridge openning' River Flow, the 7th International Conference on Fluvial Hydraulics, 3-5 September, Lausanne, Switzerland, Pages 693–699, Print ISBN: 978-1-138-02674-2, eBook ISBN: 978-1-4987-0442-7, DOI: 10.1201/b17133-95'.

Kara, S., Stoesser, T., Sturm, T. W. and Mulahasan, S. (2015) 'Flow dynamics through a submerged bridge opening with overtopping', *Journal of Hydraulic Research,* 53(2), 186-195.

Kim, S. J. and Stoesser, T. (2011) 'Closure modeling and direct simulation of vegetation drag in flow through emergent vegetation', *Water Resources Research,* 47(10), W10511.

Kingston, S. (2006) 'Backwater Effects Caused by Bridges', *Report Universidad Politecnica de Cartagena, Cartagena, Spain.*, 1-12.

Koftis, T., Prinos, P. and Papakyritsis, C. (2014) 'Reynolds stress modeling of flow in compound channels with vegetated floodplains', *ICHE , Hamburg - Lehfeldt & Kopmann (eds) - © Bundesanstalt für Wasserbau ISBN 978-3-939230-32-8*, pp: 215-223.

Koken, M. and Constantinescu, G. (2008) 'An investigation of the flow and scour mechanisms around isolated spur dikes in a shallow open channel: 1. Conditions corresponding to the initiation of the erosion and deposition process', *Water Resources Research,* 44(W08406).

Koken, M. and Constantinescu, G. (2009) 'An investigation of the dynamics of coherent structures in a turbulent channel flow with a vertical sidewall obstruction', *Physics of Fluids (1994-present),* 21(8), 085104.

Koken, M. and Constantinescu, G. (2011) 'Flow and turbulence structure around a spur dike in a channel with a large scour hole', *Water Resources Research,* 47(12).

Kothyari, U. C., Hayashi, K. and Hashimoto, H. (2009) 'Drag coefficient of unsubmerged rigid vegetation stems in open channel flows', *Journal of Hydraulic Research,* 47(6), 691-699.

Kozioł, A. and Kubrak, J. (2015) 'Measurements of turbulence structure in a cmpound channel' in Rowiński, P. and Radecki-Pawlik, A., eds., *Rivers – Physical, Fluvial and Environmental Processes*, Springer International Publishing, 229-254.

Krogstad, P.-Å., Andersson, H. I., Bakken, O. M. and Ashrafian, A. (2005) 'An experimental and numerical study of channel flow with rough walls', *Journal of Fluid Mechanics,* 530, 327-352.

Leal, J. B., Filonovich, M., Azevedo1, R. and Rojas-Solorzano, L. R. (2010) 'Simulation of the velocity feild in compound channel flow using closure models', *1st European IAHR Congress,4-6 May, Edinburg, Scotland*, 1-6.

Lee, D., Nakagawa, H., Kawaike, K., Baba, Y. and Zhang, H. (2010) 'Inundation flow considering overflow due to water level rise by river structures', *Annuals of Disaster Prevention Research Institute„ Kyoto University, No. 53 B.*

Li, Y., Anim, D. O., Wang, Y., Tang, C., Du, W., Yu, Z. and Acharya, K. (2014) 'An open-channel flume study of flow characteristics through a combined layer of submerged and emerged flexible vegetation', *Ecohydrology,* 7(2), 633-647.

Liu, C. and Shen, Y. (2008) 'Flow structure and sediment transport with impacts of aquatic vegetation ', *Journal of Hydrodynamics, Ser. B,* 20(4), 461–468.

Malavasi, S. and Guadagnini, A. (2003) 'Hydrodynamic loading on river bridges', *Journal of Hydraulic Engineering,* 129(11), 854-861.

Malavasi, S. and Guadagnini, A. (2007) 'Interactions between a rectangular cylinder and a free-surface flow', *Journal of Fluids and Structures,* 23(8), 1137-1148.

Manes, C., Pokrajac, D., Coceal, O. and McEwan, I. (2008) 'On the significance of form-induced stress in rough wall turbulent boundary layers', *Acta Geophysica,* 56(3), 845-861.

Manes, C., Pokrajac, D. and McEwan, I. (2007) 'Double-averaged open-channel flows with small relative submergence', *Journal of Hydraulic Engineering,* 133(8), 896-904.

Marjoribanks, T. I., Hardy, R. J., Lane, S. N. and Parsons, D. R. (2014) 'High-resolution numerical modelling of flow—vegetation interactions', *Journal of Hydraulic Research,* 52(6), 775-793.

Masterman, R. and Thorne, C. (1992) 'Predicting influence of bank vegetation on channel capacity', *Journal of Hydraulic Engineering,* 118(7), 1052-1058.

Mazurczyk, A. (2007) 'Scales of turbulence in compound channels with trees on floodplains', *PUBLS. INST. GEOPHYS. POL. ACAD. SC.,*, 169-176.

Merville, B. W. (1995) 'Bridge abutment scour in compound channels', *Journal of Hydraulic Engineering,* 121(12), 863-868.

Mignot, E., Barthelemy, E. and Hurther, D. (2009a) 'Double-averaging analysis and local flow characterization of near-bed turbulence in gravel-bed channel flows', *Journal of Fluid Mechanics,* 618, 279-303.

Mignot, E., Hurther, D. and Barthelemy, E. (2009b) 'On the structure of shear stress and turbulent kinetic energy flux across the roughness layer of a gravel-bed channel flow', *Journal of Fluid Mechanics,* 638, 423-452.

Miyab, N. M., Afzalimehr, H. and Singh, S. P. (2015) 'Experimental investigation of influence of vegetation on flow turbulence', *International Journal of Hydraulic Engineering,* 4(3), 54-69.

Mulahasan, S., Stoesser, T. and Alvarez, F. (2015) 'Visualization of shear layers in compound channel flows', *10th Pacific Symposium on Flow Visualization and Image Processing Naples, Italy, 15-18 June,* Paper ID: 25.

Nagata, N., Hosoda, T., Nakato, T. and Muramoto, Y. (2005) 'Three-dimensional numerical model for flow and bed deformation around river hydraulic structures', *Journal of Hydraulic Engineering,* 131(12), 1074-1087.

Nehal, L., Yan, Z. M., Xia, J. H. and Khaldi, A. (2012) 'Flow through non-submerged vegetation', *Sixteenth International Water Technology Conference, IWTC 16, Istanbul, Turkey*.

Nepf, H. M. (1999) 'Drag, turbulence, and diffusion in flow through emergent vegetation', *Water Resources Research,* 35(2), 479-489.

Nezu, I. and Onitsuka, K. (2001) 'Turbulent structures in partly vegetated open channel flows with LDA and PIV measurements', *Journal of Hydraulic Research,* 39(6), 629-642.

Nezu, I. and Sanjou, M. (2008) 'Turburence structure and coherent motion in vegetated canopy open-channel flows', *Journal of Hydro-environment Research,* 2(62-90), 62.

Nikora, V. (2009) 'Friction factor for rough-bed flows: interplay of fluid stresses, secondary currents,non-uniformity, and unsteadiness', *Proceedings of the 33rd IAHR Congress, Vancouver (CDROM)*.

Nikora, V., Goring, D., McEwan, I. and Griffiths, G. (2001) 'Spatially Averaged Open-Channel Flow over Rough Bed', *Journal of Hydraulic Engineering,* 127(2), 123-133.

Nikora, V., McEwan, I., McLean, S., Coleman, S., Pokrajac, D. and Walters, R. (2007a) 'Double-Averaging Concept for Rough-Bed Open-Channel and Overland Flows: Theoretical Background', *Journal of Hydraulic Engineering,* 133(8), 873-883.

Nikora, V., McLean, S., Coleman, S., Pokrajac, D., McEwan, I., Campbell, L., Aberle, J., Clunie, D. and Koll, K. (2007b) 'Double-Averaging Concept for Rough-Bed Open-Channel and Overland Flows: Applications', *Journal of Hydraulic Engineering,* 133(8), 884-895.

Nugroho, E. O. and Ikeda, S. (2007) 'Comparison study of flow in a compound channel: Experimental and numerical method using large eddy simulation SDS-2DH Model', *Eng. Sci.,* 39 B(No.2), 67-97.

Okamoto, S., Seo, S., Nakaso, K. and Kawai, I. (1993) 'Turbulent shear flow and heat transfer over the repeated two-dimensional square ribs on ground plane', *Journal of fluids engineering,* 115(4), 631-637.

Oliveto, G. and Hager, W. H. (2002) 'Temporal evolution of clear-water pier and abutment scour', *Journal of Hydraulic Engineering,* 128(9), 811-820.

Pagliara, S. and Chiavaccini, P. (2006) 'Flow resistance of rock chutes with protruding boulders', *Journal of Hydraulic Engineering,* 132(6), 545-552.

Pagliara, S., Das, R. and Carnacina, I. (2008) 'Flow resistance in large-scale roughness condition', *Canadian Journal of Civil Engineering,* 35(11), 1285-1293.

Paik, J., Ge, L. and Sotiropoulos, F. (2004) 'Toward the simulation of complex 3D shear flows using unsteady statistical turbulence models', *International Journal of Heat and Fluid Flow,* 25(3), 513-527.

Paik, J. and Sotiropoulos, F. (2005) 'Coherent structure dynamics upstream of a long rectangular block at the side of a large aspect ratio channel', *Physics of Fluids (1994-present),* 17(11), 115104.

Parola, A. C., Hagerty, D. J. and Kamojjala, S. (1998) 'Highway infrastructure damage caused by the 1993 upper Mississipi River basin flooding', *Report No. 417-NCHRP, Transportation Research Board, Washington, DC.*

Pasche, E. and Rouvé, G. (1985) 'Overbank flow with vegetatively roughened floodPlains', *Journal of Hydraulic Engineering,* 111(9), 1262-1278.

Perry, A. E., Schofield, W. H. and Joubert, P. N. (1969) 'Rough wall turbulent boundary layers', *Journal of Fluid Mechanics / Volume 37 / Issue 02 / June 1969, pp 383- 413,* 37(02), pp 383- 413.

Petryk, S. and Bosmajian, G. (1975) 'Analysis of flow through vegetation', *Journal of the Hydraulics Division,* 101(7), 871-884.

Picek, T., Havlik, A., Mattas, D. and Mares, K. (2007) 'Hydraulic calculation of bridges at high water stages', *Journal of Hydraulic Research,* 45(3), 400-406.

Pope, S. B. (2000) 'Free shear flows". In Turbulent flows, Cambridge University', 139–144.

Rajaratnam, N. and Ahmadi, R. (1981) 'Hydraulics of channels with flood-plains', *Journal of Hydraulic Research,* 19(1), 43-60.

Rameshwaran, P. and Shiono, K. (2007) 'Quasi two-dimensional model for straight overbank flows through emergent vegetation on floodplains', *Journal of Hydraulic Research,* 45(3), 302-315.

Raupach, M. R., Antonia, R. A. and Rajagopalan (1991) 'Rough-wall turbulent boundary layers', *Applied Mechanics Reviews,* 44(1), 1–25.

Rickenmann, D. and Recking, A. (2011) 'Evaluation of flow resistance in gravel-bed rivers through a large field data set', *Water Resources Research,* 47(7), W07538.

Roussinova, V. and Balachandar, R. (2011) 'Open channel flow past a train of rib roughness', *Journal of Turbulence*, N28.

Rummel, A., Brocchini, M., Stocchino, A. and Piattella, A. (2006) 'Horizontal mixing in compound channels: a global shear layer model?'.

Sanjou, M., Nezu, I. and Itai, K. (2010) 'Space-time correlation and momentum exchanges in compound channel flow by simultaneous measurements of two sets of ADVs', *River Flow*, 495-502.

Sarkar, S. and Dey, S. (2010) 'Double-averaging turbulence characteristics in flows over a gravel bed', *Journal of Hydraulic Research,* 48(6), 801-809.

Sellin, R. H. J. (1964) 'A laboratory investigation into the interaction between the flow in the channel of a river and that over its flood plain', *La Houille Blanche,* (7), 793-802.

Shields Jr, F. D. and Gippel, C. J. (1995) 'Prediction of effects of woody debris removal on flow resistance', *Journal of Hydraulic Engineering,* 121(4), 341-354.

Shiono, K. and Knight, D. W. (1991) 'Turbulent open-channel flows with variable depth across the channel', *J . Fluid Meeh.,* 222, 617-646.

Shiono, K., Takeda, M., Yang, K., Sugihara, Y. and Ishigaki, T. (2012) 'Modeling of vegetated rivers for inbank and overbank flows', *Proceedings of the International Conference on Fluvial Hydraulics: River Flow-September 5-7, San Jose, Costa Rica.*, 263-269.

Singh, K., Sandham, N. and Williams, J. (2007) 'Numerical simulation of flow over a rough bed', *Journal of Hydraulic Engineering,* 133(4), 386-398.

Soldini, L., Piattella, A., Mancinelli, A., Bernetti, R. and Brocchini, M. (2004) 'Macrovortices-induced horizontal mixing in compound channels', *Ocean Dynamics,* 54(3-4), 333-339.

Stocchino, A. a. and Brocchini, M. (2010) 'Horizontal mixing of quasi-uniform straight compound channel flows', *Journal of Fluid Mechanics,* 643, 425-435.

Stoesser, T., Kim, S. and Diplas, P. (2010) 'Turbulent flow through idealized emergent vegetation ', *Journal of Hydraulic Engineering,* 136(12), 1003-1017.

Stoesser, T. and Nikora, V. (2008) 'Flow structure over square bars at intermediate submergence: Large Eddy Simulation study of bar spacing effect', *Acta Geophysica,* 56(3), 876-893.

Stoesser, T. and Rodi, W. (2004) 'LES of bar androd roughened channel flow', *The 6th International Conference on Hydroscience and Engineering (ICHE-2004), Brisbane, Australia*.

Stone, B. and Shen, H. (2002) 'Hydraulic resistance of flow in channels with cylindrical roughness', *Journal of Hydraulic Engineering,* 128(5), 500-506.

Sturm, T. W. (2006) 'Scour around bankline and setback abutments in compound channels', *Journal of Hydraulic Engineering,* 132(1), 21-32.

Sun, X. and Shiono, K. (2009) 'Flow resistance of one-line emergent vegetation along the floodplain edge of a compound open channel', *Advances in Water Resources,* 32(3), 430-438.

Tamai, N., Asaeda, T. and Ikeda, H. (1986) 'Study on Generation of Periodical Large Surface Eddies in a Composite Channel Flow', *Water Resources Research,* 22(7), 1129-1138.

Tang, X. and Knight, D. W. (2008) 'Lateral depth-averaged velocity distributions and bed shear in rectangular compound channels', *Journal of Hydraulic Engineering,* 134(9), 1337-1342.

Tang, X., Sterling, M. and Knight, D. W. (2010) 'A General analytical model for lateral velocity distributions in vegetated channels', *River Flow 2010 - Dittrich, Koll, Aberle & Geisenhainer (eds) - © 2010 Bundesanstalt für Wasserbau ISBN 978-3-939230-00-7*.

Tanino, Y. and Nepf, H. (2008) 'Laboratory investigation of mean drag in a random array of rigid, emergent cylinders', *Journal of Hydraulic Engineering,* 134(1), 34-41.

Terrier, B. (2010) 'Flow characteristics in straight compound channels with vegetation along the main channel', *Dissertation presented to Department of Civil and Building Engineering Loughborough University*.

Terrier, B., Peltier, Y., Shiono, K., Paquier, A. and Rivière, N. (2011) 'Influence of one-line vegetation on the edge of the floodplain on velocity and boundary shear stress distributions in compound channel', *Conference: 34th IAHR Congr.: Balance and Uncertainty, Water in a Changing World, 26 June - 01 July 2011, At Brisbane, Australia.*

Terrier, B., Robinson, S., Shiono, K., Paquier, A. and Ishigaki, T. (2010) 'Influence of vegetation to boundary shear stress in open channel for overbank flow', *River Flow*

2010 - Dittrich, Koll, Aberle & Geisenhainer (eds) - © 2010 Bundesanstalt für Wasserbau ISBN 978-3-939230-00-7, 1-8.

Teruzzi, A., Ballio, F. and Armenio, V. (2009) 'Turbulent stresses at the bottom surface near an abutment: laboratory-scale numerical experiment', *Journal of Hydraulic Engineering,* 135(2), 106-117.

Teymourei, E., Barani, G. A., Janfeshan , H. and A., D. A. (2013) 'Determination of SKM mathematical model for estimation of transverse velocity distribution in compound channels', *Journal of Basic and Applied Scientific Research,* 3(2s), PP:682-688.

Thompson, S. M. and Campbell, P. L. (1979) 'Hydraulics of a large channel paved with boulders', *Journal of Hydraulic Research,* 17(4), 341-354.

Thornton, C. I., Abt, S. R., Morris, C. E. and Fischenich, J. C. (2000) 'Calculating shear stress at channel-overbank interfaces in straight channels with vegetated floodplains', *Journal of Hydraulic Engineering,* 126(12), 929-939.

Tinoco, R. O. and Cowen, E. A. (2013) 'The direct and indirect measurement of boundary stress and drag on individual and complex arrays of elements', *Experiments in fluids manuscript,* 54(4), 1-16.

Tominaga, A. and Nezu, I. (1991) 'Turbulent structure in compound open-channel flows', *Journal of Hydraulic Engineering,* 117(1), 21-41.

Tsihrintzis, V., Wu, F., Shen, H. and Chou, Y. (2001) 'Discussion and Closure: Variation of roughness coefficients for unsubmerged and submerged vegetation', *Journal of Hydraulic Engineering,* 127(3), 241-245.

Uijttewaal, W. (2011) 'Horizontal mixing in shallow flows', *Proceedings of the 34th World Congress of the International Association for Hydro- Environment Research and Engineering: 33rd Hydrology and Water Resources Symposium and 10th Conference on Hydraulics in Water Engineering*.

Valyrakis, M., Liu, D., Mcgann, N., Turker, U. and Yagci, O. (2015) 'Characterrising the effect of increasing river bank vegetation on the flow field across the channel', *E-proceedings of the 36th IAHR World Congress 28 June – 3 July, 2015, The Hague, the Netherland*.

van Prooijen, B. C., Battjes, J. A. and Uijttewaal, W. S. J. (2005) 'Momentum exchange in straight uniform compound channel flow', *Journal of Hydraulic Engineering,* 131(3), 175 - 183.

van Prooijen, B. C. and Uijttewaal, W. S. J. (2002) 'A linear approach for the evolution of coherent structures in shallow mixing layers', *Physics of Fluids,* 14(12), 4105-4114.

Vermaas, D. A., Uijttewaal, W. S. J. and Hoitink, A. J. F. (2011) 'Lateral transfer of streamwise momentum caused by a roughness transition across a shallow channel', *Water Resources Research,* 47(2), 1-12.

White, B. L. and Nepf, H. M. (2007) 'Shear instability and coherent structures in shallow flow adjacent to a porous layer', *Journal of Fluid Mechanics,* 593, 1-32.

White, B. L. and Nepf, H. M. (2008) 'A vortex-based model of velocity and shear stress in a partially vegetated shallow channel', *Water Resources Research,* 44(1).

Wu, F.-C., Shen, H. W. and Chou, Y.-J. (1999) 'Variation of roughness coefficients for unsubmerged and submerged vegetation', *Journal of Hydraulic Engineering,* 125(9), 934-942.

Wunder, S., Lehmann, B. and Nestmann, F. (2011) 'Determination of the drag coefficients of emergent and just submerged willows', *International Journal of River Basin Management,* 9(3-4), 231-236.

Yagci, O. and Kabdasli, M. S. (2008) 'The impact of single natural vegetation elements on flow characteristics', *Hydrological Processes,* 22(21), 4310-4321.

Yang, K., Cao, S. and Knight, D. (2007) 'Flow patterns in compound channels with vegetated floodplains', *Journal of Hydraulic Engineering,* 133(2), 148-159.

Yang, K., Nie, R., Liu, X. and Cao, S. (2013) 'Modeling depth-averaged velocity and boundary shear stress in rectangular compound channels with secondary flows', *Journal of Hydraulic Engineering,* 139(1), 76-83.

NOMENCLATURE

The following symbols were used in this paper:

A	cross sectional area of flow
A_{bed}	area of bed occupied by vegetation
A_f	projected area
A_{shear}	shear area
A_{veg}	area of vegetation
a	vegetation density
B	lateral constriction width
B_B	percent flow blockage
B_{comp}	overall compound channel width
B_{mc}	main channel width
C_D	drag coefficient
C_{D_v}	vegetated drag coefficient
D	cylinder diameter
F_B	percentage blockage
F_D	drag force
F_f	wall friction
F_G	gravity force
Fr	Froude number
F_S	bed shear force
F_τ	interface shear stress force
f	Darcy-Weisbach friction factor
g	gravitational acceleration
H	flow depth
H_m	maximum depth
H_{mc}	depth of flow in the main channel
h_f	depth of flow on the floodplain

h_a	bridge opening height
h_d	bridge thickness
k	roughness height
L	roughness height
L_s	longitudinal spacing
l	channel reach length
m	number of cylinders per unit area
Q	discharge
q	discharge per unit width
R	hydraulic radius
Re	Reynolds number based on bulk velocity
Re_D	cylinder Reynolds number
Re_R	Reynolds number based on hydraulic radius
Re_τ	friction Reynolds number
Re_v	vegetated Reynolds number
r_v	vegetated-related hydraulic radius
S	channel bed slope
s	centre-to-centre spacing
U	streamwise velocity
u	depth-averaged longitudinal velocity
U_a	average velocity approaching the cylinder
U_b	bulk flow velocity
U_{dip}	velocity of the flow near to the interface
U_{fp}	velocity of flow on the floodplain
U_{mc}	velocity of flow in the main channel
U_{veg}	velocity of flow within the vegetation elements
u_{bulk}	bulk flow velocity
u_*	shear velocity
V_{veg}	volume occupied by vegetation

W	flume width
x	streamwise interval
y	lateral distance
y_c	critical depth
z	vertical elevation
α_0 & α_1	functions of solid volume fraction
γ	specific weight of water
ξ	parameter representing the cylinder staggered pattern
ν	kinematic viscosity
ρ	density of water
τ	bed shear stress
τ_b	bed shear stress
τ_{int}	apparent shear stresses at the interface
ϕ	vegetation density
φ	roughness geometry function
Ψ	proportionality coefficient
ψ	streamfunction
λ	crest-to-crest bar spacing
$\delta 1$	shear layer thickness inside the vegetation
$\delta 2$	shear layer thickness inside the main channel
H/k	submergence ratio; roughness height
L_s/D	aspect ratio
p/k	spacing ratio
D/W	blockage factor
B/W	contraction ratio

ABBREVIATIONS

FP	floodplain
MC	main channel
LES	Large Eddy Simulation
PIV	particle image velocimetry
SVF	solid volume fraction
tke	total kinetic energy

APPENDIXES I

Table 0-1: Hydraulic characteristics of flow conditions over large-scale roughness

Slope	Discharge Q (l/s)	Water depth H (cm)	Pitch-to-pitch λ (cm)	Bulk velocity U_b (m/s)	Shear velocity u* (m/s)	Reynolds number $Re=U_bH/\nu$	Roughness Reynolds number $Re^*=U_bk/\nu$	Froude number $Fr=U_b/(gH)^{0.5}$	Friction factor $f=8gRS/U_b^2$
0.020	1.70	2.53	6.25	0.224	0.070	5346	13206	0.286	0.677
	2.00	2.68	6.25	0.249	0.073	6289	14667	0.318	0.577
	2.50	2.93	6.25	0.284	0.076	7862	16770	0.363	0.476
	3.00	3.16	6.25	0.316	0.079	9434	18659	0.404	0.409
	3.88	3.52	6.25	0.367	0.083	12201	21664	0.469	0.331
	6.00	4.35	6.25	0.460	0.092	18868	27109	0.587	0.250
	8.00	5.07	6.25	0.526	0.100	25157	31043	0.672	0.214
	1.70	2.96	12.5	0.191	0.076	5346	11288	0.244	1.059
	2.00	3.21	12.5	0.208	0.079	6289	12246	0.265	0.962
	2.50	3.54	12.5	0.235	0.083	7862	13880	0.301	0.811
	3.00	3.93	12.5	0.254	0.088	9434	15003	0.325	0.755
	4.00	4.09	12.5	0.326	0.090	12579	19222	0.416	0.475
	6.00	4.37	12.5	0.458	0.093	18868	26985	0.584	0.254
	8.00	5.60	12.5	0.476	0.105	25157	28077	0.608	0.282
0.005	1.60	3.70	6.25	0.144	0.043	5031	8499	0.184	0.561
	2.00	3.91	6.25	0.171	0.044	6289	10053	0.218	0.419
	2.50	4.37	6.25	0.191	0.046	7862	11244	0.244	0.365
	3.00	4.81	6.25	0.208	0.049	9434	12258	0.266	0.331
	4.00	5.40	6.25	0.247	0.051	12579	14559	0.315	0.256
	5.00	6.07	6.25	0.275	0.055	15723	16190	0.351	0.225
	6.00	6.75	6.25	0.296	0.058	18868	17470	0.378	0.208
	8.00	7.75	6.25	0.344	0.062	25157	20288	0.439	0.169
	10.00	9.70	6.25	0.344	0.069	31447	20262	0.439	0.196
	1.70	4.03	12.5	0.141	0.044	5346	16582	0.127	0.630
	2.00	4.20	12.5	0.159	0.045	6289	18718	0.143	0.511
	2.50	4.68	12.5	0.178	0.048	7862	20998	0.161	0.441
	3.00	5.19	12.5	0.193	0.050	9434	22721	0.174	0.408
	4.00	5.84	12.5	0.228	0.054	12579	26923	0.206	0.316
	5.00	6.63	12.5	0.251	0.057	15723	29644	0.227	0.286
	6.00	7.33	12.5	0.273	0.060	18868	32176	0.246	0.260
	8.00	7.95	12.5	0.335	0.062	25157	39555	0.303	0.181
0.001	1.60	5.11	6.25	0.104	0.019	5302	12969	0.147	0.275
	2.00	5.74	6.25	0.116	0.020	6627	14431	0.155	0.242
	2.50	6.36	6.25	0.131	0.021	8284	16281	0.166	0.204
	3.00	6.95	6.25	0.144	0.022	9940	17878	0.174	0.180
	4.00	8.05	6.25	0.166	0.023	13254	20580	0.186	0.150
	5.00	9.10	6.25	0.183	0.024	16567	22757	0.194	0.133
	6.00	10.05	6.25	0.199	0.024	19881	24730	0.200	0.119
	8.00	11.51	6.25	0.232	0.025	26508	28795	0.218	0.095
	10.00	12.86	6.25	0.259	0.026	33135	32207	0.231	0.081
	1.70	5.64	12.5	0.100	0.020	5633	12484	0.135	0.319
	2.00	6.06	12.5	0.110	0.021	6627	13669	0.143	0.280
	2.50	6.96	12.5	0.120	0.022	8284	14877	0.145	0.260
	3.00	7.60	12.5	0.132	0.022	9940	16349	0.152	0.229
	4.00	8.80	12.5	0.152	0.023	13254	18826	0.163	0.190
	6.00	11.07	12.5	0.181	0.025	19881	22441	0.173	0.153
	8.00	12.50	12.5	0.213	0.026	26508	26508	0.193	0.118

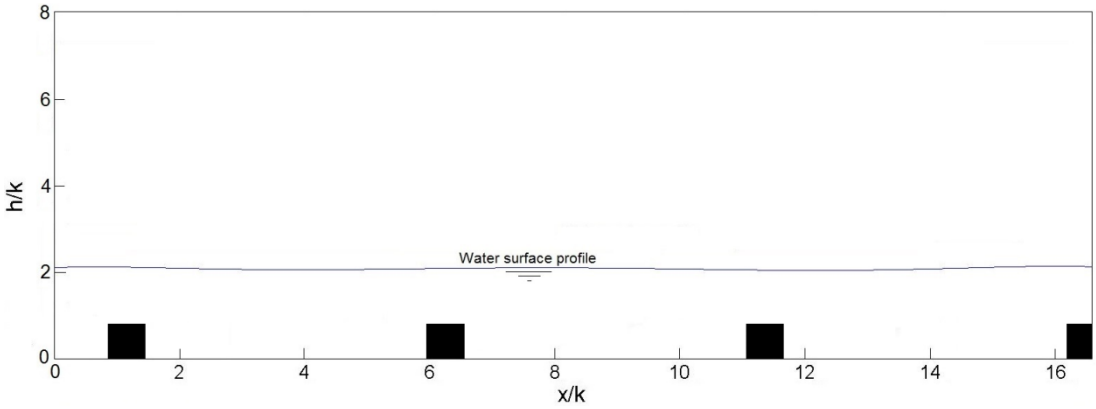

Figure 0-1 Mean-averaged free surface profile (average of 1500 images) of Q=1.7 l/sec, S=1:50, p=6.25 cm and H=2.53 cm.

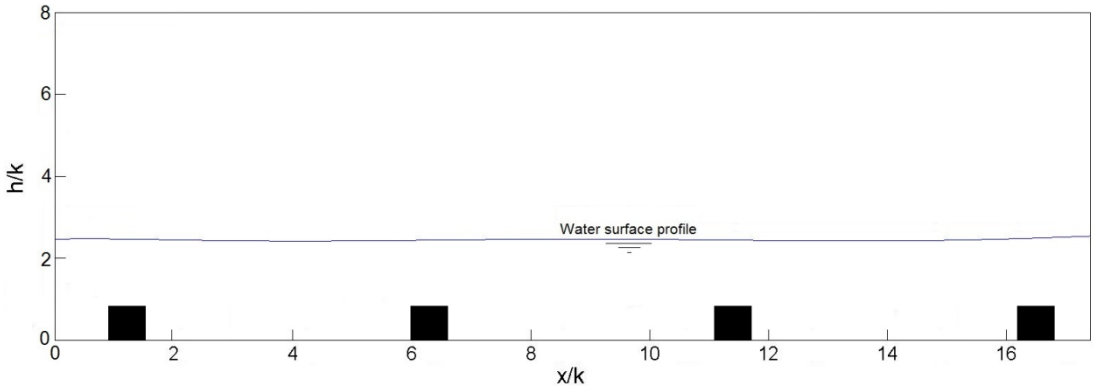

Figure 0-2 Mean-averaged free surface profile (average of 1500 images) of Q=2.5 l/sec, S=1:50, p=6.25 cm and H=2.93 cm.

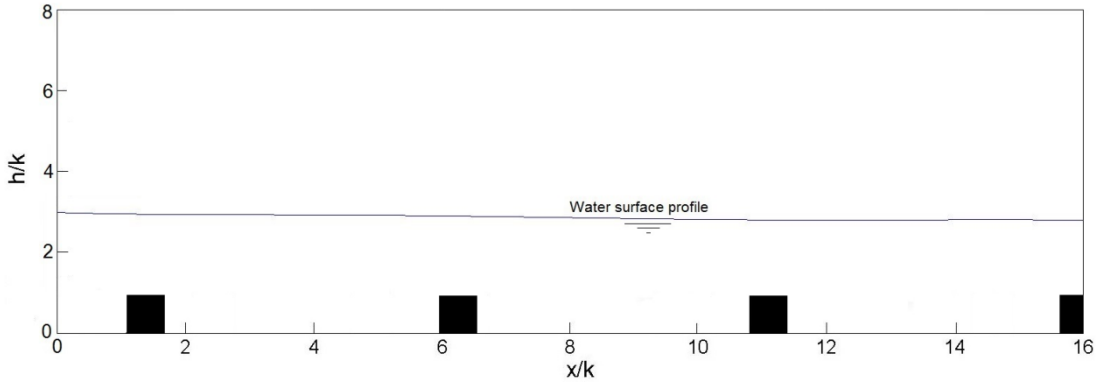

Figure 0-3 Mean-averaged free surface profile (average of 1500 images) of Q=4.0 l/sec, S=1:50, p=6.25 cm and H=3.52 cm.

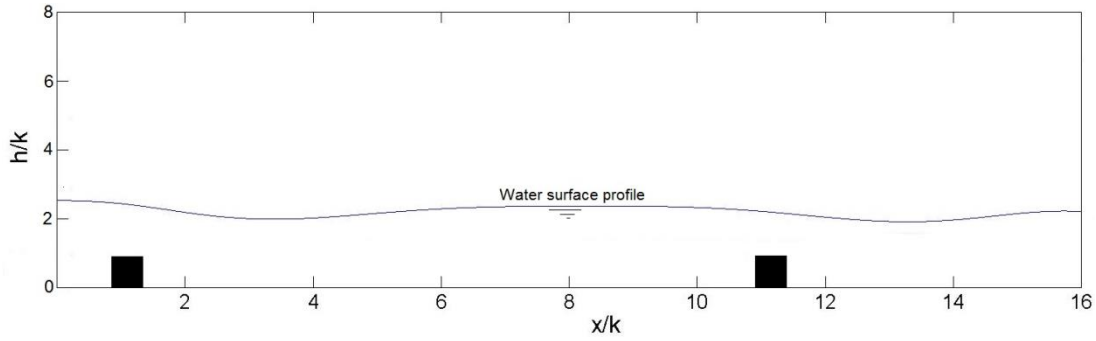

Figure 0-4 Mean-averaged free surface profile (average of 1500 images) of Q=1.7 l/sec, S=1:50, p=12.5 cm and H=2.96 cm.

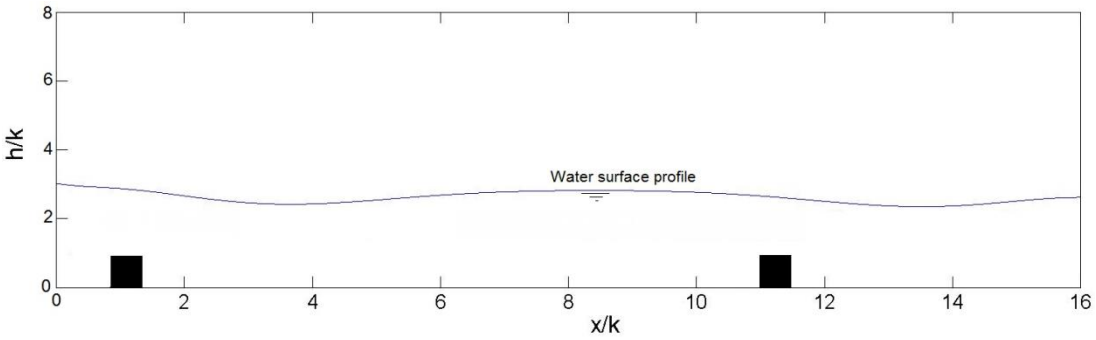

Figure 0-5 Mean-averaged free surface profile (average of 1500 images) of Q=2.5 l/sec, S=1:50, p=12.5 cm and H=3.54 cm.

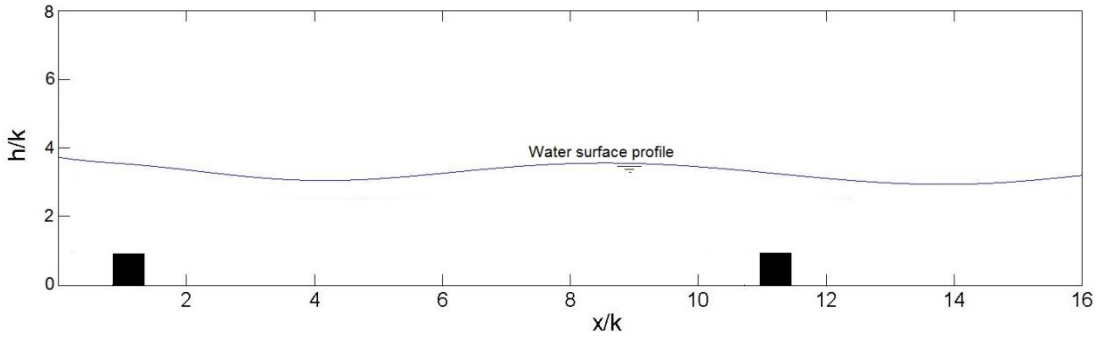

Figure 0-6 Mean-averaged free surface profile (average of 1500 images) of Q=4.0 l/sec, S=1:50, p=12.5 cm and H=4.24 cm.

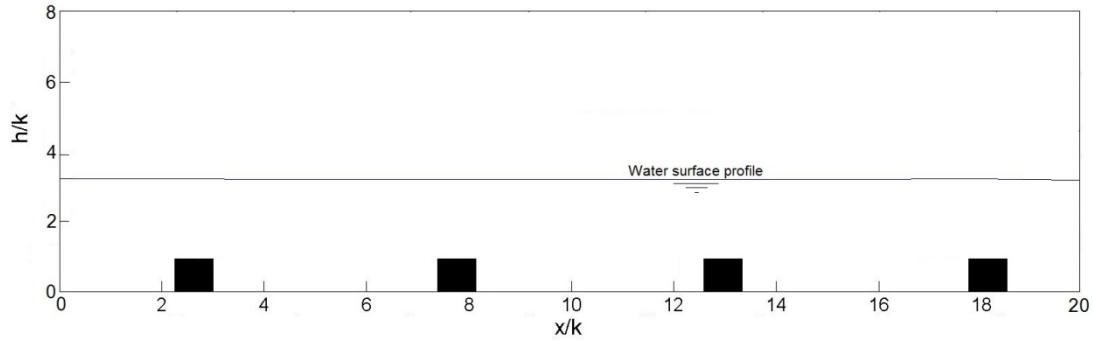

Figure 0-7 Mean-averaged free surface profile (average of 1500 images) of Q=1.7 l/sec, S=1:200, p=6.25cm and H=3.89 cm.

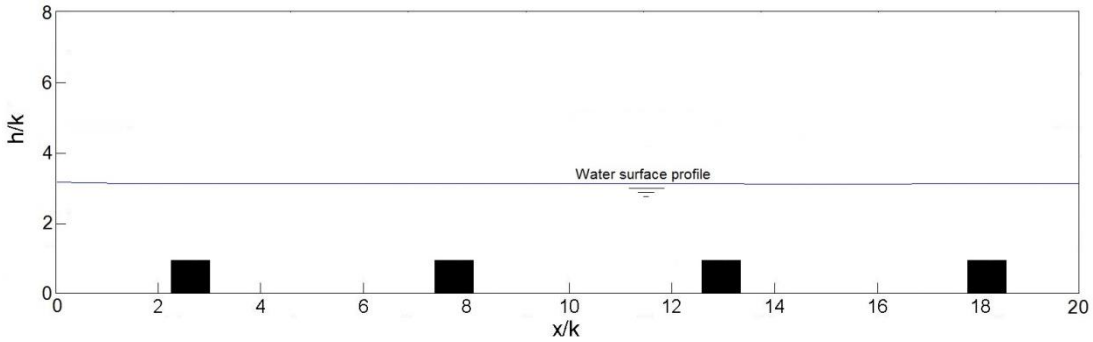

Figure 0-8 Mean-averaged free surface profile (average of 1500 images) of Q=2.5 l/sec, S=1:200, p=6.25 cm and H=4.30 cm.

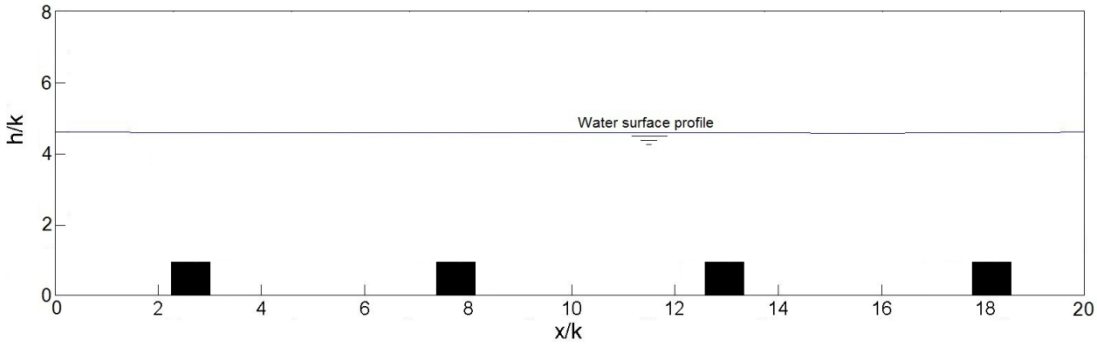

Figure 0-9 Mean-averaged free surface profile (average of 1500 images) of Q=4.0 l/sec, S=1:200, p=6.25 cm and H=5.40 cm.

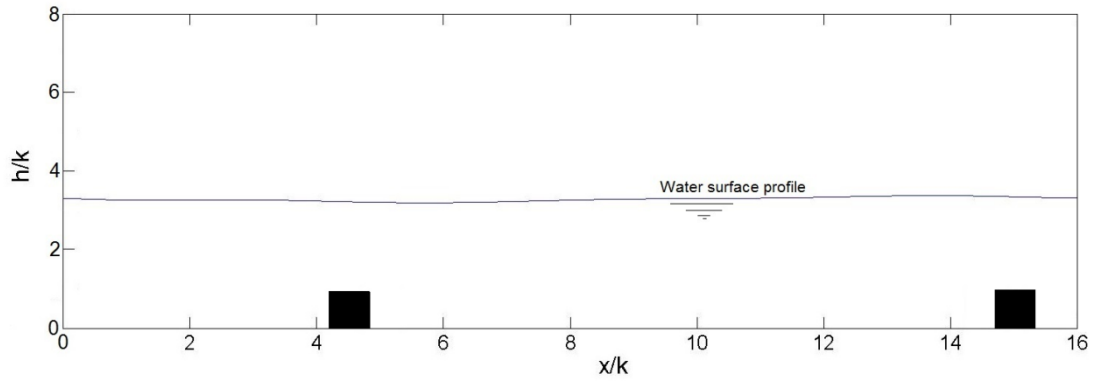

Figure 0-10 Mean-averaged free surface profile (average of 1500 images) of Q=1.7 l/sec, S=1:200, p=12.5 cm and H=4.03 cm.

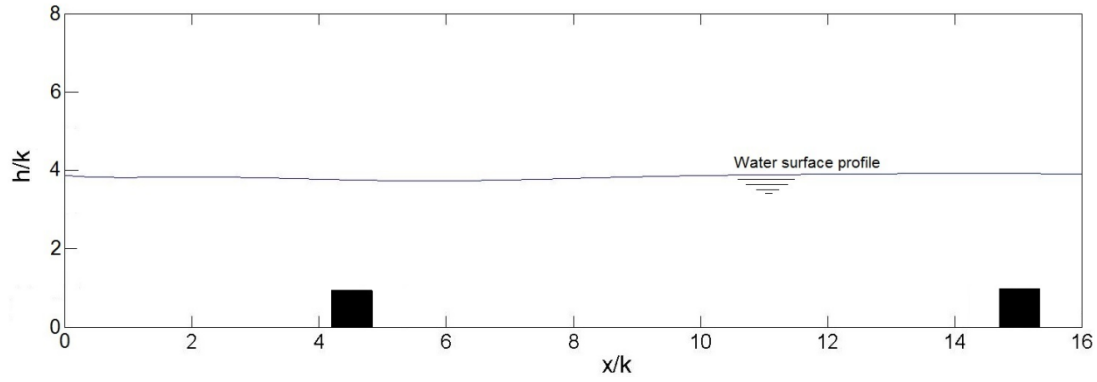

Figure 0-11 Mean-averaged free surface profile (average of 1500 images) of Q=2.5 l/sec, S=1:200, p=12.5 cm and H=4.68 cm.

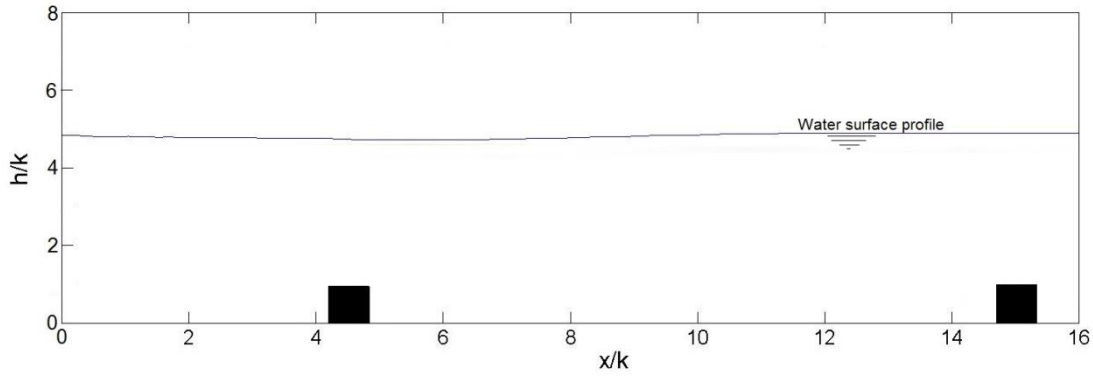

Figure 0-12 Mean-averaged free surface profile (average of 1500 images) of Q=4.0 l/sec, S=1:200, p=12.5 cm and H=5.84 cm.

a)

b)

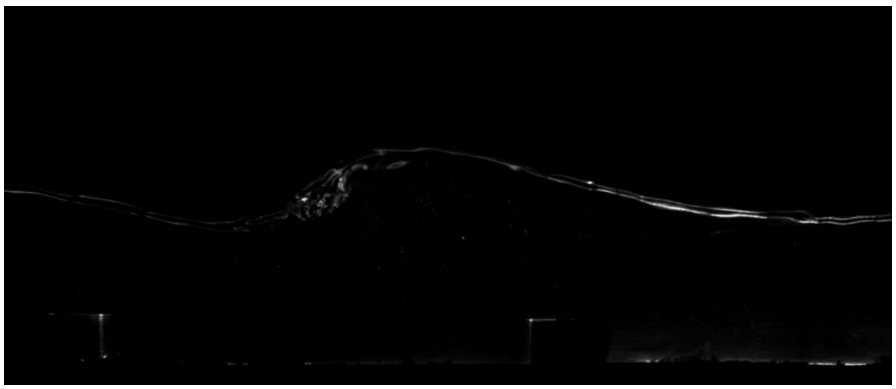

c)

Figure 0-13: Examples of instantaneous free surface profiles of bed slope S=0.02 and roughness spacing, λ/k = 10.4 for a) and H/k = 2.4, b) H/k= 2.95, and c) H/k = 3.53.

a)

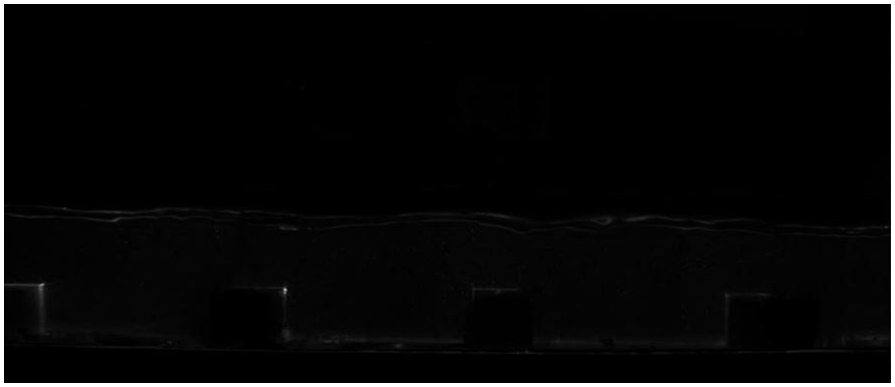

b)

c)

Figure 0-14: Examples of instantaneous free surface profiles of bed slope S=0.02 and roughness spacing, λ/k = 5.2 for a) and H/k = 2.1, b) H/k= 2.44, and c) H/k = 2.93.

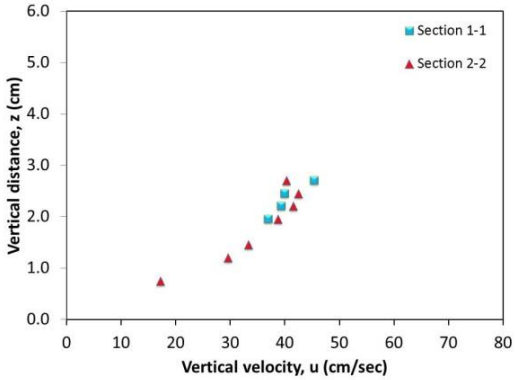

a) Q=1.7 l/sec, S=1/50, λ/k=5.2

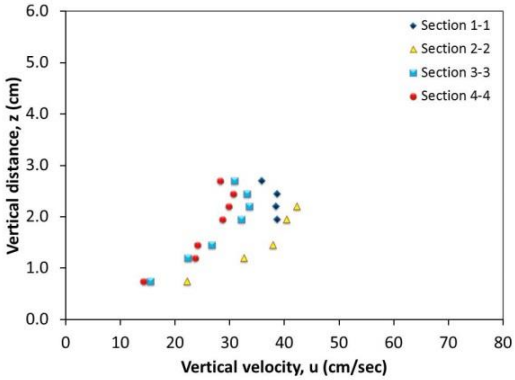

b) Q=1.7 l/sec, S=1/50, λ/k=10.4

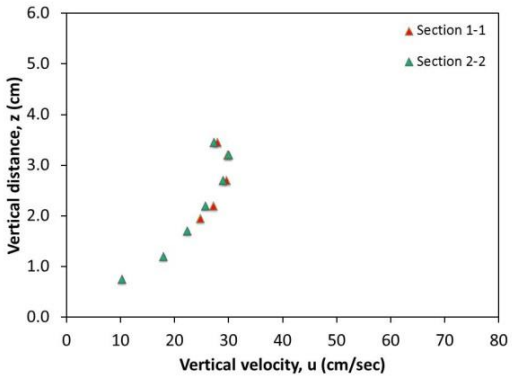

c) Q=1.7 l/sec, S=1/200, λ/k=5.2

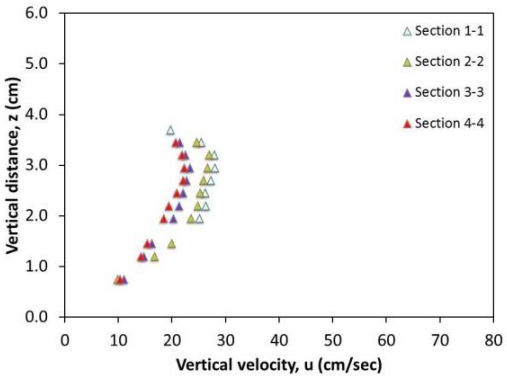

d) Q=1.7 l/sec, S=1/200, λ/k=10.4

Figure 0-15: Vertical distribution of main flow velocity of flow rate Q=1.7 l $s^{-1}$for a) S=1/50, λ/k=5.2, b) S=1/50, λ/k=10.4, c) S=1/200, λ/k=5.2 and d) S=1/200, λ/k=10.4.

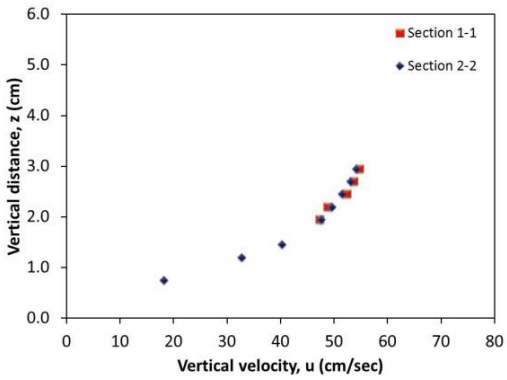

a) Q= 2.5 l/sec, S=1/50, λ/k=5.2

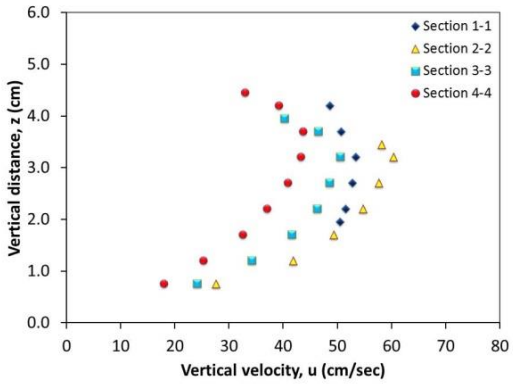

b) Q= 2.5 l/sec, S=1/50, λ/k=10.4

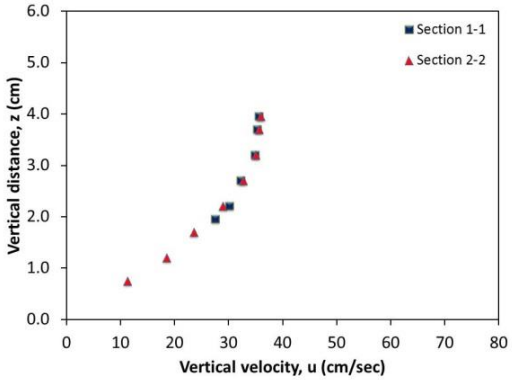

c) Q=2.5 l/sec, S=1/200, λ/k=5.2

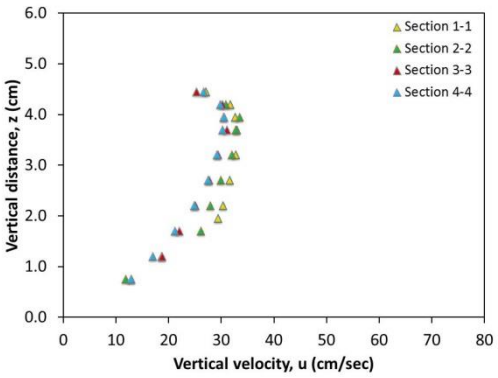

d) Q=2.5 l/sec, S=1/200, λ/k=10.4

Figure 0-16: Vertical distribution of main flow velocity of flow rate Q=2.5 l $s^{-1}$for a) S=1/50, λ/k=5.2, b) S=1/50, λ/k=10.4, c) S=1/200, λ/k=5.2 and d) S=1/200, λ/k=10.4.

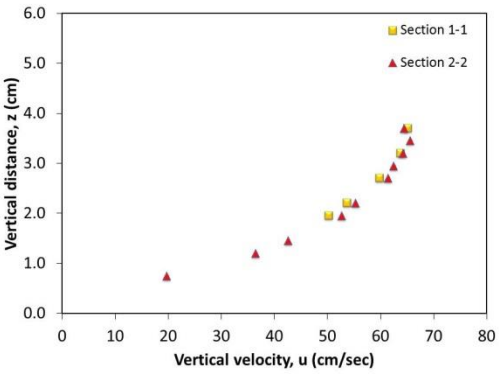

a) Q=4.0 l/sec, S=1/50, λ/k=5.2

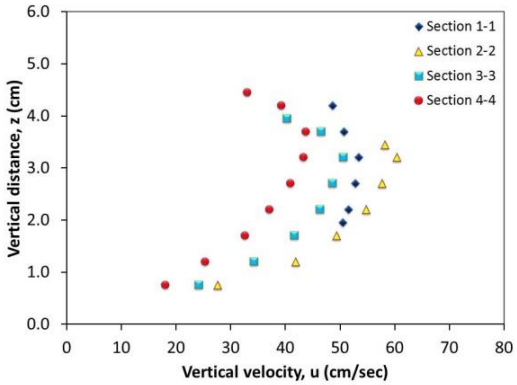

b) Q=4.0 l/sec, S=1/50, λ/k=10.4

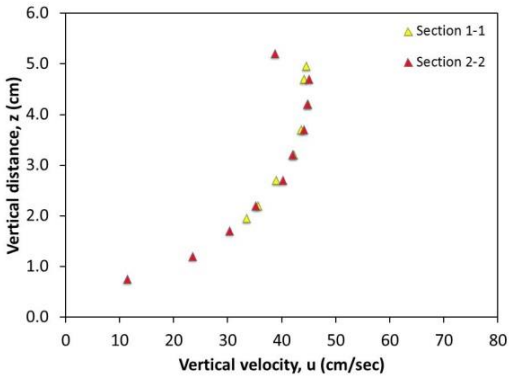

c) Q=4.0 l/sec, S=1/200, λ/k=5.2

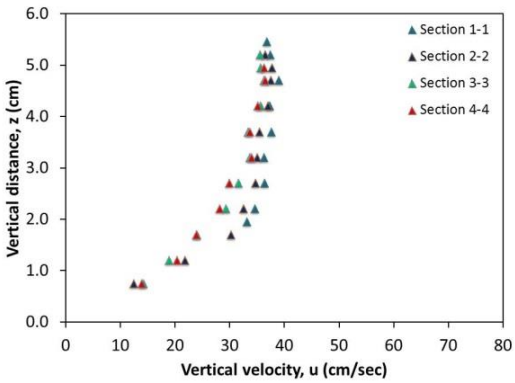

d) Q=4.0 l/sec, S=1/200, λ/k=10.4

Figure 0-17: Vertical distribution of main flow velocity of flow rate Q=4.0 l $s^{-1}$for a) S=1/50, λ/k=5.2, b) S=1/50, λ/k=10.4, c) S=1/200, λ/k=5.2 and d) S=1/200, λ/k=10.4.

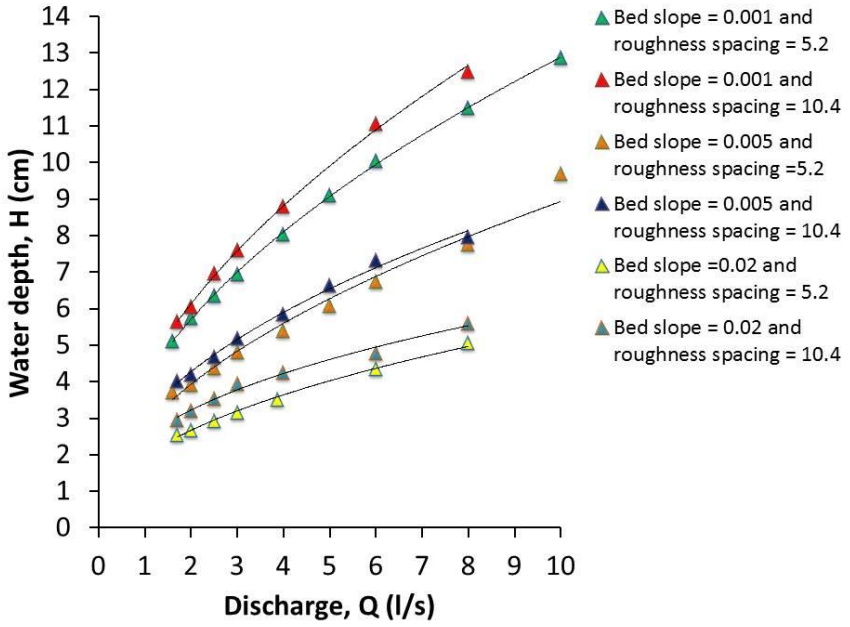

Figure 0-18: Uniform flow depth and flow discharge relationship

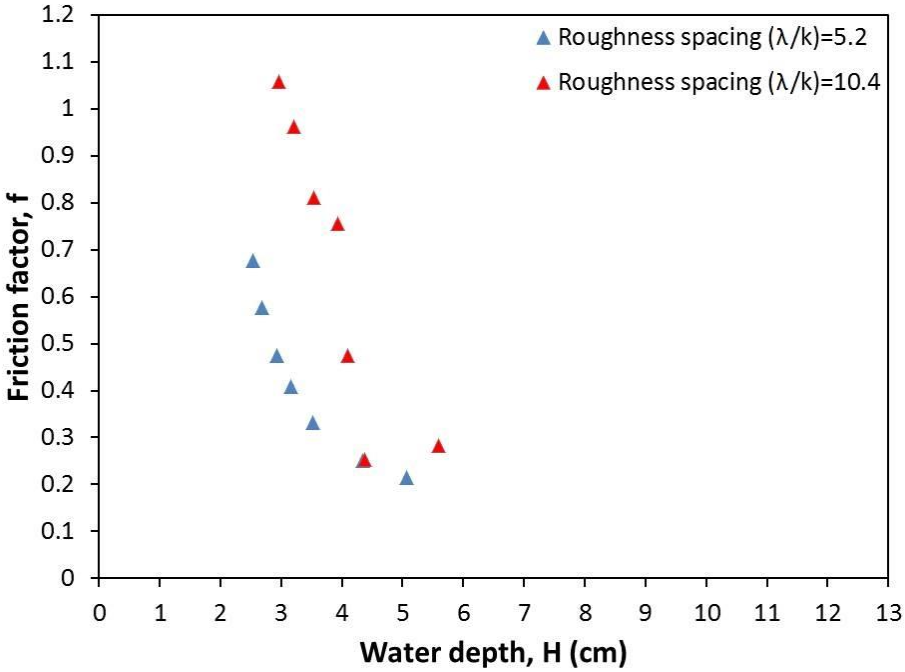

Figure 0-19: Friction factor-water depth relationship for ribbed flume of 30 cm width and bed slope of 1/50.

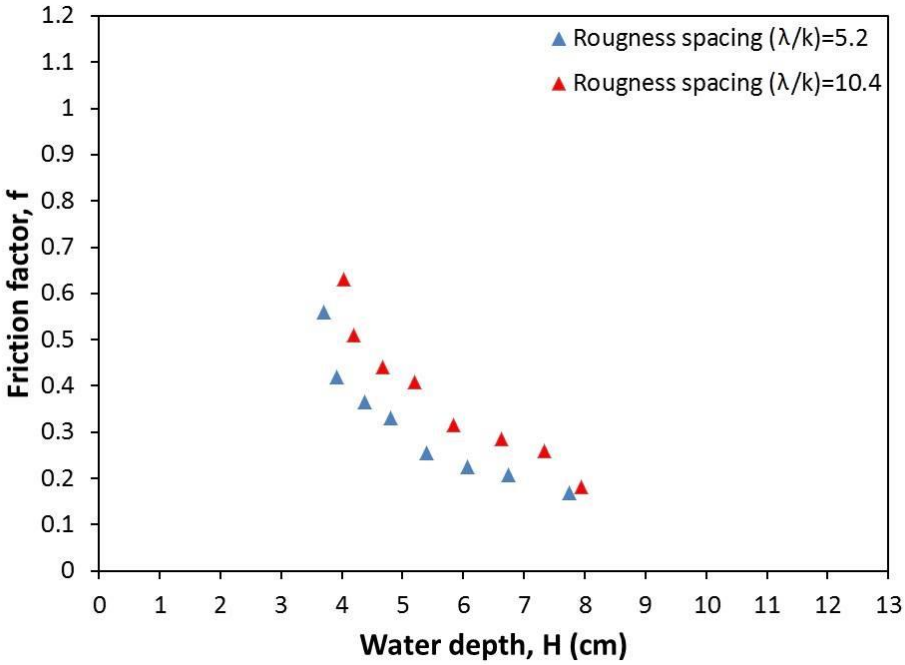

Figure 0-20: Friction factor-water depth relationship for ribbed flume of 30 cm width and bed slope of 1/200.

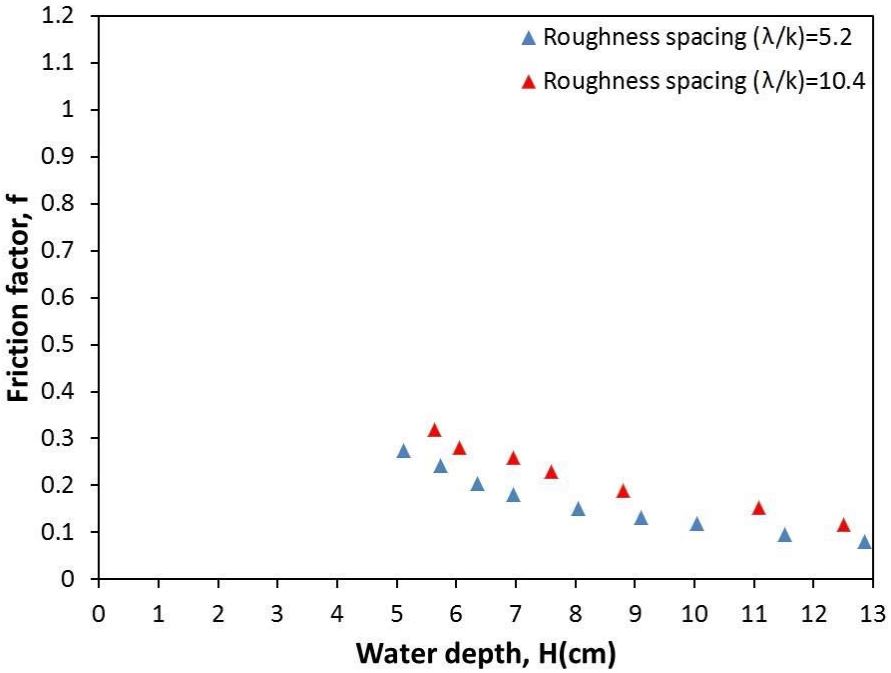

Figure 0-21: Friction factor-water depth relationship for ribbed flume of 30 cm width and bed slope of 1/1000.